Impact of saline plume on containment properties of natural porous materials in geological disposal context : An experimental and REV simulation approach to go beyond Archie's law

Ashish Rajyaguru

PSL UNIVERSITÉ PARIS

THÈSE DE DOCTORAT
DE L'UNIVERSITÉ PSL

Préparée à MINES ParisTech

Impact d'un panache salin sur les propriétés de confinement de matériaux poreux naturels : Approche expérimentale et numérique pour aller au-delà de la loi de Archie

Soutenue par
RAJYAGURU Ashish
Le 22 Octobre 2018

Ecole doctorale n° 398
Géosciences, Ressources Naturelles et Environnement

Spécialité
Géosciences et Géo-ingénierie

Composition du jury :

M. Emmanuel TERTRE Prof, University of Poitiers, France	*Président*
M. Urs MÄDER PD Dr, Institut für Geologie, Switzerland	*Rapporteur*
M. Laurent TRUCHE ISTerre Grenoble, France	*Rapporteur*
Mme. Catherine NOIRIEL Asst Prof, GET Toulouse, France	*Examinateur*
M. Charles WITTEBROODT Dr, IRSN, Fontenay aux Roses, France	*Invité*
M. Valery DETILLEUX Dr, BEL V, Belgium	*Invité*
M. Sébastien SAVOYE Dr. HAB, CEA Saclay, France	*Directeur de thèse*
M. Vincent LAGNEAU Prof., Mines ParisTech, France	*Directeur de thèse*

MINES ParisTech | PSL

PSL UNIVERSITÉ PARIS

THÈSE DE DOCTORAT
DE L'UNIVERSITÉ PSL

Préparée à MINES ParisTech

Impact of saline plume on containment properties of natural porous materials in geological storage context: An experimental and REV simulation approach to go beyond Archie's law

Soutenue par
RAJYAGURU Ashish
Le 22 Octobre 2018

Ecole doctorale n° 398
Géosciences, Ressources Naturelles et Environnement

Spécialité
Géosciences et Géo-ingénierie

Composition du jury :

M. Emmanuel TERTRE Prof, University of Poitiers, France	*Président*
M. Urs MÄDER PD Dr, Institut für Geologie, Switzerland	*Rapporteur*
M. Laurent TRUCHE ISTerre Grenoble, France	*Rapporteur*
Mme. Catherine NOIRIEL Asst Prof, GET Toulouse, France	*Examinateur*
M. Charles WITTEBROODT Dr, IRSN, Fontenay aux Roses, France	*Invité*
M. Valery DETILLEUX Dr, BEL V, Belgium	*Invité*
M. Sébastien SAVOYE Dr. HAB, CEA Saclay, France	*Directeur de thèse*
M. Vincent LAGNEAU Prof., Mines ParisTech, France	*Directeur de thèse*

MINES ParisTech | PSL

DE LA RECHERCHE À L'INDUSTRIE cea

IRSN INSTITUT DE RADIOPROTECTION ET DE SÛRETÉ NUCLÉAIRE

BEL V

Acknowledgments

I would like to thank, Dr. Urs Mäder, Prof. Laurent Truche, Prof. Emmanuel Tertre and Dr. Catherine Noiriel for accepting to be jury members and providing constructive remarks in thesis and presentation.

I would like to sincerely acknowledge Bel V (Belgium), IRSN FAR and CEA Saclay for cofounding this thesis program.

This thesis would not have been possible without contribution of many people.

Prof. Vincent Lagneau for sharing his understanding into the subject, for teaching me like an undergrad student the various concepts of reactive transport and for bringing up confidence at various moments.

Dr. Olivier Bildstein for helping me perform 1D and 2D simulations, timely remarks in developing scientific arguments at various fronts, and good moments at Amboise and Goldschmidt.

Dr. Valery Detilleux for his interest into this subject and providing constructive remarks during thesis.

Dr. Charles Wittebroodt being my mentor throughout this thesis, for all the discussion to carry out experiments, presentations and reports. Your support has been an important factor for the success of this thesis.

Dr. Sebastien Savoye for accepting me as an intern and then as a doctoral student despite my limited knowledge in geochemistry. I would thank you for giving me a sight of a true experimentalist, for bringing out the very best from me, for being a mentor that every student would wish for and for being a wonderful role model as a person and as a scientist.

Dr. Emelie L'Hôpital for her deep involvement in performing tomography images and for being a wonderful colleague to work with.

I would thank my colleagues from L3MR for their help at various stages, for regular Apéro, and for being wonderful people. Dr. Romain Dagnelie for all the tennis discussion and the wonderful times at Paris masters. I hope the FeDal rivalry would be continued in the lab. Dr. Natalie Mace for guiding me at different stages right from the internship. I hope the biryani treat continues in the lab. Mme. Virginie Blin for being a wonderful head of the lab and supporting me at different times in the thesis (I thank you allowing me stay late in the lab).

I would like to thank Pou, Hiren, Abhishek, Bhavin, Akshay, Jogidas, Jagdhish, Divyesh, Mahimna, Lien, Levent, Fabien, Mathilde, Erika, Malik, Anshuman Karan, Amarnath, Thomas and Emma for being the wonderful friends. Your support has been

one of the driving factors for my success in life. I would thank to a newly-wed couple Lucia and Felipe. Thank you for all the wonderful times in Murcia and Galicia. Felipe, I would thank your mother for cooking wonderful dishes in chilly winter nights of Mula and for coming to my defense.

Ritu, you have been a teacher of life, a woman of patience and dignity. Like a season, you have been a vibrant person and everlasting love of my life. Finally, I would sincerely thank my parents, Prakashbapu, Kishorkaka, Meghabha and Santok fai for guarding me during several stormy nights of life.

Foreword

Once a philosopher was asked a question, "who are you?".

The philosopher replied

"मनोबुद्ध्यहङ्कार चित्तानि नाहं , न च श्रोत्रजिह्वे न च घ्राणनेत्रे।, न च व्योम भूमिर्न तेजो न वायुः, चिदानन्दरूपः शिवोऽहम् शिवोऽहम्" *-Nirvanashatakam by Adi Jagat Guru Shankaracharya*

Meaning: Neither am I the Mind, nor the Intelligence or Ego, neither am I the organs of Hearing (Ears), nor that of Tasting (Tongue), Smelling (Nose) or Seeing (Eyes), Neither am I the Sky, nor the Earth, Neither the Fire nor the Air, But I am the Ever-Pure Blissful Consciousness.

The person then asked the philosopher, "what is this ever-pure blissful consciousness?"

The philosopher smiled and replied,

या निशा सर्वभूतानां तस्यां जागर्ति संयमी | यस्यां जाग्रति भूतानि सा निशा पश्यतो मुनेः *Bhagvad Gita chapter 2, verse 69*

Meaning: "Where the world is awake, there the man of self-control is sleeping. Where the world sleeps, there he is waking." It is in this awakening the ever-pure blissful consciousness is attained.

The curious man then asked two final questions, "what is the practice to attain this awakening? And what is the advantage of such attainment?"

For the first question the philosopher hence replies,

योगश्चित्तवृत्तिनिरोधः *Verse-2, Yog Patanjali sutras*

Meaning: The act to awaken the self (I) is yoga, because this act involves cessation of movements of mind.

And for the final question the philosopher replies,

तदा द्रष्टुः स्वरूपेऽवस्थानम् *Verse-3, Yog Patanjali sutras*

Meaning: There is neither gain or loss in this act. There is no motive, no characteristics attached to this act as it involves cessation of all desires which are abstract (and thus not eternal, temporary, believed truth). However, the result of this act is that when mind is calm and clear like a lake (undisturbed from all the movements), the witness within is revealed in its true (eternal reality, universal truth, the true I) nature. This witness is the ever-pure blissful consciousness. In this discussion the person asking questions is the world spirit and the philosopher answering them is time (the ever learned, everlasting entity that acompasses the knowledge from the origin (which is unknown) until the end (which is unknown)).

It is said that the "synthesis of world spirit (freedom, knowledge, religion, science, logic etc.) is derived from the historical figures of time." *Introduction, Philosophy of history by Hegel.*

Thus, the effort and essence of natural philosophy presented in this thesis is a tribute to Mme. Marie Curie, Shri J.N. Tata, Shri Mohandas Karamchand Gandhi, Sardar Patel, Swami Vivekananda, Shankaracharya and Victor Hugo.

TABLE OF CONTENTS

ABSTRACT

Several countries such as France, Belgium and Switzerland have proposed to host a deep geological facility to confine high and mid-level long-lived radioactive waste within argillaceous formations. Such formations are considered as potential host-rock, because of their very high containment properties, *i.e.* high retention capacity and very low permeability. However, normal evolution of some waste containers is expected to lead to the release large amounts of soluble salts of nitrate and/or sulfate nature. These saline plumes would generate physicochemical imbalance and, by enhancing mineral dissolution and/or precipitation, could modify the local rock porous network. Thus, for safety assessment of such facility, the evolution of rock containment properties in response to these physicochemical phenomena over large time and space scale needs to be carefully assessed. This can be done by using diffusion-reaction numerical simulators based on equivalent (macroscopic) continuum approach considering representative elementary volume (REV). However, while these codes rely on processes to evaluate chemistry and transport at the REV scale, they rely on empirical relationships, such as Archie's law, to inject information on the feedback of chemistry on diffusive transport properties. Thus, prior to long-term prediction, it is essential to create a set of data to test and improve the description of the feedback of chemistry on transport. In this view, this thesis work deals with developing such reactive diffusion experiments to estimate mineral precipitation impacts on containment properties of porous materials under diffusive transport regime; the capability of REV chemistry transport codes to reproduce such an experimental dataset can then be evaluated.

In order to design these simplified experiments, three proxy porous materials (micritic chalk, compacted kaolinite and compacted illite) were chosen to address specific property describing claystones (clay surface charge, pore size distribution). Two sulfate-alkali minerals were selected as precipitating minerals: barite and gypsum, which present two end-members in reference to their kinetic rate of precipitation and solubility. In a first step, intact properties of each proxy material were determined (pore size distribution, effective diffusion coefficient (D_e) of water tracers (HTO & HDO) and anionic tracer, $^{36}Cl^-$). Barite precipitation was studied in all the proxy materials and gypsum precipitation was studied in chalk only. During these through diffusion experiments, we monitored the evolution of reactant concentration in the reservoirs at both ends of the sample. Furthermore, after a known experimental time, $^{36}Cl^-$ and/or water tracers were allowed to diffuse through the porous samples impacted by precipitation. In addition to diffusive testing, the combined impact of pore structure and intrinsic property of mineral (solubility and kinetic rate of precipitation) on final evolution of mineral in each proxy material was quantified using X-ray tomography (µCT) and Scanning Electron Microscopy (SEM).

Despite similar porosity and diffusivity at intact conditions, chalk, kaolinite and illite were very distinctly impacted by barite precipitation. For chalk, D_e(HTO) and $D_e(^{36}Cl^-)$ decreased by factors of 4 and 32 (*resp*),.For kaolinite, *De*(HTO) is reduced by a factor of 200 and a total clogging was highlighted for $^{36}Cl^-$,. Finally, for illite, no impact on diffusivity was observed. In fact, the µCT and SEM images showed that depending upon the pore structure of each proxy material the distribution of barite mineral was very different. Moreover, the distinct diffusive behavior of $^{36}Cl^-$ compared to HTO in chalk and kaolinite, clearly indicates that the newly formed barite has negative surface charge, capable of changing these neutral porous materials in semi-permeable membranes. For gypsum, the diffusive results showed that this mineral precipitation led to lower impact on diffusivity compared to barite in chalk. The µCT and SEM images further showed that compared to barite (thin precipitated zone in sample center) gypsum mineral had very different evolution (formation of isolated spherical clusters) in chalk. It was demonstrated that this difference stems from the fact that spatial variability in properties of pore structure (heterogeneous diffusivity and porosity) governed selective gypsum precipitation. Thus, the precipitation experiments of barite in three proxy materials and gypsum in chalk underline the role played by the characteristics of material pore structure and the intrinsic properties of the precipitating mineral.

Finally, to test the robustness of chemistry transport codes, the results from the reactive diffusion experiments where barite or gypsum precipitated in chalk were numerically described in 1D and 2D using two codes namely HYTEC and CrunchTope. At 1D both codes were only able to reproduce the experimental results by adjusting several parameters such as cementation factor, kinetic rate constant. At 2D, when characteristics of the porous material (heterogeneous diffusivity field) were considered, HYTEC code well described the evolution of barite and gypsum precipitation in chalk.

RÉSUMÉ

Plusieurs pays tels que la France, la Belgique et la Suisse prévoient de confiner leurs déchets radioactifs de moyenne et haute activité à vie longue dans des installations souterraines sises au sein de formations argileuses profondes. Ces formations constituent en effet de très bonnes barrières ultimes contre la dispersion des radionucléides, de par leur grande capacité de rétention et leur très faible perméabilité. Néanmoins, la dégradation de certains colis de déchets devrait libérer d'importantes quantités de sels nitratés et sulfatés solubles. Ainsi, ces panaches salins en déséquilibre chimique avec l'encaissant devraient conduire à des phénomènes de dissolution et/ou précipitation, faisant évoluer localement la structure porale de la roche argileuse. Aussi, pour estimer la performance de telles installations souterraines, l'évolution des propriétés de confinement de ces roches en réponse à ces processus physicochimiques se doit d'être étudiée, et ce, sur des échelles de temps et d'espace représentatives du stockage. Cela est réalisé à l'aide de codes couplés chimie-transport basés sur une approche continue, à l'échelle de volumes élémentaires représentatifs (VER). Cependant, si ces codes reposent sur une description des processus pour évaluer la chimie et le transport, ils s'appuient sur des relations empiriques, telle la relation d'Archie, pour apporter de l'information sur l'effet de rétroaction de la chimie sur les propriétés de transport diffusif. De ce fait, il est primordial, avant les simulations long-termes de tester la robustesse de ces relations. Dans ce cadre, le présent travail de thèse s'est intéressé au développement d'expériences de diffusion réactives pour estimer (i) l'impact de la précipitation de minéraux sur les propriétés de confinement de matériaux poreux "modèles" et (ii) la capacité des codes de chimie-transport à reproduire ce jeu de données expérimentales.

La mise au point de ces expériences simplifiées a nécessité de se focaliser sur trois matériaux poreux « modèles », de la craie, de la kaolinite et de l'illite, choisis pour décrire une propriété spécifique des roches argileuses (charges de surface des argiles ou structure du réseau poreux). Par ailleurs, deux minéraux sulfatés, gypse et barytine, ont été sélectionnés comme minéraux susceptibles de précipiter car ils représentent deux extrêmes vis-à-vis de leur cinétique de précipitation et de leur solubilité. Dans un premier temps, les propriétés initiales de chaque matériau « modèle » ont été déterminées : distribution de taille de pores, coefficient de diffusion effectif (D_e) des traceurs de l'eau (HTO ou HDO) ou d'un traceur des anions ($^{36}Cl^-$). La précipitation de la barytine a été étudiée sur les trois matériaux « modèles », tandis que celle du gypse uniquement au travers des échantillons de craie. Durant ces expériences de diffusion réactive, l'évolution des concentrations des réactifs dans les deux réservoirs enserrant l'échantillon poreux a été suivie, et, après un temps déterminé, le $^{36}Cl^-$ et/ou les traceurs de l'eau ont été injectés dans le réservoir amont pour diffuser au travers des échantillons déjà impactés par la précipitation. En complément des essais

de diffusion, des caractérisations des échantillons par micro-tomographie X (µCT) et par observation au Microscope électronique à Balayage (MEB) ont permis de préciser le rôle joué par la structure porale initiale du matériau « modèle » et celui des propriétés intrinsèques du minéral précipitant.

Malgré des valeurs de porosité et de diffusivité associées à leur état initial assez proches, les trois matériaux « modèles » ont été impactés de façon très différente par la précipitation de barytine. Pour la craie, les valeurs de D_e(HTO) et D_e($^{36}Cl^-$) baissent par des facteurs 4 et 32 (*resp.)*. Pour la kaolinite, la valeur de D_e(HTO) est réduite par un facteur 200 et un colmatage total est mis en évidence pour $^{36}Cl^-$. Enfin, pour l'illite, aucun impact sur la diffusivité de deux traceurs n'a été observé. Les images acquises par µCT et MEB ont montré que la distribution des précipités de barytine était très dépendante de la structure porale de chaque matériau modèle. De plus, le comportement diffusif distinct du $^{36}Cl^-$ par rapport à HTO, observé dans la craie et la kaolinite, montre clairement que la barytine néoformée possède une charge de surface négative capable de transformer ces matériaux poreux initialement neutres en membranes semi-perméables. Pour le cas du gypse, les résultats d'expériences de diffusion réactives dans la craie montrent que ce minéral conduit à un impact moins prononcé sur la diffusivité que la barytine. Les observations faites par µCT et par MEB révèlent que, comparé au cas de la barytine qui précipite sous forme d'une fine couche au centre de l'échantillon, le gypse a une évolution totalement différente, avec la formation de larges sphères isolées. Il a été démontré que cela est dû à la variabilité spatiale de la structure porale de la craie, associée aux propriétés thermodynamiques et cinétiques du gypse, qui gouvernent la précipitation localisée de gypse. Au final, toutes ces expériences de diffusion réactives soulignent le rôle prédominant joué par les caractéristiques de la structure porale du matériau et par les propriétés intrinsèques des minéraux précipitants.

Enfin, l'estimation de la robustesse des codes de chimie transport a été réalisée à l'aide de deux codes, HYTEC et CrunchTope, à l'aide de simulations 1D et 2D. En 1D, les deux codes n'ont été capables de reproduire les données expérimentales qu'après un ajustement de certains paramètres (facteur de cimentation, constante de cinétique de précipitation). En passant en 2D, quand les caractéristiques du matériau poreux ont été prises en compte (champ hétérogène de diffusivité), le code HYTEC a bien décrit l'évolution distincte de la précipitation de barytine et de gypse au sein de la craie.

INTRODUCTION

Several countries have proposed to confine their mid-level and high-level long-lived radioactive wastes in deep geological facilities that are based up using a multi-barrier concept. In France, Switzerland and Belgium, argillaceous formations are considered as a potential host-rock, acting as the ultimate barrier, because this type of material displays very good containment properties, i.e. high retention capacity and very low permeability.

However, the presence of exogenous materials (iron, cement-based materials, etc.) creates physicochemical imbalances that will generate some evolutions at different locations in and around the repository. For instance, over time, the degradation of waste containers will allow the release of part of their content. Hence, the release of large amount of soluble salts or the degradation of the cement-made packages will lead to the generation of saline or alkaline plumes. These plumes would interact locally with the host rock and enhance perturbations such as mineral dissolution or precipitation down to possible clogging. Thus, the rock containment properties would evolve locally over time. This evolution is considered in the evaluation of the overall behavior of the repository, both by the industry and the Technical Safety Organization (TSO).

The impacts of leached plumes on intact rock properties are studied by TSO such as French Institute for Radiological Protection and Nuclear Safety (IRSN) and BEL V in Belgium. To carry out such experiments, IRSN has developed an *in situ* experimental Underground Research Laboratory (URL) in Tournemire (Aveyron, France). One of these *in situ* experiments focused on interactions of cement/argillite for a duration of 15 years (Gaboreau et al., 2011). The experimental results showed some clogging at the cement-clay/argillite interface; also, due to dissolution, large pores were generated in cement and fissures with large porosities were observed in the argillite. This experiment shows that over large time and scale, hyper alkaline plume can change the containment property of the claystone. Another *in situ* study that is ongoing since 15 years at Mont Terri Rock laboratory deals with examining the fate of nitrate leaching from nitrate-containing bituminized radioactive waste, in a clay host rock for geological disposal (Leupin et al., 2018). This study shows that the release of nitrate plume may generate conditions favorable for microbial growth. This microbial growth can in turn potentially affect the environment of a repository by influencing redox conditions, metal corrosion and gas production or consumption under favorable conditions. Since the nitrate plume would be principally released from bituminized waste, such

microbial activity is expected in the proximity of a geological repository, *i.e.* in the excavation damaged zone, the engineered barriers, and first containments (the containers).

Since the half-life of some radionuclides is of million years, for safety assessment, the impact of physicochemical perturbations induced by the exogenous materials on intact rock properties needs to be envisaged for larger time scales.

Such long-term prediction can only be performed using representative elementary scale (REV) scale chemistry transport codes. The early work of such reactive transport simulation dates back to the early 1980's, with the founding paper by (Yeh and Tripathi, 1989) where different approaches were discussed. During the 1990's, an intensive phase of development took place, in several laboratories around the world (Lichtner, 1996; Steefel and MacQuarrie, 1996; Van der Lee, 1997). They were motivated by a new need in the Earth Sciences to develop models for some of the subsurface applications like:

1. research into development of radioactive waste storage;
2. need for long term performance assessment of the facilities;
3. upscaling from laboratory scale (experiments ~a few weeks to a few years, centimeter to meter scale) to disposal scale.

The strength of these codes is that they rely on processes (chemistry, transport), which gives robustness to their results. However, the feedback of chemical/mineralogical evolution on transport properties stems from the evolution of the pore structure, which only represented globally in the REV approach. Some empirical laws are then used to bridge the gap. For safety assessment, it is therefore necessary to evaluate the validity of the impact predicted by chemistry transport codes for long time scale and the actual impact of mineral perturbation on rock properties. Since, experimental long-term actual impacts are out of reach, the objective of this thesis is to determine the predictability limit of these chemistry transport codes. In this view, this thesis is thus divided into two parts. In the first part, laboratory scale experiments are performed to determine mineral precipitation impact on properties (porosity, diffusivity) of several porous materials. Then, a set of experimental results are reproduced using two codes (HYTEC and CrunchTope). Finally, by comparing the experimental and numerical results the limits of some relationships such as Archie's law are presented. Such approach is necessary, as it will open new directions towards improving the predictability of these codes.

In view of the aforementioned general objective, this thesis is divided into four main parts.

1. In the first part the basic properties of materials and the reactive transport simulation approach are explained. Then a detailed bibliographic work in connection with current thesis presented. From the results of these works, a methodology is extracted and based on which the experimental and numerical task are presented in rest of the thesis.
2. In the second part, the experimental results dealing with mineral precipitation in different porous materials are presented. At the end of this chapter, a general discussion on the clogging phenomena is presented.
3. In the third part a set of experimental results are reproduced numerically using HYTEC and CrunchTope in 1D and 2D.

From experimental and numerical results, a final conclusion is presented. A roadmap is then proposed which will allow future development in view of increasing predictability of chemistry transport codes.

1 References

Gaboreau, S., Prêt, D., Tinseau, E., Claret, F., Pellegrini, D., Stammose, D., 2011. 15 years of in situ cement-argillite interaction from Tournemire URL: Characterisation of the multi-scale spatial heterogeneities of pore space evolution. Applied Geochemistry 26, 2159–2171. https://doi.org/10.1016/j.apgeochem.2011.07.013

Leupin, O.X., Bernier-Latmani, R., Bagnoud, A., Moors, H., Leys, N., Wouters, K., Stroes-Gascoyne, S., 2018. Fifteen years of microbiological investigation in Opalinus Clay at the Mont Terri rock laboratory (Switzerland), in: Bossart, P., Milnes, A.G. (Eds.), Mont Terri Rock Laboratory, 20 Years: Two Decades of Research and Experimentation on Claystones for Geological Disposal of Radioactive Waste. Springer International Publishing, Cham, pp. 345–356. https://doi.org/10.1007/978-3-319-70458-6_18

Lichtner, P.C., 1996. Continuum formulation of multicomponent-multiphase reactive transport. Reviews in Mineralogy and Geochemistry 34, 1–81.

Steefel, C.I., MacQuarrie, K.T.B., 1996. Approaches to modeling of reactive transport in porous media. Reviews in Mineralogy and Geochemistry 34, 85–129.

Van der Lee, J., 1997. Modélisation du comportement géochimique et du transport des radionucléides en présence de colloïdes, PhD thesis, École des Mines de Paris, Paris, France.

Yeh, G.T., Tripathi, V.S., 1989. A critical evaluation of recent developments in hydrogeochemical transport models of reactive mutichemical components. Water Resources Research 25, 93–108. https://doi.org/10.1029/WR025i005p01066

CHAPTER-1: STATE OF THE ART

RÉSUMÉ

En France, la formation géologique du Callovo-Oxfordien a été sélectionnée comme roche-hôte susceptible d'accueillir le centre industriel de stockage géologique (Cigéo) de déchets nucléaires. Or, parmi ces déchets, certains peuvent relâcher d'importantes quantités de sels solubles, capables d'induire des déséquilibres chimiques avec la roche encaissante et de ce fait, d'en modifier ses propriétés de confinement. Un tel phénomène peut être étudié à l'échelle du laboratoire, et ensuite extrapolé à des échelles de temps et d'espace plus représentatives de ce qui est attendu *in situ*, et ce, à l'aide de codes de chimie-transport. Pourtant, une telle extrapolation demande de vérifier au préalable la capacité des codes de chimie transport à prendre en compte de façon satisfaisante ces perturbations chimiques induites par les panaches salins. L'altération des propriétés de confinement de milieux poreux a été étudiée auparavant au CEA/L3MR par G. Berthe(2012) – sur les effets de la dissolution dans les argilites -, et par I. Fatnassi (2015) – sur les effets de la précipitation dans de la craie. Les résultats ainsi acquis à partir de leurs expériences de diffusion/réaction ont été modélisés à l'aide de codes comme HYTEC, ChunchFlow et PHREEQC. Cependant, il apparaît que ces expériences ne sont pas décrites de façon satisfaisante par ces codes. De la même manière, des limitations numériques ont été aussi notées par d'autres auteurs (Chagneau, 2015 et Poonoosamy, 2015). Il a été observé dans tous ces travaux que la distribution et la morphologie d'un précipité donné dépendent fortement de la distribution de taille de pores, des propriétés de surface et des propriétés intrinsèques du minéral. Aussi, selon les matériaux poreux, la distribution locale et la morphologie du précipité peut avoir un impact très différent sur la diffusivité des traceurs étudiés. Sachant que la précipitation dans les codes de chimie transport est décrite par un modèle de solubilité construit à partir des résultats obtenus en chimie en solution et que son impact sur la diffusivité est décrit par une loi empirique, la loi d'Archie, il est pertinent de s'interroger sur la capacité prédictive de ces codes. Aussi, ce chapitre est consacré à une revue de la littérature, plus particulièrement sur (i) les différents modes de transport des ions au travers de milieux poreux neutres ou chargés électriquement et (ii) les théories conventionnelles utilisées pour décrire les mécanismes de dissolution/précipitation dans les codes, ainsi que leur comparaison avec des approches plus récentes (S-N-T, PCS), qui prennent en compte les effets de confinement de la solution sur la dissolution/précipitation. En se basant sur cette revue bibliographique, il a été alors possible de proposer une approche méthodologique globale qui nous a servi à mieux évaluer l'importance de certains paramètres gouvernant le mécanisme de précipitation à l'échelle du pore. Une telle approche a pour but final de tester et d'améliorer la robustesse des lois utilisées dans les codes pour prédire l'impact de la précipitation sur la diffusivité à des échelles de temps et d'espace comparables à celles envisagées pour Cigéo.

1 Literature Review

1.1 The materials of interest: the argillaceous rocks

Argillaceous rocks (or claystones) display diversified mineral composition, clay (and other) minerals and varying porosity (depending upon their compaction). For instance, the mineralogical composition of Tournemire claystones consists of 40-50% of clay minerals, 20-30% of carbonate, 15-20% of quartz, and the remaining part for accessory minerals, such as pyrite, and organic matter. The gravimetric water content in Tournemire claystones is about 4% and their total porosity about 11%[1].

1.1.1 Physical properties of clay minerals

Clay minerals belong to the phyllosilicate subclass of silicate minerals. These minerals are formed from two basic sheet structures, *i.e.* tetrahedral and octahedral sheets, held together by ionic bonds[2]. In a tetrahedral sheet, the central ion of tetrahedron is mostly a silicon ion (Si^{4+}) surrounded by four oxygen ions (O^{2-}) at the apex of each unit, carrying one unsatisfied valence bond. These tetrahedral sheet units are formed with general formulae $n((Si_2O_5)^{2-})$. The octahedral sheets are formed, either with general formula $n(Al_2(OH)_6)$ giving gibbsite, or $n(Mg_3(OH)_6)$ giving brucite. For octahedral sheets when the central ion is trivalent (*e.g.* Al^{3+}), only 2/3 of the possible central space is occupied to balance the negative and positive charges. However, if the central ion is divalent (*e.g.* magnesium), all the positions must be filled for balancing the charge, forming a trioctahedral structure. These tetrahedral and octahedral sheets further link with each other in two different ways to form different groups of minerals. When one tetrahedral sheet is fused to one octahedral sheet, 1:1 type of linking is formed (Figure 1A). When two tetrahedral sheets are fused to an octahedral sheet, 2:1 type of linking is formed (Figure 1A).

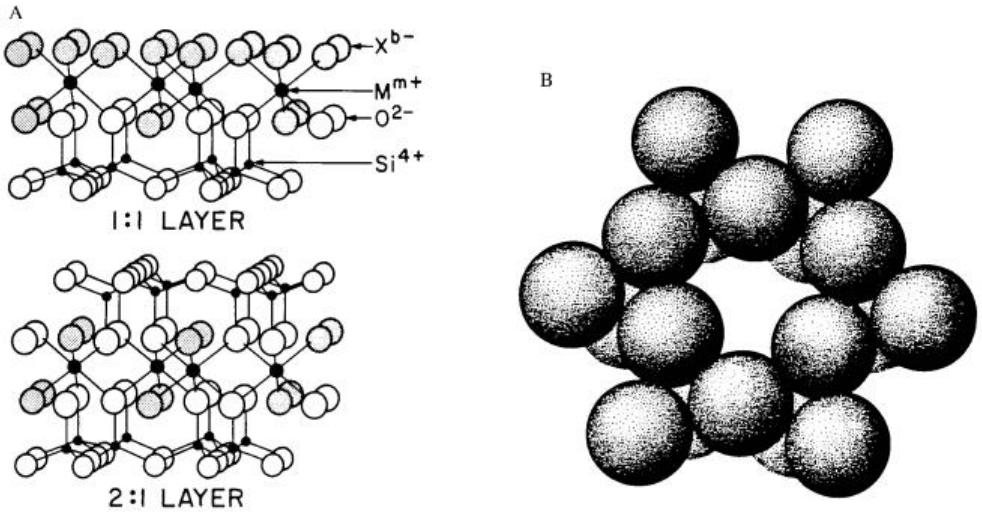

Figure 1: A) Crystal structures of 1:1 and 2:1 type clay minerals. Here, M represents a cation central atom (Al, Mg, Fe, Si etc.), X (shaded circles) is usually OH, B) Siloxane cavity in the basal plane of the tetrahedral sheet[2]

In mineral formed by 2:1 type of layer stacking, the plane of oxygen atoms on each side of such layer forms a siloxane surface (Figure 1B)[2]. This siloxane consists of a hexagonal cavity formed by six corner sharing Silicon tetrahedra. It is bordered by six oxygen atoms with hydroxyl group rooted at the bottom in the octahedral sheet. The reactivity of this siloxane cavity further depends on the distribution of charges in the layer of silicate structure. In absence of isomorphic substitution, the O atoms bordering the siloxane cavity will function as electron donors that can bind neutral molecules by means of van der Waals force of interaction. Under these circumstances, the siloxane layer would act as mild hydrophobic. However, if in the octahedral sheet, the isomorphic substitution of Al^{3+} occurs by a metal ion of lower valence (Mg^{2+}), a negative structural charge is created that can attract cations and polar molecules. And, if this isomorphic substitution replaces Si^{4+} by Al^{3+} in the tetrahedral sheet, then an excess of negative charge is created much nearer to siloxane surface. This results in strong attraction of cations and polar molecules. These substitutions in octahedral and tetrahedral sheets disturb the original mild hydrophobic nature of siloxane surface. Hence, the 2:1 type of minerals possess heterogeneous basal surface, comprised of hydrophobic patches infused between the hydrophilic sites. The functional groups of these sites further interact with pore solution to form two kinds of complexes (Figure 2A): 1) If no water molecule is interposed between the surface site functional group and the ion or molecule it binds, it is known as inner sphere complexation and, 2) If at least one water molecule is interposed between the surface functional group of surface site and the ion or

molecule it binds, it is called outer sphere complexation [3].Figure 2B shows such type of complexation of surface site[2].

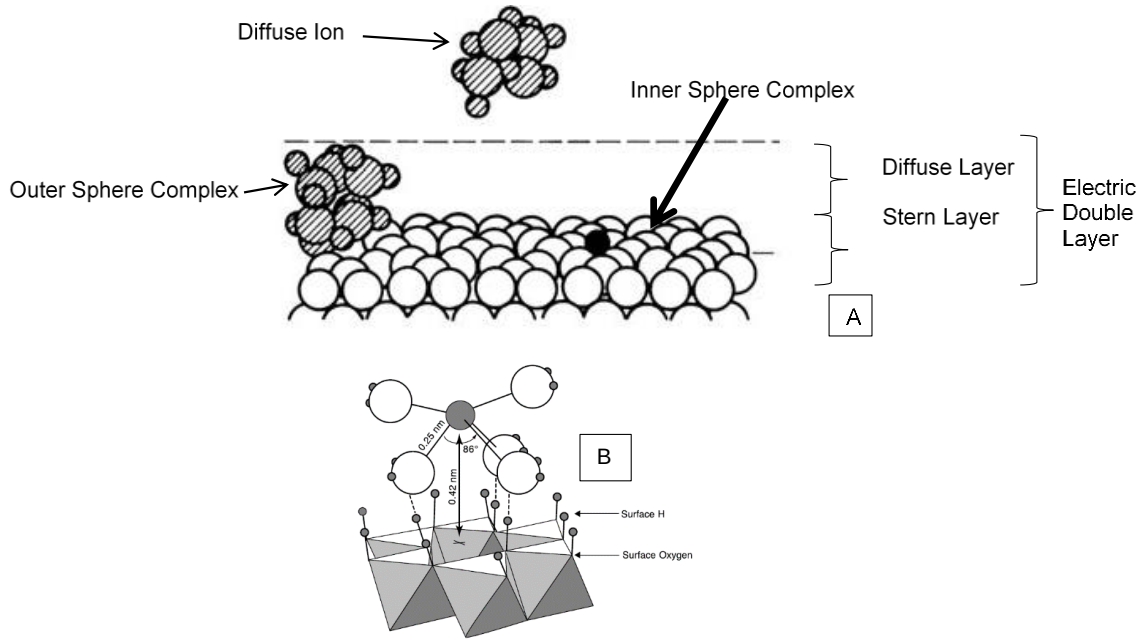

Figure 2: A) The inner sphere complexation, outer sphere complexation, and diffuse ion adsorption, illustrated for cations adsorbing on montmorillonite. B) Outer shell electrostatically bonded with the metal surface [2]

The inner sphere complexes involve ionic or covalent bonding, and the outer sphere complexes involve electrostatic bonding. Due to this reason, inner sphere complexes are more stable and form specific adsorption. Figure 2A shows an adsorption of monovalent cation on montmorillonite (a 2:1 type of clay mineral) where the ion is adsorbed in cavity of the siloxane due to inner sphere complexation. In Figure 2A, the combination of outer sphere and inner sphere complexes results in formation of the Stern layer on the siloxane site. Some of these solvated ions do not form complexes with charged surface functional group, but instead they screen the surface charge in a delocalized manner. These ions are said to be adsorbed in diffused-ion swarm and are fully dissociated from surface functional groups. Like outer-sphere complexes, these ions too undergo electrostatic complexation. These diffuse swarm ions further collectively produce a diffuse charge that exactly counters the negative surface charge. The combination of the surface charge altogether with the diffuse charge forms the electric double layer (EDL) (Figure 2A). However, if the swarm ions can move freely in the solution, a characteristic charge distribution arises which gives rise to diffuse double layer.

The thickness of this double layer in Debye lengths (κ^{-1}) can be calculated using Boltzmann distribution equation[3]:

$$\kappa = \sqrt{\frac{2F^2 1000I}{\varepsilon RT}} \qquad \text{---------- (1)}$$

I is the non-dimensional ionic strength

ε is the water dielectric constant (F.m^{-1})

F is the Faraday constant (C.mol^{-1})

R is the universal gas constant (J.mol^{-1}.K^{-1})

T is the temperature (K)

In nature, these diffuse swarm ions of double layer are subjected to two opposing tendencies. Electrostatic forces attract them towards the negatively charged surface, whereas diffusion drags these ions towards the equilibrium where their concentration is smaller. Simultaneously, if the ions are of the same sign as of the surface charge, then they are repelled out of the double layer (anionic exclusion)[1].

1.1.2 Porous medium

A material that contains pores or voids is termed as a porous material. The total porosity of this material is the ratio of the total volume of voids to the total volume of the material. As our material of interest is claystone and clay minerals, their porosity can be defined as $\phi = \left(1 - \frac{\rho_b}{\rho_s}\right)$, where ρ_b(g.cm^{-3}) is the bulk dry density of the material and ρ_s(g.cm^{-3}) is the grain density of the material[3]. These pores can further be divided into three classes: 1) pores with diameter less than 2 nm are called nanopores, 2) pores with diameter between 2 and 50 nm are called mesopores and, 3) the pores whose diameter exceeds 50 nm are called macropores[3].

The admixture of these diversified pores constitutes a pore size distribution in a porous system. For a given pore of diameter *D* (m), the pore size distribution can be calculated by estimating the

---

[1] One must note that this is one way to describe the sorption double layer and triple layer for clayey system. In literature there are other models surface complexation models to describe the double layer and triple layer system for clayey systems[34–36].

number of pores of diameter between *D* and *D*+$\delta(D)$ that are contained in total pore fraction, $\alpha(D)$. Mathematically, it can be represented as:

$$\int_0^\infty \alpha(D)d(D) = 1 \qquad \text{---------- (2)}$$

The volumetric flux of the fluid (Darcy flux) in a given porous medium can be estimated using Darcy's relationship. This relationship establishes proportionality between the Darcy flux, q (m.s^{-1}), and the hydraulic gradient, dh/dx:

$$q = \frac{K\mathrm{dh}}{\mathrm{dx}} \qquad \text{---------- (3)}$$

Where, K is the hydraulic conductivity (m.s^{-1})

$\frac{\mathrm{dh}}{\mathrm{dx}}$ is the hydraulic gradient (-)

The proportionality factor *K* is the hydraulic conductivity of the porous medium. This factor depends upon the nature of a given porous medium (porosity, shape and size of pores) and also on the fluid (viscosity and density). However, Tournemire claystone possess very low hydraulic conductivity (10^{-14} < K < 10^{-12} m.s^{-1}[1]). Therefore, diffusion is assumed to be the main governing transport phenomenon of neutral/ionic solvated species[4].

1.2 Transport through uncharged/charged porous medium

1.2.1 Theory

Case I: Diffusive transport under a concentration gradient

In neutral systems, the diffusion process is concentration driven, and it governs Fick's first law of diffusion. This law states that the diffusive flux of a species i in solution (J_i) (mol.m^{-2}.s^{-1}) is proportional to its concentration c_i (mol.L^{-1}) gradient:

$$J_i = -D_{e,i}\frac{\partial c_i}{\partial x} \qquad \text{---------- (4)}$$

where, $D_{e,i}$ is the effective diffusion coefficient that is specific to chemical species i (m^2.s^{-1})

x is the distance(m)

Case 2: Diffusive transport under an electrochemical potential gradient: multicomponent diffusion

The diffusive flux of ionic species *i* (*Ji*) through charged porous medium under the influence of electrochemical potential gradient is[5,6]:

$$J_i = \frac{u_i c_i}{|z_i|F}\frac{\partial \mu_i}{\partial x} - \frac{u_i z_i c_i}{|z_i|}\frac{\partial \psi}{\partial x} \qquad \text{---------- (7)}$$

z_i is the charge number (-)

F is the Faraday constant (C.mol^{-1})

where, u_i is the mobility of ions (m^2.s^{-1}V^{-1})

ψ is the electric potential (V)

The term μ_i in equation 7 is the electrochemical potential and it can further be elaborated as:

$$\mu_{i,} = \mu_i^0 + RTlna_i + z_i F\psi \qquad \text{---------- (8)}$$

μ_i^0 is the standard potential (J.mol^{-1})

z_i is the charge number (-)

F is the Faraday constant (C.mol^{-1})

$a_{i,}$ is the activity in water

Finally, in absence of electrical current, $\sum z_i J_i = 0$. We can calculate the value of $\frac{\partial \psi}{\partial x}$ in equation 7:

$$\frac{\partial \psi}{\partial x} = -\frac{\sum_{j=1}^{n} \frac{u_j z_j c_j}{|z_j|F}\frac{\partial \mu_i}{\partial x}}{\sum_{j=1}^{n} \frac{u_j z_j^2 c_j}{|z_j|}} \qquad \text{---------- (9)}$$

where subscript j is used to notify in forthcoming equations that they origin from potential term:

Using this equation of electrical potential in equation 7, we get,

$$J_i = \frac{u_i c_i}{|z_i|F}\frac{\partial \mu_i}{\partial x} + \frac{u_i z_i c_i}{|z_i|}\frac{\sum_{j=1}^{n} \frac{u_j z_j c_j}{|z_j|F}\frac{\partial \mu_i}{\partial x}}{\sum_{j=1}^{n} \frac{u_j z_j^2 c_j}{|z_j|}} \qquad \text{---------- (10)}$$

1.2.2 Multicomponent diffusion modeling in clay systems (Appelo et Wersin, 2007)

Aim: To investigate the behavior of diffusing neutral specie HTO and charged species I^- and $^{22}Na^+$ into a modeled column containing surface charge.

Experimental setup and methodology used

A column of 0.2 m diameter and 0.5 m length was numerically designed using PHREEQC code. This column is contacted with 0.8 L porewater containing three tracers namely HTO, I^-, $^{22}Na^+$ which can diffuse[2] into the column under two conditions:

1) When column contained no surface charge
2) When column contained surface charge equal to 0.11 $eq.kg^{-1}$.

1.2.3 Results and discussion

Case I: When column contained no surface charge

Figure 3A represents the evolution of concentration in HTO, I^- and $^{22}Na^+$ at the injection point, during the diffusion simulation with or without surface charge. This figure shows that, as the diffusion coefficient in bulk water is higher for HTO than sodium ion, HTO invades the column faster than Na^+, so that HTO concentration decrease in the reservoir was higher than sodium. Figure 3B represents the situation when HTO, I^- and $^{22}Na^+$ diffused through the same column containing surface charge equal to 0.11 $eq.kg^{-1}$. Due to the presence of this surface charge, the double layer occupies half of the pore volume.

[2] The diffusion coefficients of HTO,I^-,$^{22}Na^+$ in free water were taken from database given by Appelo et Wersin (2007)[5]

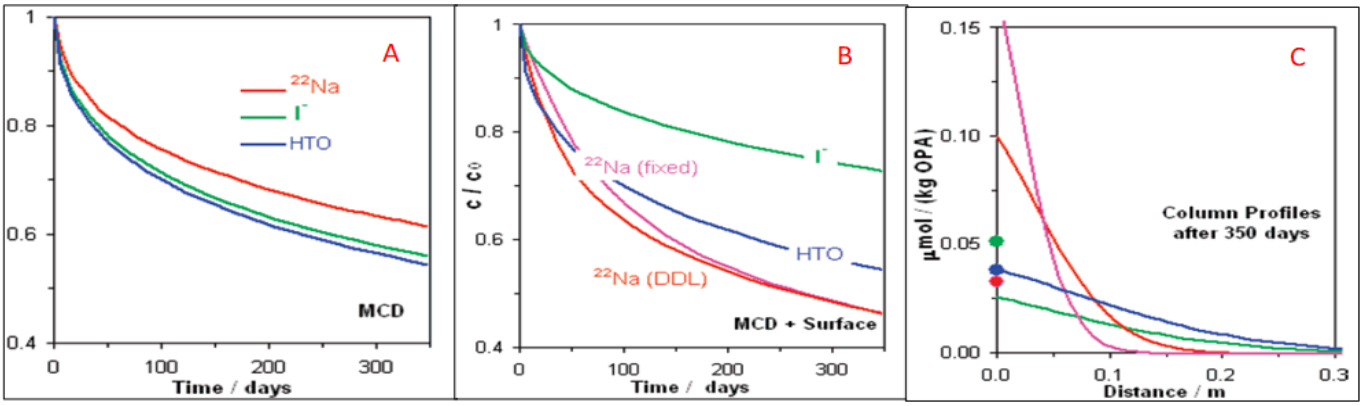

Figure 3: A) Multicomponent diffusion of tracers HTO, I^-, and $^{22}Na^+$through the modeled column without introducing surface charge. B) Multicomponent diffusion of tracers HTO, I^-, and $^{22}Na^+$through the modeled column containing surface charge equal to 0.11 eq/kg. C) Tracer concentration profiles in column (µmol/kg Opalinus clay), the circles in this figure indicate concentrations in column inlet[5]

Case II: When column contained surface charge equal to 0.11 $eq.kg^{-1}$.

This figure shows that the decrease in concentration of water tracer (HTO) is unaffected by the presence of surface charge. But, in the same column, when anionic I^- specie was injected, due to the presence of diffuse layer in half of the column, iodide was repelled away from the DDL. This anionic exclusion of iodide, resulted in lower decrease in its concentration compared to case-I.

Contrary to iodide diffusion, when $^{22}Na^+$ was injected in this surface charge-bearing column, it was either adsorbed in the DDL (outer-sphere complex or swarm diffuse ion) or was sorbed on the surface site (inner sphere complex) This type of sorption/adsorption resulted in steep decrease of $^{22}Na^+$ from bulk water (Figure 3B). This fixation of $^{22}Na^+$ on surface sites (Su^-) can be represented by the following equations:

$$Su^- + Na^+ \leftrightarrow SuNa \qquad K_{SuNa} = 1 \qquad \text{---------- (15)}$$

$$Su^- + K^+ \leftrightarrow SuK \qquad K_{SuK} = 5 \times K_{SuNa} \qquad \text{---------- (16)}$$

The value of this equilibrium constant K (-)[5] can be calculated using the following equation:

$$K_i = \frac{a_{SuNa}}{a_{Su^-} . a_{Na^+}} \qquad \text{---------- (17)}$$

where, $a_{SuNa}$is the activity of site plus ion(-)

a_{Su^-} is the activity of surface site(-)

a_{Na^+} is the activity of present Na^+(-)

e.g. If $K_i = 10^5$, from equation 15 and 16, we can see that only a fraction of diffused Na^+ would be present in DDL and the rest of all the other cations would be fixed from DDL to surface. Using this value of equilibrium constant, the decrease in $^{22}Na^+$ concentration is shown in Figure 3B. This figure shows two distinct curves of decrease in $^{22}Na^+$ concentration from bulk water either by adsorption in DDL (red line) or sorption in surface sites (pink line). The concentration profile of these ionic species, as shown in Figure 3C, were also investigated during this modeling process. Iodide shows the effect of anion exclusion in the downward concentration jump at the borehole perimeter.

Since only half of the pore space contains I^-, the concentration in the rock (green line) appears to be halved compared to that in the borehole (green circle). This figure also shows that, when $^{22}Na^+$ was injected in this column, its rapid fixation on negative surface (inner sphere complexation) took place. Due to this fixation, $^{22}Na^+$ concentration near the surface sites increased as compared to initially injected concentration. But, in this case as $^{22}Na^+$ was permanently fixed, its diffusion was inhibited to a very short distance. When a fraction of the injected $^{22}Na^+$ was not fixed on the surface sites but was adsorbed in the mobile DDL zone (outer sphere complex), $^{22}Na^+$ diffused to a distance greater than the fixed case.

Finally, from this first multicomponent diffusion modeling through charged porous column, Appelo *et* Wersin(2007)[5] showed that the presence of surface charge determines the fate of ionic transport through such media. However, there are some limitations of their approach. The most important limitation lies on the use in their modelling of several input parameters whose value can only be adjusted, especially when these authors applied their approach to a real case: the diffusion in Opalinus Clay. For instance, it is unclear how much Na is assigned to fixed sites or to the diffuse layer in the given clayey system, or what is the pore size available for anion diffusion.

1.3 Reactive Transport experiments

1.3.1 Introduction to precipitation and dissolution phenomena

To understand the concept of precipitation/dissolution mechanisms, let us begin this discussion with formation of orthosilicic acid solution from silica mineral. This acid is formed when silica reacts with water, and this reaction can be written as[7]:

$$SiO_2 + 2H_2O \underset{precipitation}{\overset{dissolution}{\rightleftharpoons}} H_4SiO_4$$ ---------- (18)

In equation 18, the solubility (K_{sp}) of SiO_2 (s), is the maximum amount of this mineral that can be dissolved in a given volume of water. This solubility is a thermodynamic dependent property[7].Thus, when the solid SiO_2(s) mineral is in equilibrium with the orthosilicic acid solution, this equilibrium reaction can be written as:

$$K_{sp} = (H_4SiO_4)$$ ---------- (19)

Where (H_4SiO_4) is the activity of formed orthosilicic acid. This equilibrium condition defines the saturation state of orthosilicic solution. However, if more H_4SiO_4 is added in the solution, then the solution contains an excess of orthosilicic acid larger compared to the solubility (K_{sp}). In this situation, the solution is said to be an oversaturated solution. From a thermodynamic point of view, SiO_2(s) should precipitate from this solution. On the contrary, if the activity of (H_4SiO_4) in a given solution is smaller than $K_{sp,}$ then the dissolution of SiO_2(s) solid phase would start until$(H_4SiO_4) = K_{sp}$ or the solid SiO_2(s) disappears.

In general, for a given mineral $A_mB_{n(s)}$ dissolving in water, its stoichiometric equation can be written as[7]:

$$A_mB_{n(s)} \underset{precipitation}{\overset{dissolution}{\rightleftharpoons}} mA^{+n} + nB^{-m}$$ ---------- (20)

In equation 19, to define the equilibrium condition, we compared the activity of orthosilicic acid with the solubility of SiO_2(s) mineral, *i.e.* we compared the solubility of SiO_2(s), with solvated ions of this mineral. These solvated ions can be mathematically represented in form of ion activity product (IAP):

$$IAP = (A^{+n})^m(B^{-m})^n$$ ---------- (21)

$\left(A_m{}^{+n}\right)$ and $(B_n{}^{-m})$ are the activies of the dissolved species (-)

From these theories, three important conventions can be drawn out:

$IAP = K_{sp}$	(saturated solution)	Equilibrium between activities of dissolved species and K_{sp}.
$IAP < K_{sp}$	(undersaturated solution)	The product of the activities of dissolved species is lower than K_{sp}, thus solid mineral will further dissolve into the solution until IAP= K_{sp} or the mineral disappears.
$IAP > K_{sp}$	(oversaturated solution)	The product of the activities of dissolved species is higher than K_{sp}, and thus, mineral phase will start precipitating from solution.

The precipitation/dissolution phenomena using aforementioned theories for solubility and ion activity product are well defined for the salts dissolving in bulk water. However, we want to investigate these precipitation/dissolution reactions in small volume of solution contained in pores whose size ranges from nm to µm.

For this investigation, Rijniers et al[8] used a Nuclear Magnetic Resonance (NMR) technique to investigate the impact of pore pressure on the bulk solubility of sodium sulfate salt. They showed that the pores of diameter 7 nm and 10 nm-size imparted pore pressure of 13 MPa and 9 MPa respectively. Due to this high pore pressure, the solubility of sodium sulfate increased by a factor of 3 (resp. 2.1) in 7 nm (resp. 10 nm) pores at 10°C. In another study, Putnis et Mauthe[9] investigated the impact of pore size on halite solubility within sandstone. They found that, in a well cemented sandstone sample, all of the halite was dissolved within 10 µm-size pores, but, halite in 40 µm-size pore was still present in the porous network.

Both of these studies show that as we decrease the volume of confined media, some other parameters such as disjunction pressure, tensile energy imparted by crystal size and pore size needs to be taken into considerations in addition to thermodynamic solubility in open solutions. In one study by Emmanuel *et* Ague(2008)[10] and Emmanuel *et al*.(2010)[11] compared two models, the classical constant solubility model and pore scale solubility (PCS) model. .In the constant solubility

model the thermodynamic solubility was used to describe stylolite precipitation in a range of pore size distribution (10^{-8}m to 10^{-4}m).In the PCS model, different parameters such as interfacial energy to initiate precipitation, pore size dependency, molar volume of mineral were considered in addition to the thermodynamic stylolite solubility. The end results of pore size distribution evolution in response to stylolite precipitation by both models showed that pore scale solubility model, contrary to constant one, enables to find a solubility product of stylolite that is much higher in nanopores.

The impact of confined pore volumes on salt precipitation was seen in the work of J. Poonoosamy (2016)[12]. While investigating the barite precipitation in 10 μm^3 and 100 μm^3 pore volumes, she observed that in 100 μm^3 pore volumes, nano-crystalline barite of size 10 nm precipitated at a rate of 1.1 nm/h, whereas, in 10 μm^3 pore volumes, a rim of barite overgrowth was seen on the surface of pores at the rate of 10 nm/h.

This work clearly shows that confined pore volumes play an important role in determining the precipitation rate of a given salt and also the morphology of the precipitate. For such an investigation, Supersaturation-Nucleation-Time (SNT) diagrams have been developed for each of the pore volumes. These diagrams are necessary to determine the time until which confined solution, enriched with salt, remained supersaturated, without nucleating. However, to develop such diagrams, one needs to determine the time and the supersaturation value at which the first visible nucleus is seen in the confined pore volume.

Thus, in next section, an experimental method developed by Putnis et al.(1995)[13] is discussed first. In this method, for a given reactant concentration and pore volumes, one can determine the supersaturation value needed for formation of first stable nucleus in these pore volumes. Incorporating these supersaturation values in classical nucleation theory, we can then develop the S-N-T diagrams.

1.3.2 Qualitative analysis of barite and gypsum precipitation in silica gel porous medium (Putnis et al.,1995)

To determine the supersaturation values for a given reactant concentration in porous medium, Putnis et al.(1995)[13] used a counter diffusion technique which inspired the setup used by Fatnassi (2015)[14] and Chagneau (2015)[15].

In this experiment, a silica gel sample of 9 mm in diameter and 280 mm long is prepared, by an acidification of sodium silicate solution to a pH of 5.5. This prepared gel is then solidified in a U-

tube arrangement. After some time, when the gel hardens, the resulting silica hydrogel now contains 95.6% water within the interconnecting pores. This hardened gel has pores of diameter ranging between 100 and 500 nm.

This gel sample is then sandwiched between two reservoirs, to prepare a counter diffusion cell setup. Figure 4 shows a schematic view of such counter-diffusion cell used by Putnis *et al. (1995)*[13]. At both ends of this material, two reservoirs are attached, where one of the reservoirs is filled with cationic reactant-bearing solutions, and the other with anionic reactant-bearing solution.

Due to the concentration gradient, these saline solutions will counter-diffuse through the pores of silica gel to meet and induce a potential precipitation. As more and more of these reactants accumulate, the pore solution is oversaturated. And, at one point, the salt will then start precipitating in the pores.

To evaluate the evolution of supersaturation over the period of experimental time, a set of 5 cells are prepared. Each of these cells is assigned to a specific diffusion time after which the reactants from the reservoirs are removed to stop the experiment. The gel column from the cell is then removed and sliced into 10 mm long section (Figure 4). These slices are then chemically analyzed to measure the concentration of the precipitating phase. From these measured concentrations, it is then possible to calculate the supersaturation value at each diffusion time.

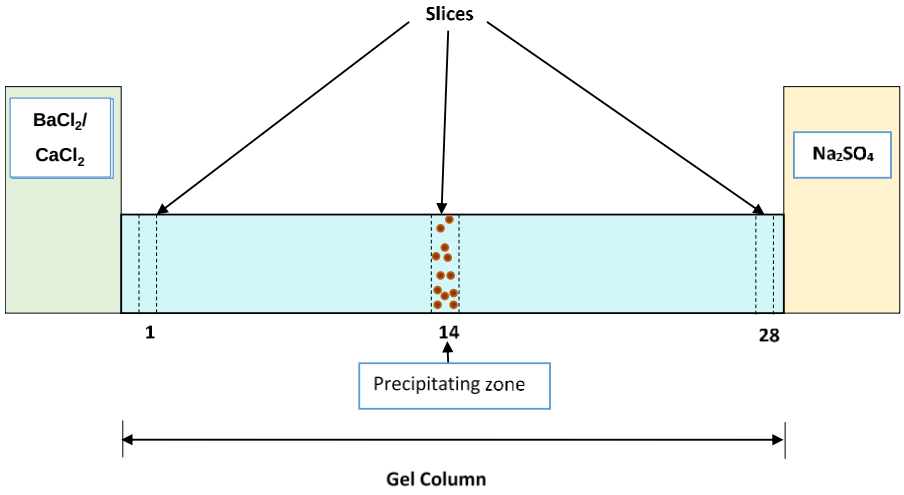

Figure 4: Schematic view of gel through diffusion experiment used in works of Prieto et al.(1989)[16]. Slices 1 to 28 follow the pattern used to cut the column for chemical analysis at each diffusion time

To calculate the supersaturation (β) for these experiments, a non-stoichiometric equation was used. This equation can mathematically be written as:

$$\beta = \frac{\prod a_i^{vi}}{K_{sp}} \qquad \text{---------- (22)}$$

where, $\prod a_i^{vi}$ is the ion activity product (-)

v_i is the stoichiometric ion number *i* in the solute formula (-)

K_{sp} is the solubility product (-)

$a_{i,}$ is the activity of the species *i* in water (-)

The activities of ions in equation 22 can be estimated using Debye-Hückel theory for moderately concentrated solution[12]. Table 1 shows the supersaturation values of gypsum, calculated at each diffusion time in the experiment where 1M of $CaCl_2$ and Na_2SO_4 were injected from opposite ends of the reservoir. These supersaturation values can be plotted *versus* diffusion times (Figure 5). The interpolation of this curve gives an equation, using which the supersaturation at any given time in the experiment can be calculated. Finally, the derivative of this curve dβ/dt is the supersaturation rate *(R_{β})*.

Table 1:Supersaturation and supersaturation rate evolution for the given diffusion time applied in experiments of Putnis et al (1995)[13]

	$CaSO_4$. $2H_2O$	
Diffusion Time (h)	Supersaturation β(-)	Supersaturation rate, R_{β} (h^{-1})
750	1.5	0.009
1000	2.5	0.012
1250	3.75	0.015
1500	7.5	0.018
1750	12.5	0.021
2000	15	0.024

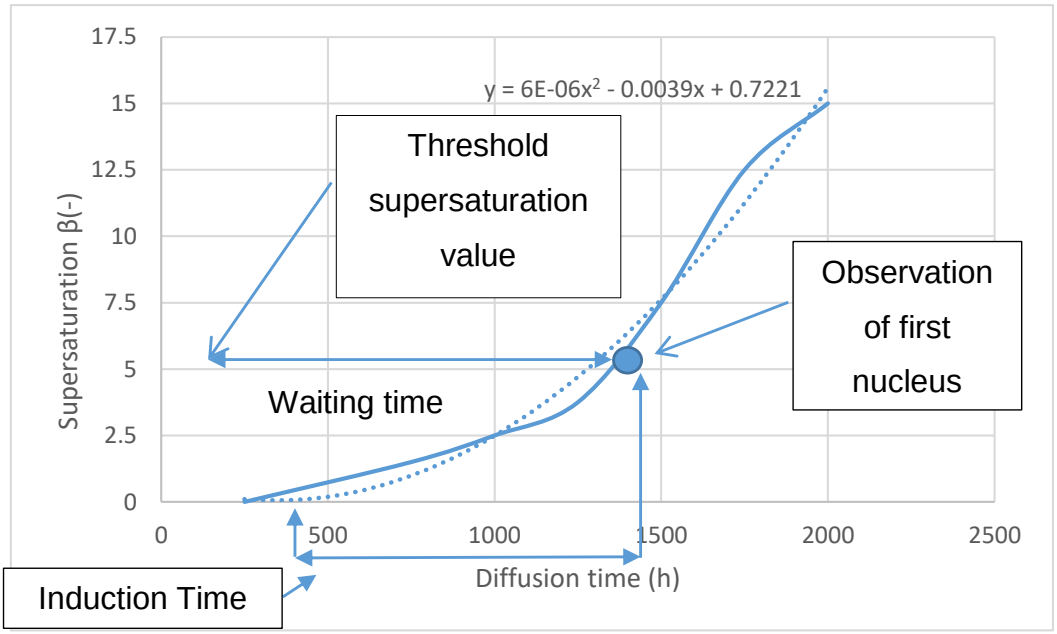

Figure 5: Plot of supersaturation vs. diffusion time for 1M $CaCl_2$-Na_2SO_4, at the point where nucleation took place [13]

In addition to the supersaturation data, the optical observation of the silica gel enables to detect the first nucleus in the experiment and to determine the time required for starting precipitation, called "waiting time (t_w)". Thus, by means of this time, the supersaturation value at which the first nucleation was seen can be estimated as shown in Figure 5. This value is called the threshold (β_{th}) supersaturation. This parameter gives a way to assess the impact of the pore size on precipitation phenomenon. In works of Putnis *et al.*(1995)[13], they concluded that the smaller the pores of the medium used (gelatin with large pores or silica gel), the higher the threshold supersaturation. Therefore, for any given reactant concentration, Putnis *et al.*(1995)[13] determined the values of the threshold supersaturation and waiting time (t_w). Table 2 and Table 3 show these values for gypsum and barite precipitations at different reactant concentrations in reservoirs.

Table 2: Supersaturation rates calculated for gypsum precipitation for experiments with different reservoir concentrations [13]

$CaCl_2$ (M)	**Na_2SO_4 (M)**	**t_w (waiting time) (h)**	**β_{th} (-)**	**R_β (h^{-1})**
0.5	0.5	1792	4.09	0.0037
0.3	0.5	2024	2.23	0.0003

Table 3: Supersaturation rates calculated for barite precipitation for experiments with different reservoir concentrations [13]

$BaCl_2$ (M)	**Na_2SO_4 (M)**	**t_w (waiting time) (h)**	**β_{th} (-)**	**R_β (h^{-1})**
0.5	0.5	360	11663	109.8
0.1	0.1	572	1929	7.2

Table *2* and Table *3* clearly show the impact of both the reactant concentrations and the nature of the salt on the threshold supersaturation values and on the supersaturation rate. Hence, we can now conclude that, while studying the counter diffusion precipitation phenomena, if we know the reservoir concentrations, the methodology developed by Putnis *et al.(1995)*[13] can be used to determine the threshold supersaturation and the waiting time (t_w) for this experiment.

1.3.3 Applications of Classical Nucleation Theory (CNT)

In the previous section, we discussed how to determine the threshold supersaturation (β_{th}) and the waiting time (t_w) for a given precipitation experiment. However, both terminologies are dependent on the nature of the salt and concentration of reactants in the reservoirs, as mentioned before. Our interest lies in understanding the impact of confined pore volumes on dissolution/precipitation reactions. Thus for this reason, a method recently developed by Prieto (2014)[17] is discussed in this section. In this method, he used the experimental data obtained from the work of Putnis *et al*. (1995)[13] to develop Supersaturation-Nucleation-Time (S-N-T) diagrams. The aim of developing such diagram was to determine the rate at which a certain type of nucleation phenomenon occurs in confined pores volumes. These different types of nucleation were developed using some concepts from the classical nucleation theory (CNT). This theory states

that when a solution is oversaturated with a given salt, the salt nuclei will form clusters in the solution. As the size of the cluster overcomes a critical size, it forms a stable nucleus and then precipitates from the solution. However, the conversion of this cluster into stable nucleus depends upon surrounding in which it nucleates. Indeed, if these clusters are present in a solution where all the sites are potential sites for nucleation, then the precipitation will follow a Homogeneous type of Nucleation (HON). Conversely, if these clusters form stable nuclei in presence of a foreign substrate, then this type of nucleation is called Heterogeneous Nucleation (HEN) [17–19]. But according to CNT, for both nucleation phenomena to occur, the cluster needs to overcome the interfacial energy, *i.e.* the surface energy of the cluster/solution interface[17,18], *e.g.* If barite crystals form homogeneously (HON), they will require 1.37 $J.m^{-2}$ of interfacial energy for this nucleation. If barite overgrows on the substrate (HEN), the interfacial energy decreases to 0.45 $J.m^{-2}$. Due to this difference in associated interfacial energies for stable formation of nuclei, the HON and HEN types of nucleation will take place at different nucleating rates.

To reproduce such S-N-T diagrams, the waiting time needs to be replaced by the induction time (Figure 5). We know that, the time elapsed between starting of experiment (no supersaturation) and observation of first nuclei (threshold supersaturation) is known as the waiting time. However, the induction time is the time elapsed between the 'instantaneous' creation of supersaturation and the detection of nucleation (see Figure 6). This time also known as induction time represents the metastability limit of solution during which a solution can remain supersaturated without nucleating. This induction time t(s) can mathematically be calculated as[18]:

$$t = 1/JV \qquad \text{---------- (23)}$$

where V is volume of the fluid (m^3)

J is the nucleating rate ($m^{-3}.s^{-1}$)[3]

However, this equation is only suitable for measuring the induction time in systems where counting the number N of nuclei or detecting the appearance of a single nucleus in the solution is possible[18].Thus, for other cases, when it is not possible to count the single forming nucleus, or detectable volumes, the induction times can be calculated using the following equation:

[3] The detailed description of how to calculate the nucleation rate can be found in works of J. Poonoosamy (2016)[12]

$$t_{exp} = \left(\frac{3\alpha_v}{\pi G^3 J}\right)^{\frac{1}{4}} \quad \text{---------- (24)}$$

Where α_v is the $\frac{V_d}{V_p}$, *i.e.* the detectable volume fraction of the nucleating phase (-)

$G = \frac{dR}{dt}$ is the growth rate of the nucleating phase ($m.s^{-1}$)

R is the crystallite radius (m) obtained after completion of experiment

V_p is the pore volume (m^3)

V_d is the detectable volume of the nucleating phase (m^3)

To illustrate the applicability of this induction time for the case where counting of forming nuclei is not feasible, the calculations done by J. Poonoosamy (2016)[12] for barite precipitation in compacted sand pores is presented. In this study, the barite precipitation was done by injecting a solution with 0.5 M of $BaCl_2$ into celestite-bearing compacted sand under an advective regime. This injection resulted in dissolution of celestite and precipitation of barite. To investigate the evolution of barite precipitates for pre-determined diffusion times, 5 sets of experimental cells were used. Each of these cells was assigned to reference diffusion times of 9, 28, 156, 200 and 300 hours since the starting of the experiments[12]. At the end of each diffusion time, the experiment in the cell was stopped. The reactant solutions were pumped out and the sandstone sample was sliced into thin sections. These thin sections were then subjected to SEM observations to determine the barite growth in compacted sand pores over these diffusion times.

Finally, to calculate the equation 24, the experimental dataset used were as follows:

1) The detectable volume of the nucleating phase $V_{d,}$ was assumed to be 1 μm^3. This value corresponded approximately to the resolution of SEM images;
2) Two pore volumes V_p were taken in this study, *i.e.* 10 μm^3 and 100 μm^3;
3) During these experiments, after first diffusion time of 9 hours, 10 nm-size barite nanoparticles were found in sandstone pores. Thus, the growth rate $G = \frac{dR}{dt}$ = 10^{-8} m / 32400 s = 3.09×10^{-13} $m.s^{-1}$.

To reproduce the induction times, the interfacial energy was taken equal to 45 $mJ.m^{-2}$ for HEN, and 137 $mJ.m^{-2}$ for HON. In CNT theory, the nucleation takes place when clusters of a certain size overcome the critical size for nucleation. CNT theory also states that these clusters are formed from the monomers present in the solution. In the case of Poonoosamy (2016)[12] work, the number

of dissolved monomers in pore solution was assumed to be N_1 = 2.94 × 10^{23} m^{-3}. Finally, using these calculated parameters, the Supersaturation - Nucleation – Time diagram was constructed for a saturation index [4](SI or Ω) value equal to 4 (directly taken from the experimental results).

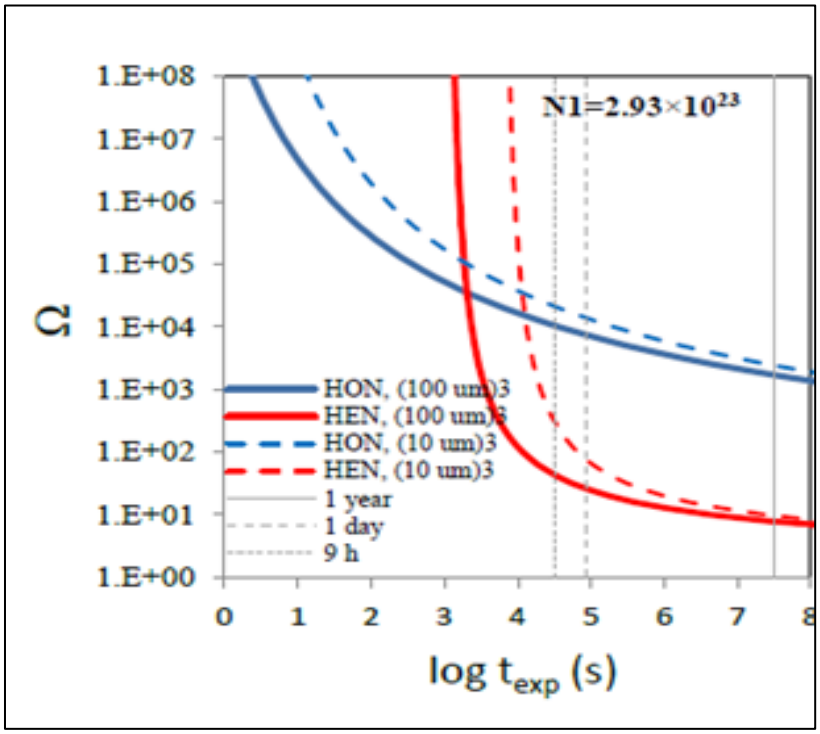

Figure 6: SNT diagrams for homogeneous and heterogeneous nucleation in 10 and 100 µm³ characteristic pore volumes, optimized for barite precipitation experiments. N1 represents the monomer concentration of barite[12]

Observations:

Figure 6 represents the S-N-T diagram for barite precipitation in pore volumes of 10 and 100 µm³. In this figure, we can see that, knowing the number of monomers available for nucleation, at SI = 4, the induction times for HEN and HON in 10 and 100 µm³ pores are clearly different. The induction time for HON in 100 µm³ pore volume is equal to 9 hours and the one in 10 µm³ pore

[4] Saturation index SI is the ratio of ion activity product of ions contributing to precipitation and the solubility product of forming mineral, i.e. SI = IAP/$K_{sp.}$ The importance of saturation index in precipitation is already described in section 1.3.1.

volume is equal to 319 hours. Similarly, the induction times for HEN in 100 μm^3 and 10 μm^3 pore volume are equal to 1 hours and 4 hours respectively

Using these observations of S-N-T, and comparing them with experimental observations, Poonoosamy (2016)[12] concluded that the barite grew at different rates in small and large pores. In small pores, the occurrence of barite overgrowth is due to the fact that HEN is the governing phenomenon, whereas in big pores, nano-crystalline barite precipitates because HON is the governing phenomenon. Thus, all of the observations from the works of Putnis *et al.* (1995)[13] and J. Poonoosamy (2016)[12] reveal some important key points:

1) While studying the counter-diffusion precipitation experiments, the threshold supersaturation of the precipitate depends upon reactant concentration and the nature of precipitating salt;
2) By lowering the reactant concentrations, the waiting time for nucleation increases;
3) Determination of supersaturation at different diffusion times is helpful to develop the evolution of supersaturation as a function of the experimental time;
4) The threshold supersaturation can be then taken as a reference supersaturation value in S-N-T diagrams;
5) Using this S-N-T diagram, we can determine the rate at which a certain nucleation phenomenon takes place in a given pore volume;
6) Finally, if the nucleation takes place in a polymodal pore-size distributed system, the precipitation will take place at different rates.

1.4 Reactive Transport Simulation Codes

In previous two sections we tried to understand 1) the modes of ionic diffusive transport through charged/neutral porous media and, 2) the dissolution/precipitation phenomena that could take place in porous media.

In the third step, it is now time to quantify the impact induced by these precipitation/dissolution phenomena on ionic/neutral species transport through porous medium.

This quantification can be done using some existing chemistry transport codes. Most of these codes use continuum approach, which incorporate physical laws to quantify the aforementioned impacts. Thus, the next sections briefly explain the continuum approach and the physical laws used in these codes.

1.4.1 Continuum approach

A claystone is composed of mineral grains and pore spaces or voids. It can be simply stated as a porous medium. This porous medium is a highly heterogeneous structure that contains physical discontinuities. This porous medium can further be defined by the boundaries of pore walls in order to separate the claystone solid from the void space[20,21].

Although it is possible, in principle at least, to describe this pore-void system at each individual microscale, a precise description of such system becomes difficult as the size of the system increases. Thus, it is generally necessary to approximate the system by a more manageable one. "One quantitative description of the transport of fluids and their interaction with rocks is based on a mathematical idealization of the real physical system referred to as a continuum[22]." In continuum theory, the actual discrete physical system, consisting of aggregates of mineral grains, interstitial pore spaces and fractures, is replaced by a system in which physical variables describing the system vary continuously in space [5]. The value of each physical variable assigned to a point in continuum space is obtained by locally averaging the actual physical property over some Representative Elementary Volume (REV). For example, the temperature in continuum can be defined as $T(r,t)$, where r refers to a point in the continuum space with spatial coordinates (x,y,z), and t represents the time. Similarly, at this point r, the porosity, liquid saturation, and liquid concentration are represented as $\phi(r,t)$, $s_l(r,t)$, $C^l_i(r,t)$ and $C^g_i(r,t)$, where l and g refers to liquid and gas phase, and i represents the i^{th} solute respectively[22].All these physical parameters can then be incorporated in a single volume of REV:

$$V_{REV}(r,t) = V_s(r,t) + V_p(r,t) \qquad \text{---------- (25)}$$

where $V_s(r,t)$ is solid volume at point r in continuum space and time t

$V_p(r,t)$ is the porous volume at point r in continuum space and time t

[5] The governing diffusive transport equations used in continuum approach, have already been explained in section 1.2. Thus in this section they have not been re-listed

1.4.2 *Mineral dissolution and precipitation*

In reactive transport codes, mineral dissolution/precipitation phenomena can take place either at the thermodynamic equilibrium (*i.e.* with no supersaturation) or with some kinetics effects quantified by the rate equation (*i.e.* "the rate at which this mineral tends to dissolve or precipitates"). This rate (R_s) can be mathematically written as[23]:

$$R_s = -A_s\, k_{rate}(1 - Q_s/K) \qquad \text{---------- (26)}$$

where k_{rate}denotes the kinetic rate constant (mol.m^{-2}. s^{-1})

$-A_s$ is the specific surface area $\mathrm{m^2 g^{-1}_{mineral\ phase}}$

K is the equilibrium constant (-)

The Q_s in equation 26 is the ion activity product which can further be defined as:

$$Q_s = a_i^{-1} \prod_{j=1}^{N_c} a_j^{vij} \qquad \text{---------- (27)}$$

where a_j and a_i are the ion activity products of the primary and secondary species in the reactions (-)

The kinetic rate constant in this case is calculated using Arrhenius equation[23]:

$$k_{rate} = k^0_{rate} \frac{A(T)}{A(T_0)} \left[-\frac{1}{R} \left(\frac{1}{T} - \frac{1}{T_0} \right) \Delta E_m \right] \qquad \text{---------- (28)}$$

k^0_{rate} denotes the rate constant(mol.m^2.s^{-1}) at temperature T_0

R is the universal gas constant (J.mol^{-1}. K^{-1}.)

ΔE_m is the activation energy (kJ.mol^{-1})

$A(T)$ is the pre-exponential factor

And the evolution of surface area[6] in response to mineral precipitation can be written as[21]:

$$A_s = \frac{A_{bulk} V_m}{\phi_m MW_m} \quad \text{---------- (29)}$$

A_{bulk} is the bulk surface area ($m^2.m^{-3}_{porous\ medium}$)

V_m is the molar volume of the solid phase($m^3.mol^{-1}$)

ϕ_m is the initial volume fraction (-)

MW_m is the molecular weight of the precipitating phase ($g.mol^{-1}$)

1.4.3 Porosity changes

As the precipitation/dissolution phenomena progress, the change in molar volumes of minerals is created by hydrolysis reactions (*i.e.*, anhydrous phases, such as feldspars, reacting with aqueous fluids to form hydrous minerals such as zeolites or clays). The molar volumes of these newly generated minerals are either larger or smaller than those of the primary reactant minerals. Therefore, constant molar dissolution–precipitation reactions may either lead to porosity expansion or reduction[20]. The response of this evolution of the porosity ϕ to changes in molar volumes of the medium can be mathematically written in the form:

$$\phi = 1 - \sum_{m=1}^{N_m} \phi_m \quad \text{---------- (30)}$$

Where N_m is the number of minerals (-)

ϕ_m is the volume fraction of mineral m in the rock (-)

[6] One must note that this is one way to describe the reactive surface area. However, depending upon the geometry of the reactive surface (plane, sphere *etc*.) there are many other possibilities to define this surface area.

1.4.4 *Archie's law*

The impact of precipitation/dissolution phenomena on diffusion can be coupled using Archie's law, and it can be mathematically written as:

$$D_e = D_w \phi^m \quad \text{---------- (31)}$$

Where D_e is the effective diffusion coefficient ($m^2.s^{-1}$)

D_w is the diffusion coefficient in bulk water ($m^2.s^{-1}$)

ϕ is the porosity of the medium (-)

m is the fitting factor or cementitious factor (-)

1.4.5 *Some issues to address*

The rate equation for precipitation/dissolution reactions uses a kinetic rate constant, k_m, at which the mineral precipitates/dissolves. However, in the section dedicated to precipitation and dissolution phenomena, we observed two important points:

- In the work of Putnis *et al.* (1995)[13], it was seen that, when reactants react in pores, the solute-rich solution firstly remains supersaturated for a certain time and then precipitation takes place. For both of these cases, the rate at which the supersaturation and the precipitation took place was not the same;

- In the same section, we also illustrated an example dedicated to applications of CNT. In this illustration, Poonoosamy (2016)[12] demonstrated that two types of barite precipitated in compacted SiO_2 pores, for which precipitation rates were pore-specific. Therefore, the open question is "what is the true rate constant when the precipitation itself is taking place at different rates?" For the case of surface area, in literature, it is still ambiguous to accurately define the reactive surface area in continuum approach. It is noteworthy that existing codes differently integrate this surface area.

E.g. in CRUNCH flow, the reactive surface area is defined as[21]:

$$A_{bulk} = A_{bulk}^{initial}\left(\frac{\phi}{\phi^{initial}}\right)^{2/3}\left(\frac{\phi_m}{\phi_m^{initial}}\right)^{2/3}$$

Dissolution

$$= A_{bulk}^{initial}\left\{\left(\frac{\phi}{\phi^{initial}}\right)\right\}^{2/3} \quad \text{---------- (32)}$$

Precipitation

Where, $\phi^{initial}$ is the initial porosity (-)

$\phi_m^{initial}$ is the initial individual mineral volume fraction (-)

ϕ_m is the individual mineral volume fraction (-)

This defined surface is only valid for the cases where:

1) If the volume fraction, ϕ_m, of a mineral tends to 0, its surface area also tends to 0.

2) $\left\{\left(\frac{\phi}{\phi_0}\right)\right\}^{2/3}$ = 0, then the porosity of the medium tends to 0.

Furthermore, Oelkers (1996)[24] demonstrated that, when the fluid is channeled from a large space to a fracture, the reactive surface decreases by an order of more than 5. Thus, for a rock pore-sizes ranging from nanometers to micrometers, the reactive surface area is going to change significantly, and true averaging might not result in a proper evolution of porosities due to precipitation/dissolution phenomena. In the Archie's law, the cementation factor remains constant for a given porous material. However, when precipitation in the pores of this material occurs, or when mineral from the pores are dissolved, it is obvious that the tortuosity[7] in this rock sample is going to change, due to pore expansion or reduction. Thus, when the porosity of the rock is evolving, the use of one cementation factor may not always be true. Thus, under this condition, the true reduction/increase in effective diffusivity of a given solute, after precipitation/dissolution

[7] The tortuosity is defined as the average ratio of the microscopic path length L (m) to the macroscopic path length in x (m) in medium or, $\tau = L/x$. This ratio is always greater than or equal to one and represents the tortuous pore channels generated from interconnected void spaces in a porous medium.

reaction, is hard to calculate using Archie's law. Recall that this law is an empirical law and it was developed to calculate the resistivity of a family of rocks, where the pore space does not evolve but remains constant.

2 *Review of Studies Related to Current Problematic*

The previous section was dedicated to list the conventional theories used to describe (1) solute transport through porous medium, (2) the precipitation/dissolution phenomena through porous medium, and (3) how transport and precipitation/dissolution phenomena can be explained in continuum approach, using physical laws and rate equations in codes. In addition to this, some recent approaches, such as CNT and PCS were also given. However, the aim of the current thesis work is to assess the ability of the chemistry transport codes to tackle chemical perturbation induced by saline plume. Therefore, it would be now useful to correlate the bibliographic review with the works already done in the context of this thesis. Table 4, presents a non-exhaustive list of experimental or/and numerical works dealing with the current problematic. Note that in the current manuscript, only the studies dedicated to precipitation or dissolution were analyzed.

Table 4: List of experimental and numerical works dealing with current problematic

	Precipitation	**Dissolution**	**Salinity gradient**
Neutral medium	Fatnassi (2015) Chalk + gypsum	Fatnassi (2015) Chalk + HCl	
Clay model medium	Chagneau (2015) Compacted illite + SrSO4		
Claystones		Berthe (2012) TRNM + CO_2 enriched waters	-Ezzouhri (2014) Torunemire claystone (TRNM) at constant ionic strength (IS) -Leroy (2005) (Callovo-Oxfordian claystone) CO_x with IS gradient ⇔ osmosis Tremosa (2010) TRNM + IS gradient

2.1 Precipitation reaction in neutral or charged medium

2.1.1 Barite precipitation experiment in neutral porous medium

2.1.1.1 Materials and Methodology

To investigate the impact of precipitation on a simple porous medium, Fatnassi (2015)[25] carried out barite precipitation in a compacted chalk sample under diffusive transport. This chalk samples contained 97% of calcite with total porosity of 45% and a mean pore diameter of 660 nm. The sample was sandwiched between two reservoirs as shown in Figure 7. Each of the reservoirs was then filled with equilibrated water. This step enabled to reach a saturation state for the sample and a chemical equilibrium between the reservoir-rock-reservoir system. When equilibrium was achieved, a tritiated water (HTO) of known activity was injected in the upstream reservoir. Let us call this time of injection as $t_0 = 0$. At this time, the concentration of this tracer in downstream is zero. Thus, due to tracer concentration gradient between the two reservoirs HTO diffused from upstream towards downstream reservoir. Using a semi-analytical approach developed by Radwan *et al*. (2006)[26] and Didierjean *et al.* (2004)[27] for through diffusion setups, the effective diffusion coefficient of this injected tracer through intact chalk sample was calculated. Note that this step was previously performed by Descostes *et al.* (2012)[28]. However, contrary to Fatnassi (2015), they used in their setup Peek perforated plates to maintain the chalk sample. Several studies have shown that such perforated plates tend to decrease the diffusive rate and thus, underestimate the effective diffusion coefficient. Therefore, this means that the value of 3.8 x 10^{-10} $m^2.s^{-1}$ used by Fatnassi (2015) from Descostes *et al.* (2012)[28] for the intact chalk is an underestimated value.

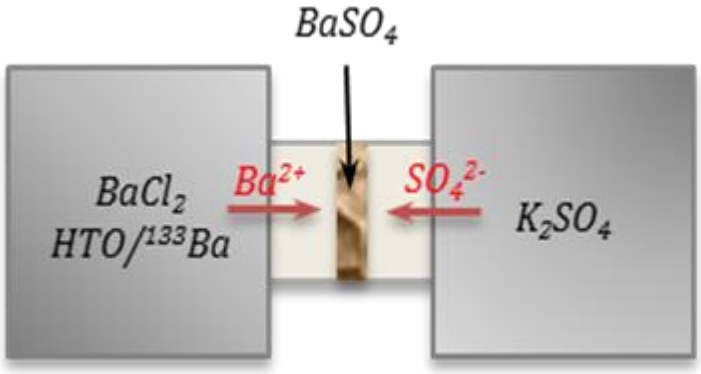

Figure 7: Classical through diffusion setup for barite precipitation (Fatnassi, (2015)[25])

After this step, the equilibrated water was replaced by reactive solutions, *i.e.* solutions with 20 mM of $BaCl_2$ in upstream and 20 mM of K_2SO_4 in downstream reservoirs, respectively. Similar to previous step, HTO was also added in upstream reservoir to monitor the impact of precipitation on the diffusive flux of an inert tracer. Finally, radioactive ^{133}Ba was also injected in upstream reservoir to investigate the barium concentration profile in post-mortem analysis. The barium from upstream and sulfate from downstream gradually diffused into the pores of sandwiched chalk sample and reacted with each other. This reaction further generated a barite-rich pore solution. As more and more of these ions diffused, their continuous reaction in pores oversaturated the pore solution. At one point, from this highly oversaturated solution, barite starts precipitating into the pore of chalk sample. As this precipitation reaction progressed, the forming precipitates partially or fully filled the pore space (or voids) decreasing the porosity of chalk sample.

2.1.1.2 Results

The experimental observations of this barite precipitation are divided into four parts:

1) Determination of effective diffusion coefficient of HTO before and during barite precipitation in chalk samples

The value of effective diffusion coefficient for HTO through intact chalk sample was equal to 3.8 ± 0.5 x 10^{-10} m^2 s^{-1}. This value was taken from the works of Descostes *et al.* (2012)[28] for HTO through intact chalk sample. In the reactive step, a similar approach as in "non-reactive" step was followed to calculate the D_e for HTO during the barite precipitation in chalk sample. The new value of D_e during the barite precipitation was equal to 2.5 x 10^{-10} m^2 s^{-1}, *i.e.* 1.5 times lower than for intact chalk sample. Note that this approach is not strictly correct because the porous medium evolves continuously during the reactive experiment.

2) Determination of porosity reduction of chalk sample through mass balance calculations:

In parallel to determine the impact of precipitation in diffusivity of HTO tracer, Fatnassi (2015)[25] investigated the impact of barite precipitation on total porosity. This step was done by measuring the reactant concentrations at regular time intervals in solution. For the mass balance calculations, it was assumed that the volume of pores in the chalk sample (~ 2.7 mL) was negligible compared to volume of the reservoirs (130 + 170 mL). Using this assumption, the precipitated volume of the mineral was estimated from the change in the reactant concentration in the reservoirs using the molar volume of barite (52.1 $cm^3.mol^{-1}$). Figure 8 shows the evolution of the calculated porosity

for barite precipitation reaction. From this figure, we can see that the porosity decrease is relatively slow and small. For instance, starting from an initial porosity of 45 %, the porosity after 130 days is 42.5 % for the barite experiment.

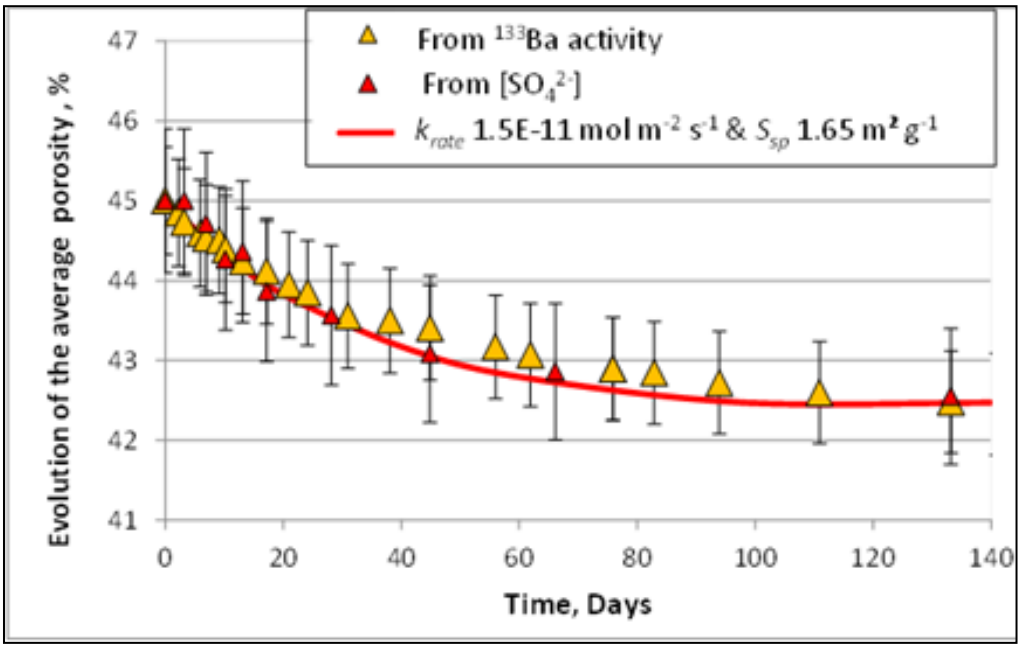

Figure 8: The precipitated volume of barite calculated from decrease in ^{133}Ba concentration in upstream and SO_4 concentration in downstream reservoir. This precipitated mineral volume corresponded to decrease in porosity[25]

2.1.1.3 Post mortem analysis

To investigate the localization and the thickness of barite precipitated layer in chalk sample, optical and EDS-SEM analyses were done. These investigations revealed that the precipitation layer started at 2.85 ± 0.10 mm from inlet reservoir (Ba + HTO reservoir), *i.e.* not exactly in the middle of the sample. The thickness of this layer further was not larger than 100 µm, as shown in Figure 9.

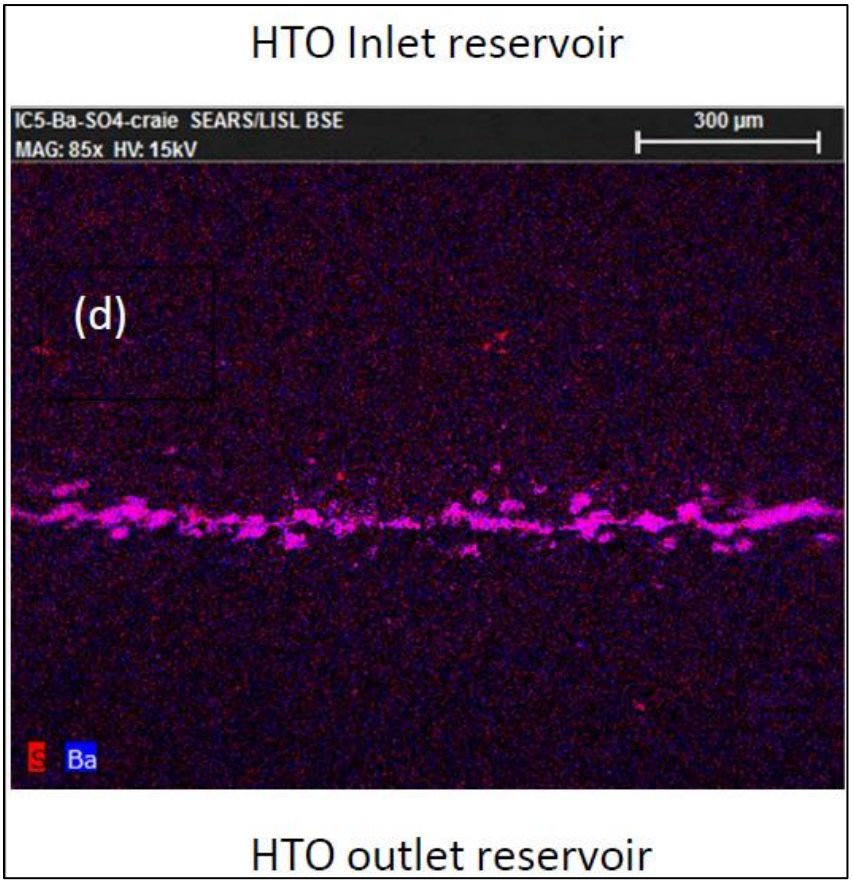

Figure 9: EDS-SEM observation of barite precipitation (pink line) in chalk porous medium. The precipitation zone observed is not strictly perpendicular. This zone consists of a densely precipitated barite (continuous pink line) with some barite precipitate islands nearby this continuous zone (pink spots)[25]

The thickness of this precipitating layer can also be estimated using mass balance calculation with the chemical monitoring in solution. This technique allows us to estimate the amount of precipitating barite within chalk. In barite precipitation experiment, a volume of 0.14 cm^3 of precipitating barite was estimated using this technique. If we assume that all the pores of this zone were filled by barite, then a thickness of about 350 µm can be deduced from this technique. However, the value of this thickness directly contradicts the precipitation zone thickness observed using EDS-SEM. This difference clearly indicates a discrepancy, addressing the issue of the precipitation phenomenon, *i.e.* the kinetic rate, the supersaturation, *etc.*

2.1.1.4 Numerical modeling

The aforementioned experimental results were quantified using the chemistry transport code CRUNCH Flow[21]. The effective diffusion coefficient of HTO for intact chalk was reproduced by

performing simulations without any chemical reaction and a cementation factor of 2.1 in the Archie's law. This cementation factor was determined from the value of D_e given by Descostes *et al.* (2012)[28] and with a D_0 equal to 2 x 10^{-9} m^2 s^{-1} for water tracer (HTO)[28]. The diffusion curve for HTO was similar to the curve calculated from the semi-analytical approach. In next step, to reproduce the barite precipitation, a precipitation rate value of 1.5 x 10^{-11} $mol.m^{-2}.s^{-1}$ and a specific surface area value of 1.65 m^2 g^{-1} were introduced into the chemistry transport codes from a literature review[29]. Similarly, during this precipitation reaction, the evolution of reactant was also reproduced in CRUNCH code. The mass balance calculations were carried out. Figure 10 shows the impact of barite precipitation on porosity of chalk sample. The mass balance calculation done by CRUNCH resulted in generating a barite precipitate with a thickness of 350 µm. This value directly contradicted the optical observations (Figure 9), where the thickness of the precipitated layers was approximately 100 µm.

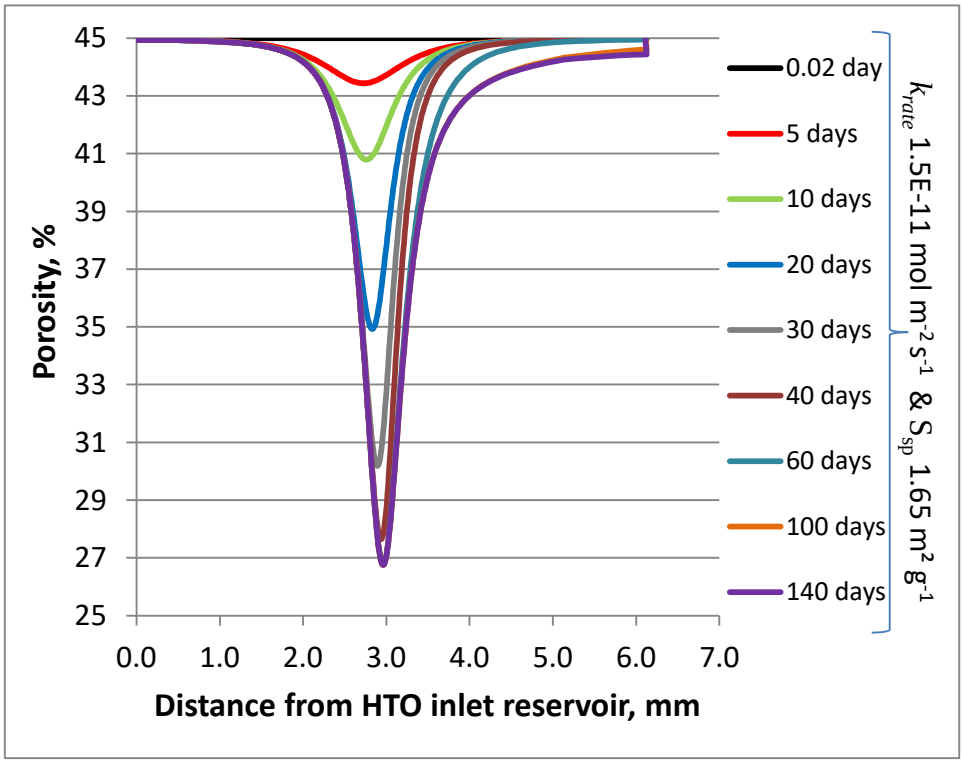

Figure 10: Evolution of barite precipitation zone in chalk pores, predicted by Crunch flow using mass balance calculations[25]

2.1.2 Precipitation in surface charged porous medium

2.1.2.1 Materials and methodology

The clay material used in the study of Chagneau (2015)[15] was the illite-du-Puy, a natural clay extracted from the Puy-en-Velay (Massif Central, France) Upper Eocene clay formation. The material contained carbonates and quartz, with a clay fraction composed primarily of illite (80-100%)[30]. The illite-du-Puy used in this study was purified (removal of quartz and carbonaceous phases) and Na-exchanged in a standardized way, described in details by Glaus *et al. (2012)*[30] . This illite-du-Puy was further compacted to a bulk dry density of 1700 $kg.m^{-3}$. The total accessible porosity was 42%, with anion accessible porosity equal to 25%. The compacted illite-du-Puy clay was then sandwiched between two reservoirs containing equilibrated water and maintained by means of two perforated plates like Descostes *et al.* (2012)[28] did. The experimental setup adopted by Chagneau (2015)[15] is shown in Figure 11.

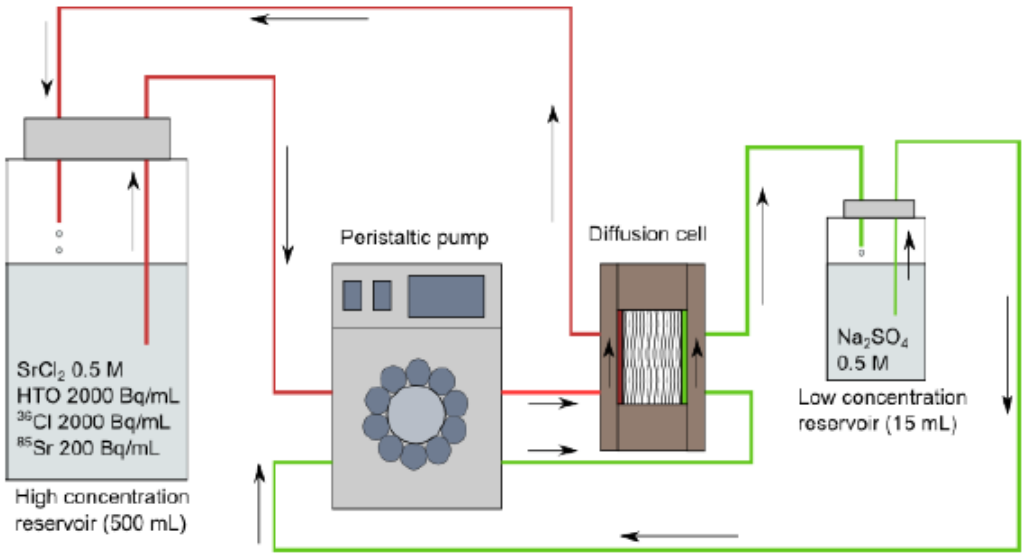

Figure 11: Schematic view of through diffusion setup used by Chagneau (2015) for celestite precipitation

In the first step, ionic equilibrium between sample pores was achieved using 0.5 M NaCl solution in reservoirs. After this step, reservoirs solutions were replaced by 0.5 M of $SrCl_2$ and Na_2SO_4 in upstream and downstream reservoir respectively to launch celestite precipitation. To investigate the impact of celestite precipitation on diffusion of neutral and anionic species, the upstream reservoir was spiked with HTO (neutral) and $^{36}Cl^-$ (anionic) as the reference tracers. The upstream reservoir was also spiked with $^{85}Sr^{2+}$ as a reactive tracer. The upstream reservoir solution of

volume 500 mL was not renewed during the duration of the experiments. This large volume ensured that the system was kept under constant boundary conditions (concentration variation of less than 5%). Also, since the volume withdrawn at periodic sampling was very small (1 to 2 mL), the variation in the volume was not significant. However, the downstream reservoir contained solution of volume 15 mL. Contrary to upstream case, the downstream solution was completely replaced every day at the initial phase of the experiment, then every week when the flux of tracers significantly decreased. A peristaltic pump circulated the solutions at a constant rate (50 µL.min^{-1}) through each end pieces.

2.1.2.2 Results

In this experiment, the normalized flux for HTO[8] was taken as 1.3×10^{-8} m.s^{-1}, and for ^{36}Cl it was 5.9×10^{-9} m.s^{-1}. After the celestite precipitation for 70 days, the HTO flux decreased to 7.0×10^{-9} m.s^{-1} and the ^{36}Cl flux decreased to 1.0×10^{-9} m.s^{-1}. To evaluate this decrease in HTO and ^{36}Cl flux, it was necessary to evaluate the decrease in total porosity and anion accessible porosity after the celestite precipitation took place in illite sample. For this reason, a post-mortem analysis was done on this illite sample. In this analysis, a tomography (µCT) scan was used to locate the position of the precipitation front. Figure 12 shows the shape of precipitation zone obtained after the µCT scan. In this post-mortem analysis, the average porosity was found to be 52% in the undisturbed zone and 29% in the precipitated zone (for porosity calculation an additional post treatment called autoradiography was used, the details of this technique is detailed in Chagneau(2015)[15]. From these results, Chagneau (2015)[15] concluded that celestite precipitated in larger pores where the extent of the anionic exclusion is the smallest. As the reaction progressed, these pores were occupied by celestite precipitates and the ^{36}Cl path available for diffusion too was blocked. Thus, this resulted in higher decrease in the diffusive flux of ^{36}Cl than HTO.

[8] In this thesis work, the impact on total porosity and anion accessible porosity was estimated by comparing the normalized flux of HTO and ^{36}Cl in intact illite clay. As no initial and final values of effective diffusion coefficients were mentioned, in this discussion the flux are represented.

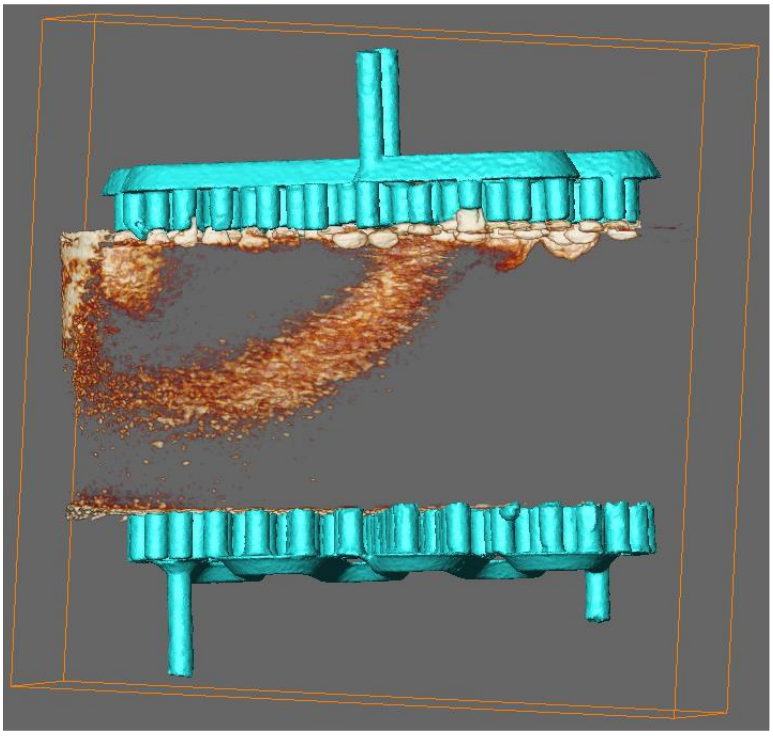

Figure 12: 3D reconstitution of the precipitation front (orange) in the in the illite sample[15]

From Figure 12, we can see that, on contrary to Fatnassi (2015) experiment dealing with barite precipitation, the precipitating zone in this illite sample is not localized in the middle of the sample; on the contrary, it displays clear asymmetry, major precipitation within the perforated plate. As no explanation for such shape was found in the work of Chagneau (2015), this point remains for further discussion.

2.1.3 Dissolution reaction in neutral and charged medium

2.1.3.1 Calcite dissolution in neutral porous medium

To investigate the impact of dissolution in simple porous medium, Fatnassi (2015) investigated the impact of an acid attack on porous network of unimodal chalk sample. In this dissolution study, the same through diffusion setup as used in barite precipitation in chalk medium was used. In a first step, a tritiated water was injected in the upstream reservoir. The effective diffusion coefficient of this tracer[28] through intact chalk was equal to 3.8×10^{-10} $m^2.s^{-1}$. In second step, to induce dissolution, an equilibrated water with 0.1 M of HCl was injected in the upstream reservoir. This resulted in dissolution reaction and in an increase in the effective diffusion coefficient of water tracer to 6×10^{-10} $m^2.s^{-1}$ within 5 days since the beginning of the experiment. Due to the rapid

dissolution of calcite, large amount of CO_2 was generated in the upstream reservoir. However, the experimental methodology adopted required to regularly open the upstream reservoir valve for sampling the solutions. Thus, when the upstream reservoir valve was opened, a de-gassing of CO_2 was observed. Due to this frequent loss of CO_2, an intermediate condition between an open system and closed one was created, making almost impossible an accurate reproduction of these data by means of a chemistry transport codes, without assuming very strong assumptions.

2.1.3.2 Calcite dissolution in three tournemire claystones

2.1.3.2.1 Materials and Methodology

The main aim of Berthe's (2012)[31] work was to investigate the containment properties of clay rocks aged by an acid attack for mimicking CO_2 storage. By means of the Tournemire experimental facility, three different claystones with different amount of carbonate minerals were investigated. Their mineralogy is presented in Figure 13, with:

- Upper Toarcian level: drilled from depth of 15.76 meters below tunnel level with calcite and dolomite content equal to 15% and 1% respectively.
- Paper Shale: drilled from depth of 149.90 meters with calcite and dolomite content equal to 34% and 2% respectively.
- The Domerian: drilled from depth of 214.85 meters with calcite and dolomite content equal to 7% and 2% respectively.

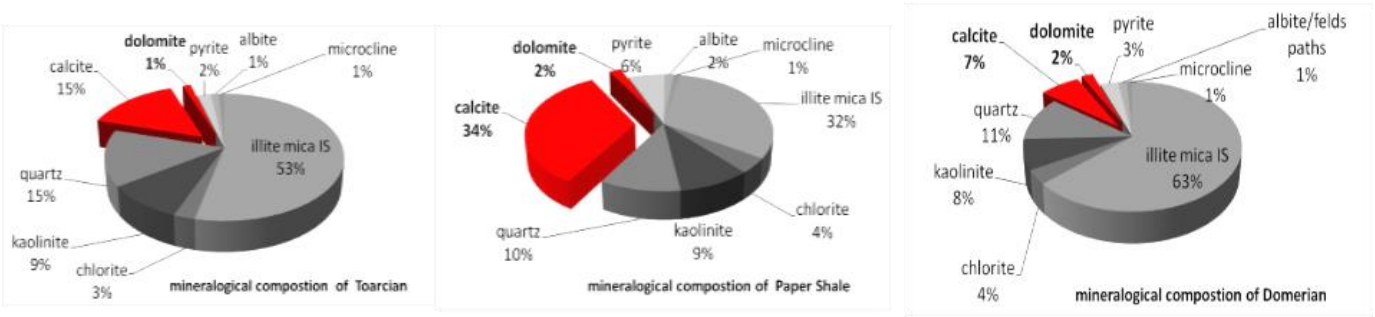

Figure 13: Different mineral compositions of Domerian, Paper Shale and Toarcian clays

To demonstrate the impact of CO_2-rich acid attack on these three clays, a brief description of the experimental setup used by Berthe (2012)[31] is explained here (note that only results obtained on the Upper Toarcian level are presented in the current report). To prepare this experimental setup, the aforementioned clay samples were initially cut into 5 to 15 mm thickness and 30-35 mm

diameter slices. These samples were then sandwiched in a through diffusion setup and were pre-equilibrated with pore water of known ionic concentration (Figure 14). After few days, when chemical equilibrium was reached, a neutral tracer (HDO or HTO) and an anionic tracer ($^{36}Cl^-$) were injected in the upstream reservoir. This step was necessary to estimate the anionic accessible porosity and total porosity of the intact sample. After this step, in upstream reservoir, pure CO_2 gas was injected at pressure pCO2 = 1 atm, and in downstream reservoir, a mixture of N_2/CO_2 was injected at $pCO_2 = 10^{-2.4}$ atm to achieve the in-situ conditions of Tournemire claystone. The injection of pure CO_2 in upstream reservoir generated an acidic solution of pH ~ 5, but the pH of downstream reservoir was maintained at 7.8. To investigate the evolution of pH and chemistry throughout the experiment, samples were regularly taken in both reservoirs for analyses. Finally, in upstream reservoir, HTO and ^{36}Cl of known concentration were injected. The evolution of these tracers was then evaluated by measuring their concentration in downstream at regular time intervals.

2.1.3.2.2 Results

The effective diffusion coefficients of HTO and ^{36}Cl for intact Upper Toarcian sample were calculated using the same methodology adopted by Fatnassi (2015)[25]. In work of Berthe (2012)[31], the effective diffusion coefficient for HTO was found to be $D_{e,HTO} = 7.6 \times 10^{-12}$ $m^2.s^{-1}$. The effective diffusion coefficient for ^{36}Cl was found to be $D_{e,36Cl} = 6.0 \times 10^{-13}$ $m^2.s^{-1}$.The total and anion accessible porosity for this clay was found to be 12% and 3%, respectively. In second step, the acid attack was launched by injecting CO_2 rich solution in the upstream reservoir. Within 10 days Berthe (2012)[31] observed that the effective diffusion coefficient of HTO instantaneously increased to a value of 11.1×10^{-12} $m^2.s^{-1}$ and total porosity increased from 12% to 15%. In the same time, the anionic accessible porosity increased to 6%, with $D_{e,36Cl} = 2.1 \times 10^{-12}$ $m^2.s^{-1}$.

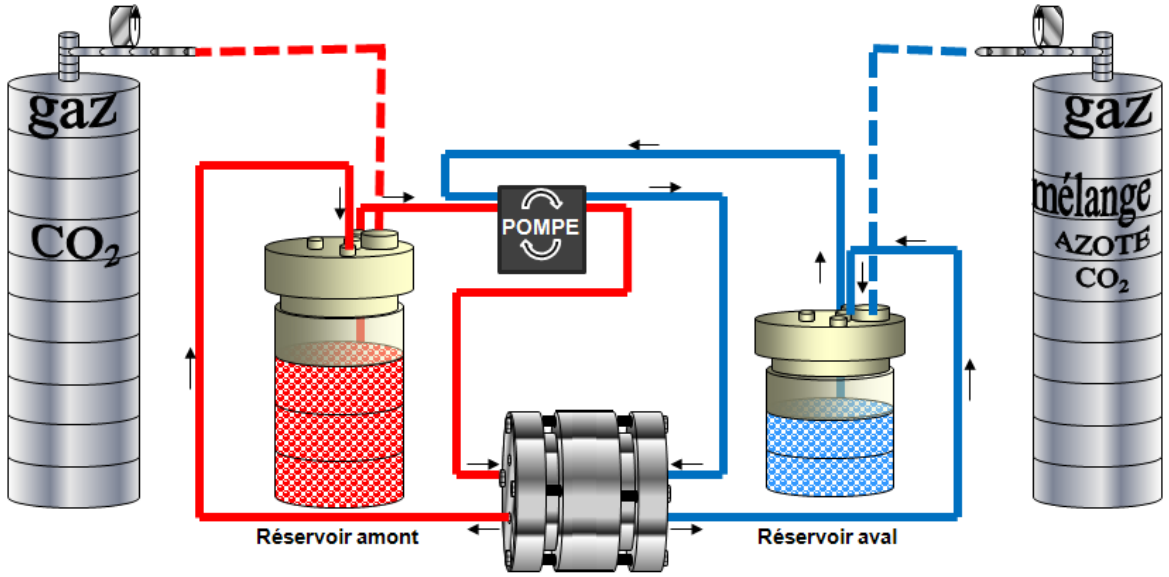

Figure 14: Schematic view of the through diffusion setup used for acid attack on Tournemire claystone samples. In upstream reservoir CO_2 is injected at partial pressure 1 atm. In downstream reservoir, a mixture of N_2 and CO_2 is injected at partial pressure $10^{-2.4}$ atm. The solutions from both of the reservoirs are circulated through a perstaltic pump[31]

1. Evolution of ion concentration and pH in upstream and downstream reservoirs:

Table 5 represents the ionic concentration of upstream reservoir solution before and after acid attack. From this table, we can see that, except Ca^{2+}, Mg^{2+} and HCO_3^- almost all of the other ions stabilized during the acid attack. The significant increase in Ca^{2+}, Mg^{2+} and HCO_3^- ions clearly resembles the scenario of calcite and dolomite dissolution through Upper Toarcian argillite pores.

Table 5: Ionic concentration in upstream reservoir, before and after dissolution experiment

Ions	Upper Toarcian pore water mmol/L	Increase in Ion concentration by acid attack 120 days after mmol/L
Na	13	16
K	0.30	0.5
Mg	0.30	1.2
Ca	0.50	5
Cl	9.10	9
SO_4	1.00	1.1
HCO_3	3.70	16
pH[9]	7.8	5.5

At the end of the experiment, the amount of calcium dissolved from Upper Toarcian claystone was determined by measuring the calcium concentration in upstream reservoir. Comparing this calcium with the mineralogical calcite present in Upper Toarcian clay, it was found that only 3% of the calcite was dissolved. Also, from the post-mortem analysis, it was found a good consistency between the dissolution of this 3% of calcium, and the almost 400 µm of calcite layer dissolved (Figure 15).

[9] The pH value corresponding to 7.8 is before injecting CO_2 gas (p_{CO2} = 1atm). When CO_2 attack began, the pH dropped down to 4.

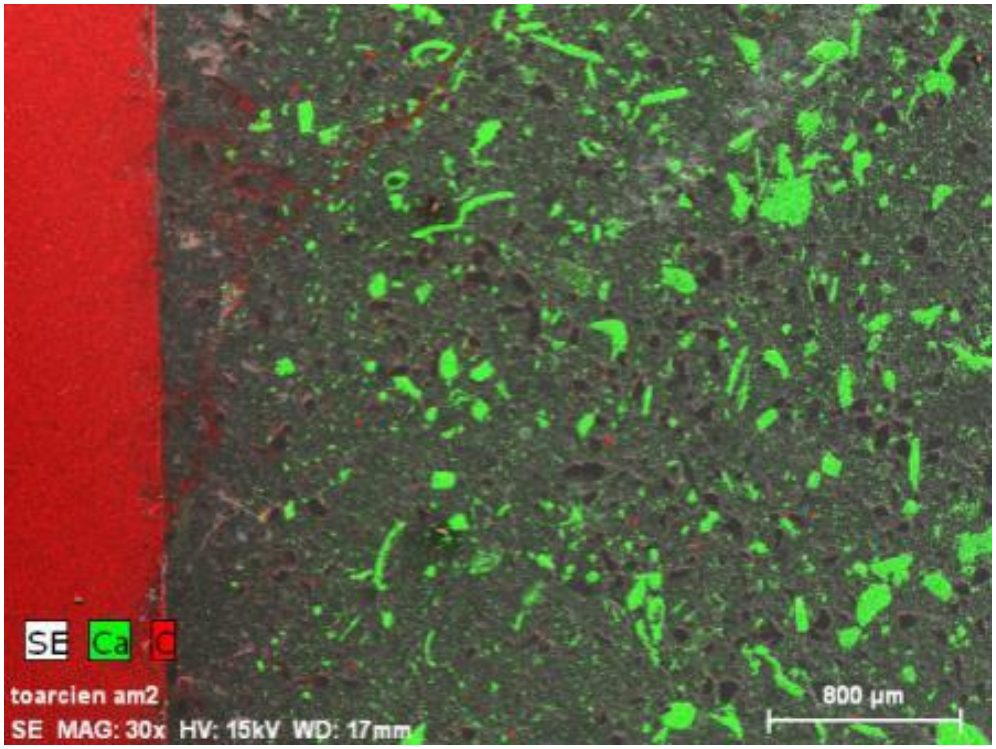

Figure 15: MEB observation of Upper Toarcian clay. The green spots represent the calcium (i.e. the carbonate phase) present in the sample. On the left hand side, we can see that due to acid attack about 400 µm of calcite is dissolved from the clay sample[31]

2.1.3.2.3 Numerical modeling

The chemical changes in reservoirs of cells were numerically reproduced by Berthe (2012)[31] with the geochemical code PhreeqC-1D by coupling chemistry and transport. Two solutions have been described on each side of the sample: one representing the upstream solution (Upper Toarcian synthetic pore water with a pCO_2 ~ 1 atm) and the other representing the downstream solution (Upper Toarcian synthetic pore water with a pCO_2 ~ $10^{-2.4}$ atm). In this code, the sample description was done by inserting the right proportion of mineral reacting in the dissolution mechanisms. Thus, the mineral amounts were 26.64 mol/(Kg of water) of calcite, 0.97 mol/KgW of dolomite and 24.64 mol/KgW of illite[32]. The equilibrated water prepared for Upper Toarcian clay experiment, further was taken as a representative of pore water for modeling.

The input parameters for the transport correspond to the initial transport properties of HTO obtained experimentally on intact Upper Toarcian sample. This means that a unique diffusion coefficient is considered for all the species with a unique accessible porosity. Moreover, as the geochemical code PhreeqC does not allow feedback on the porosity, it was therefore not

considered in this model. The dissolution rate was directly taken from the works of Lasaga (1998)[23] and the kinetic rate from Palandri *et al.* (2004)[33], and the description of the cation exchange sites was also integrated[31]. Finally, the varying parameter in this model was the amount of carbonated minerals available for a possible dissolution in Figure 16 shows the comparison of the experimental and calculated data for calcium and magnesium in the upstream reservoir as a function of time. This good consistency was obtained assuming a reduction of the amounts of calcite and dolomite accessible for dissolution by a factor of 5.

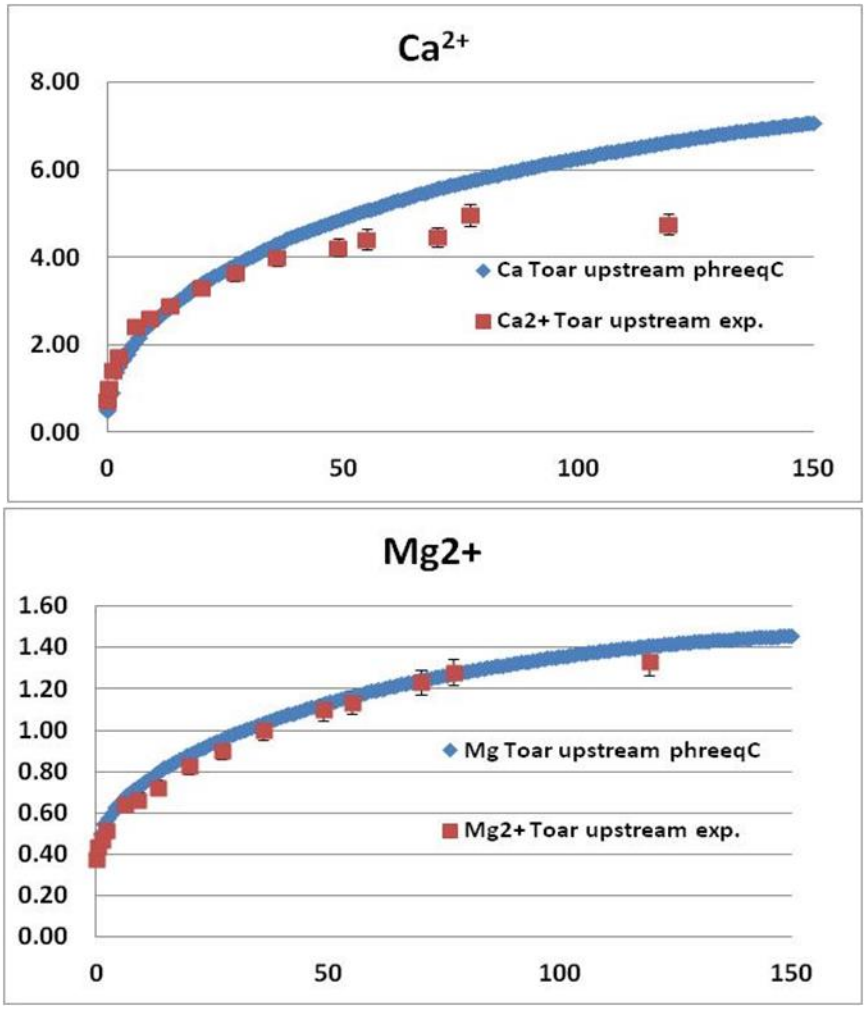

Figure 16: Comparison of the experimental and calculated concentrations of calcium and magnesium as a function of time in the upstream reservoir (Berthe, 2012)

2.1.3.2.4 Semi-analytical Modeling

Using the semi-analytical approach developed by Didierjean et al.(2004)[27] and Radwan (2006)[26], a representative double layer model of Upper Toarcian clay was developed (Figure 17). This double layer model consists of a 400 µm-thick layer, altered by the CO_2 attack and a second one composed of 4.6 mm of intact Upper Toarcian rock

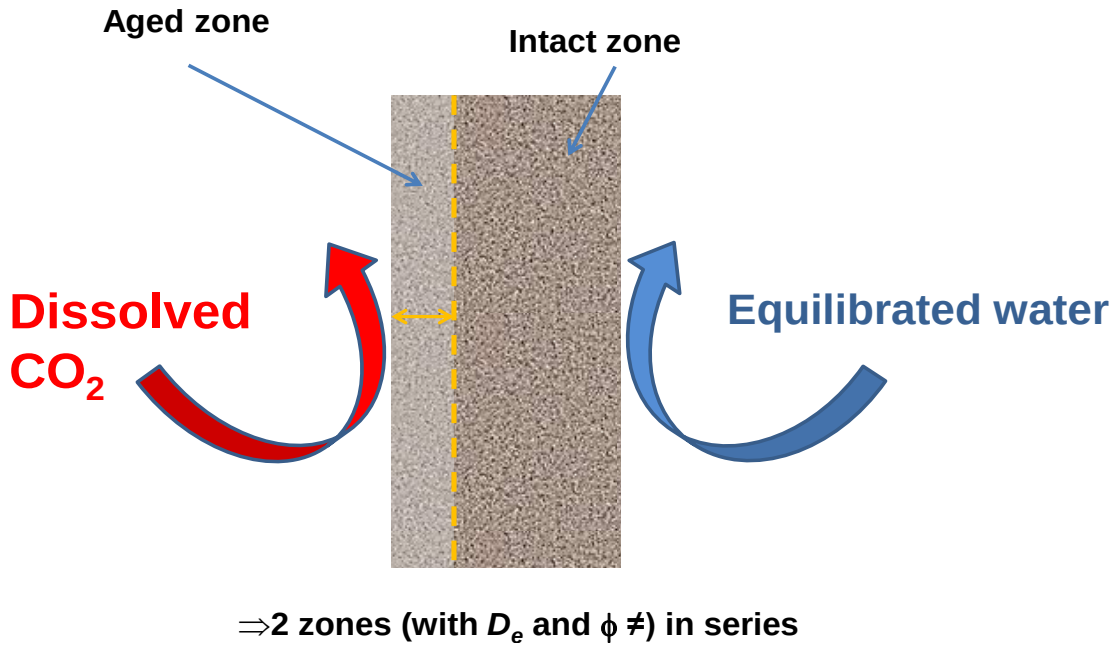

Figure 17: Schematic view of the two layer model[31]

Berthe (2012)[31] kept constant the values of the diffusive parameters for the intact layer, while for the aged layer, the effective diffusion coefficient and the porosity were adjusted to try to reproduce the diffusive flux of HTO and ^{36}Cl. In experiments the author demonstrated that the increase in diffusivity of tracers at the CO_2 inlet was primarily due to increased pore size along the sample (due to dissolution) rather than homogeneous dissolution of minerals. Thus, since, the code does not incorporate any processes to account for pore enlargement, it failed to reproduce experimental data set for HTO and ^{36}Cl after the dissolution process.

In literature the work of Putnis *&* Mauthe (2001)[9] also showed that halite dissolution in sandstone pores was dependent on the pore size. In smaller pores faster dissolution was observed compared to dissolution in large pores. From this analogy, the enlargement of pores in Tournemire claystone can be explained as follows: at the initial stage of experiment, CO_2 led to homogeneous dissolution of minerals near the inlet surface of the sample. After this, as CO_2 enriched solution diffused further

into the sample, the minerals from the smallest pores were rapidly dissolved. This dissolution opened new pathways for CO_2 to penetrate the sample and dissolution front progressed into the sample. Over time due to dissolution in smallest pores long channels were opened which then allowed higher diffusion of HTO and ^{36}Cl tracers.

3 Conclusions and adopted methodology for this study

The two principal mineral perturbation extensively studied in literature are mineral dissolution and precipitation in porous media. A two-step approach is generally adopted: firstly, using laboratory scale experiments to determine the evolution of intact rock properties in response to each phenomenon, secondly reproducing these results using coupled chemistry transport codes for larger times and space scale.

The impact of mineral dissolution on the intact properties of claystones is presented in the work of Berthe (2012)[31]. This study dealt with demonstrating macroscopic dissolution phenomena in three types of Tournemire claystones of varying distribution of pore size, carbonate minerals and clayey minerals. The dissolution phenomena were studied by CO_2 attack on carbonate minerals. The impact of dissolution on intact properties of claystones was determined using water tracer (HTO) and anionic tracer (chloride-36). The end results from this study showed that the macroscopic impact of carbonate mineral dissolution on extent of water tracers and chloride-36 diffusivity increase for the three claystones was similar. However, different dissolution patterns of carbonate minerals were observed in each claystone. This study thus showed that the evolution of claystone properties will depend upon the texture and distribution of carbonate minerals. This means that the initial local pore space and its evolution may potentially govern the evolution of rock containment properties. However, the chemistry transport codes (explained in section 1.4), usually at the REV scale, explicitly rely on average properties: e.g. an overall porosity and not a pore size distribution. The long-term impact of mineral perturbation on diffusivity of reference tracers in chemistry transport codes is envisaged using empirical Archie relationship on a local average scalar porosity.

However, the works of Berthe (2012)[31], showed that dissolution led to evolution (transformation, modification) of the pore structure and not the porosity. Moreover, in literature it has not yet been established if mineral dissolution due to CO_2 attack on porous materials with same total porosity as Tournemire claystones but very different pore structure and distribution of carbonate minerals will lead to similar impact on diffusivity of HTO and ^{36}Cl. In absence of these experiments, it cannot

be stated forehand if porosity evolution due to dissolution on one porous material can be used to predict such impact on different porous materials. Thus, the robust dataset of Berthe *(2012)*[31] cannot be used on first hand to test the limitations of Archie's relationship.

The study of the second mineral perturbation, "mineral precipitation impacts on intact properties of claystone" is even more complex. This is because the consolidated argillaceous rocks possess very low porosity, heterogeneous pore network with presence of clayey minerals with negative surface charge. Thus, there is sorption of cationic species and exclusion of anionic species from the pore network. From an experimental point of view, it is complex to engineer laboratory scale setups that can derive interpretable data sets showing evolution of claystone properties in response to mineral clogging. Like dissolution case, a strong experimental results dataset for clogging impacts on simple proxy materials is required.

For this reason, two major works dealing with clogging phenomena under diffusive regime were carried out on proxy materials. The first dealt with celestite precipitation in compacted sand and in compacted illite[15]. Both experiments were carried out using a counter diffusion technique that is briefly explained in section 2.1.2. In such setups, the reactants counter diffuses from their respective reservoirs through the sample and generate a mineral precipitate into the porous system. In both cases the evolution of reactants concentration in reservoirs in response to precipitation was not determined. This step is essentially important for strontium ion as in compacted sand it purely contributes to precipitation in the sample pores. But in illite it contributes to precipitation and sorption on pore surface. Thus, for both cases, it is necessary to quantify the strontium behaviour in upstream in response to precipitation in samples. This chemistry evolution in reservoir can then be used in chemistry transport codes to determine if code can capture same effect that is seen experimentally.

Moreover, for numerical simulations of compacted sand experiment, the total celestite amount and minimum porosity fitting was used to reproduce the impact on water tracer diffusivity. However, from the works of Poonoosamy (2016)[12] and Prieto (2014)[17], it is known that the local evolution of mineral is pore size dependent. This local evolution will then determine the effectiveness of clogging in changing the intact properties of studied material[10]. Thus, to test if Archie relationship is predictive for determining long term evolution of rock containment properties, such fitting is not sufficient. In illite experiment the impact of celestite precipitation on diffusivity of water tracer and anionic tracer (chloride-36) was studied[15]. The end results showed total clogging of anionic tracer through celestite precipitated illite sample. One of the hypotheses presented for such observation

was, “the newly formed celestite mineral possessed negative surface charge.” But the clay surface possesses the negative surface charge and the µCT images showed celestite precipitation at the clay surface-perforated plate interface. Moreover, since surface charge of celestite precipitated on neutral pore surface (*i.e.* compacted sand) remains unknown the clogging results of illite are still under debate. A similar work was carried out by Fatnassi (2015)[25] on series of neutral porous materials such as sandstone, glass frits and chalk. This study also used counter diffusion setup to engineer mineral precipitation in porous sample. In each case the evolution of reactants in response to precipitation was demonstrated. However, in all of the studies the water tracers were injected in one reservoir at the very beginning of the experiments. The impact of precipitation on diffusion was then measured by their diffusive behaviour in counter reservoir. However, in all of the cases, before enough mineral precipitated to generate effective clogging, the water tracers reached equilibrium in the counter reservoirs. Thus, precipitation impact on diffusivity was not sufficiently demonstrated. Moreover, in absence of rigorous post mortem analyses such as micro-tomography, scanning electron microscopy and abrasive peeling the evolution and morphology of mineral precipitates were not properly quantified. This step is necessary as the distribution and morphology of mineral precipitates in porous sample are essential to explain the macroscopic observations: chemistry evolution in reservoirs and impact on diffusivity.

Both of these studies present a rigorous experimental approach to explain the mineral clogging phenomena in series of proxy porous materials. However, these experiments still do not explain “whether Archie relationship can be generalized for clogging phenomena on any porous media.” For such demonstration, following three questions needs to be answered:

1. Can clogging phenomena be generalized for materials with same porosity but different pore size distributions?
2. Will a same precipitating mineral lead to same effectiveness of clogging on two materials with same porosity but different surface charge properties?
3. Will precipitating minerals of very different intrinsic properties such as solubility, kinetic rate of precipitation leads to same impact on diffusivity of a single porous material?

In view of these questions, this thesis deals with engineering experiments to properly quantify the mineral precipitation in three proxy porous materials. In the first step, the intact properties such as pore size distribution and diffusion coefficients of reference tracers for each sample are determined. The pore size distribution of each sample was determined using mercury intrusion

and extrusion porosimetry and diffusion coefficients of reference tracers were measured using through diffusion technique.

In the second step the impact of mineral precipitation on intact properties of each of the sample was carried out using counter diffusion setup. In these experiments, the behaviour of reactants in the reservoirs were measured using reservoir monitoring technique. At this time, the impact of precipitation on diffusivity of reference tracers was determined. This step was similar to intact diffusion step.

In the third step the evolution of precipitated minerals in each sample were determined using post-treatment analysis such as x-ray microtomography and Scanning electron microscopy.

In the final step the chalk experiments were reproduced using chemistry transport codes: HYTEC and CrunchTope. This step helped us test the validity of Archie's relationship compared to experimentally derived impact on diffusivity. The simulations were performed first in 1D, then in 2D to investigate the impact of spatial variability.

The first proxy material in our study, chalk sample is composed of grain matrix and randomly distributed coccoliths that add spatial variability in properties such as heterogeneous diffusive pathways and reactive surface area for precipitation. The second proxy materials is compacted illite which presents a pore size and negative surface charge closer to claystones. Thus, chalk and illite samples present end members in terms of surface charge on pore and pore size distribution. The third proxy material is compacted kaolinite which has pore size distribution closer to illite with presence of weak negative surface charge. Thus, the final porous material allowed us to test how mineral precipitation behaviour changes when pore size is decreased, and surface charge is gradually increased.

For chalk, clogging experiments were carried to using two sulfate alkali minerals: barite and gypsum. These minerals present two opposites in terms of intrinsic properties such as solubility and kinetic rate of precipitation. Thus, chalk experiments will demonstrate if spatial variability with intrinsic properties will lead to similar evolution of barite and gypsum in chalk porosity. These experiments will eventually demonstrate if, for the same porous material, clogging phenomena impacts induced by the precipitation of different minerals can be generalized or not. For kaolinite and illite, barite precipitation was carried out to demonstrate if precipitation of this mineral leads to similar impact on diffusivity of water tracer as observed in chalk. This comparison eventually tests

similarity or difference in precipitation when “the pore size is reduced, and pore possess negative surface charge”.

In all the three studies, anionic tracer (chloride-36) is injected in parallel to water tracer. This step was necessary to test whether newly formed barite mineral on the pore surface of chalk, kaolinite and illite samples has surface charge or not.

Finally, based upon the aforementioned approach, this thesis is divided into following sections:

1. In the first part, clogging experiments dealing with barite and gypsum evolution in chalk and their impact on water tracer diffusivity are explained in length.
2. The first half of the second part deals with barite precipitation experiments in kaolinite. The obtained results are then compared with barite precipitation in chalk. Finally, the impact of surface charge of newly formed mineral barite on diffusivity of chloride-36 for chalk and kaolinite is assessed.

   In the second half of this part, barite precipitation in compacted illite and its impact on diffusivity of water tracer and anionic tracer is presented.
3. A general discussion from all of the experimental results is finally presented.
4. In the last part of this manuscript, the chalk experiments are numerically simulated in 1D and 2D using HYTEC and CrunchTope.

4 References

(1) Savoye, S. Apport Des Traceurs à La Compréhension Des Processus de Transport Au Sein de Formations Argileuses Indurées. Mémoire d'habilitation à diriger des recherches de l'Université Paris-Sud, IRSN, Collection HDR 80pp., **2008**.

(2) Sposito, G. *The Chemistry of Soils*; Oxford university press, **2008**.

(3) Horseman, S. T.; Higgo, J. J. W.; Alexander, J.; Harrington, J. F. Water, Gas and Solute Movement through Argillaceous Media. *Nuclear Energy Agency Rep. CC-96/1. OECD, Paris* **1996**.

(4) Altmann, S.; Tournassat, C.; Goutelard, F.; Parneix, J.-C.; Gimmi, T.; Maes, N. Diffusion-Driven Transport in Clayrock Formations. *Applied Geochemistry* **2012**, *27* (2), 463–478.

(5) Appelo, C. A. J.; Wersin, P. Multicomponent Diffusion Modeling in Clay Systems with Application to the Diffusion of Tritium, Iodide, and Sodium in Opalinus Clay. *Environmental science & technology* **2007**, *41* (14), 5002–5007.

(6) Tournassat, C.; Steefel, C. I. Ionic Transport in Nano-Porous Clays with Consideration of Electrostatic Effects. *Reviews in Mineralogy and Geochemistry* **2015**, *80* (1), 287–329.

(7) Stumm, W.; Morgan, J. J. *Aquatic Chemistry: Chemical Equilibria and Rates in Natural Waters*; John Wiley & Sons, 2012; Vol. 126.

(8) Rijniers, L. A.; Huinink, H. P.; Pel, L.; Kopinga, K. Experimental Evidence of Crystallization Pressure inside Porous Media. *Physical Review Letters* **2005**, *94* (7), 23–26.

(9) Putnis, A.; Mauthe, G. The Effect of Pore Size on Cementation in Porous Rocks. *Geofluids* **2001**, *1* (1), 37–41.

(10) Emmanuel, S.; Berkowitz, B. Effects of Pore-Size Controlled Solubility on Reactive Transport in Heterogeneous Rock. *Geophysical Research Letters* **2007**, *34* (6), 1–5.

(11) Emmanuel, S.; Ague, J. J.; Walderhaug, O. Interfacial Energy Effects and the Evolution of Pore Size Distributions during Quartz Precipitation in Sandstone. *Geochimica et Cosmochimica Acta* **2010**, *74* (12), 3539–3552.

(12) Poonoosamy, J.; Curti, E.; Kosakowski, G.; Grolimund, D.; Van Loon, L. R.; Mäder, U. Barite Precipitation Following Celestite Dissolution in a Porous Medium: A SEM/BSE and µ-XRD/XRF Study. *Geochimica et Cosmochimica Acta* **2016**, *182* (April), 131–144.

(13) Putnis, A.; Prieto, M.; Fernandez-Diaz, L. Fluid Supersaturation and Crystallization in Porous Media. *Geological Magazine* **1995**, *132* (1), 1–13.

(14) Altmann, S.; Tournassat, C.; Goutelard, F.; Parneix, J.-C.; Gimmi, T.; Maes, N.; Bensenouci, F.; Appelo, C. A. J.; Wersin, P.; Oelkers, E. H.; et al. Impact of Porosity Variation on Diffusive Transport: Experimentation vs Simulation. *Geochimica et Cosmochimica Acta* **2015**, *1* (1), 447–460.

(15) Chagneau, A. The Effects of Porosity Clogging on the Transport Properties of Porous Materials under Geochemical Perturbation.Universitat Berlin **2015**.

(16) Prieto, M.; Fernández-Díaz, L.; López-Andrés, L.; López-Andrés, S. Supersaturation Evolution and First Precipitate Location in Crystal Growth in Gels; Application to Barium and Strontium Carbonates. *Journal of crystal growth* **1989**, *98* (3), 447–460.

(17) Prieto, M. Nucleation and Supersaturation in Porous Media (Revisited). *Mineralogical Magazine* **2014**, *78* (6), 1437–1447.

(18) Kashchiev, D.; van Rosmalen, G. M. Review: Nucleation in Solutions Revisited. *Crystal Research and Technology* **2003**, *38* (78), 555–574.

(19) Sangwal, K. Additives and Crystallization Processes: From Fundamentals to Applications; John Wiley & Sons, 2007.

(20) Steefel, C. I.; Appelo, C. A. J.; Arora, B.; Jacques, D.; Kalbacher, T.; Kolditz, O.; Lagneau, V.; Lichtner, P. C.; Mayer, K. U.; Meeussen, J. C. L.; et al. *Reactive Transport Codes for Subsurface Environmental Simulation*; 2015; Vol. 19.

(21) Steefel, C. I. CrunchFlow Software for Modeling Multicomponent Reactive Flow and Transport. User's Manual. *Earth Sciences Division. Lawrence Berkeley, National Laboratory, Berkeley, CA. October* **2009**, 12–91.

(22) Lichtner, P. C. Continuum Formulation of Multicomponent-Multiphase Reactive Transport. *Reviews in Mineralogy and Geochemistry* **1996**, *34* (1), 1–81.

(23) Lasaga, A. C. *Kinetic Theory in the Earth Sciences*; Princeton university press, 2014; Vol. 402.

(24) Oelkers, E. H. Physical and Chemical Properties of Rocks and Fluids for Chemical Mass Transport Calculations. *Reviews in Mineralogy and Geochemistry* **1996**, *34* (1), 131–191.

(25) Fatnassi, I. Impact de la variation de la porosite sur le transport diffusif : experimentation vs simulation. Université de Montpellier, **2015**.

(26) Radwan, J.; Hanios, D.; Grenut, B. Qualification Expérimentale de La Plate-Forme ALLIANCES . 1 Ère Partie : Calculs Préliminaires, NT-CEA, DPC / SECR 06-051 indice A 2006.

(27) Didierjean, S.; Maillet, D.; Moyne, C. Analytical Solutions of One-Dimensional Macrodispersion in Stratified Porous Media by the Quadrupole Method: Convergence to an Equivalent Homogeneous Porous Medium. *Advances in Water Resources* **2004**, *27* (6), 657–667.

(28) Descostes, M.; Pili, E.; Felix, O.; Frasca, B.; Radwan, J.; Juery, A. Diffusive Parameters of Tritiated Water and Uranium in Chalk. *Journal of Hydrology* **2012**, *452–453*, 40–50.

(29) Bosbach, D.; Wood, S. A. Linking Molecular-Scale Barite Precipitation Mechanisms with Macroscopic Crystal Growth Rates. *Water-Rock Interactions, Ore Deposits, and Environmental Geochemistry: A Tribute to David A. Crerar* **2002**, *1*, 97–110.

(30) Altmann, S.; Aertsens, M.; Appelo, T.; Bruggeman, C.; Gaboreau, S.; Glaus, M.; Jacquier, P.; Kupcik, T.; Maes, N.; Montoya, V.; et al. Processes of Cation Migration in Clayrocks : Final Scientific Report of the CatClay European Project HAL Id : Cea-01223753. **2015**.

(31) Berthe, G. Évolution Des Propriétés de Confinement Des Roches-Couvertures Type Argilite Soumises à Des Fluides Enrichis En CO2: Impact Des Discontinuités Naturelles et Artificielles. Université Paris Sud 2012.

(32) Bensenouci, F. Apport Des Traceurs Naturels à La Compréhension Des Transferts Au Sein Des Formations Argileuses Compactées. Université Paris Sud 2010.

(33) Palandri, J. L.; Kharaka, Y. K. A Compilation of Rate Parameters of Water-Mineral Interaction Kinetics for Application to Geochemical Modeling; Geological Survey Menlo Park CA, 2004.

(34) Dzombak, D. D.; Morel, F. M. M. Surface Complex Modeling. *Hydrous Ferric OxideWiley, New York* **1990**.

(35) Borkovec, M.; Westall, J. Solution of the Poisson-Boltzmann Equation for Surface Excesses of Ions in the Diffuse Layer at the Oxide-Electrolyte Interface. *Journal of Electroanalytical Chemistry and Interfacial Electrochemistry* **1983**, *150* (1–2), 325–337.

(36) Leroy, P.; Revil, A. A Triple-Layer Model of the Surface Electrochemical Properties of Clay Minerals. *Journal of Colloid and Interface Science* **2004**, *270* (2), 371–380.

CHAPTER-2: EXPERIMENTAL PART

Chapter-2.1: Barite and Gypsum Precipitation in Chalk

RÉSUMÉ

Les réactions induites par la diffusion de réactifs provenant de sources multiples peuvent notablement modifier les propriétés de confinement d'une roche *via* des phénomènes de dissolution/précipitation prévalant au sein de sa porosité. De ce fait, ces mécanismes doivent être pris en compte pour évaluer les performances de confinement à court et long terme de roches de faible perméabilité utilisées pour accueillir un stockage souterrain. Cet article présente et analyse deux expériences conduites sous un régime diffusif et focalisées sur la précipitation de deux types de minéraux sulfatés (gypse : $CaSO_4.2H_2O$ et barytine : $BaSO_4$) dans une craie de faible perméabilité. Les changements dans le temps de la porosité et du coefficient de diffusion effectif (D_e) ont été évalués tout au long de la durée des expériences (envions 140 jours). Pour ce faire, nous avons procédé à une analyse du comportement de traceurs passifs et à une évaluation de la quantité de gypse ou de barytine précipitée à partir de la mesure de l'évolution des réactifs dans les réservoirs situés aux deux extrémités de l'échantillon. Ensuite, des observations par MEB-EDS et par micro-tomographie à rayons X (µCT) ont été effectuées pour étudier l'évolution de la structure de la roche suite à la précipitation. Les résultats ont montré que le changement du volume poreux global (de 45% jusqu'à 43%) correspondant au volume de minéraux sulfatés ayant précipité est similaire pour les expériences impliquant le gypse ou la barytine. Inversement, l'impact de la précipitation sur les propriétés de diffusion des traceurs de l'eau injectés, 70 jours après le début des expériences est radicalement différent pour chacun des minéraux sulfatés étudiés. La précipitation de la barytine a généré un impact plus significatif que celui du gypse, i.e. $D_{e,intact} = 4.15\times10^{-10}$ $m^2.s^{-1}$ vs. $D_{e,barite} = 1.1\times10^{-10}$ $m^2.s^{-1}$ and $D_{e,gypsum} = 2.5\times10^{-10}$ $m^2.s^{-1}$. Les observations post-mortem des échantillons ont révélé la présence d'une fine zone de précipitation (~ 250 µm) au centre de l'échantillon pour les expériences impliquant la barytine, tandis que dans le cas de la précipitation du gypse, des nodules de forme sphérique ont été observées. Les images obtenues avec le µCT à de plus hautes résolutions ont montré que la précipitation de la barytine n'est pas totalement homogène, ce qui explique la courbe de diffusion de HTO. Pour le gypse, les images post-mortem autour des amas sphériques ont montré la présence significative de macro-pores, appartenant à la porosité connectée, non encore remplis. Ces zones de craie intacte permettraient à HDO de diffuser à travers la zone précipitée, réduisant ainsi l'impact de la diffusivité sur le traceur de l'eau. Ces résultats expérimentaux indiquent que la morphologie et la distribution des précipités de barytine sont principalement contrôlées par un phénomène de nucléation homogène et hétérogène, alors que la précipitation du gypse est contrôlée par la variabilité spatiale des propriétés du système poreux initial (porosité, surface réactive, tortuosité, structure du réseau poral).

Experimental characterization of coupled diffusion reaction mechanisms in low permeability chalk

A. Rajyaguru [1,2,*], E. L'Hôpital[3], S. Savoye [1], C. Wittebroodt [3], O. Bildstein [4], P. Arnoux [1], V. Detilleux [5], I. Fatnassi[1,6], P. Gouze [6], V.Lagneau[2]

(1) Den-Service d'Etude du Comportement des Radionucléides (SECR), CEA, Université Paris-Saclay, F-91191 Gif-sur-Yvette
(2) MINES ParisTech, Centre de géosciences, France

(3) IRSN, PSE-ENV, SEDRE, LETIS, Fontenay Aux Roses, France

(4) CEA, Den, DTN, Laboratory for modeling of transfers in the Environment, France
(5) Bel V, Belgium
(6) Géosciences Montpellier, UMR 5243, CNRS, Université de Montpellier, France

* corresponding author, ashish.rajyaguru@cea.fr

Article accepted as Rajyaguru et al 2019, volume 503, pg. 29-39,Chemical Geology

Abstract

Reactions caused by the diffusion of reactants from different sources can alter rock diffusivity and are therefore the critical mechanisms for evaluating short and long-term behavior of low-permeability rocks used as confinement layers for underground storage, for instance. This paper presents and discusses a set of two diffusion-driven reaction experiments focusing on precipitation of two end-member types of sulfate minerals (gypsum: $CaSO_4.2H_2O$ and barite: $BaSO_4$) in low-permeability chalk. The time-resolved changes in porosity and effective diffusion coefficient (D_e) were evaluated along the duration of the experiments (~ 140 days), by analyzing the behavior of passive tracers and evaluating the amount of precipitated gypsum or barite from measuring the reactant concentration evolution in the reservoirs at both ends of the sample. Then SEM-EDS and X-ray microtomography (µCT) imaging were used to characterize the initial rock structure and the precipitated materials. Results showed that the change in porosity (from 45 % to about 43 %) corresponding to the volume of sulfate precipitated, are similar for gypsum and barite. Conversely, the precipitation impact on diffusion properties of the water tracers that were injected 70 days after the beginning of the precipitation step is distinctly different for the each of the studied sulfate mineral. The precipitation of barite generated a more significant impact than gypsum: D_e^{intact} = 4.15×10^{-10} $m^2.s^{-1}$ *vs.* D_e^{barite} = 1.1×10^{-10} $m^2.s^{-1}$ and D_e^{gypsum} = 2.5×10^{-10} $m^2.s^{-1}$. Post-mortem imaging revealed a thin precipitated zone (~ 250 µm) in the center of the sample for the barite precipitation experiment, whereas isolated quasi-spherical clusters resulted from the gypsum precipitation. The µCT images at higher resolution showed that the precipitation of barite is heterogeneous at small scale, which explains the HTO diffusion curve. For gypsum, the post mortem imaging around the quasi-spherical clusters showed a significant presence of initial macropores of the connected porosity that were still unfilled. These intact chalk zones allowed HDO to diffuse through the precipitated zone lowering the impact on water tracer diffusivity. These experimental results indicate that the morphology and the distribution of barite precipitates is mainly controlled by homogeneous and heterogeneous nucleation phenomena, whereas gypsum precipitation is mainly controlled by the spatial variability of the initial porous system properties (reactive surface area, tortuosity, pore network structure).

1 Introduction

Deep geological clayey rocks are the center of study in fields concerning development of facilities for hosting disposal of radioactive waste and sealing anthropogenic CO_2 storage facilities **(**(Bachu, 2002); (Gaucher et al., 2004)**)**. These consolidated rocks are composed of clayey minerals such as illite, kaolinite and smectite, and other minerals such as quartz, carbonates, feldspars, sulfides and oxides. These rocks usually display very small pore sizes of few tens of nanometers with clayey minerals of permanent negative surface charge. Thus, these rocks have very low intrinsic permeability so that diffusion of ionic species is the governing transport phenomenon through such porous matrix. The negative surface charge present on pore surface imposes a strong anionic exclusion and strong adsorption of cationic species on pore surface of these rocks. Both of these properties are important factors to delay radionuclide diffusion from radioactive waste deep disposal facility to the surrounding geosphere. Similarly, the storage of captured anthropogenic CO_2 in oil-depleted reservoirs relies on the very high tightness of these clayey formations acting as cap-rocks.

However, in both of these fields' physicochemical phenomena such as mineral dissolution and precipitation can alter rock properties and pose potential challenges at operational as well as geological time scales. For instance, in the case of the French concept of radioactive waste disposal the degradation of some waste packages over time can generate saline or alkaline plumes which are expected to interact with pore-water and enhance dissolution/precipitation phenomena **(**(De Windt et al., 2008)**;** (Dagnelie et al., 2017). Conversely, in the case of the Swiss concept, the decay of fission products from high-mid level long lived radioactive waste such as ^{134}Cs and ^{137}Cs will produce few kilograms per package of barium (Curti et al., 2010). Over the period of time due to corrosion the waste package can break and the interaction of released barium and sulfate-rich bentonite pore-water could precipitate barite (NAGRA, 2002)**.** Estimating the amount of generated barite is a key issue as barite can incorporate ^{226}Ra ((Grandia et al., 2008); (Brandt et al., 2015)) known to have a low affinity towards bentonite (Tachi et al., 2001). Similarly, in the case of CO_2 storage the diffusion of anthropogenic CO_2 and ionic species through the cap-rocks can be accelerated when CO_2-enriched fluid interacts with cap-rock minerals such as calcite and dolomite. At lab-scale several experiments have demonstrated the increase in diffusive parameters of ionic species in response to dissolution of carbonate minerals from the rock matrix **(**(Credoz et al., 2009); (Wollenweber et al., 2009); (Berthe et al., 2011)**)**.

Thus, such evolutions of rock containment properties over time must be characterized for the long-term performance assessment of these deep facilities. Such estimation can be carried out using numerical models that couple the chemical and hydro-dynamical processes. Usually, these numerical models are based on a continuum approach that uses a macroscopic description of the mass, momentum and energy conservation from macroscopically measurable parameters. Most of the time, the parameters used in these coupled models are not measured directly. However, these parameters are critical to predicting the evolution of the system at large time and space scales. For instance, the changes in permeability and diffusivity in response to dissolution/clogging are often modeled by empirical relationships with porosity, such as the Kozeny-Carman' and the Archie's laws. These laws were developed for (highly) simplified pore geometry while the natural rocks display a large variability of structures **(**(Archie, 1942); (Carrier and Asce, 2003)**)**. Furthermore, the empirical nature of these laws and their parametrization makes their use more questionable for predicting the impact of dissolution or precipitation reactions on transport parameters **(**(Le Gallo et al., 1998); (Noiriel, 2015); (Noiriel et al, 2016); (Gouze and Luquot, 2011)**)**.

Thus, prior to long-term simulations on repository space scale, it is essential to test the robustness of such empirical laws on labscale experiments. In literature most experimental results that involve dissolution and/or clogging concern reservoir rocks, where solute transport occurs by both advection and dispersion **(**(Tartakovsky et al., 2008); (Katz et al., 2011); (Poonoosamy et al., 2015)**)**. Overall, these studies point out that continuum simulations using the Advection-Dispersion Equation (ADE) reproduce partially the effect of dissolution (Luquot and Gouze, 2009) and usually fails to reproduce the experimental data for clogging processes (Poonoosamy et al., 2015). The reason for that is the lack of detailed information obtained at scales smaller than those approximated by continuum models, while it is established that for instance the morphology and size of the precipitates as well as their localization in the pore space play a critical role on the resulting macroscopic behavior **(**(Luquot and Gouze, 2009); (Luquot et al., 2012)**)**.

For the clay-rich materials or tight carbonated rocks the dominant transport of solutes (reactants) should be considered as purely diffusive **(**(Andra, 2005); (Brosse et al., 2005); (Berne et al., 2010); (Savoye et al., 2010); (Savoye et al., 2012a)**)**. In this case, diffusion parameters are commonly determined by means of *through-diffusion* methods, in which a non-reactive tracer diffuses through a sample from an inlet reservoir to an outlet reservoir (Shackelford, 1991). However, the presence of diversified clayey minerals and complex pore geometry together (Keller et al., 2013) makes it

challenging to engineer a laboratory scale setup for deriving reliable clogging impact models of the claystone porosity on tracer diffusivity.

For this reason, it is crucial to investigate clogging impacts on proxy materials for which it is easier to perform controllable precipitation of a mineral.

One of such study on a proxy material dealt with investigating the celestite precipitation in compacted low permeable illite (Chagneau et al., 2015). However, these studies have not been carried out to investigate the barite and gypsum clogging effectiveness on a low permeable porous material displaying a complex pore geometry.

Thus, in the current paper we describe and discuss a set of reactive diffusion experiments through low-permeable chalk samples of micritic type (Descostes et al., 2012). The chalk matrix is mostly composed of calcite and thus prevents cationic adsorption on pore surface and anionic exclusion processes that are encountered in clay-rich rocks. In this study the change in properties of the chalk sample triggered by the precipitation of two sulfate alkali minerals (barite and gypsum) is investigated. Barite is a sparingly soluble mineral ($K_{sp}^{(barite)} = 10^{-9.97}$) with slow kinetics of precipitation ($k_{rate,\ barite} = 1.5\times10^{-11}$ mol.m^{-2}.s^{-1}) and gypsum is a fairly soluble mineral ($K_{sp}^{(gypsum)} = 10^{-4.58}$) with fast kinetics of precipitation ($k_{rate,\ gypsum} = 1.0\times10^{-6}$ mol.m^{-2}.s^{-1}) ((Zhang and Nancollas, 1992); (Potgieter and Strydom, 1996); (Nagaraja et al., 2007)). Thus, these mineral presents the two extremities of sulfate alkali minerals due to the difference in their intrinsic properties.

For this experimental study the sample properties and the experimental protocol are provided in Section 2. Counter-diffusion technique is used to induce precipitation of barite and gypsum minerals within chalk samples. The results of the coupled diffusion and reaction experiments are then detailed in Section 3 where using X-ray micro-tomography (µCT) the evolution of the porosity and impact on diffusivity through the sample are used to characterize the process. Then, using back-scattering electron mode scanning electron microscopy (BSE-SEM), the different patterns obtained experimentally for barite and gypsum precipitation are discussed in Section 4.

2 Materials and Methods

2.1 Materials

The sample used in this work is a micritic chalk. It is primarily composed of skeletal debris of calcareous nanofossils, mainly coccoliths, minor foraminifera, calcispheres and macrofossil fragments (Hjuler and Fabricius, 2009). During sedimentation stage the coccosphere usually falls apart, but occasionally some of the robust coccospheres can remain intact in the sediment. Due to compaction processes over time and very low cementation due to dissolution and re-precipitation of calcite, micritic chalk samples have high porosity (40 % to 50 %) and very low permeability (Faÿ-Gomord et al., 2017). In the current study, such chalk samples were selected from Upper Cretaceous formations belonging to chalk aquifer of Paris Basin in Champagne region (France). These samples were derived from core sections (85 mm diameter) of a borehole P3 (-53.0 m; -54.0 m below ground surface) that crossed the Lower-Campanian age stratigraphic layer (approximately 83 My). The chalk samples extracted from this zone are labelled 6Cb (Descostes et al., 2012)**.** The extracted core was then cut into 0.65 cm-thick and 3.5 cm-diameter slices perpendicularly to the bedding plane using a diamond wire saw (no lubricating fluid was used). The mineralogy of these sliced chalk samples was quantified using X-ray powder diffraction analysis with a XRD 5000 INEL powder X-ray diffractometer using CuKα radiation, equipped with a CPS120 curve detector Si/Li. The analysis showed a dominant presence of calcite as expected (> 97 wt%) with minor fraction of quartz (< 3 wt%). The total accessible porosity of these chalk samples was determined by mercury intrusion porosimetry (MIP) with a Micromeritics Autopore III 9420 apparatus. The resulting total porosity was equal to 45 % with critical pore throat of 660 ± 100 nm.

2.2 Methods

2.2.1 The through diffusion cells

A reactive diffusion experiment was set up to achieve two main objectives: evaluate the precipitation impact on total chalk porosity and its subsequent impact on water tracer diffusivity. Figure 1 represents a schematic diagram of a through diffusion experimental cell (Savoye et al., 2015) used here for chalk samples. The chalk sample is sandwiched in-between two polypropylene reservoirs, namely the upstream and the downstream reservoirs of volume 178 ml

and 138 ml respectively. It is worth noticing that in a diffusion cell, the names upstream and downstream do not refer to advective flux but refer to the diffusive flux of the tracer injected in the upstream reservoir. In such setup, the concentration gradient was generated by injecting a tracer into the upstream reservoir and the downstream reservoir was filled with the tracer-deficient solution. Thus, the generated gradient allowed the tracer to diffuse through the chalk sample to the opposite reservoir. Two similar cells were prepared: CELL-A to study barite precipitation, and CELL-B to study gypsum precipitation.

For these experiments, five synthetic pore-waters with different ionic compositions were prepared as listed in Table 1. The concentration values of ions in solutions were selected to have similar ionic strength in reservoirs and sample, calcite equilibrium with pore solution, and prohibition of secondary minerals such as witherite (for barite case) and anhydrite (for gypsum case). These calculations were performed using PHREEQC (Parkhurst and Appelo, 1999)**.** The solutions were prepared with ultra-pure deionized water (18.2 MΩ.cm^{-1}) and high purity salts. All the experiments were carried out at temperature 21 ± 1°C and pH ~7.7 in upstream and downstream reservoirs.

In a first step, the upstream and downstream reservoirs were filled with the equilibrated synthetic solution. This allows establishing chemical equilibrium between the reservoirs and the pore solution. After this step, the reservoir solution was changed to set the boundary conditions of the reactive diffusion experiments: upstream solution enriched in $BaCl_2$ (*resp.* $CaCl_2$) for the barite experiment CELL-A (*resp.* gypsum experiment CELL-B), the downstream solution was enriched in K_2SO_4. The upstream reservoir was also spiked with 400 µL of ^{133}Ba isotope of activity 1.78 MBq.L^{-1} (*i.e.* an activity of the reservoir water of 4 kBq.L^{-1}) and labelled CERCA ELSB45N°5245. Note that the concentration of reactants reported in Table 1 for barite and gypsum experiment are different. These concentrations were fixed to demonstrate the impact on diffusivity when similar amount of each mineral precipitates in chalk sample. The initial barium concentration in upstream was also the upper limit for prohibiting witherite precipitation in chalk sample and in reservoirs.

2.2.2 Estimation of precipitate amounts using reservoir concentrations

A reservoir monitoring technique was used to evaluate the amount of minerals precipitated. The reactant concentration was measured periodically both in the upstream and downstream reservoirs by withdrawing 100µL of solutions. The concentration of major ions (Na^+, K^+, Mg^{2+}, Ca^{2+}, Cl^-, SO_4^{2-}) in each sampled solution was measured using Ionic Chromatography (Dionex 500

and 120 equipped respectively with AS14 IonPac column and CS12A IonPac column). Note that chemistry evolution in both reservoirs for barite and gypsum experiments is given in Supplementary material. At the end of the experiment the final concentration of barium in upstream for CELL-A and sulfate in downstream for CELL-B were determined. At this stage it is assumed that all the reactants lost in reservoirs contributed to the precipitation in the chalk sample. Thus, using mass balance equation $n_{reactant,chalk} = n_{initial} - (n_{downstream,final} + n_{upstream,final})$, the reactant contribution to barite and gypsum precipitation in chalk is calculated. Using this value and knowing the molar volume of precipitated mineral (52.1 $cm^3.mol^{-1}$ for barite, 74.5 $cm^3.mol^{-1}$ for gypsum), the resulting total porosity decrease due to precipitation can be estimated.

One must note by means of the chemistry of upstream and downstream reservoirs at each sampling time, the saturation index of secondary mineral anhydrite was checked using PhreeQc. The code estimated that this mineral remained under saturation. This step allowed us to demonstrate that only gypsum governed the clogging phenomena and there is no secondary mineral formation. A limitation of this method is that it assumes that precipitation process in the reservoirs is negligible. In practice, this may be a limitation for the experiments associated to precipitation of minerals with a high solubility (such as gypsum), as ions could have the time to diffuse from one reservoir to the counter reservoir, possibly leading to mineral precipitation in both reservoirs. However, even though in the gypsum case this method could overestimate the amount of precipitates in chalk, this allows an estimation of the status of the precipitation over time. Moreover, a direct estimation of precipitates within chalk samples was performed for crosschecking the values derived from reservoir monitoring.

2.2.3 Estimation of precipitate amounts using abrasive peeling

For the CELL-A, barite precipitation amount was also estimated using abrasive peeling technique. At the end of experiment (140 days) the sample was removed from the supporting rim of CELL-A, and successive peeling of ~80 µm thick chalk layers was carried out. The recovered chalk powder from each peeled layer was suspended in 4 ml of MiliQ water. The activity within this suspended solution was analyzed by gamma counting (Packard 1480 WIZARD, USA). Thus, by measuring ^{133}Ba activity in all peeled layers a distribution of ^{133}Ba activity in precipitated and non-precipitated zones within the chalk sample was obtained (for detailed abrasive peeling technique see **(**(Van Loon and Eikenberg, 2005)**;** (Savoye et al., 2012a)**)**. Finally, the cumulative amount of activity was then converted into the amount of stable barium from the ratio of initial concentration of stable barium in upstream reservoir, and injected ^{133}Ba activity. The resulting cumulative amount of stable

barium obtained from this distribution should thus represent the true amount of stable barium lost in upstream reservoir.

2.2.4 Estimation of precipitate amount by leaching

No radioactive tracer was used for the gypsum experiment. A small piece of the chalk sample containing precipitated gypsum was powdered and subjected to successive leaching technique in order to directly measure total gypsum having precipitated in chalk sample. For this operation, the sample was saturated with deionized water and then allowed to equilibrate for one week after which the sulfate concentration was measured in the solution recovered by ultracentrifugation. The residual powder was again dissolved in water, equilibrated and sulfate concentration is measured in centrifuged solution. This step was repeated until no sulfate is measured in leached water. Finally, the amount of recovered sulfate through this technique was compared with the amount of sulfate contributed to gypsum precipitation in chalk using the reservoir monitoring technique. Note that the concentration of sulfate at each leaching step was measured using the same chromatography technique used for reservoir monitoring step in section 2.2.2.

2.2.5 Water tracer diffusivity in initial intact chalk

Water tracer diffusivity in the chalk sample was estimated by injecting 30 µL of pure deuterated water in the upstream solution. By periodical sampling 100 µl of both upstream and downstream reservoirs the HDO concentration evolutions in both reservoirs was then followed for 70 days. The HDO concentration in each sampled volume was measured using a cavity-ringdown laser absorption spectrometer (Los Gatos Research LGR 100).

Through-diffusion setup can be treated as a finite system of fixed initial conditions with constant diffusive parameters like accessible porosity (ε_a), tracer effective diffusion coefficient (D_e). At t = 0, the upstream reservoir tracer concentration is C_0, while the chalk sample and the downstream reservoir are tracer-depleted. In this case the classical analytical solution of Fick's 2nd law for 1D transport through a finite membrane given by ((Carslaw, H. and Jaeger, 1959)**;** (Crank, 1975)**)** can be used as the reference solution.

$$\frac{\partial C}{\partial t} = \frac{D_e}{\varepsilon_a}\frac{\partial^2 C}{\partial x^2} \quad \text{..... (1)}$$

where C is the concentration per volume unit (mol.m^{-3}), t is the time (s), ε_a *is* porosity (-), and D_e is the effective diffusion coefficient (m^2 s^{-1}).

However, at $t > 0$, these boundary conditions are released, and it is necessary to solve Fick's second law for 1D transport numerically. At this stage, it was done, for a given value of the effective diffusion coefficient and porosity, by solving the Fick's second law using numerical inversion of Laplace domain yielding a semi-analytical solution given by **(**(Didierjean et al., 2004); (Moridis, 1998)**)**. In our case, this operation was carried out using CEA's tool called Interpretation Model of Diffusion Experiments (I-Mode)(Radwan et al., 2006). This tool was implemented in Excel software using Visual Basic for Applications.

Finally, to reduce the uncertainty range associated to the diffusive transport parameters (effective diffusion coefficient D_e and accessible porosity, ε_a) for HDO, two successive diffusion experiments on the same intact chalk sample were conducted.

2.2.6 Water tracer diffusivity in mineral precipitated chalk

Water tracer diffusivity values were estimated by injecting water tracers 70 days after the beginning of the reactive diffusion step. 70 days was chosen based on the reactant concentration monitoring in reservoirs when weak evolution of most of the reactant concentrations was observed. The upstream reservoir of CELL-B was spiked with 30 µL of pure deuterated water. The upstream of CELL-A was spiked with 300 µL of tritiated water (HTO) of activity 1 $MBq.L^{-1}$ (*i.e.* an initial upstream reservoir activity of 1.68 $kBq.L^{-1}$) and labelled CERCA ELSB45 n°7601122/A.

Similar to measurement at diffusion step through intact chalk (section 2.2.5.), regular samplings of 100 µL were carried out in the upstream and downstream reservoirs in cells CELL-A and CELL-B. The HTO activity of the sampled solutions was measured using a liquid scintillation recorder Packard Tricarb 2500. The HDO concentration within each of the sample was measured using a cavity ring-down laser absorption spectrometer (Los Gatos Research LGR 100). The uncertainties were estimated by propagation of the analytical error variances following the Gaussian error propagation law (see Savoye et al. (2012b) for details) for both the analytical methods. The resulting diffusive curves obtained through barite and gypsum precipitated chalk samples were fitted using I-MODE to estimate effective diffusion coefficient values for water tracers through the disturbed samples.

2.2.7 Post-mortem 3D imaging (µCT)

The 3D evolution of reacted chalk samples was carried out at two different resolutions using a Skyscan 1272, Bruker X-ray microtomography (µCT). In the first scan the milled barite and gypsum

chalk samples were scanned at 100 kV and 100 µA with a 0.11 mm copper filter. The rotation step was set at 0.4° and the frame averaging is set to 3. The resulting image size is 3280 x 4904 (binning 1) with a pixel size of 5.5 µm for the chalk/barite sample and of 5 µm for the chalk/gypsum sample.

For the second scan, to achieve high resolution, small samples of 1×1×1 mm^3 were prepared from barite and gypsum precipitated chalk samples. The milled samples were scanned at 70 kV and 114 µA with a 0.5 mm aluminium filter for the second scan. The rotation step was set at 0.3° and the frame averaging was set to 8. The images size is 3280 x 4904 (binning 1) with a pixel size of 0.5 µm for the chalk/barite sample and of 1 µm for the chalk/gypsum sample.

The reconstruction and the post processing were performed with the software NRecon with the InstaRecon algorithm and CTan. A median filter with 5 pixels round core, image cleaning and thresholding were applied. The same protocol was used for both barite and gypsum scans at 0.5 µm and 1.0 µm pixel size.

2.2.8 Post-mortem imaging, BSE-SEM

The local morphology of barite and gypsum precipitates *i.e.* shape of crystals in coccoliths and grain porosity was determined using back-scattering electron mode scanning electron microscope (BSE-SEM). For this operation post precipitation reaction chalk samples of dimension 1×1×1 mm^3 were cut using a diamond wire. The thin slices were then polished using an ion milling system (SEMPrep 2 from Technoorg LINDA) to remove the dust coating generated when the samples were polished with sandpaper. Samples were then carbon-coated and analysed by BSE-SEM (using 7000F JEOL at 15 kV).

3 Results

3.1 Imaging

3.1.1 Barite experiment

Figure 2A shows the µCT image at 5.5 µm pixel size of barite precipitates distributed within a zone of thickness ~250 µm and located at the center of the chalk sample. However, this pixel size is much larger than the mean throat-pore size of chalk, *i.e.* 0.660 µm. Thus, the residual empty pores and the morphology of barite precipitates in the pores are below the resolution. Figure 2C shows

the result of a scan performed on a smaller sample, carried out at a pixel size of 0.5 µm. The presence of some macro porosity of size greater than 0.5 µm can be seen: even in the barite precipitated zone, some macro-pores remain empty (black holes in the Figure 2C). These empty pores would correspond to coccoliths as macro porosity present in the chalk sample. Note that empty pores of size less than 0.5 µm cannot be captured by the scan but might still be present. To roughly estimate the quantitative amount of porosity in the precipitated zone a small part of this scan was selected and treated by image processing. The segmented image (Figure 2E) shows that the residual macro porosity represents at least 1 % of the volume of this area.

3.1.2 *Gypsum experiment*

Figure 2B shows the µCT image at 5.5 µm pixel size. Large isolated spherical gypsum precipitates can be clearly observed, distributed around the center of the chalk sample. At this resolution, intact chalk matrix can also be seen around each sphere. Similar to the barite case, a smaller sample was chosen to focus on the spherical precipitated zone. Due to the difference in type of evolution, the post-treatment included qualitatively estimating porosity in and around the spherical gypsum precipitates. The area of residual porosity inside the gypsum spheres (Figure 2D) is less than 1 %. Outside of the spheres, large area of macro porosity can be observed (Figure 2F).

3.2 *estimation of the amount of precipitates*

3.2.1 *Barite experiment*

Figure 3 shows the concentration evolution of reactants in the upstream and the downstream reservoirs for CELL-A. No counter diffusion was measured in the reservoirs: barium (*resp.* sulfate) concentration stays below detection limit in the downstream (*resp.* upstream) reservoirs. Indeed, the solubility of barite is very low ($K_{sp}^{(barite)} = 10^{-9.97}$) so that saturation (and even supersaturation to initiate precipitation) is reached easily, and barite precipitation buffers barium and sulfate concentrations at very low levels (around 10^{-5} mol.L^{-1} if barium and sulfate have similar concentrations).

Using the mass balance equation (section 2.2.2.) the total amount of barium removed from the upstream reservoir is estimated to be 2.7 mmol. From this amount the total porosity decrease due to precipitation was calculated in the following manner. The molar volume of barite mineral is 52.1 cm^3.mol^{-1}. Using this molar volume, the equivalent volume occupied by 2.7×10^{-3} mol of barite is 0.141 cm^3, while the pore volume in the intact chalk before experiment was 2.65 cm^3.

Thus, the volume at the end of the experiment is 2.51 cm^3, *i.e.* a total porosity value of 42.5 %. Thus, if averaged on the whole sample, the overall porosity decrease caused by barite precipitation is 0.025.

Figure 4 displays the amount of stable barium obtained from ^{133}Ba activity measured within ~80 µm of subsequently peeled chalk layers from upstream face towards downstream face for the total chalk sample thickness of 6 mm. The profile ($x = 0$ at the inlet) shows no precipitation up to x = 2 mm, then a sharp 200 µm-thick peak at x = 3 mm, consistent with the 250 µm-thick layers observed by µCT. Around this peak a diffuse and highly variable presence of barium can be observed denoting the occurrence of multiple isolated precipitated barite clusters. Finally, a long tail can be observed downstream from the peak. This is probably an artefact: due to chalk low density compared to barite, it is possible that, as the peeling progresses, the chalk surface freshly abraded would be contaminated with some precipitated zone barite/chalk powder not recovered by sand paper. The total amount of barite precipitates was estimated using the abrasive peeling results. The conversion of recovered activity to total barium is done using the ratio of stable Ba/^{133}Ba (mol/Bq) known in the upstream reservoir of CELL-A at the beginning of the experiment. Thus, the cumulative Ba calculated using this technique is equal to 2.48 ± 0.05 mmol. This value is in good agreement with the 2.70 mmol of Ba estimated from reservoir monitoring step.

3.2.2 *Gypsum experiment*

The concentration evolution of calcium and sulfate over the experiment CELL-B duration is given in Figure 5. An accumulation of calcium and sulfate can be seen in the downstream and upstream (*resp.*) reservoirs. Indeed, contrary to barite, gypsum is a fairly soluble mineral ($K_{sp}^{(gypsum)} = 10^{-4.58}$), so that (with equal concentration boundary conditions) calcium and sulfate concentrations increase in the reservoirs, until the equilibrium value is reached. The concentrations are then buffered by gypsum, and stay on a plateau at 13 ± 0.5 $mmol.L^{-1}$ throughout the experiment after 20 days (see Fig. 3S in Supporting information, for gypsum saturation index as a function of time).

Using the mass balance equation for sulfate, the estimated amount of gypsum precipitated in the chalk sample is 4 mmol. However, in this case, precipitation of gypsum in reservoirs cannot be excluded. Therefore, a direct estimation was performed using successive leaching experiment. The estimated gypsum precipitated is then 1.5 mmol. Thus, knowing the molar volume of gypsum (74.5 $cm^3.mol^{-1}$), the overall chalk porosity decreases due to precipitation estimated using the same methodology in section 3.2.1. (again, if averaged on the whole sample) is equal to 0.02.

3.3 Determination of water tracer diffusivity on intact chalk sample

Figure 6 shows the experimental cumulative concentration evolution (red triangles) of HDO-enriched water tracer in upstream and downstream reservoirs of the CELL-A. The two successive through-diffusion experiments were well reproduced numerically (dashed red line in Figure 6 for the first experiment) by I-Mode, using an effective diffusion coefficient value equal to 4.15×10^{-10} $m^2.s^{-1}$ and an accessible porosity value equal to 45%. For a sample coming from the same core, the effective diffusion coefficient value noted in literature was 3.8×10^{-10} $m^2.s^{-1}$ (Descostes et al., 2012). Note that the chalk samples in Descostes et al. were covered with perforated plates which could have delayed the diffusion and thus could explain a possible lower estimation of effective diffusion coefficient.

3.4 Determination of water tracer diffusivity on reacted chalk sample

The evolution of the diffusion coefficient was estimated after 70 days of reactive diffusion experiment. Figure 7A shows the cumulative activity evolution of the tritiated water (HTO) in the downstream reservoir of CELL-A. Similarly**,** Figure 7B shows the evolution of the cumulative concentration changes of the deuterated water (HDO) in the downstream reservoir of CELL-B. In both of the figures the experimental curves were compared to diffusion curves computed for the intact chalk (black dashed lines) using D_e value (obtained in section 3.1).

The effective diffusion coefficient values estimated for reproducing both the experiments are equal to 1.1×10^{-10} $m^2.s^{-1}$ for barite, and 2.5×10^{-10} $m^2.s^{-1}$ for gypsum.

4 Discussion

The amounts of barite and gypsum precipitating within chalk samples after 140 days of reactive diffusion experiment are similar, i.e. ~ 2.5 mmol of barium for barite estimated from abrasive peeling and 1.5 mmol of sulfate for gypsum from successive leaching. However, these two newly precipitated minerals led to distinct impact on water tracer diffusivity with barite showing a higher global impact on diffusivity than gypsum: $D_e^{barite} = 1.1\times10^{-10}$ $m^2.s^{-1}$ vs $D_e^{gypsum} = 2.5\times10^{-10}$ $m^2.s^{-1}$.

These differences can be investigated using the detailed analysis of the µCT images. For the barite experiment, a sharp local porosity decrease is observed within the precipitated zone (Figure 2E). This homogeneous layer with very low porosity would have a large overall impact on diffusion.

406 The residual macro porosity shown in Figure 2E, contributes only for a small fraction of the volume
407 in the precipitated zone, and could allow the diffusion of HTO through this layer.

408 For the gypsum case, the µCT image (Figure 2B) shows that precipitation might have drastically
409 reduced the porosity in the spherical zones. However, the remaining intact zones between the
410 spheres allowed HDO to diffuse through the sample. Thus, the overall impact on diffusivity is
411 reduced compared to the barite case.

412 This discrepancy leads to another question: “why the precipitated barite and gypsum in the chalk
413 sample have dissimilar behaviors?” An answer may be searched by comparing the intrinsic
414 properties of barite and gypsum, such as solubility and mineral precipitation rate.

415

416 Barite case:

417 The chalk matrix is composed of calcite with neutral pore surface. In such a system there is no
418 alteration of the diffusion of ionic species such as barium and sulfate. Moreover, in free water both
419 barium and sulfate ions possess similar diffusion coefficients (8.5×10^{-10} and 10.7×10^{-10} $m^2.s^{-1}$
420 respectively, Li and Gregory, 1973). In the counter-diffusion setup, both ions are expected to meet
421 in the center of the sample and saturate the pore solution with respect to barite in this zone. As
422 the experiment progresses, the incoming barium and sulfate create supersaturated conditions in
423 the pore solution in the center of the sample due to the very low solubility of barite.

424 Once supersaturation is reached, stable nuclei of barite are formed in these pores. Thus, there is
425 a positive feedback where the nuclei will enhance precipitation kinetics locally, therefore “draining”
426 the reactants in the vicinity (down to saturation with respect to barite). As a result, precipitation is
427 prevented out of the first line of precipitates. However, the initial growth of these nuclei and the
428 resulting barite morphology depends on the locally governing nucleation phenomena.

429 Figure 8A shows a SEM image obtained on the barite precipitated zone in the chalk sample. This
430 image reveals a partly continuous barite precipitated line, surrounded by some delocalized barite
431 islands. Higher magnification BSE-SEM images were recorded to observe barite morphology in
432 the precipitated zone (Figure 8B). In this figure, big crystals of barite can be clearly observed within
433 macro-pores voids of diameter ~20 µm. The formation of such large crystals can be attributed to
434 homogeneous nucleation phenomena. In large pore volumes, each point of pore solution can be
435 treated as a potential site that can form a super critical barite cluster, which will then convert into

436 stable nucleus. Such supercritical clusters (or stable nucleus) are formed when one of the instable
437 cluster overcomes the interfacial energy of homogeneous nucleation (Nielsen and Sohnel, 1969).
438 Then these nuclei will allow barite growth and enhance the precipitation in the larger pore voids
439 (Kashchiev and van Rosmalen, 2003).

440 Figure 8B shows a second morphology of barite in carbonate matrix, distinctly different from the
441 barite crystals formed in big voids. Prieto (Prieto, 2014) showed that the time required for
442 homogeneous nucleation to initiate precipitation is increased by 9 orders of magnitude when the
443 pore size is reduced from 100 µm to 0.1 µm. Thus, barite growths preferentially occur by
444 heterogeneous nucleation in smaller pore volumes (<1 µm) (Prasianakis et al., 2017). In our
445 experiments, pores of mean throat-size of 0.660 µm form the majority of the matrix. Thus, the
446 origin of this particular barite morphology (resembling overgrowth) can be attributed to
447 heterogeneous nucleation. For such growth the surface of small and intermediate void spaces of
448 matrix will act as a substrate on which the growth of the barite crystals occurs at lower interfacial
449 energy values (Kashchiev and van Rosmalen, 2003).

450 Gypsum case:

451 Figure 9A shows the SEM imaging of a small selected region of the gypsum precipitated zone.
452 This image shows gypsum precipitated zone connected through a nodular line. Below this zone,
453 an isolated gypsum sphere of diameter of ca. 400 µm can be observed, in which gypsum has
454 precipitated within coccoliths and the surrounding matrix. A higher magnification was used to
455 determine the morphology of gypsum in the two regions (Figure 9B). Contrary to the barite case,
456 gypsum does not display distinct morphologies both within the coccoliths and the surrounding
457 chalk matrix. This can be attributed to the nucleation phenomena. It has been noted in literature
458 that heterogeneous nucleation prevails at lower supersaturation (saturation index < 4), while
459 homogeneous nucleation phenomena is dominant at higher supersaturation values (Alimi et al.,
460 2003). In our study, the saturation index with respect to gypsum within the reservoirs remains near
461 equilibrium throughout the experimental duration (see Fig. 3S in the supporting information). Thus,
462 heterogeneous nucleation mechanism is expected to dominate gypsum precipitation resulting in
463 a single type of morphology for gypsum.

464 Nevertheless, the nucleation mechanism does not explain the formation of the isolated clusters at
465 the center of the sample. To explain this observation, the potential role of spatial variability can be
466 investigated according to two scenarios.

Scenario-1: Gypsum evolution without spatial variability

In the absence of spatial variability (diffusion, surface area, nucleation probability, or/and surface roughness), the counter diffusion of calcium and sulfate would equally saturate pores located at the center of the sample. These points are at the center of the sample because calcium and sulfate exhibit very close diffusion coefficient values in free water ($7.9\times10^{-10}$and $10.7\times10^{-10}\,m^2.s^{-1}$ respectively) (Li and Gregory, 1973), and non-charged chalk would not modify this ratio. Thus, in these pores, there is an equal probability of formation of stable gypsum nuclei. Formation of these nuclei should generate a positive feedback and would enhance precipitation kinetics locally draining the reactants in the vicinity of these nuclei. Following this scenario, a thin precipitated layer similar to barite should be observed at the end of the experiment. However, the µCT images contradict this scenario, with isolated clusters of precipitates.

Thus, a second scenario can be proposed in which spatial variability occurring within the porous system would govern gypsum precipitation. Note that such an impact of spatial variability on gypsum growth was observed for advection-controlled transport **(**e.g. (Singurindy and Berkowitz, 2003); (Xie et al., 2015)**)**.

Two sub-cases were considered: the first one dealing with the presence of reactive mineral surface variability, and the second one with the occurrence of heterogeneous pore structure.

Scenario-2a): Gypsum evolution in presence of reactive surface variability

Gypsum precipitation was largely driven by heterogeneous nucleation phenomena, *i.e.* gypsum growth on pore surface at the mineral surface at near-equilibrium condition. In such scenario, the surface roughness and active surface area (acting as substrate) for precipitation are the main controlling parameters. A variable distribution of the surface roughness and area can be conjectured because the chalk matrix is composed of a mixture of grains and coccoliths. Thus, the variability of surface area available for gypsum growth will control nucleation distribution and kinetics at the center of sample even though the counter diffusing calcium and sulfate would equally saturate the pore volumes over time.

These nuclei would then follow the similar positive feedback phenomena discussed in scenario-1 and locally enhance precipitation. They will evolve as isolated more or less spherical clusters because they are initially irregularly distributed at the center of sample.

Scenario-2b): Gypsum evolution in presence of heterogeneous pore structure

The chalk sample used in this study is composed of apparently randomly orientated coccoliths within carbonate grains. This mixture generates a heterogeneous pore network. Albeit gypsum precipitation occurs close to equilibrium conditions, small differences in saturation index may enhance or delay precipitation locally. This variability in the saturation results from the heterogeneity of the pore structure. For instance, less tortuous paths will trigger faster meeting of calcium and sulfate, and consequently faster gypsum nucleation, compared to more tortuous paths, even though calcium and sulfate have similar diffusive behavior in pore water. Then these nuclei will generate a positive feedback and evolve in similar fashion as in scenario-1 and will evolve as isolated more or less spherical clusters similarly to the scenario 2a. From the experimental data we gathered, it is not possible to infer which of the two aforementioned scenarios (2a and 2b) is dominant. However, both of them are linked to the spatial variability of the pore structure that has a critical role in controlling the early stage of the precipitation of gypsum characterized by a fast kinetics and high solubility.

5 Conclusion

We reported experimental results concerning the change of the diffusive parameters of two water tracers (HDO and HTO) diffusing through chalk samples wherein either gypsum (CaSO4) or barite (BaSO4) precipitated. Results indicated that the amount of barium contributing to barite precipitation and the amount of sulfate contributing to gypsum to precipitation cause similar reduction of the chalk porosity (~0.02) after 140 days. However, the diffusive behavior of water tracers injected 70 days after the beginning of the precipitation step showed that barite impacts more on global diffusivity compared to gypsum, i.e. $D_e^{\text{barite}} = 1.1\times10^{-10}\ m^2.s^{-1}$ vs $D_e^{\text{gypsum}} = 2.5\times10^{-10}\ m^2.s^{-1}$.

Post-mortem imaging revealed a thin barite precipitated zone in the center of the sample (~ 250 µm) whereas gypsum formed isolated quasi-spherical clusters in the center of the sample. For barite case, the µCT images at higher resolution showed presence of some fraction of unfilled macro porosity in the precipitated zone. For gypsum case, post mortem imaging showed a very small presence of empty pores within quasi-spherical clusters. However, a significant unfilled macro pores still remained surrounding these clusters of gypsum precipitates. Thus, barite and gypsum experiments show distinct microstructural changes in the precipitated zone inducing distinct impact on diffusivity of water tracers.

Thus, one concludes that barite precipitation is governed by both homogeneous and heterogeneous nucleation phenomena, while gypsum precipitation is largely controlled by the spatial variability of the connected pore structure (surface roughness, heterogeneous porous structure).

These experimental results should be used to perform quantitative simulations to test the hypothesis provided (supersaturation, spatial variability impact) in discussion section for both barite and gypsum case. Using a similar approach, barite and gypsum precipitation would be studied in low permeable clayey minerals that resemble surface charge and mean pore size close to claystones. The chalk results obtained in this paper would thus be used as a reference dataset in understanding derived results from clayey experiments. Such data set can be used to test empirical laws such as Archie's law at REV scale.

Acknowledgements: This work received financial support from CEA, IRSN and Bel V. The authors thank Eric Pili from CEA/DAM for providing the chalk core used in the study; Cécile Blanc, Jérome Varlet from the LISL (CEA) and Corinne Segarra LECBA (CEA) for the SEM observations; Bernard Grenut from LECBA (CEA) for mercury intrusion & extrusion porosimetry tests; Wafaa Ezzhouri from L3MR (CEA) for preparation of some of the diffusion cells.

Finally, we thank the two anonymous reviewers for their constructive remarks to improve the quality of this manuscript.

6 References

Alimi, F., Elfil, H., Gadri, A., 2003. Kinetics of the precipitation of calcium sulfate dihydratein a desalination unit. Desalination 157, 9–16.

Andra, 2005. Dossier 2005 Argile - Synthèse Evaluation de la faisabilité du stockage géologique en formation argileuse 240.

Archie, G.E., 1942. The Electrical Resistivity Log as an Aid in Determining Some Reservoir Characteristics. Transactions of the AIME 146, 54–62. https://doi.org/10.2118/942054-G

Bachu, S., 2002. Sequestration of CO2 in geological media in response to climate change: Road map for site selection using the transform of the geological space into the CO2 phase space. Energy Conversion and Management 43, 87–102. https://doi.org/10.1016/S0196-8904(01)00009-7

Berne, P., Bachaud, P., Fleury, M., 2010. Diffusion Properties of Carbonated Caprocks from the Paris Basin. Oil & Gas Science and Technology – Revue de l'Institut Français du Pétrole 65, 473–484. https://doi.org/10.2516/ogst/2009072

Berthe, G., Savoye, S., Wittebroodt, C., Michelot, J.L., 2011. Changes in containment properties of claystone caprocks induced by dissolved CO2seepage. Energy Procedia 4, 5314–5319. https://doi.org/10.1016/j.egypro.2011.02.512

Brandt, F., Curti, E., Klinkenberg, M., Rozov, K., Bosbach, D., 2015. Replacement of barite by a (Ba,Ra)SO4 solid solution at close-to-equilibrium conditions: A combined experimental and theoretical study. Geochimica et Cosmochimica Acta 155, 1–15. https://doi.org/10.1016/j.gca.2015.01.016

Brosse, E., Bildstein, O., Swennen, R., 2005. Gas-water-rock interactions induced by reservoir exploitation, CO2sequestration, and other geological storage. Oil and Gas Science and Technology 60, 9–18. https://doi.org/10.2516/ogst:2005002

Carrier, D., Asce, F., 2003. Goodbye, Hazen; Hello, Kozeny-Carman 129, 1054–1056. https://doi.org/doi:10.1061/(ASCE)1090-0241(2003)129:11(1054)

Carslaw, H. and Jaeger, J., 1959. Heat in solids, 1st ed. Clarendon Press, Oxford. https://doi.org/978-0198533689

Chagneau, A., Tournassat, C., Steefel, C.I., Bourg, I.C., Gaboreau, S., Esteve, I., Kupcik, T., Claret, F., Schäfer, T., 2015. Complete restriction of36Cl-diffusion by celestite precipitation in densely compacted illite. Environmental Science and Technology Letters 2, 139–143. https://doi.org/10.1021/acs.estlett.5b00080

Crank, J., 1975. The Mathematics of Diffusion, 2nd ed. Oxford.

Credoz, A., Bildstein, O., Jullien, M., Raynal, J., Pétronin, J.C., Lillo, M., Pozo, C., Geniaut, G., 2009. Experimental and modeling study of geochemical reactivity between clayey caprocks and CO2 in geological storage conditions. Energy Procedia 1, 3445–3452. https://doi.org/10.1016/j.egypro.2009.02.135

Curti, E., Fujiwara, K., Iijima, K., Tits, J., Cuesta, C., Kitamura, A., Glaus, M.A., Müller, W., 2010. Radium uptake during barite recrystallization at 23±2°C as a function of solution composition: An experimental133Ba and226Ra tracer study. Geochimica et Cosmochimica Acta 74, 3553–3570. https://doi.org/10.1016/j.gca.2010.03.018

Dagnelie, R.V.H., Arnoux, P., Enaux, J., Radwan, J., Nerfie, P., Page, J., Coelho, D., Robinet, J.C., 2017. Perturbation induced by a nitrate plume on diffusion of solutes in a large-scale clay rock sample. Applied Clay Science 141, 219–226. https://doi.org/10.1016/j.clay.2017.02.025

De Windt, L., Marsal, F., Tinseau, E., Pellegrini, D., 2008. Reactive transport modeling of geochemical interactions at a concrete/argillite interface, Tournemire site (France). Physics and Chemistry of the Earth 33, 295–305. https://doi.org/10.1016/j.pce.2008.10.035

Descostes, M., Pili, E., Felix, O., Frasca, B., Radwan, J., Juery, A., 2012. Diffusive parameters of tritiated water and uranium in chalk. Journal of Hydrology 452–453, 40–50. https://doi.org/10.1016/j.jhydrol.2012.05.018

Didierjean, S., Maillet, D., Moyne, C., 2004. Analytical solutions of one-dimensional macrodispersion in stratified porous media by the quadrupole method: Convergence to an equivalent homogeneous porous medium. Advances in Water Resources 27, 657–667. https://doi.org/10.1016/j.advwatres.2004.02.022

Faÿ-Gomord, O., Soete, J., Davy, C.A., Janssens, N., Troadec, D., Cazaux, F., Caline, B., Swennen, R., 2017. Tight chalk: Characterization of the 3D pore network by FIB-SEM, towards the understanding of fluid transport. Journal of Petroleum Science and Engineering 156, 67–74. https://doi.org/10.1016/j.petrol.2017.05.005

Gaucher, E., Robelin, C., Matray, J.M., Négrel, G., Gros, Y., Heitz, J.F., Vinsot, A., Rebours, H., Cassagnabère, A., Bouchet, A., 2004. ANDRA underground research laboratory: Interpretation of the mineralogical and geochemical data acquired in the Callovian-Oxfordian formation by investigative drilling. Physics and Chemistry of the Earth 29, 55–77. https://doi.org/10.1016/j.pce.2003.11.006

Gouze, P., Luquot, L., 2011. X-ray microtomography characterization of porosity, permeability and reactive surface changes during dissolution. Journal of Contaminant Hydrology 120–121, 44–55. https://doi.org/10.1016/j.jconhyd.2010.07.004

Grandia, F., Merino, J., Bruno, J., 2008. Assessment of the radium-barium co-precipitation and its potentialinfluence on the solubility of Ra in the near-field TR-08-07, 52.

Hjuler, M.L., Fabricius, I.L., 2009. Engineering properties of chalk related to diagenetic variations of Upper Cretaceous onshore and offshore chalk in the North Sea area. Journal of Petroleum Science and Engineering 68, 151–170. https://doi.org/10.1016/j.petrol.2009.06.005

Kashchiev, D., van Rosmalen, G.M., 2003. Review: Nucleation in solutions revisited. Crystal Research and Technology 38, 555–574. https://doi.org/10.1002/crat.200310070

Katz, G.E., Berkowitz, B., Guadagnini, A., Saaltink, M.W., 2011. Experimental and modeling investigation of multicomponent reactive transport in porous media. Journal of Contaminant Hydrology 120–121, 27–44. https://doi.org/10.1016/j.jconhyd.2009.11.002

Keller, L.M., Schuetz, P., Erni, R., Rossell, M.D., Lucas, F., Gasser, P., Holzer, L., 2013. Characterization of multi-scale microstructural features in Opalinus Clay. Microporous and Mesoporous Materials 170, 83–94. https://doi.org/10.1016/j.micromeso.2012.11.029

Le Gallo, Y., Bildstein, O., Brosse, E., 1998. Coupled reaction-flow modeling of diagenetic changes in reservoir permeability, porosity and mineral compositions. Journal of Hydrology 209, 366–388. https://doi.org/10.1016/S0022-1694(98)00183-8

Li, Y.-H., Gregory, S., 1973. Diffusion of Ions in Sea Water and in Deep Sea Sediments. Geochimica et Cosmochimica Acta, 1974 38, 703–714. https://doi.org/10.1016/0016-7037(74)90145-8

Luquot, L., Andreani, M., Gouze, P., Camps, P., 2012. CO2percolation experiment through chlorite/zeolite-rich sandstone (Pretty Hill Formation - Otway Basin-Australia). Chemical Geology 294–295, 75–88. https://doi.org/10.1016/j.chemgeo.2011.11.018

Luquot, L., Gouze, P., 2009. Experimental determination of porosity and permeability changes induced by injection of CO2into carbonate rocks. Chemical Geology 265, 148–159. https://doi.org/10.1016/j.chemgeo.2009.03.028

Moridis, G.J., 1998. A SET OF SEMIANALYTICAL SOLUTIONS FOR PARAMETER ESTIMATION IN DIFFUSION CELL EXPERIMENTS. Sciences-New York.

Nagaraja, B.M., Abimanyu, H., Jung, K.D., Yoo, K.S., 2007. Preparation of mesostructured barium sulfate with high surface area by dispersion method and its characterization. Journal of Colloid and Interface Science 316, 645–651. https://doi.org/10.1016/j.jcis.2007.09.004

NAGRA, 2002. Project Opalinus Clay—Safety Report: Demonstration of disposal feasibility for spent fuel, vitrified high-level waste and long-lived intermediate-level waste (Entsorgungsnachweis). Wettingen, Switzerland.

Nielsen, A.E., Sohnel, O., 1969. Nucleation and Growth of Crystals at High Supersaturation. Kristall und Technik 4, 17–38. https://doi.org/10.1002/crat.19690040105

Noiriel, C., 2015. Resolving Time-dependent Evolution of Pore-Scale Structure, Permeability and Reactivity using X-ray Microtomography. Reviews in Mineralogy and Geochemistry 80, 247–285. https://doi.org/10.2138/rmg.2015.80.08

Parkhurst, B.D.L., Appelo, C. a J., 1999. User's Guide To PHREEQC (version 2) — a Computer Program for Speciation, and Inverse Geochemical Calculations. Exchange Organizational Behavior Teaching Journal D, 326. https://doi.org/Rep. 99-4259

Poonoosamy, J., Kosakowski, G., Van Loon, L.R., Mäder, U., 2015. Dissolution-precipitation processes in tank experiments for testing numerical models for reactive transport calculations: Experiments and modelling. Journal of Contaminant Hydrology 177–178, 1–17. https://doi.org/10.1016/j.jconhyd.2015.02.007

Potgieter, J.H., Strydom, C.A., 1996. An investigation into the correlation between different surface area determination techniques applied to various limestone-related compounds. Cement and Concrete Research 26, 1613–1617. https://doi.org/10.1016/S0008-8846(96)00159-7

Prasianakis, N.I., Curti, E., Kosakowski, G., Poonoosamy, J., Churakov, S. V., 2017. Deciphering pore-level precipitation mechanisms. Scientific Reports 7, 1–9. https://doi.org/10.1038/s41598-017-14142-0

Prieto, M., 2014. Nucleation and supersaturation in porous media (revisited). Mineralogical Magazine 78, 1437–1447. https://doi.org/10.1180/minmag.2014.078.6.11

Radwan, J., Hanios, D., Grenut, B., 2006. Qualification expérimentale de la plate-forme ALLIANCES . 1 ère Partie : Calculs préliminaires . GIF SUR YVETTE. https://doi.org/NT DPC / SECR 06-051 indice A DO 190

Savoye, S., Beaucaire, C., Fayette, A., Herbette, M., Coelho, D., 2012. Mobility of cesium through the callovo-oxfordian claystones under partially saturated conditions. Environmental Science and Technology 46, 2633–2641. https://doi.org/10.1021/es2037433

Savoye, S., Beaucaire, C., Grenut, B., Fayette, A., 2015. Impact of the solution ionic strength on strontium diffusion through the Callovo-Oxfordian clayrocks: An experimental and modeling study. Applied Geochemistry 61, 41–52. https://doi.org/10.1016/j.apgeochem.2015.05.011

Savoye, S., Frasca, B., Grenut, B., Fayette, A., 2012. How mobile is iodide in the Callovo-Oxfordian claystones under experimental conditions close to the in situ ones? Journal of Contaminant Hydrology 142–143, 82–92. https://doi.org/10.1016/j.jconhyd.2012.10.003

Savoye, S., Page, J., Puente, C., Imbert, C., Coelho, D., 2010. New experimental approach for studying diffusion through an intact and unsaturated medium: A case study with callovo-oxfordian argillite. Environmental Science and Technology 44, 3698–3704. https://doi.org/10.1021/es903738t

Shackelford, C.D., 1991. Laboratory diffusion testing for waste disposal - A review. Journal of Contaminant Hydrology 7, 177–217. https://doi.org/10.1016/0169-7722(91)90028-Y

Singurindy, O., Berkowitz, B., 2003. Evolution of hydraulic conductivity by precipitation and dissolution in carbonate rock. Water Resources Research 39, 1–14. https://doi.org/10.1029/2001WR001055

Tachi, Y., Shibutani, T., Sato, H., Yui, M., 2001. Experimental and modeling studies on sorption and diffusion of radium in bentonite. Journal of Contaminant Hydrology 47, 171–186. https://doi.org/10.1016/S0169-7722(00)00147-9

Tartakovsky, A.M., Redden, G., Lichtner, P.C., Scheibe, T.D., Meakin, P., 2008. Mixing-induced precipitation: Experimental study and multiscale numerical analysis. Water Resources Research 44, 1–19. https://doi.org/10.1029/2006WR005725

Van Loon, L.R., Eikenberg, J., 2005. A high-resolution abrasive method for determining diffusion profiles of sorbing radionuclides in dense argillaceous rocks. Applied Radiation and Isotopes 63, 11–21. https://doi.org/10.1016/j.apradiso.2005.02.001

Wollenweber, J., Alles, S. a., Kronimus, A., Busch, A., Stanjek, H., Krooss, B.M., 2009. Caprock and overburden processes in geological CO2 storage: An experimental study on sealing efficiency and mineral alterations. Energy Procedia 1, 3469–3476. https://doi.org/10.1016/j.egypro.2009.02.138

Xie, M., Mayer, K.U., Claret, F., Alt-Epping, P., Jacques, D., Steefel, C., Chiaberge, C., Simunek, J., 2015. Implementation and evaluation of permeability-porosity and tortuosity-porosity relationships linked to mineral dissolution-precipitation. Computational Geosciences 19, 655–671. https://doi.org/10.1007/s10596-014-9458-3

Zhang, J., Nancollas, G.H., 1992. Influence of calcium/sulfate molar ratio on the growth rate of calcium sulfate dihydrate at constant supersaturation. Journal of Crystal Growth 118, 287–294. https://doi.org/10.1016/0022-0248(92)90073-R

List of Figures:

List of Table

Table 1. Chemical composition of the solutions used for the experiments

Ions	Rock-equilibrated Solution $mmol.L^{-1}$	Barite experiment – CELL-A		Gypsum experiment – CELL-B	
		Upstream $mmol.L^{-1}$	Downstream $mmol.L^{-1}$	Upstream $mmol.L^{-1}$	Downstream $mmol.L^{-1}$
Na	159.40	119.40	159.40	0.50	0.89
K	-	-	40.00	-	160.20
Ca	20.62	20.62	20.62	80.50	1.25
Mg	0.07	0.07	0.07	0.07	0.07
Ba	-	20.00	-	-	-
Cl	200.20	200.39	200.20	161.30	1.34
SO4	-	-	20.00	-	80.10
HCO3	0.39	0.39	0.39	0.23	2.12
pCO_2 (atm)	-3.5	-3.5	-3.5	-3.5	-3.5

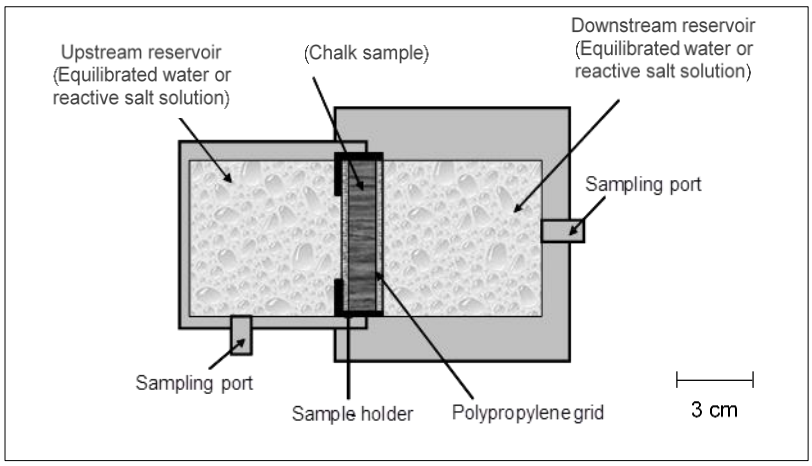
Upstream reservoir
(Equilibrated water or
reactive salt solution)
(Chalk sample)
Downstream reservoir
(Equilibrated water or
reactive salt solution)
Sampling port
Sampling port
Sample holder
Polypropylene grid
3 cm

Figure 1

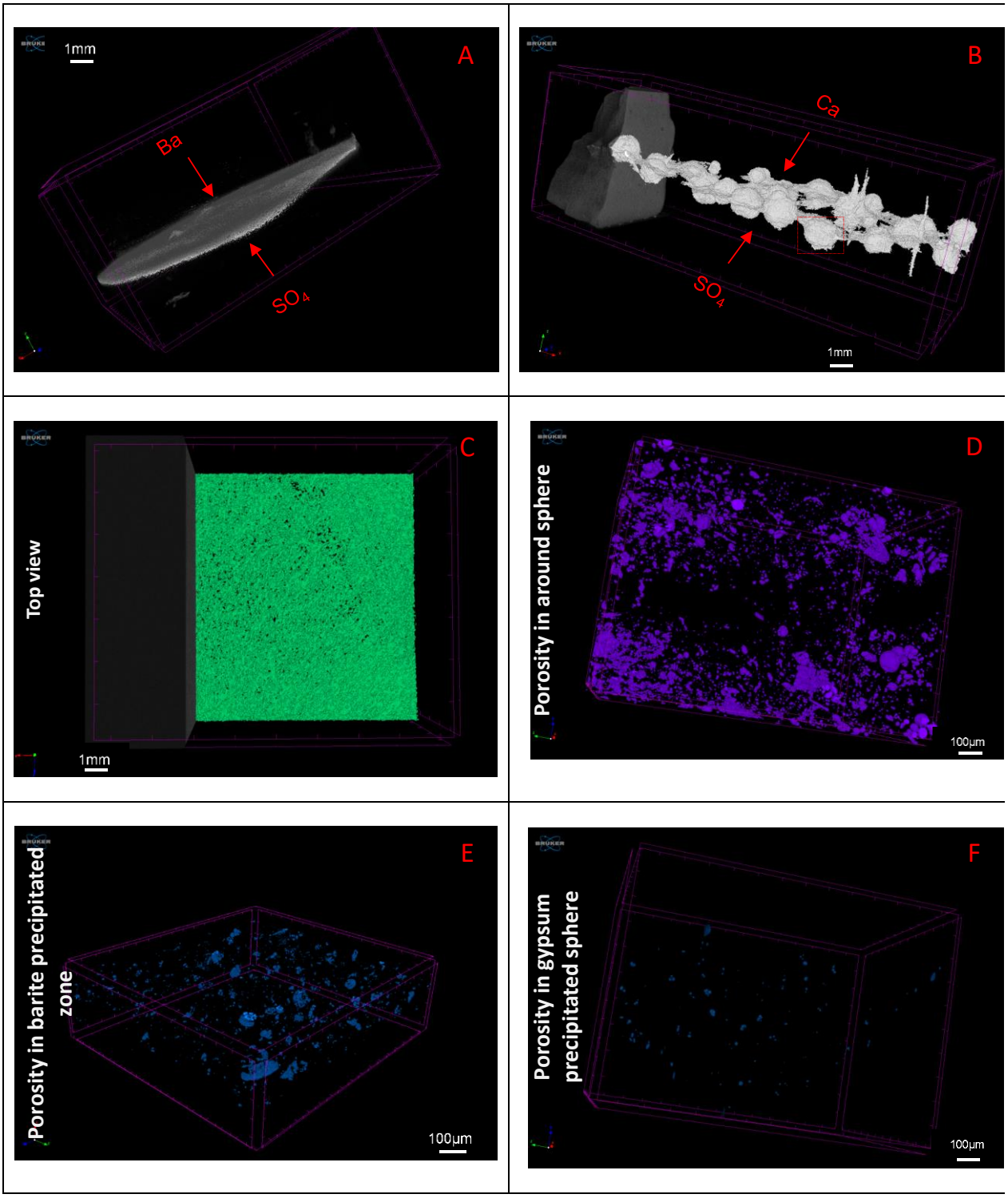
1mm
A
Ba
SO4
B
Ca
SO4
1mm
C
Top view
1mm
D
Porosity in around sphere
100µm
E
Porosity in barite precipitated zone
100µm
F
Porosity in gypsum precipitated sphere
100µm

Figure 2

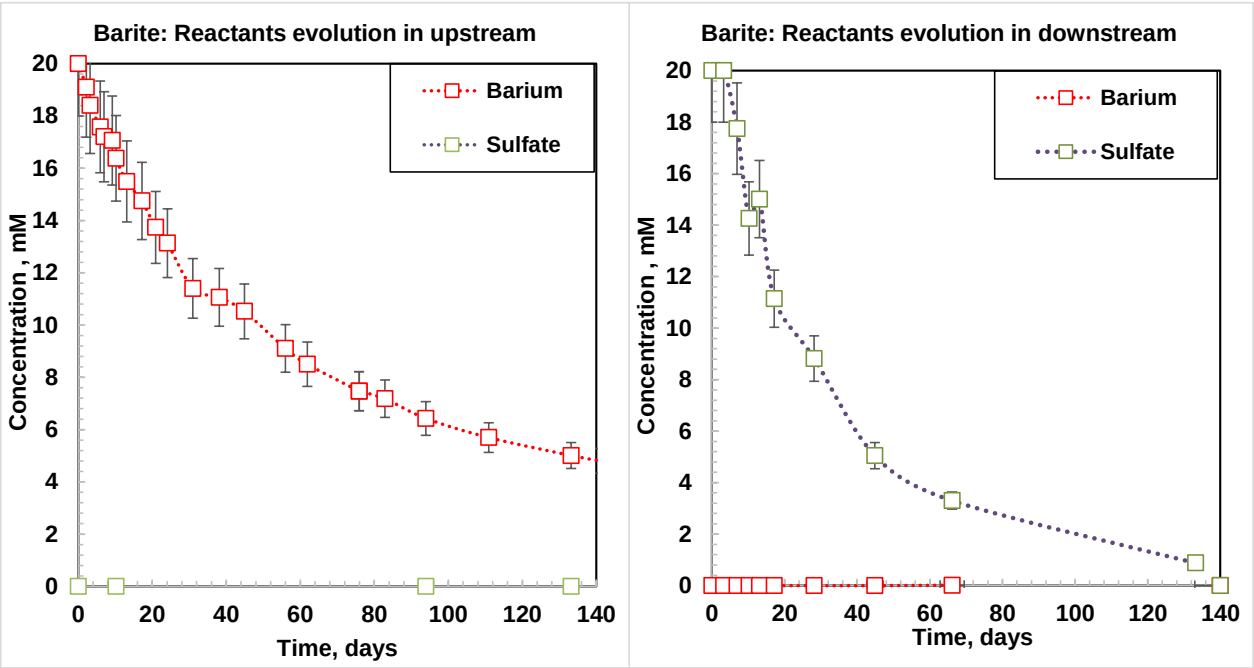
Barite: Reactants evolution in upstream
Barium
Sulfate
Concentration , mM
Time, days
0
2
4
6
8
10
12
14
16
18
20
0
20
40
60
80
100
120
140
Barite: Reactants evolution in downstream
Barium
Sulfate
Concentration , mM
Time, days

Figure 3

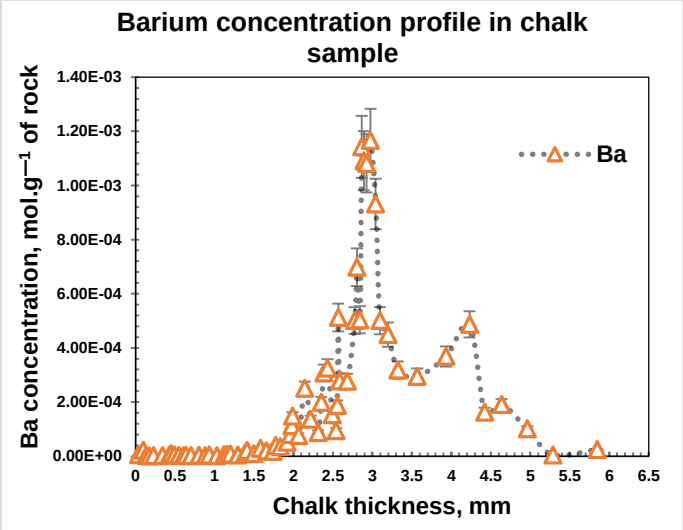
Barium concentration profile in chalk sample
Ba concentration, mol.g⁻¹ of rock
1.40E-03
1.20E-03
1.00E-03
8.00E-04
6.00E-04
4.00E-04
2.00E-04
0.00E+00
0
0.5
1
1.5
2
2.5
3
3.5
4
4.5
5
5.5
6
6.5
Chalk thickness, mm
Ba

Figure 4

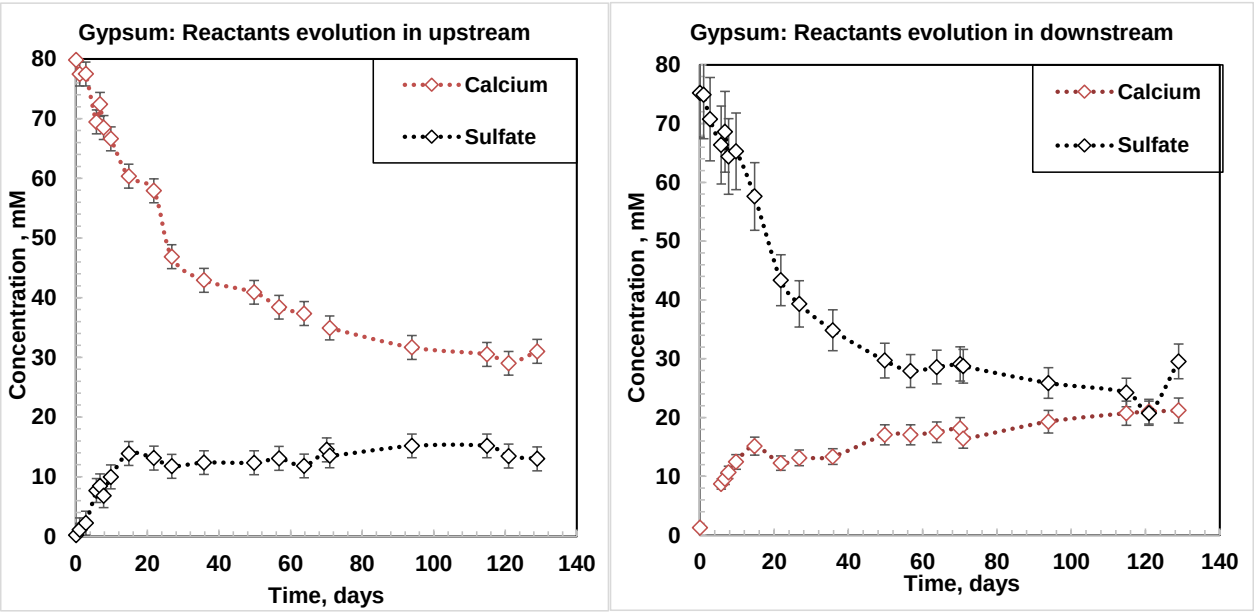
Gypsum: Reactants evolution in upstream
Calcium
Sulfate
Concentration , mM
Time, days
0
10
20
30
40
50
60
70
80
0
20
40
60
80
100
120
140
Gypsum: Reactants evolution in downstream
Calcium
Sulfate
Concentration , mM
Time, days

Figure 5

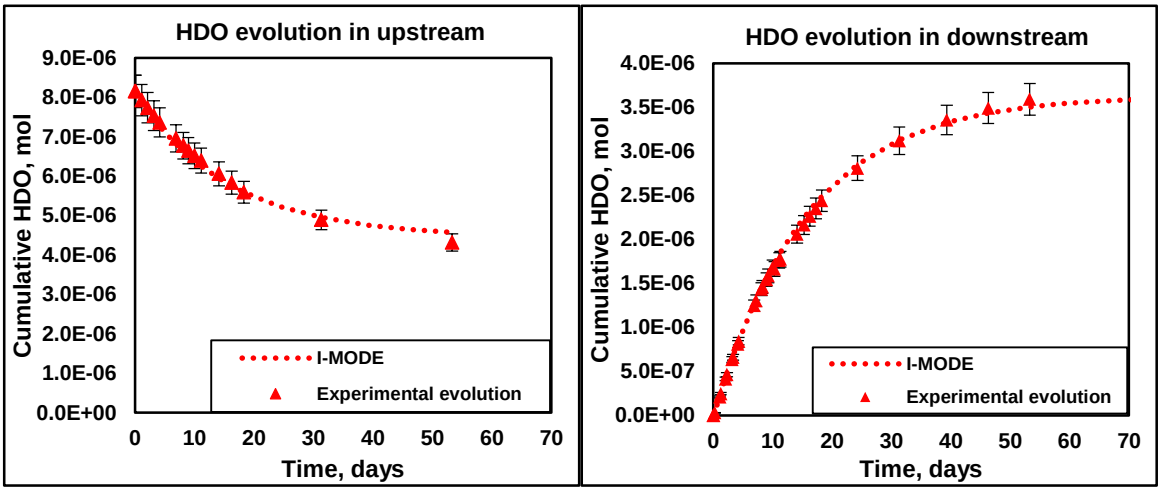
HDO evolution in upstream
Cumulative HDO, mol
9.0E-06
8.0E-06
7.0E-06
6.0E-06
5.0E-06
4.0E-06
3.0E-06
2.0E-06
1.0E-06
0.0E+00
0
10
20
30
40
50
60
70
Time, days
I-MODE
Experimental evolution
HDO evolution in downstream
Cumulative HDO, mol
4.0E-06
3.5E-06
3.0E-06
2.5E-06
2.0E-06
1.5E-06
1.0E-06
5.0E-07
0.0E+00
0
10
20
30
40
50
60
70
Time, days
I-MODE
Experimental evolution

Figure 6

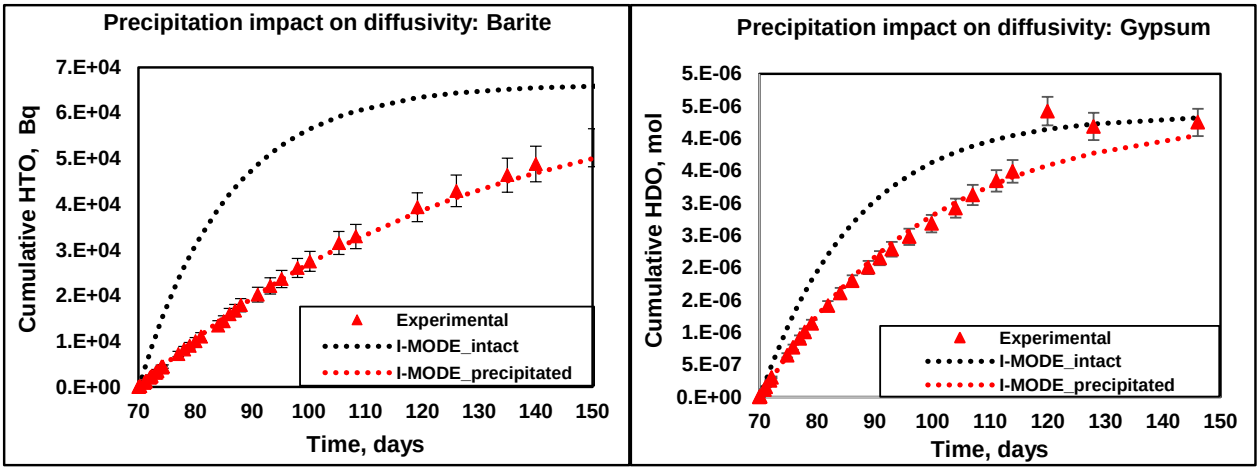
Precipitation impact on diffusivity: Barite
Cumulative HTO, Bq
7.E+04
6.E+04
5.E+04
4.E+04
3.E+04
2.E+04
1.E+04
0.E+00
70
80
90
100
110
120
130
140
150
Time, days
Experimental
I-MODE_intact
I-MODE_precipitated
Precipitation impact on diffusivity: Gypsum
Cumulative HDO, mol
5.E-06
5.E-06
4.E-06
4.E-06
3.E-06
3.E-06
2.E-06
2.E-06
1.E-06
5.E-07
0.E+00
70
80
90
100
110
120
130
140
150
Time, days
Experimental
I-MODE_intact
I-MODE_precipitated

Figure 7

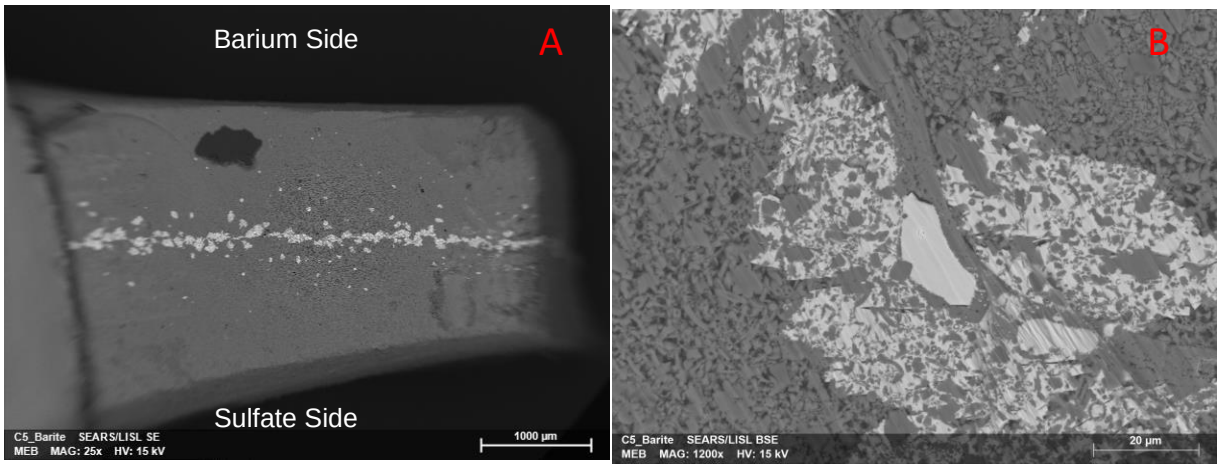
Barium Side
A
Sulfate Side
C5_Barite SEARS/LISL SE
MEB MAG: 25x HV: 15 kV
1000 µm
B
C5_Barite SEARS/LISL BSE
MEB MAG: 1200x HV: 15 kV
20 µm

Figure 8

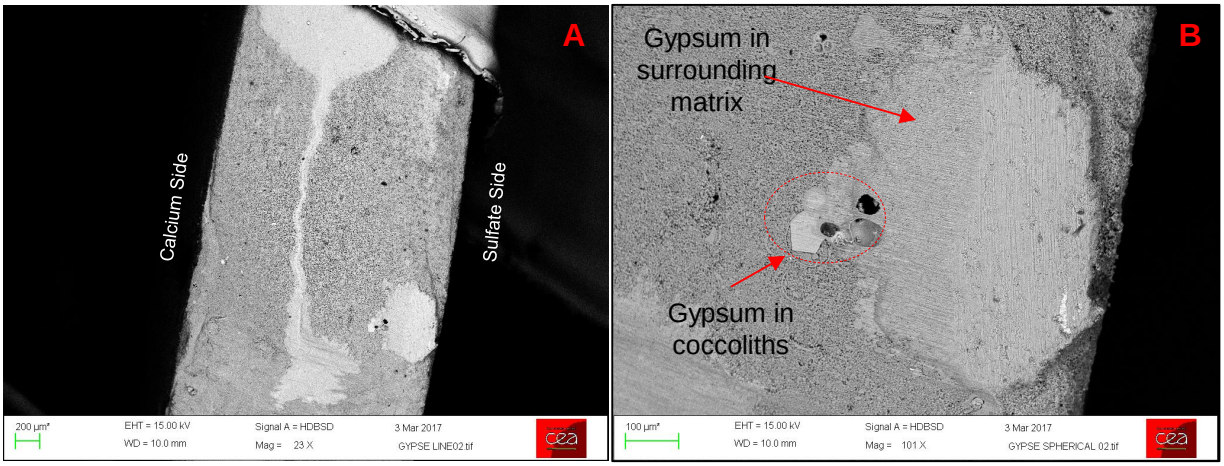
A
Calcium Side
Sulfate Side
200 µm*
EHT = 15.00 kV
WD = 10.0 mm
Signal A = HDBSD
Mag = 23 X
3 Mar 2017
GYPSE LINE02.tif
B
Gypsum in surrounding matrix
Gypsum in coccoliths
100 µm*
EHT = 15.00 kV
WD = 10.0 mm
Signal A = HDBSD
Mag = 101 X
3 Mar 2017
GYPSE SPHERICAL 02.tif

Figure 9

7 *Supplementary Material*

Fluid composition at the upstream and the downstream reservoirs

1. Calculation of the saturation index for gypsum

1. Fluid composition at the upstream and the downstream reservoirs

The evolution of the major ion concentrations in the upstream and the downstream reservoirs is reported in Tables S1 and S2 for the gypsum experiment and in Tables S3 and S4 for the barite experiment.

Table S1. Concentration measured for the fluid sampled in the HDO upstream reservoir of the gypsum experiment.

Sampling time	**[Na^+]**	**[K^+]**	**[Mg^{2+}]**	**[Ca^{2+}]**	**[Cl^-]**	**[SO_4^{2-}]**
Day	mmol/L	mmol/L	mmol/L	mmol/L	mmol/L	mmol/L
0.06	4.5	0.8		79.8	158.8	0
1.05	4.7	3.5		77.5	155.7	1.1
2.77	4.8	9.2		77.5	156.5	2.2
5.77	1.3	14.5	0.5	69.5	140.7	7.7
6.77	1.5	17.8	0.5	72.4	137.2	8.4
7.76	4.7	20.0		68.5	143.7	6.8
9.77	1.4	23.0	0.5	66.6	122.0	10.0
14.77	1.3	30.0	0.5	60.4	124.8	13.9
21.81	4.7	40.0		57.9	122.8	13.1
26.78	1.4	41.1	0.4	46.9	112.2	11.7
35.80	1.4	47.5	0.4	42.9	111.2	12.4
49.80	4.9	54.9		40.9	108.8	12.3
56.77	3.2	53.9	0.1	38.4	104.4	13.1
63.79	3.2	54.4	0.1	37.3	102.0	11.8
70.11	1.6	56.2	0.4	37.3	101.4	14.5
70.93	0.5	54.0	0.3	34.9	98.9	13.5
93.88	0.3	56.9	0.3	31.7	93.3	15.2
114.86	0.4	61.4	0.3	30.5	85.6	15.2
120.93					110.2	13.5
128.92					102.6	13.0

Table S2. Concentration measured for the fluid sampled in the HDO downstream reservoir of the gypsum experiment.

Sampling time	**[Na^+]**	**[K^+]**	**[Mg^{2+}]**	**[Ca^{2+}]**	**[Cl^-]**	**[SO_4^{2-}]**
Day	mmol/L	mmol/L	mmol/L	mmol/L	mmol/L	mmol/L
0.06	6.4	162.4	0.0	1.3	5.1	75.2
1.05	7.1	158.9	0.0		8.9	74.9
2.77	7.1	152.4	0.0		15.1	70.8
5.77	2.8	141.7	0.1	8.7	20.7	66.4
6.77	3.2	135.7	0.1	9.6	24.2	68.6
7.76	7.0	141.4	0.0	10.7	27.3	64.4
9.77	2.8	132.3	0.1	12.5	30.9	65.3
14.77	3.4	119.1	0.2	15.1	40.1	57.6
21.81	7.7	117.1	0.0	12.2	50.3	43.4
26.78	3.0	102.1	0.2	13.1	50.6	39.3
35.80	2.8	89.1	0.2	13.4	57.1	34.8
49.80	7.1	95.7	0.0	17.1	66.9	29.7
56.77	4.7	87.7		17.1	67.5	27.9
63.79	4.7	87.5		17.5	71.7	28.6
70.11	2.6	88.6	0.3	18.2	69.3	29.1
70.93	0.4	82.8	0.1	16.4	64.3	28.7
93.88	0.5	79.8	0.2	19.3	72.3	25.9
114.86	0.5	76.9	0.2	20.7	78.2	24.3
120.93					80.6	20.7
128.92					71.0	29.6

Figure S1 shows the evolution of the inert counter ion concentrations, i.e. chloride for calcium and potassium for sulfate for the gypsum experiment. One can notice a regular evolution until the concentration reach an asymptotic value corresponding to the quasi-equilibrium of concentrations between the two reservoirs.

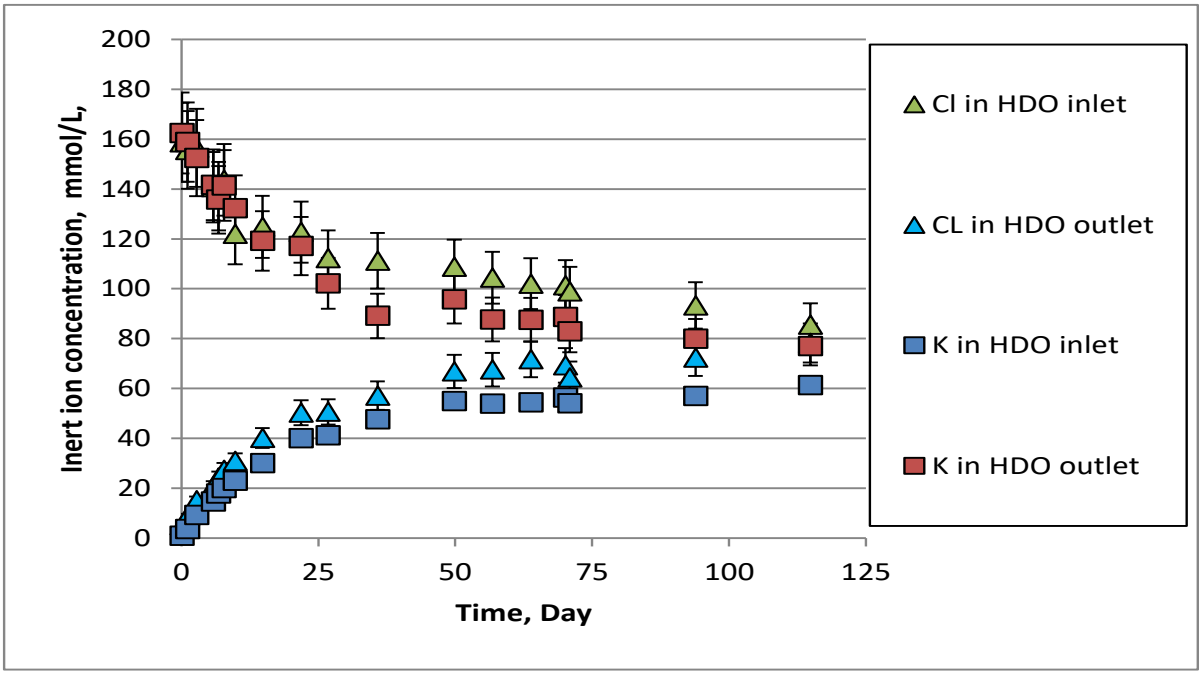

Figure S1. Evolution of Cl and K concentrations as a function of time in the gypsum cell. Inlet means upstream and outlet downstream.

Table S3. [Ba^{2+}] and [SO_4^{2-}] concentration measured in the HTO downstream reservoir of the barite experiment.

Sampling time	**[Ba^{2+}] from ^{133}Ba**	**[SO_4^{2-}]**
Day	mmol/L	mmol/L
0.02	20.0	< 0.01
2.22	19.1	
3.22	18.4	
5.93	17.6	
6.95	17.2	
9.19	17.1	
10.22	16.4	
13.14	15.5	< 0.01
17.20	14.7	
20.95	13.7	
24.13	13.1	
30.98	11.4	
38.10	11.1	
44.90	10.5	
56.00	9.1	
61.90	8.5	
75.90	7.5	
82.90	7.5	
93.93	7.2	
110.94	6.4	< 0.01
133.20	5.7	
140.98	5.0	< 0.01

Potassium and sulfate concentrations in mEq.L-1 measured in the HTO downstream reservoir is given in FigureS2.

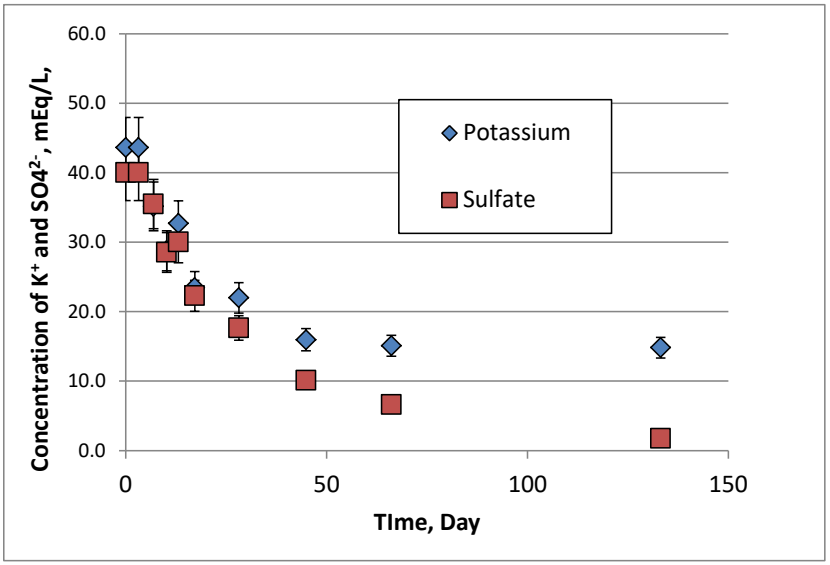

Figure S2. Comparison of K and SO_4 concentration versus time in the HTO downstream reservoir for the barite experiment.

It is noteworthy that, while the sulfate concentration continued to decrease regularly, the potassium concentration stopped decreasing after less than 50 days. Indeed, potassium concentration reached the equilibrium between the inlet and outlet reservoirs, while sulfate continued to react with barium.

Table S4. Composition of the fluid recurrently sampled in the HTO downstream reservoir during the barite experiment. Note that the ^{133}Ba concentration in all the samples was below the detection limit (< 0.01 mmol L^{-1}).

Sampling time	**[Na^+]**	**[K^+]**	**[Ca^{2+}]**	**[Cl^-]**	**[SO_4^{2-}]**
Day	mmol/L	mmol/L	mmol/L	mmol/L	mmol/L
0.02	165.4	43.6	27.3	221.8	20.0
3.22	165.4	43.6	27.3	221.8	20.0
6.95	145.3	35.1	23.8	208.5	17.7
10.22	129.3	28.7	21.0	185.4	14.3
13.14	157.0	32.7	25.5	214.1	15.0
17.20	122.7	23.4	19.7	179.3	11.1
28.17	144.0	22.0	23.3	204.1	8.8
44.90	127.5	16.0	19.8	183.0	5.5
66.13	132.6	15.1	21.3	205.3	3.3
133.20	129.0	14.8	21.4	195.3	0.9

2. Calculation of the saturation index for gypsum

The gypsum saturation index was calculated using the Phreeqc software for each of the sampled volume of fluid in the upstream and the downstream reservoirs. Figure S3 shows that the saturation is rapidly achieved in both reservoirs for t > 10 days.

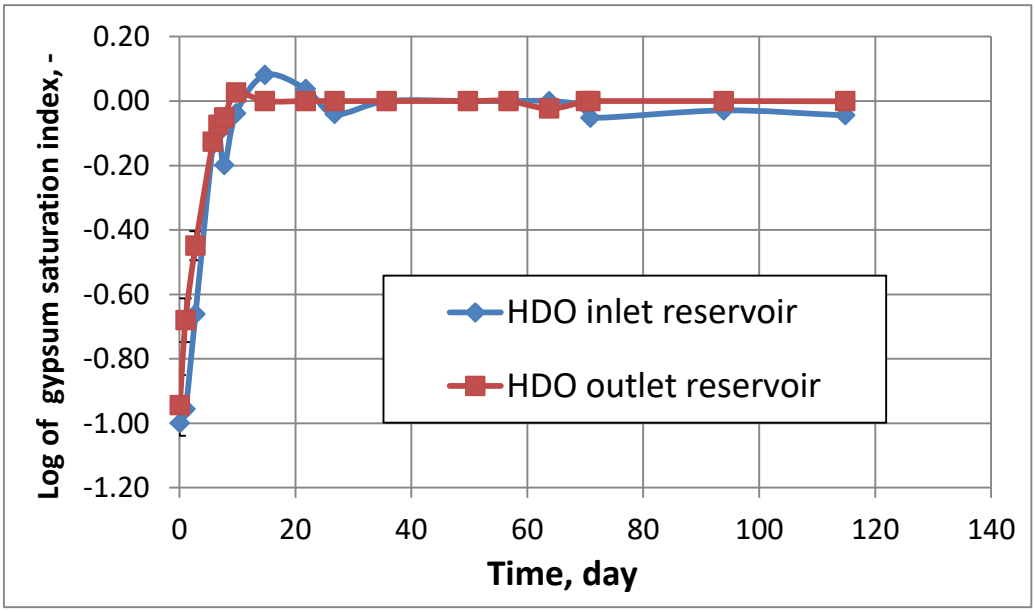

Figure S3. Gypsum saturation versus time measured in the upstream and downstream reservoir. Inlet means upstream and outlet downstream

.

Chapter-2.2: Barite precipitation in Micritic Chalk and Compacted Kaolinite

RÉSUMÉ

Le chapitre précédent proposait une expérience pour déterminer l'évolution du comportement d'un même milieu poreux (la craie) sous l'effet de la précipitation de deux minéraux (barytine et gypse). Les résultats sont prolongés dans ce chapitre avec un dispositif expérimental similaire de contre-diffusion, appliqué à la précipitation du même minéral (barytine) dans un nouveau milieu poreux : la kaolinite compactée. Craie micritique et de la kaolinite compactée présentent des propriétés similaires de porosité totale accessible et de diffusivité vis-à-vis de l'eau et des traceurs anioniques ($^{36}Cl^-$). En revanche, ils montrent une distribution de taille des pores très distincte. Les résultats de la tomographie à rayons X obtenus à différents temps d'expérience réactive ont montré des comportements différents pour la précipitation de la barytine dans la craie et dans la kaolinite : une fine zone de précipitation est observée dans la craie, tandis que la kaolinite montre la présence de groupes d'amas sphériques. Dans ce cas, la précipitation de la barytine a entrainé une diminution de la diffusivité de HTO d'un facteur de 28 dans la craie et de 1000 dans la kaolinite par rapport aux conditions intactes. La précipitation de la barytine conduit également à une diminution de la diffusivité de $^{36}Cl^-$ par un facteur 450 dans la craie, et un colmatage total dans la kaolinite, ce qui indiquerait que la barytine nouvellement formée aurait une charge de surface négative, capable de repousser les anions, tels que $^{36}Cl^-$. Ces résultats soulignent clairement l'impact de la distribution de la taille des pores sur l'évolution et la distribution des précipités minéraux, ainsi que la capacité de la barytine néoformée à transformer des échantillons poreux comme la craie et la kaolinite en membranes semi-perméables.

Barite precipitation in neutral porous media: experimental evidence of the impact of pore structure and surface charge on evolution of diffusion

A.Rajyaguru[1,2], S. Savoye[1], C. Wittebroodt[3], O. Bildstein[4], V. Detilleux[5], V.Lagneau[2]*

(1) Den-Service d'Etude du Comportement des Radionucléides (SECR), CEA, Université Paris-Saclay, F-91191 Gif-sur-Yvette

(2) MINES ParisTech, Centre de géosciences, France

(3) IRSN, LETIS, Fontenay Aux Roses, France

(4) CEA, DEN, DTN, Laboratory for modeling of transfers in the Environment, France

(5) Bel V, Belgium

*Corresponding author: Ashish RAJYAGURU, email: ashish.rajyaguru90@gmail.com

Article under revision in ACS journal, Environment Science and Technology

Abstract: Pore scale process such as mineral precipitation has major impact in broad range of scientific fields: CO_2 storage, deep geological radioactive waste disposal, oil recovery/fracking, batteries research to name some. To predict the evolution of porous material transport properties, it is however essential to test precipitation behavior in different confined volumes. In this view a classical counter diffusion approach was used to study barite precipitation in two porous materials namely micritic chalk and kaolinite. Both materials presented similar diffusivity of water and anionic tracers, and total accessible porosity, but very distinct pore size distribution.

X-ray tomography results at different times showed distinct patterns of barite precipitation in chalk and kaolinite: thin precipitated zone in chalk *vs* spherical clusters in kaolinite. Barite precipitation led to HTO diffusivity decrease by a factor of 28 in chalk and 1000 in kaolinite respectively compared to intact conditions. While barite precipitation led to chloride-36 diffusivity decrease by factor of 450 in chalk and total clogging in kaolinite, clearly demonstrating that newly formed barite possesses negative surface charge.

Thus, these results outline the impact of pore size distribution on evolution and distribution of mineral precipitates, and capability of newly formed barite mineral to add semi-permeable membrane properties to neutral porous samples such as chalk and kaolinite.

Keywords:

Experiment; diffusion; precipitation; chalk; kaolinite; barite; surface charge; pore structure.

Abstract: Pore scale process such as mineral precipitation has major impact in broad range of scientific fields: CO_2 storage, deep geological radioactive waste disposal, oil recovery/fracking, batteries research to name some. To predict the evolution of porous material transport properties, it is however essential to test precipitation behavior in different confined volumes. In this view a classical counter diffusion approach was used to study barite precipitation in two porous materials namely micritic chalk and kaolinite. Both materials presented similar diffusivity of water and anionic tracers, and total accessible porosity, but very distinct pore size distribution.

X-ray tomography results at different times showed distinct patterns of barite precipitation in chalk and kaolinite: thin precipitated zone in chalk *vs* spherical clusters in kaolinite. Barite precipitation led to HTO diffusivity decrease by a factor of 28 in chalk and 1000 in kaolinite respectively compared to intact conditions. While barite precipitation led to chloride-36 diffusivity decrease by factor of 450 in chalk and total clogging in kaolinite, clearly demonstrating that newly formed barite possesses negative surface charge.

Thus, these results outline the impact of pore size distribution on evolution and distribution of mineral precipitates, and capability of newly formed barite mineral to add semi-permeable membrane properties to neutral porous samples such as chalk and kaolinite.

Keywords:

Experiment; diffusion; precipitation; chalk; kaolinite; barite; surface charge; pore structure.

INTRODUCTION

In France, Switzerland and Belgium, argillaceous formations are considered as potential rocks to host radioactive waste disposal facilities[1,2]. Similarly, for CO_2 sequestration such indurated rocks are used as cap rocks to seal anthropogenic CO_2 reservoirs[3–5]. These rocks have been selected due to their high containment properties, related to their very low permeability, making diffusion the main mass transport process, and the presence of negative surface charge on clay minerals, capable of adsorbing radionuclides under cationic form. However, in both cases, physicochemical imbalances between radioactive waste or CO_2, and these rocks should generate over a long period of time mineral dissolution and/or precipitation, changing the rock containment properties[6,7]. For instance, some radioactive waste should release large amount of soluble nitrate and sulfate salts, when they will be degraded. These saline plumes should then enhance precipitation and thus clog the claystone porosity. Similarly, the anthropogenic CO_2 should interact with cemented minerals of cap rock and lead to dissolution of carbonate minerals.

In view of the safety assessment of such facilities, long-term evolution of rock containment properties due to such chemical unbalanced conditions are generally estimated using chemistry transport codes. These codes use empirical Archie's law to take into account the feedback of chemistry on diffusion driven mass transport. However, only a few laboratory scale experiments have been carried out to test the validity of such law used for reactive numerical models which couple chemical and diffusive processes via strong porosity changes.[8,9] Recently, Rajyaguru *et al.*[9] showed that two sulfate alkali minerals, i.e. barite and gypsum, precipitating in chalk samples had very different impact on the diffusion of water tracer. The intrinsic properties of the two minerals (solubility, precipitation rate) combined with spatial variability in properties of chalk (pore

structure, reactive surface) led to two very distinct precipitation patterns, suggesting that clogging phenomenon cannot be generalized for different minerals precipitating in the same porous material. Chagneau *et al.*[8] investigated celestite precipitation impact on water tracer diffusion in a compacted sand, a simplified system, having very large pores (~100 µm) compared to the porous medium of interest, i.e. the claystones, with main pore size ca. 20 nm. Both of these studies suggest that precipitation and its feedback on diffusion is governed more by the pore size distribution of the hosted material than by the porosity itself, contrary to the paradigm of the widely used Archie' law. Moreover, the role played by the potential surface charge of the newly formed mineral on diffusion was recently suggested by Chagneau *et al.*[10] to explain the complete restriction of $^{36}Cl^-$ diffusion by celestite precipitation in compacted illite. However, since this clay mineral also possesses negative surface charge, the authors were unable to decipher the respective contribution of each repulsing phase.

Therefore, the objective of the current study is twofold. The first is estimate the role played by pore size distribution on the feedback of precipitation on diffusion. The second is to know whether newly formed precipitates are able to change a neutral porous medium into a semi-permeable membrane due to their surface charge. For that purpose, reactive-diffusion experiments were carried out with barite as the precipitating mineral in two neutral porous materials, chalk and compacted kaolinite, with similar porosity and water tracer diffusivity, but very different pore size distribution. Two different tracers were used for estimating the precipitation impact on their diffusive behavior: tritiated water (HTO) was used as the classical water tracer, and $^{36}Cl^-$ in order to quantify the extent of anionic exclusion induced by barite precipitation.

MATERIALS AND METHODS

Sample Preparation and Characterization. Kaolinite KGa-2 under powder form (with particle size ~150 µm) was provided by the CNRS-Poitiers University. Prior to the diffusion experiments, the kaolinite powder was Na-saturated using five saturation cycles in a 1 $mol.L^{-1}$ NaCl solution. A dialysis procedure was used to remove chloride from the samples until the silver nitrate test for Cl^- was negative. Then, each size fraction was air-dried, sieved through a 150 µm mesh to avoid coarse aggregates, and stored at 25°C.

Chalk samples were selected from Upper Cretaceous formations belonging to chalk aquifer of Paris Basin in Champagne region (France). The samples derived from a core section (85 mm diameter) of a borehole that crossed the Lower-Campanian age stratigraphic layer (approximately 83 My). The extracted core was then sliced into 0.67 cm-thick and 3.3 cm-diameter slice perpendicularly to the bedding plane using a diamond wire saw (no lubricating fluid was used).

Mercury intrusion and extrusion porosimetry (MIEP) characterization was carried out both on Na-kaolinite compacted at a dry density of 1690 $kg.m^{-3}$ and chalk sample, using a Micromeritics Autopore III 9420 apparatus. The total porosity and mean pore throat derived from this analysis are 36 % and 35 nm, for kaolinite and 45% and 660 nm for chalk, respectively. The mercury intrusion-extrusion results of kaolinite and chalk samples are plotted in Figure S1 in supporting information.

Diffusion experiments. Impact of barite precipitates on HTO and $^{36}Cl^-$ diffusion was studied using the through-diffusion technique. In a first step, the diffusive parameters for tracer were determined through intact materials; then the reactive diffusion experiments were launched by injecting barium and sulfate in the counter-diffusion reservoirs. Lastly, when chemical equilibrium

was almost achieved, HTO and $^{36}Cl^-$ were injected again in order to assess the barite precipitate impact on their diffusive behavior. Note that the first step for chalk (tracer diffusive behavior at intact condition) was already detailed in Rajyaguru *et al.*[9]. Two types of setup were used, depending on the studied material.

Experimental setup used for kaolinite. The setup used for kaolinite was the one developed by Tertre *et al.* [11] It consists of a PEEK diffusion cell characterized by an inner diameter of 9.49 mm and two aqueous reservoirs (i.e. an upstream reservoir and a downstream reservoir). A peristaltic pump (Ismatec) was used to ensure the circulation of the solution from the upstream reservoir towards the upstream face of the diffusion cell and likewise on the downstream side of the sample. One must note that in counter-diffusive studies, these names (i.e. upstream and downstream) are just used to distinguish the two reservoirs and they do not bear any advective meaning. The schematic view of the complete diffusive cell connected to reservoirs is presented in Figure S2 in supporting information.

The sample was compacted directly in place in the diffusion cell at a bulk dry density of 1690 $kg.m^{-3}$ (i.e. porosity) based on the dry mass of the solid placed in the cell and the volume of the cell, leading to a thickness of 10 mm.

Each face of the cell holds two holes (inlet and outlet) to allow for the circulation of water between the reservoirs and the face of the sample. To ensure homogeneous supply of solution to the surface of the sample, before closing the diffusive cell with stainless steel covers, each face of the sample is covered with three porous layers[11]: Whatman cellulose nitrate membrane filters (manufactured by GE healthcare) of 0.8 µm mesh, then stainless-steel filter plates (pore diameter

10 µm from MOTT industrial division), and finally two grids (nominal spaces of 280 & 450 µm for monofilaments with diameters equal to 120 & 200 µm from Goodfellow).

The samples were flushed using the ascendant capillary method to completely withdraw air from the pores. In this method, the cell is placed vertically, downstream facing upwards. Both holes downstream are were connected to a vacuum pump. Simultaneously on the upstream face, the outlet is injected with nitrogen pentoxide and the inlet with a 0.1 M NaCl solution using the peristaltic pump. Due to the small size of the sample, this equilibration step is achieved in two weeks. Finally, prior to diffusion experiments, the compacted kaolinite samples were equilibrated with 0.1 M NaCl solution to ensure the ionic charge balance between the reservoir electrolytes and pore solution.

Two diffusion cells were prepared: The first diffusive cell labelled KAO-A was used to acquire diffusion parameters for tritiated water (HTO) and chloride-36 ($^{36}Cl^-$) through kaolinite at intact and reacted (barite precipitated) conditions. The second cell labelled KAO-B was used to determine the 3D-evolution of barite precipitates in kaolinite pore network after 30 days and 60 days of reactive diffusion step using X-ray microtomography.

Experimental setup used for Chalk. The barite precipitation experiments in chalk were carried out using a static diffusion cell as developed by Descostes *et al.*[12]. In this setup, the chalk sample is sandwiched in between upstream and downstream reservoirs of volume 178 mL and 140 mL respectively. The sandwiched sample was held by a sample holder and all the parts (upstream, sample, sample holder, and downstream) were assembled, glued and screwed together to generate a complete through diffusion cell. Two similar cells were prepared: one for the determination of the tracer diffusive behavior through intact and reacted chalk (labelled as CHA-A), and the second one for the post-mortem characterization of reacted chalk by X-ray microtomography and SEM-

observations (labelled as CHA-B). The details for the preparation of the cell, the equilibration step and the concentration of ions in reservoir solutions are detailed in Rajyaguru *et al.* [9]

Determination of HTO & $^{36}Cl^-$ diffusive behavior at intact kaolinite condition. After equilibration step, the total upstream reservoir solution of KAO-A was completely replaced with 100 mL of fresh 0.1 M NaCl solution. This solution was spiked with 180 µl of tritiated water (labelled CERCA ELSB45 n°760112/4) and 65 µl of $^{36}Cl^-$ (labelled E&Z 1760-100-1) to achieve volumetric activity of 1 MBq.L^{-1} for HTO and 0.5 MBq.L^{-1} for $^{36}Cl^-$. Similarly, the total downstream reservoir solution was completely replaced with 10 mL of fresh 0.1 M NaCl solution. Evolution of HTO and $^{36}Cl^-$ activity was estimated by periodic sampling in both reservoirs. To ensure a constant activity gradient between both reservoirs, the downstream solution was renewed with fresh10 mL of 0.1 M NaCl solution at each sampling. The protocol used for measurement of activity is as follows: 100 µL of upstream and downstream solutions, each mixed with 900 µL of ultrapure water and 4 mL of Ultimagold scintillation liquid in a 5 mL scintillation bottle. The activities were measured using a liquid scintillation recorder Packard Tricarb 2500.

Treatment of experimental diffusive results. The experimental activity dataset for both HTO and $^{36}Cl^-$ were interpreted numerically using Fick's second law for one-dimensional transport[13].

$$\frac{\partial C}{\partial t} = \frac{D_e}{\alpha}\frac{\partial^2 C}{\partial x^2} = \frac{D_e}{\varepsilon + R_d \rho_{app}}\frac{\delta^2 C}{\delta x^2} \qquad (1)$$

where C is the concentration in mol.m^{-3} (or activity Bq.m^{-3} in our case), t is the time in s, D_e is the effective diffusion coefficient in m^2.s^{-1}, $\alpha = \varepsilon + R_d \rho_{app}$ is the rock capacity factor, ε is the porosity, ρ_{app} is the bulk dry density in kg.m^{-3}, and R_d is the distribution ratio in m^3.kg^{-1}. The initial

and boundary conditions for this through diffusion setup in a condition when the concentration in upstream and downstream reservoir is left free to evolve are as follows:

$$C(x,t) = 0 \text{ for } t = 0 \quad (2)$$

$$C(x,t) = C_0 \text{ for } x = 0 \text{ at } t = 0 \quad (3)$$

$$C(x,t) = 0 \text{ for } x = L + 2l \text{ at } t = 0 \quad (4)$$

where C_0 is the initial concentration (or initial activity in $Bq.m^{-3}$) in the upstream reservoir at the injection time, L is sample thickness (m) and l is the filter plate thickness (m). The total porosity and effective diffusion coefficient of these filter plates, equal to 28% and $2.3x10^{-10}$ $m^2.s^{-1}$ for HTO and $2.0x10^{-10}$ $m^2.s^{-1}$ for $^{36}Cl^-$, are taken from literature[11,14]. Using the initial and boundary conditions from equation 2, 3 and 4, the semi-analytical solutions to determine the flux in downstream reservoirs is well noted in literature[12,13,15,16].

The semi-analytical solutions are implemented in CEA's tool called Interpretation Model of Diffusion Experiments[17] (I-Mode).

For through-diffusion setup, the associated errors in measured cumulative activities in downstream reservoirs were calculated using Gaussian error propagation method. The mathematical equation for this operation were taken from Savoye *et al.*[18] and Bazer-Bachi *et al.* [19]. These equations are detailed in supporting information. Finally, from these calculated associated errors and experimental data points three diffusive curves at best fitting, minimum, and maximum were reproduced using I-mode to obtain the error range in measurement of effective diffusion coefficients.

Estimation of barite precipitation impact on diffusivity. Once HTO and ^{36}Cl diffusive parameters were acquired at intact kaolinite conditions, out-diffusion of tracers from sample pores of KAO-A cell was carried out by replacing the solutions of both reservoirs with 100 mL of fresh 0.1 M NaCl solution. This step was performed for 2 weeks to ensure complete out-diffusion of radiotracers. After this step, barite precipitation experiment was launched by replacing upstream reservoir with 20 mL of fresh 0.1 M NaCl solution containing 4 mM of $BaCl_2$ (similarly downstream reservoir solution was replaced with 20 mL of 0.1M NaCl solution containing 4 mM Na_2SO_4). The upstream solution was spiked with 25 µL of ^{133}Ba (source ELSB45 CERCA n°5245 and source activity 1.78 $MBq.L^{-1}$). For chalk experiments, the upstream reservoir was filled with equilibrated solution containing $BaCl_2$ of concentration 20 mM (resp. 20 mM of Na_2SO_4 in downstream reservoir).

After this step, barium from upstream (*resp.* sulfate from downstream) diffused into the sample and oversaturated the pore solution over time with respect to barite, from which barite then precipitated. For the total experimental time, the precipitation of barite in pores was followed by periodically measuring the decrease of barium in upstream (*resp.* sulfate in downstream). Thus, this operation allowed us to determine the time at which most of the barium (*resp.* sulfate from downstream) contributed to precipitation in pores, *i.e.* when the reactant concentrations reached quasi-equilibrium in respective reservoirs. At this point, the upstream solution of each cell was spiked with HTO and ^{36}Cl radioactive tracer.

For KAO-A, using the initial ratio of stable barium concentration and ^{133}Ba activity in upstream, the sampled activities were converted into stable barium concentration. For this operation, 100 µL upstream solution was sampled periodically and mixed with 900 µL of ultrapure water. The activity

measurement for each sampling was done using gamma counter (Packard 1480 WIZARD, USA). Similarly, 100 µL downstream solution was periodically sampled and diluted in 900 µL of ultrapure water. The sulfate concentration in sampled volumes was measured using Ionic Chromatography (Dionex 500 equipped with AS14 IonPac column). Finally, barium (*resp.* sulfate in downstream) concentrations were plotted over time to determine its quasi-equilibrium in upstream.

For kaolinite experiments, same volume of the tracers was directly injected in the upstream solution 85 days after the start of the reactive experiment to achieve the same initial volumetric activity (1 MBq.L^{-1} for HTO and 0.5 MBq.L^{-1} for $^{36}Cl^{-}$) as intact case and not to disturb the chemistry of the system. For the same purpose, unlike intact-diffusive case, the downstream solution at each sampling time was not renewed but activity change was directly measured by periodically withdrawing 100 µL of solution from reservoirs. Protocol used to measure activities at each sampling in upstream and downstream is the same as intact conditions.

For chalk, the reactive diffusion experiment was continued for total experimental time of 300 days. At this stage the upstream solution was directly spiked with HTO (labelled CERCA ELSB45 n°760112/4) and $^{36}Cl^{-}$ (labelled E&Z 1760-100-1) to achieve volumetric activity of 0.4 MBq.L^{-1} for HTO and 0.30 MBq.L^{-1} for $^{36}Cl^{-}$ respectively. Protocol used for measurement of activity consisted in mixing 4 mL of Ultimagold scintillation liquid with either 50 µL of upstream solution plus 900 µL of ultrapure water or 1 mL of downstream solution in a 5 mL scintillation bottle. 1 mL of tracer-free solution was added in downstream of chalk cell at each sampling in order to keep the volume of the downstream reservoir constant.

The activity data for of HTO and ^{36}Cl for downstream of chalk and kaolinite were then fitted with I-Mode to determine the macroscopic change in effective diffusion coefficient values of these tracers at reacted chalk and kaolinite conditions.

Post-mortem 3D imaging (µCT). The 3D view of barite precipitated zone in kaolinite and chalk samples was obtained using X-ray micro-tomography (µCT) technique. For this operation, barite precipitation experiments were cell KAO-B and cell CHA-B, using the same experimental conditions as in the radioactive cells for each study.

For kaolinite experiment, after 30 days and 60 days of reactive diffusion experiment the circulation of reactants in KAO-B was temporarily stopped for about 1 day. The whole diffusion cell was disconnected from reservoirs and was placed in an X-ray micro-tomography (µCT) apparatus. After imaging, the cell was connected back to reservoirs to continue to barite precipitation process. In the case of chalk, the size of experimental setup prevented any µCT imaging during the experiment. Thus, CHA-B cell was dismantled after 140 days and barite precipitated chalk sample was removed from the supporting ring and was then used for imaging.

For both studies the micro-tomography from Skyscan 1272 (Brucker) was used to acquire images. The µCT images for kaolinite and chalk samples were compared to determine the formation of precipitated zone in natural porous media (micritic chalk) and compacted porous media (kaolinite).

Estimation of ^{36}Cl affinity towards barite. To estimate any potential affinity of ^{36}Cl towards newly formed barite, ^{36}Cl adsorption was measured in batch experiments. Barite was synthetized by over-saturating solution with respect to barite to make it precipitate. The precipitates were recovered by filtration and dried at 105°C. Five aliquots of 1 g of barite were suspended in 2 mL

of a 0.1 M NaCl background electrolyte solution and spiked with $^{36}Cl^-$ tracer (source E&Z N°1760-100-1). The 0.1 M NaCl-barite solution in each centrifuge tube was mixed for one week after which they were centrifuged. From the centrifuged solution, 100 µL of solution was sampled and mixed with 900 µL of ultrapure water and 4 mL of Ultimagold scintillation liquid. The activities were measured using a liquid scintillation recorder Packard Tricarb 2500. Finally, the distribution ratio of ^{36}Cl was estimated using equation 5.

$$R_{d,36Cl} = \frac{V}{m}\frac{A_0 - A_f}{A_f} \quad (5)$$

($m^3.kg^{-1}$), where A_o (Bq) is the initial activity present in solution, A_f (Bq) is the final activity remaining in the centrifuged solution, V (m^3) is the volume of solution in centrifuge tube, and m (kg) is the mass of barite.

Retardation of Ba by adsorption on kaolinite. To characterize ion Ba^{2+} retardation by adsorption on kaolinite during the barite precipitation, Ba^{2+} adsorption was measured in 3 batch experiments. This was done by firstly spiking 20 mL of solution containing 4 mM $BaCl_2$ reactant and 0.1 M NaCl as background electrolyte with 25 µL of ^{133}Ba source (source activity 1.78 $MBq.L^{-1}$ and source CERCA ELSB 45 n°5245). Then, in each batch, 1 g of kaolinite was suspended with 5 mL of this spiked solution. After one week, the solution was centrifuged from the clay and using the same activity measurement protocol as ^{133}Ba activity measurement for KAO-A and CHA-A, and equation 5, the distribution ratio of Ba, $R_{d,Ba}$, was measured.

RESULTS AND DISCUSSION

Diffusion of HTO and $^{36}Cl^-$ through intact materials. The experimental cumulative activity data for HTO and $^{36}Cl^-$ in downstream reservoir through intact kaolinite are reported in Figure 1.

These data were reproduced by simulated curves using I-mode with $D_{e,HTO,kaolinite} = 29\times10^{-11}$ m².s⁻¹ and $D_{e,36Cl,kaolinite} = 24\times10^{-11}$ m².s⁻¹. A small retardation factor of 2.5 for ^{36}Cl was necessary to reproduce its cumulative activity. Such small retardation can be due to the positive edges of kaolinite.[10] The diffusion coefficients for HTO and $^{36}Cl^-$, and the retardation factor for $^{36}Cl^-$ are close to values determined by Glaus *et al.*[20] for KGa-1b type of kaolinite at a dry density of 1900 kg.m^{-3}. Note that the self-diffusion coefficient of ^{36}Cl in water is slightly lower compared to HTO[21] ($D_{0,HTO} = 2\times10^{-10}$ m².s⁻¹ and $D_{0,36Cl} = 1.7\times10^{-10}$ m².s⁻¹ or $D_{0,HTO}/D_{0,36Cl} = 1.17$). The small difference in effective diffusion coefficient values ($D_{e,HTO}/D_{e,36Cl} = 1.20$) for both species through intact kaolinite is in the expected limit. For chalk, the effective diffusion coefficient for HTO determined in Rajyaguru *et al.* [9] is equal to $D_{e,HTO,chalk} = 41.5\times10^{-11}$ m².s⁻¹. For $^{36}Cl^-$ since the chalk matrix is composed of calcite (i.e. uncharged/neutral material), its diffusion is assumed to be similar to HTO in chalk, after renormalization to their respective self-diffusion coefficient in water. This means that the diffusive behavior of HTO and $^{36}Cl^-$ through intact chalk and kaolinite at a dry density of 1690 kg.m^{-3} are quite similar.

Precipitation impact on diffusion. Reservoir monitoring step showed that reactants concentration (barium in upstream and sulfate in downstream reservoir) reached quasi equilibrium in reservoirs after 85 days and ca. 70 days of reactive diffusion step in KAO-A and CHA-A (Figure S3 in supporting information). The experimental cumulative activity data for HTO and $^{36}Cl^-$ in downstream reservoir through reacted kaolinite and chalk are reported in Figure 1 A and B. For kaolinite using Gaussian error propagation, the effective diffusion coefficients with I-mode fitting are respectively $D_{e,HTO,kaolinite} = 1.5\times10^{-12}$ m².s⁻¹, $D_{e^-,HTO,kaolinite} = 6\times10^{-13}$ m².s⁻¹ and $D_{e^+,HTO,kaolinite} = 2.1\times10^{-12}$ m².s⁻¹. Similarly, the diffusive parameters for HTO and $^{36}Cl^-$ with

minimum, maximum and best fits for chalk are reported in Table 1 (the modeled curves for HTO and $^{36}Cl^-$ are reported in Figure S6, and their corresponding D_e^-, D_e *and* D_e^+ are reported in Table S1 in supporting information). For $^{36}Cl^-$ diffusion through reacted kaolinite cannot be reproduced: indeed, total clogging is observed for this tracer.

µCT imaging of the barite precipitate. For chalk, the µCT image in Figure 2 A shows that barite precipitates are distributed in the reacted zone located in center of the sample.

For kaolinite, the µCT images reported Figure 2 B and Figure 2 C after 30 days and 60 days of precipitation experiments show that compared to chalk this reacted zone shifted towards the barium reservoir. This shift is because the measured barium distribution ratio from batch experiments equal to $3x10^{-3}$ $m^3.kg^{-1}$ shows that there is a small adsorption of barium on kaolinite pore surface.

These µCT images further shows that barite precipitates resembling spheres are evenly distributed in this reacted zone. However, since the resolution of scan (16 µm) is much larger than the mean size of pores (35 nm), each of the sphere in reality represents a cluster of small barite precipitates distributed in the matrix (see Figure S5 in supporting information for SEM images acquired from similar study).

In both chalk and kaolinite experiments, the counter diffusing barium and sulfate will meet in the reacted zone and supersaturate the pore solution with respect to barite. At one-point barite precipitation will start from this solution forming stable seeds and the precipitation kinetics is locally enhanced. Consequently, the saturation is lowered down *w.r.t.* barite as the reactants concentration in surrounding solution are drained down to vicinity preventing formation of precipitates out of first points of precipitation.

In kaolinite-barite case, this mechanism can be responsible for the formation of clusters. Small heterogeneities in the system (orientation of pores, or random distribution of connectivity) enhance this process, dispersing the clusters widely around the center plane.

On the contrary, chalk-barite evolution shows that the local variation in rate of supersaturation in pores in reacted zones is compensated. This is because the large pore volumes will require longer times to be supersaturated with respect to barite. The low solubility of barite along with these pore volumes will compensate for local variations. Thus, for chalk most of the first points of precipitation fell in a single line at the center of the sample and most of the porosity reduction occurred in this zone.

Estimation of porosity and diffusive parameters in reacted zones.

The extent of precipitation impact on intact properties of chalk and kaolinite can be explained by comparing the geometric factors of intact and reacted samples. This factor can be calculated using equation 6[22,23].

$$D_e = \frac{\delta}{\tau^2}\,\varepsilon \times D_0 = G \times \varepsilon \times D_0 \qquad (6)$$

Where δ and τ are the constrictivity and tortuosity of a porous material that are usually combined in form of geometric factor G, D_e *or* $D_{e,precip}$ ($m^2.s^{-1}$) is the effective diffusion coefficient of tracer at intact or reacted condition, D_0 ($m^2.s^{-1}$) is the self-diffusion coefficient of tracer in water. Diffusion values calculated from the tracer experiments are given in Table 1.

For these calculations, the change in porosity in each reacted zone after precipitation was carried out by estimating the amount of barite precipitated in pore space from mass balance calculations (Table 1). These calculations showed that after 140 days of experimental time, the amount of

barium contributing to barite precipitation in chalk and kaolinite is equal to 2.7 mmol and 0.04 mmol respectively. Using molar volume of barite mineral (*i.e.* 0.019 mol.cm^{-3}), the volumes occupied by barite in chalk and kaolinite are 0.14 cm^3 and 0.0021 cm^3, respectively.

From µCT images and SEM observations, the thickness of chalk reacted zone is equal to *ca.* 500 µm (see Figure S6 in supporting information), with maximum and minimum thickness equal to 1 mm and 300 µm respectively. From µCT images, for kaolinite, the thickness is equal to *ca.* 2 mm, with maximum and minimum thickness equal to 3 mm and 1 mm respectively. Finally, using the intact porous volumes at each thickness and the volume occupied by barite precipitates, the residual porosity remaining after precipitation was calculated (Table S3 in supporting information). These values reported in Table 1 clearly show that barite precipitation significantly decreased the total porosity in reacted zone of chalk compared to kaolinite (12% compared to 34.5%).

The effective diffusion coefficients for HTO and $^{36}Cl^-$ in reacted zones at selected thickness from previous case can be further be calculated using equation 7. This relationship is similar to the resistance equation used for capacitors in series:

$$D_{eq} = \frac{L}{\frac{x}{D_{precip}} + \frac{L-x}{D_{e,intact}}} \quad (7)$$

where, $D_{e,intact}$ (m^2.s^{-1}) is the effective diffusion coefficient for HTO or ^{36}Cl through intact sample, and D_{eq} (m^2.s^{-1}) is the minimum, maximum and best fit equivalent effective diffusion coefficient estimated by I-mode in section "precipitation impact on diffusivity", D_{precip} (m^2.s^{-1}) is the diffusion coefficient for HTO and $^{36}Cl^-$ in reacted zone, and x and L are the thickness of reacted zone and sample respectively. The geometric factor values after integrating the effective diffusion

coefficients of HTO at thickness *ca.* 500 µm for chalk and 2 mm for kaolinite of reacted zone using equation 6 are reported in Table 1. This table shows that barite precipitation led to HTO diffusivity decrease by factor of 28 in chalk and 1000 in kaolinite respectively. The details of minimum and maximum D_e values reported in this table are explained in supporting information. The minimum, maximum and best fit diffusion coefficients reported in this table are reported in detail in supporting information (see Table S2).

From the effective diffusion coefficient for HTO and total porosity for chalk and kaolinite, equation 6 shows that at intact conditions both sample have similar geometric factor. But after precipitation the geometric factor for chalk and kaolinite in reacted zone decreased by a factor 7 and 10,000 respectively.

This observation shows that for chalk even though there was significant porosity reduction in the thin reacted zone, the residual pores still connected the intact zone on each face of reacted zone. This connected zone then allowed significant amount of HTO to diffuse through reacted zone. However, for kaolinite, the small porosity reduction corresponds to significant reduction of connectivity in the system. This strong decrease in connectivity thus led to stronger reduction in HTO diffusivity in reacted zone.

Anionic exclusion induced by the newly formed mineral. The effective diffusion coefficient determined experimentally, and the effective diffusion coefficient measured in reacted zone for $^{36}Cl^-$ are reported in Table 1. These values show that for chalk, at a same residual porosity in reacted zone, barite precipitation decreased $D_{e,36Cl,chalk}$ by factor of 450 compared to intact conditions. For kaolinite, even though HTO diffusion was measured, still total clogging of $^{36}Cl^-$ was observed. These results show that for both cases, barite precipitation has a stronger impact on

$D_{e,36Cl}$ in kaolinite compared to chalk. This difference in diffusive behavior of $^{36}Cl^-$ compared to HTO through barite precipitated zone can be explained by the presence of surface charges on barite surface. The first possibility would be the presence of positive surface charge on barite mineral which would eventually lead to an adsorption of $^{36}Cl^-$. In this case, a sharp decrease of $^{36}Cl^-$ activity in upstream reservoir is expected, related to a significant delay in $^{36}Cl^-$ breakthrough in the downstream reservoir. However, experimental data contradict such hypothesis. In chalk experiment, after 70 days of experiment, 67% of initial HTO activity and only 5% of initial $^{36}Cl^-$ activity decrease was observed in upstream reservoir. Similarly, for kaolinite, after 100 days of experiment, 70% of HTO activity and only 1% of $^{36}Cl^-$ activity decrease was observed in the upstream. The upstream graphs are presented in Figure S7 in supporting information. In chalk there was small activity evolution and in kaolinite no measurable activity were observed in downstream. Moreover, batch experiments measurement led to a very small distribution ratio value for $^{36}Cl^-$, $3x10^{-4}$ $m^3.kg^{-1}$. Thus, barite possessing positive surface charge can be excluded.

The second possibility is that barite would possess negative surface capable of excluding anionic species such as $^{36}Cl^-$ from the reacted zone. From Table 1, at equal residual porosity in reacted zone for chalk, barite precipitation generated 15 times lower geometric factor of $^{36}Cl^-$ than HTO. Similarly, using $D_{e,precip,36Cl}$ from Table 1, and geometric factor for $^{36}Cl^-$ similar to HTO (*i.e.* 0.06), equation 6 shows that of 12% total accessible porosity for HTO only 0.78% of porosity would be accessible for $^{36}Cl^-$ diffusion.

This very small accessible porosity can very well explain the smaller diffusive rate of $^{36}Cl^-$ compared to HTO both in chalk and kaolinite. Moreover, this effect would be more pronounced in kaolinite where the pore size is almost twenty times smaller than in chalk, resulting in a complete

anion exclusion of $^{36}Cl^-$. Note that such observation are consistent with literature data, where zetameter tests showed that barite in solution equilibrated with this mineral has negative surface charge.[24]

Several studies in literature have already demonstrated that the morphology of barite precipitation can be different in different void spaces.[25,26] However, the present study shows that pore structure would govern the distribution of these precipitates. This distribution would decide the effectiveness of clogging by same mineral in blocking the diffusive pathways of different pore structures. The $^{36}Cl^-$ results shows that at conditions where the pore solution is equilibrated with barium and sulfate ions, the newly formed mineral would have negative surface charge capable of partially or totally blocking the diffusion of anionic species such as $^{36}Cl^-$.

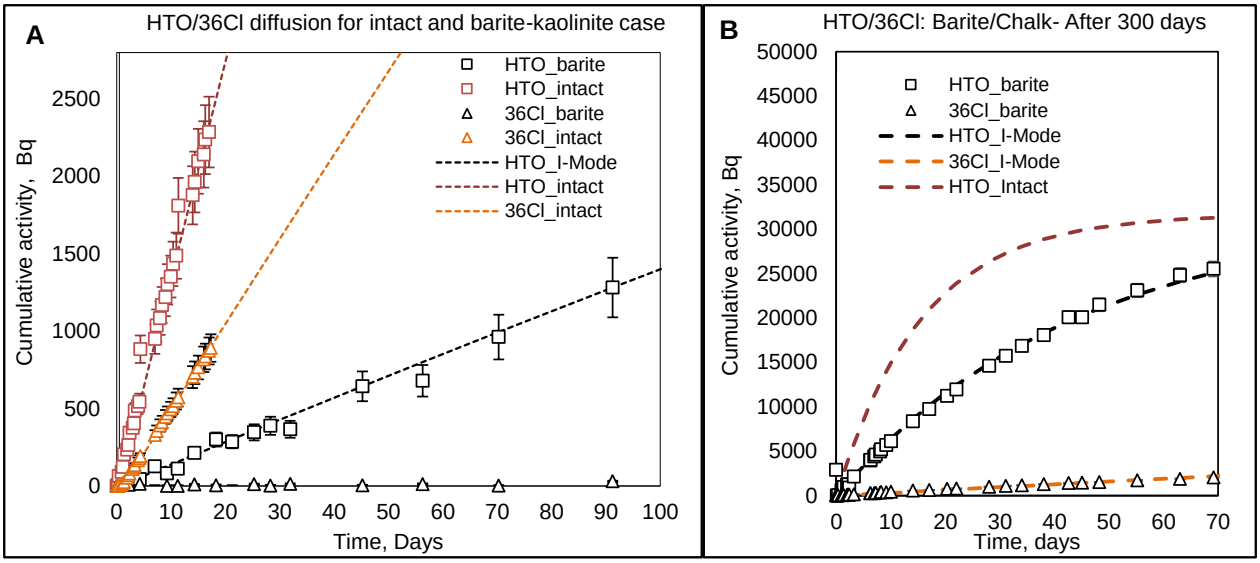

Figure 1. Cumulative total activity of HTO and 36Cl− diffusing through intact and reacted porous media, i.e. (A) compacted kaolinite and (B) micritic chalk. Simulated cumulative curves calculated by considering the diffusion parameters interpreting average experimental flux are shown as dashed lines.

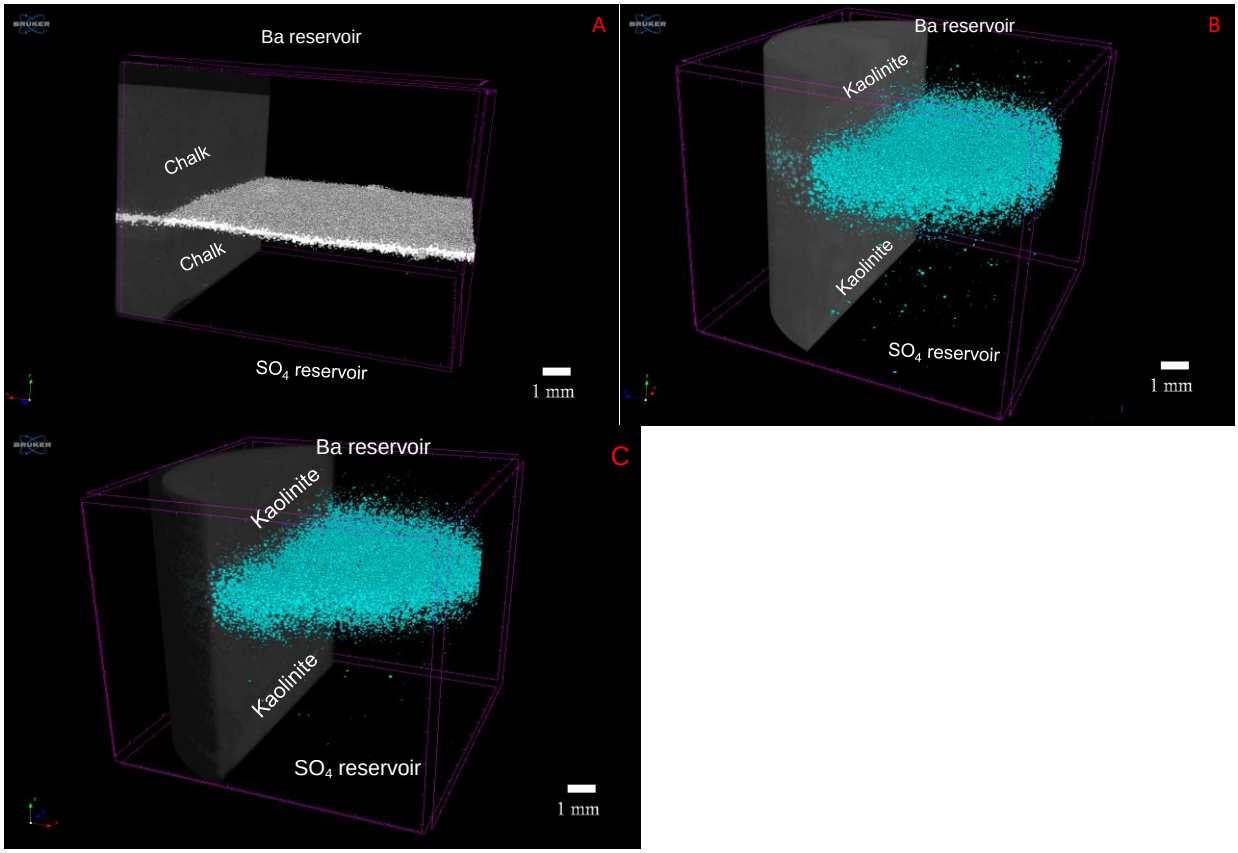

Figure 2 (A). Barite precipitated zone formed at the center of chalk sample between two intact matrix, (B). Barite precipitated zone in kaolinite shifted towards barium reservoir after 30 days, 2C: Barite precipitated zone in kaolinite shifted towards barium reservoir after 60 days.

Table 1. Porosity, effective diffusion coefficient and geometric factor values for HTO and $^{36}Cl^-$, calculated for intact sample, whole reacted sample and only reacted zone

			Porosity %	**$D_{e,\ HTO}$x10^{-11} m^2.s^{-1}**	**$D_{e,36Cl}$x10^{-11} m^2.s^{-1}**	**G_{HTO} (-)**	**G_{36Cl} (-)**
Chalk	Intact conditions		45	41.5	35.3	0.46	0.46
	Reacted conditions	Whole sample (6.5 mm)	42.5	13.5 (11.5-17.5)	1.1 (0.9-1.3)	0.16	0.015
		Reacted zone (300 µm-500 µm-1 mm)	12 (4 - 28.5)	1.48 (0.06 - 4.2)	0.08 (0.04 - 0.25)	0.06	0.004
Kaolinite	Intact conditions		36	29	23	0.4	0.38
	Reacted conditions	Whole sample (10mm)	35.5	0.15 (0.06 - 0.21)	(N/A)	0.02	N/A
		Reacted zone	34.5 (32 - 35)	0.031 (0.01 - 0.05)	(N/A)	0.00004	N/A

REFERENCES

(1) Andra 2005. Dossier 2005 argile – Evaluation de la faisabilité d'un stockage géologique en formation argileuse. Référence 266B, France http://www.andra. fr/download/site-principal/document/editions/266.pdf.

(2) NAGRA. *Project Opalinus Clay*—Safety Report: Demonstration of Disposal Feasibility for Spent Fuel, Vitrified High-Level Waste and Long-Lived Intermediate-Level Waste (Entsorgungsnachweis).; Wettingen, Switzerland, 2002.

(3) Bachu, S. Sequestration of CO_2 in Geological Media in Response to Climate Change: Road Map for Site Selection Using the Transform of the Geological Space into the CO2 Phase Space. *Energy Convers. Manag.* **2002**, *43* (1), 87–102.

(4) Berthe, G.; Savoye, S.; Wittebroodt, C.; Michelot, J. L. Changes in Containment Properties of Claystone Caprocks Induced by Dissolved CO_2 seepage. *Energy Procedia* **2011**, *4*, 5314–5319.

(5) Fleury, M.; Brosse, E. Transport in Tight Rocks. In *Geological Carbon Storage: Subsurface Seals and Caprock Integrity*; American Geophysical Union, 2018; Vol. 238, p 31.

(6) Dagnelie, R. V. H.; Arnoux, P.; Enaux, J.; Radwan, J.; Nerfie, P.; Page, J.; Coelho, D.; Robinet, J. C. Perturbation Induced by a Nitrate Plume on Diffusion of Solutes in a Large-Scale Clay Rock Sample. *Appl. Clay Sci.* **2017**, *141*, 219–226.

(7) De Windt, L.; Marsal, F.; Tinseau, E.; Pellegrini, D. Reactive Transport Modeling of Geochemical Interactions at a Concrete/Argillite Interface, Tournemire Site (France). *Phys. Chem. Earth* **2008**, *33* (SUPPL. 1), 295–305.

(8) Chagneau, A.; Claret, F.; Enzmann, F.; Kersten, M.; Heck, S.; Madé, B.; Schäfer, T. Mineral Precipitation-Induced Porosity Reduction and Its Effect on Transport Parameters in Diffusion-Controlled Porous Media. *Geochem. Trans.* **2015**, *16* (1), 1–16.

(9) Rajyaguru, A.; L'Hôpital, E.; Savoye, S.; Wittebroodt, C.; Bildstein, O.; Arnoux, P.; Detilleux, V.; Fatnassi, I.; Gouze, P.; V.Lagneau. Experimental Characterization of Coupled Diffusion Reaction Mechanisms in Low Permeability Chalk. *Chem. Geol.* **2019**, *503* (October 2018), 29–39.

(10) Chagneau, A.; Tournassat, C.; Steefel, C. I.; Bourg, I. C.; Gaboreau, S.; Esteve, I.; Kupcik, T.; Claret, F.; Schäfer, T. Complete Restriction Of $^{36}Cl^-$ Diffusion by Celestite Precipitation in Densely Compacted Illite. *Environ. Sci. Technol. Lett.* **2015**, *2* (5), 139–143.

(11) Tertre, E.; Savoye, S.; Hubert, F.; Prêt, D.; Dabat, T.; Ferrage, E. Diffusion of Water through the Dual-Porosity Swelling Clay Mineral Vermiculite. *Environ. Sci. Technol.* **2018**, *52* (4), 1899–1907.

(12) Descostes, M.; Blin, V.; Bazer-Bachi, F.; Meier, P.; Grenut, B.; Radwan, J.; Schlegel, M. L.; Buschaert, S.; Coelho, D.; Tevissen, E. Diffusion of Anionic Species in Callovo-Oxfordian Argillites and Oxfordian Limestones (Meuse/Haute-Marne, France). *Appl. Geochem.* **2008**, *23* (4), 655–677.

(13) Crank, J. *The Mathematics of Diffusion*, 2nd ed.; Press, C., Ed.; Oxford, 1975.

(14) González Sánchez, F.; Van Loon, L. R.; Gimmi, T.; Jakob, A.; Glaus, M. A.; Diamond, L. W. Self-Diffusion of Water and Its Dependence on Temperature and Ionic Strength in Highly Compacted Montmorillonite, Illite and Kaolinite. *Appl. Geochem.* **2008**, *23* (12), 3840–3851.

(15) Moridis, G. J. A set of semianalytical solutions for parameter estimation in diffusion cell experiments. *Sci. York* **1998**, Report LBNL-41857, Lawrence Berkeley National Laboratory, Berkeley, California.

(16) Didierjean, S.; Maillet, D.; Moyne, C. Analytical Solutions of One-Dimensional Macrodispersion in Stratified Porous Media by the Quadrupole Method: Convergence to an Equivalent Homogeneous Porous Medium. *Adv. Water Resour.* **2004**, *27* (6), 657–667.

(17) Radwan, J.; Hanios, D.; Grenut, B. Qualification Expérimentale de La Plate-Forme ALLIANCES . 1 Ère Partie : Calculs Préliminaires, **2006** NT-CEA, DPC / SECR 06-051 indice A.

(18) Savoye, S.; Frasca, B.; Grenut, B.; Fayette, A. How Mobile Is Iodide in the Callovo-Oxfordian Claystones under Experimental Conditions Close to the in Situ Ones? *J. Contam. Hydrol.* **2012**, *142–143*, 82–92.

(19) Bazer-Bachi, F.; Tevissen, E.; Descostes, M.; Grenut, B.; Meier, P.; Simonnot, M. O.; Sardin, M. Characterization of Iodide Retention on Callovo-Oxfordian Argillites and Its Influence on Iodide Migration. *Phys. Chem. Earth* **2006**, *31* (10–14), 517–522.

(20) Glaus, M. A.; Frick, S.; Rossé, R.; Loon, L. R. V. Comparative Study of Tracer Diffusion of HTO, $^{22}Na^{+}$ and $^{36}Cl^{-}$ in Compacted Kaolinite, Illite and Montmorillonite. *Geochim. Cosmochim. Acta* **2010**, *74* (7), 1999–2010.

(21) Li, Y.-H.; Gregory, S. Diffusion of Ions in Sea Water and in Deep Sea Sediments. *Geochim. Cosmochim. Acta,* **1974**, *38* (2), 703–714.

(22) van Brakel, J.; Heertjes, P. M. Analysis of Diffusion in Macroporous Media in Terms of a Porosity, a Tortuosity and a Constrictivity Factor. *Int. J. Heat Mass Transf.* **1974**, *17* (9), 1093–1103.

(23) Savoye, S.; Michelot, J. luc; Wittebroodt, C.; Altinier, M. V. Contribution of the Diffusive Exchange Method to the Characterization of Pore-Water in Consolidated Argillaceous Rocks. *J. Contam. Hydrol.* **2006**, *86* (1–2), 87–104.

(24) Bokern, D. G.; Hunter, K. A.; McGrath, K. M. Charged Barite - Aqueous Solution Interface: Surface Potential and Atomically Resolved Visualization. *Langmuir* **2003**, *19* (24), 10019–10027.

(25) Poonoosamy, J.; Curti, E.; Kosakowski, G.; Grolimund, D.; Van Loon, L. R.; Mäder, U. Barite Precipitation Following Celestite Dissolution in a Porous Medium: A SEM/BSE and μ-XRD/XRF Study. *Geochim. Cosmochim. Acta* **2016**, *182* (April), 131–144.

(26) Prieto, M. Nucleation and Supersaturation in Porous Media (Revisited). *Mineral. Mag.* **2014**, *78* (6), 1437–1447.

Supplementary Material

1. Mercury intrusion-extrusion porosimetry for chalk and compacted kaolinite
2. Schematic view of counter-diffusion cell
3. Reactants evolution in upstream reservoir for kaolinite & chalk experiments
4. BSE SEM of barite precipitated in chalk
5. BSE-SEM of barite precipitates in kaolinite at 1.9 $g.cm^{-3}$ dry density
6. Calculation of associated errors in cumulative activities in downstream

1. Mercury intrusion-extrusion porosimetry for chalk and compacted kaolinite

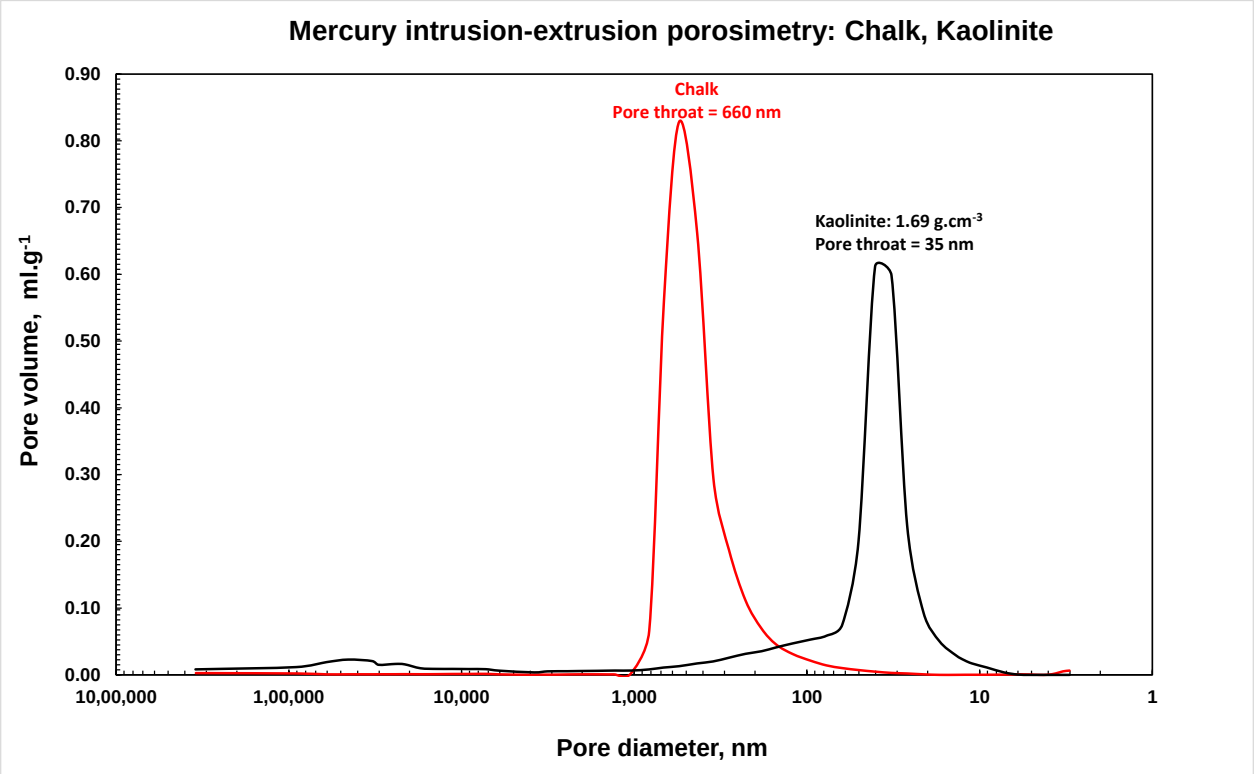

Figure S1: Pore-size distribution derived from mercury porosimetry for chalk and for compacted kaolinite

2. Schematic view of counter-diffusion cell

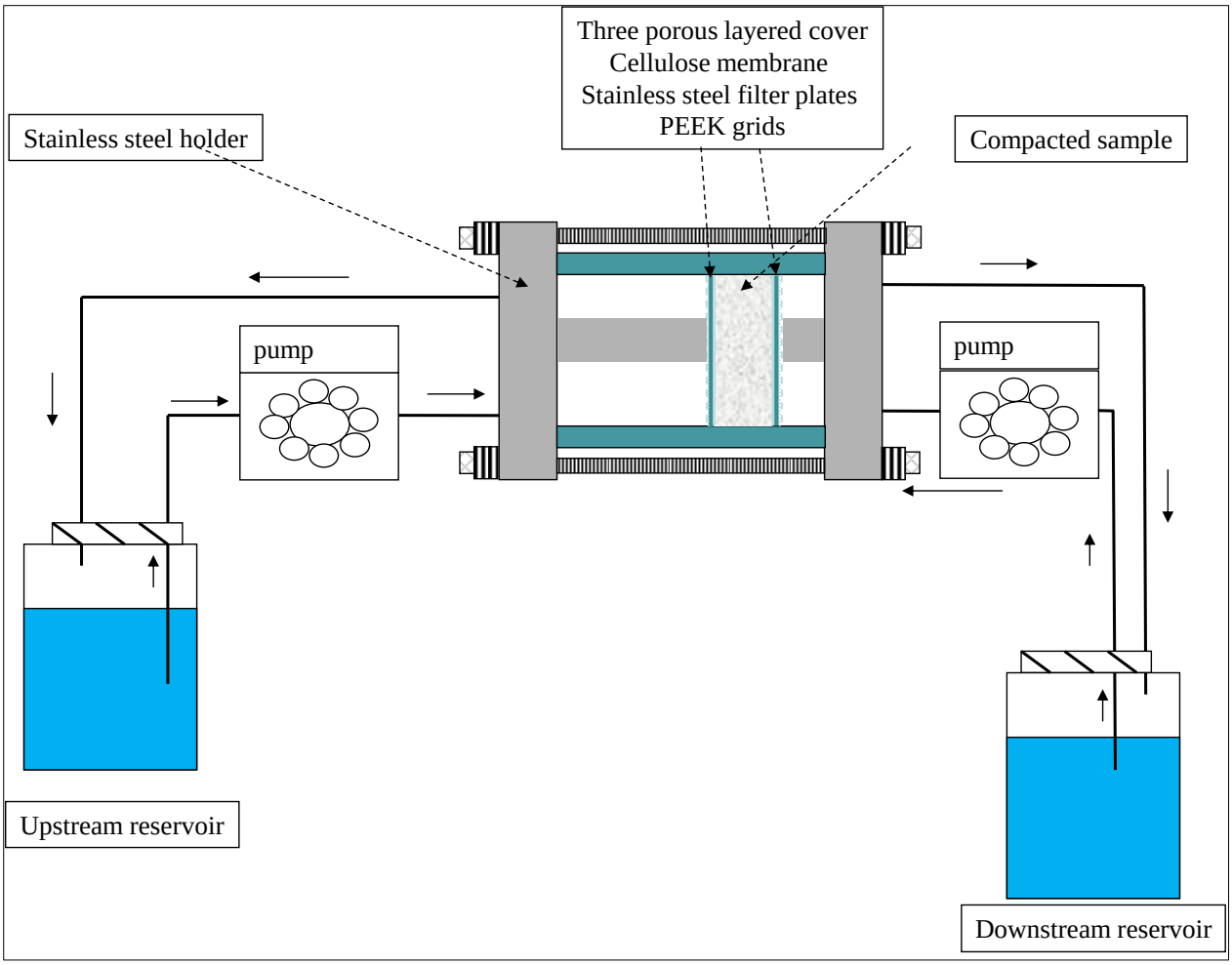

Figure S2: Counter-diffusion setup used for kaolinite experiments (the schematic figure is inspired from Savoye et al., 2011, J. Contam Hydrol.)

3. Reactants evolution in upstream reservoir for kaolinite & chalk experiments

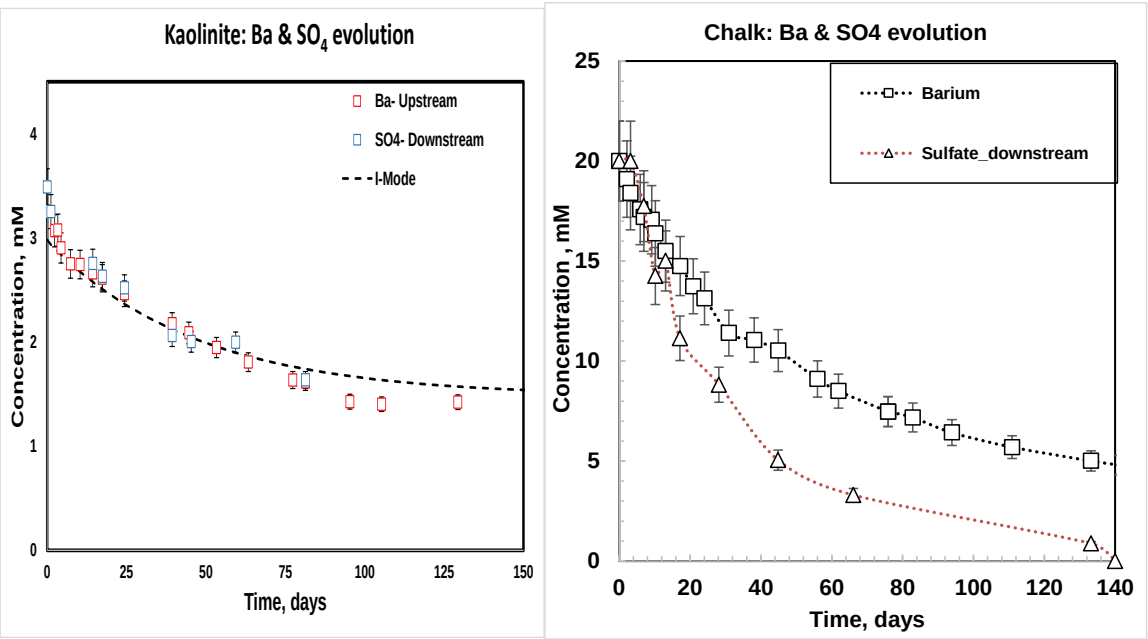

Figure S3: Evolution of Ba and SO4 concentrations as a function of time in upstream and downstream reservoirs of the barite-kaolinite cell and barite-chalk cell (results pre-obtained in Rajyaguru et al., 2019, Chem. Geol.)

4. BSE SEM of barite precipitated in chalk

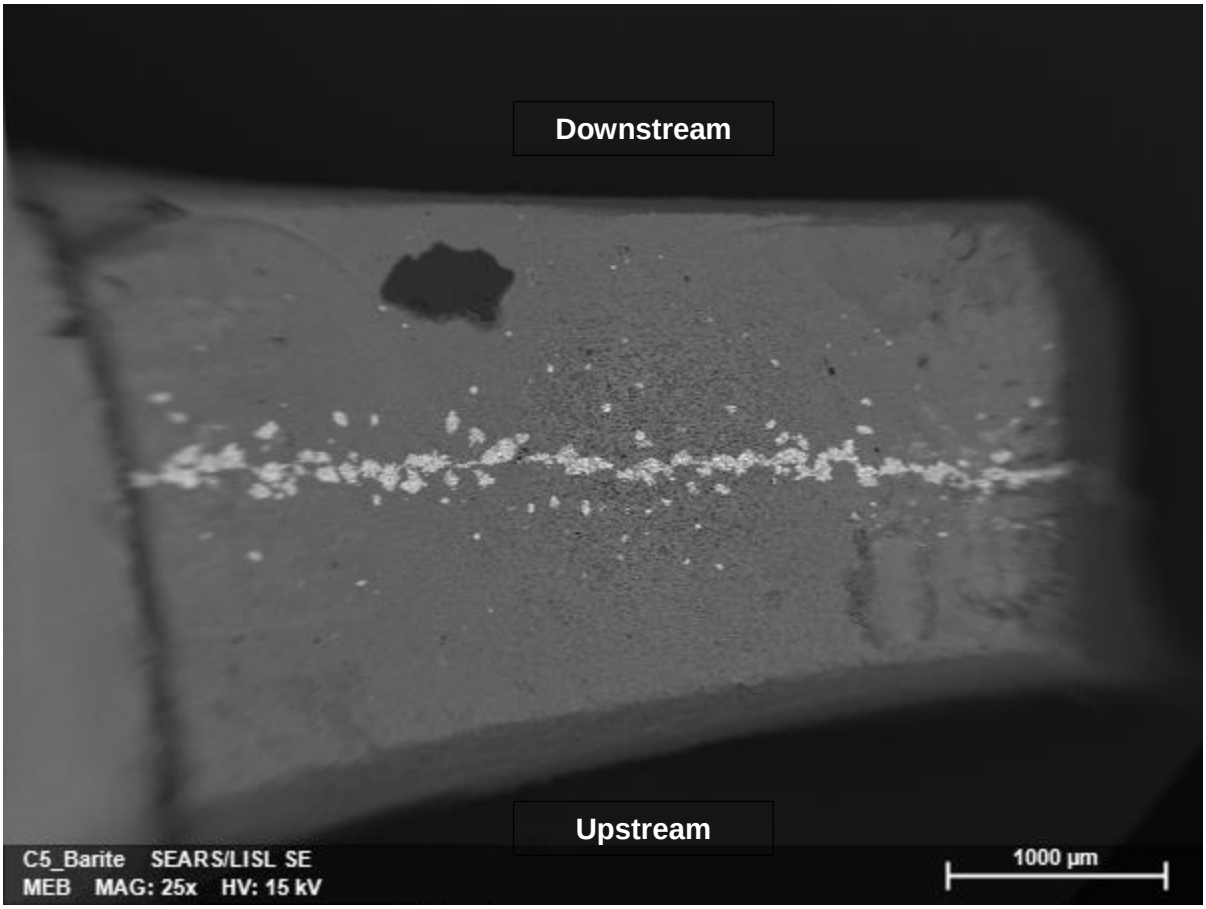

Figure S4: BSE-SEM image of barite precipitated zone of thickness ~500 µm in center of chalk sample((Rajyaguru et al., 2019))

5. BSE-SEM of barite precipitates in kaolinite at 1.9 g.cm^{-3} dry density

The evolution of barite precipitates in pore size less than 35 nm was studied by performing precipitation experiments in kaolinite compacted at dry density 1.9 g.cm^{3} The thickness and diameter of the sample were 0.6 cm and 0.9 cm respectively. The concentration of reactants was equal to 20 mM and the volume of reservoirs was equal to 50 ml. After one months of precipitation experiment the µCT image taken at resolution 15 µm showed barite precipitates distributed in the reacted zone. At this resolution each precipitate can be seen as big spheres formed in the reacted zone. However, the SEM observation showed that these spheres are in fact clusters of small barite precipitates formed in pores of size less than 35 nm. However, due to limitation of SEM images, the morphology of barite precipitates in such small porosity is still unknown.

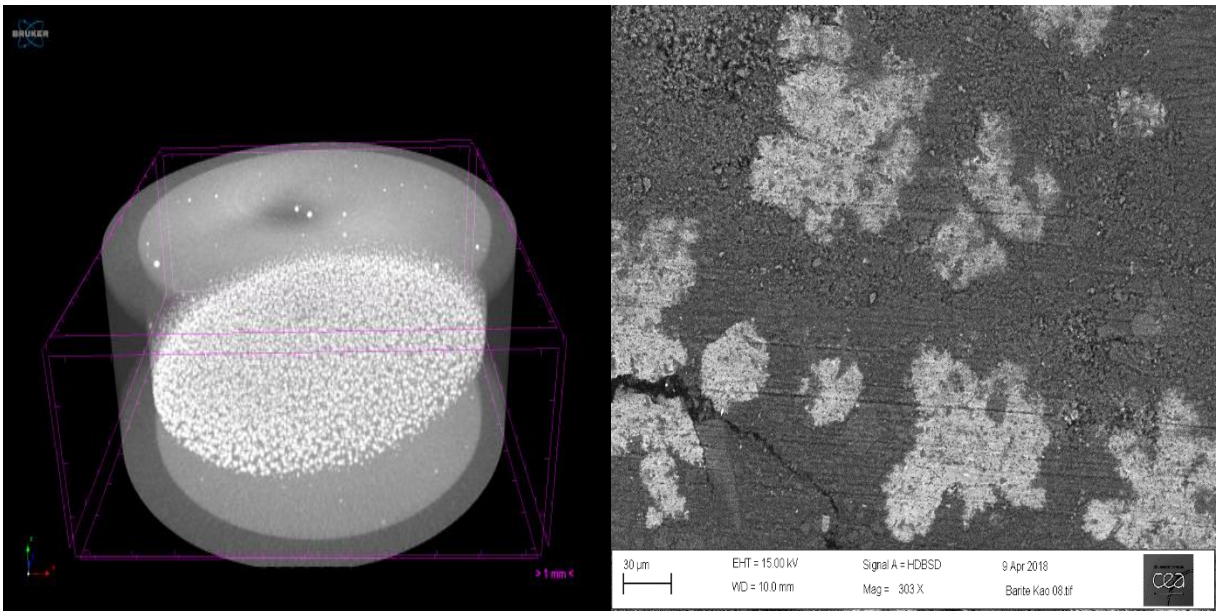

Figure S5: The µCT image after one month of precipitation experiment shows barite precipitates (resembling spheres) distributed in ~reacted zone. The SEM image of this reacted zone shows that each sphere in the reacted zone is a cluster of small barite precipitates

6. Calculation of associated errors in cumulative activities in downstream

Gauss error propagation formulae for calculating associated uncertainties

The error on the experimental cumulative total activity Q_{d,t_n} in the downstream reservoir (through-diffusion) is derived using the following equation:

$$Q_{d,t_n} = A_{d,t_n} + \sum_i^{n-1} a_{d,t_i} \quad \text{Eq. (A1)}$$

Where A_{d,t_n} (Bq) is the total activity measured at the time t_n in the reservoir, a_{d,t_i} is the activity measured in the sample at the time t_i.

$$\sigma_{Q_{d,t_n}} = \sqrt{{\sigma_{A_{d,t_n}}}^2 + \sum_i^{n-1} {\sigma_{a_{d,t_i}}}^2} \quad \text{Eq. (A2)}$$

In the same way, for the out-diffusion experiments, the cumulative total activity $Q_{d\_or\_up,t_n}$ in the downstream or the upstream reservoirs is:

$$Q_{d\_or\_up,t_n} = A_{d\_or\_up,t_n} - A_{d\_or\_up,t_0} + \sum_i^{n-1} a_{d\_or\_up,t_i} \quad \text{Eq. (A3)}$$

Where $A_{d\_or\_up,t_0}$ is the activity remaining in the downstream or upstream reservoir after the renewal of the solutions.

$$\sigma_{Q_{d\_or\_up,t_n}} = \sqrt{{\sigma_{A_{d\_or\_up,t_n}}}^2 + {\sigma_{A_{d\_or\_up,t_0}}}^2 + \sum_i^{n-1} {\sigma_{a_{d\_or\_up,t_i}}}^2} \quad \text{Eq. (A4)}$$

A_{d,t_n} is defined as: $A_{d,t_n} = \frac{a_{d,t_n} \times M_d}{m_{d,t_n}}$ Eq. (A5)

Where M_d is the total mass of the solution in the downstream reservoir (g) and $m_{d,tn}$ is the mass of the collected solution (g).

In the activity calculation, the errors $a_{d,t_{n-1}}$ induced by $m_{d,tn-1}$, and M_d are integrated in the error associated to A_{d,t_n} as:

$$\sigma_{A_{d,t_n}} = f(\sigma_{M_d}, \sigma_{a_{d,t_{n-1}}}, \sigma_{m_{d,t_{n-1}}}) \quad \text{Eq. (A6)}$$

Applying the formulae of error propagation to this equation, one obtains:

$$\sigma_{A_{d,t_n}} = \sqrt{\left(\frac{\partial A_{d,t_n}}{\partial a_{d,t_{n-1}}}\right)^2 \cdot \sigma^2_{a_{d,t_{n-1}}} + \left(\frac{\partial A_{d,t_n}}{\partial m_{d,t_{n-1}}}\right)^2 \cdot \sigma^2_{m_{d,t_{n-1}}} + \left(\frac{\partial A_{d,t_n}}{\partial M_d}\right)^2 \cdot \sigma^2_{M_d}} \qquad \text{Eq. (A7)}$$

Hence:

$$\sigma_{A_{d,t_n}} = A_{d,t_n}\sqrt{\left(\frac{1}{a_{d,t_{n-1}}}\right)^2 \cdot \sigma^2_{a_{d,t_{n-1}}} + \left(\frac{1}{m_{d,t_{n-1}}}\right)^2 \cdot \sigma^2_{m_{d,t_{n-1}}} + \left(\frac{1}{M_d}\right)^2 \cdot \sigma^2_{M_d}} \qquad \text{Eq. (A8)}$$

Finally, the cumulative activities for HTO and ^{36}Cl in downstream for reacted chalk and kaolinite were plotted with the associated certainties. The resulting curves were fitted to obtain minimum, maximum and best fits for each curve.

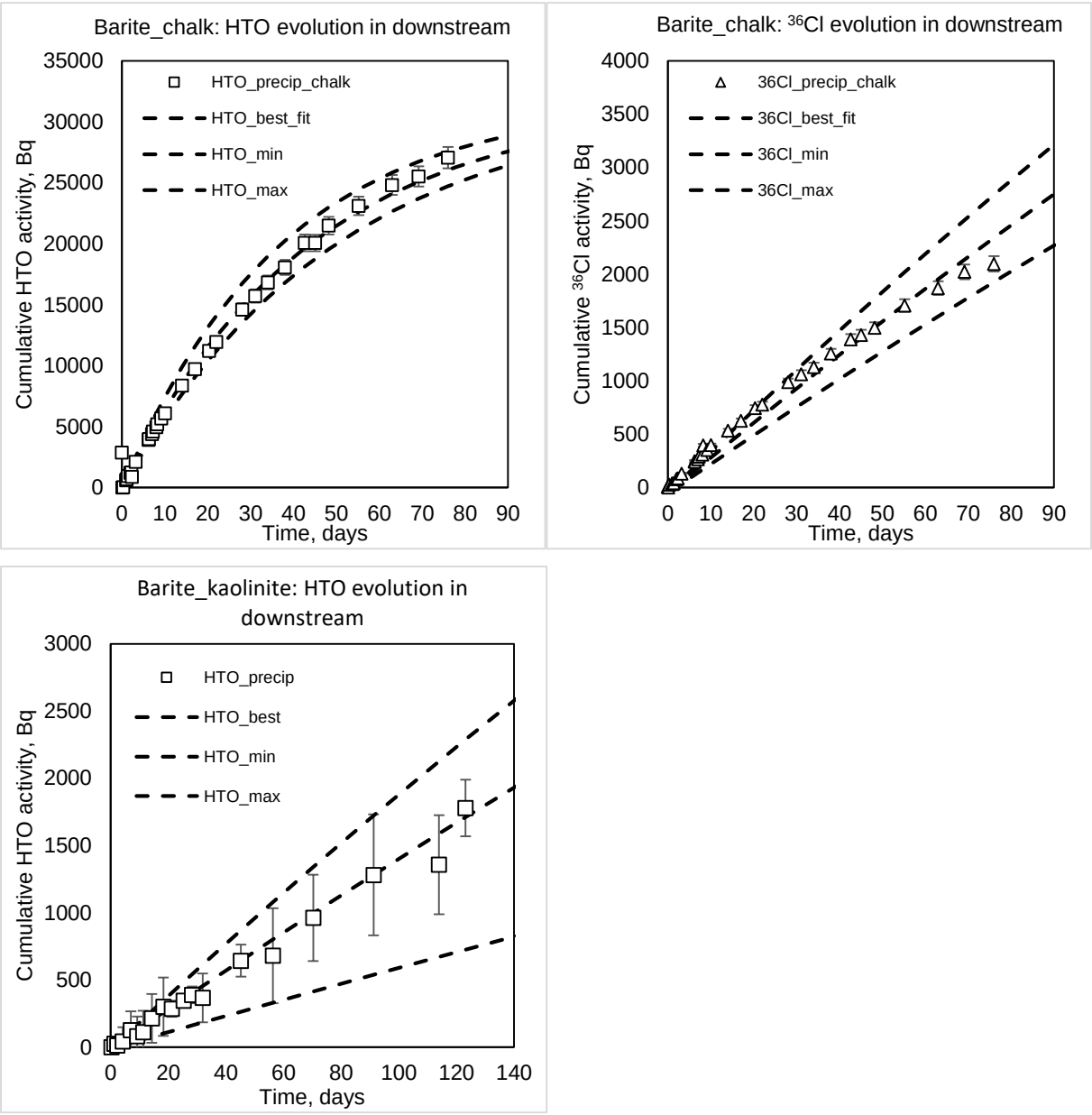

Figure S6: Experimental diffusive curves fitted with I-mode to calculate the diffusive parameter error range that are determined from the error bars of the experimental activity data, and the corresponding simulated cumulative curves[10]

[10] The HTO diffusive curve for chalk case is reported in (Rajyaguru et al., 2019).

Table-S1: Effective diffusion coefficients of HTO and ^{36}Cl for chalk and HTO for kaolinite obtained by I-mode fitting for diffusive curves with associated errors in Figure-S6

Total sample			
	Chalk HTO	36Cl HTO	Kaolinite,HTO
$D_{e,best}$	13.5	1.1	0.15
$D_{e,min}$	11.5	0.9	0.06
$D_{e,max}$	17.5	1.3	0.21

Table-S2: Diffusion coefficients of HTO and ^{36}Cl for chalk and HTO for kaolinite in reacted zones of different zones calculated using best, minimum and maximum effective diffusion coefficients from Table-S1

Reacted zone				
Chalk HTO	Thickness of reacted zone	$D_{e,best}$ x 10^{-11}	$D_{e,min}$ x 10^{-11}	$D_{e,max}$ x 10^{-11}
	1mm	2.87	2.72	4.19
	500µm	1.48	1.41	2.2
	300µm	0.9	0.6	1.06
Chalk 36Cl	Thickness of reacted zone	$D_{e,best}$ x 10^{-11}	$D_{e,min}$ x 10^{-11}	$D_{e,max}$ x 10^{-11}
	1mm	0.17	0.14	0.25
	500µm	0.086	0.07	0.12
	300µm	0.052	0.042	0.076
KaoliniteHTO	Thickness of reacted zone	$D_{e,best}$ x 10^{-11}	$D_{e,min}$ x 10^{-11}	$D_{e,max}$ x 10^{-11}
	1mm	0.15	0.006	0.22
	2mm	0.31	0.12	0.44
	3mm	0.46	0.18	0.66

Table-S3: Residual porosity calculated at different thickness of chalk and kaolinite samples

Porosity calculations	Selected Thickness	Porous volume cm^3	Barite volume cm^3	%residual Porosity
Chalk HTO	0.65	2.50	0.14	0.425
	1mm	0.855	0.14	0.285
	500µm	0.427	0.14	0.121
	300µm	0.256	0.14	0.044
Kaolinite HTO	1 cm	0.636	0.00182	0.355
	1mm	0.0636	0.00182	0.331
	2mm	0.127	0.00182	0.345
	3mm	0.19	0.00182	0.355

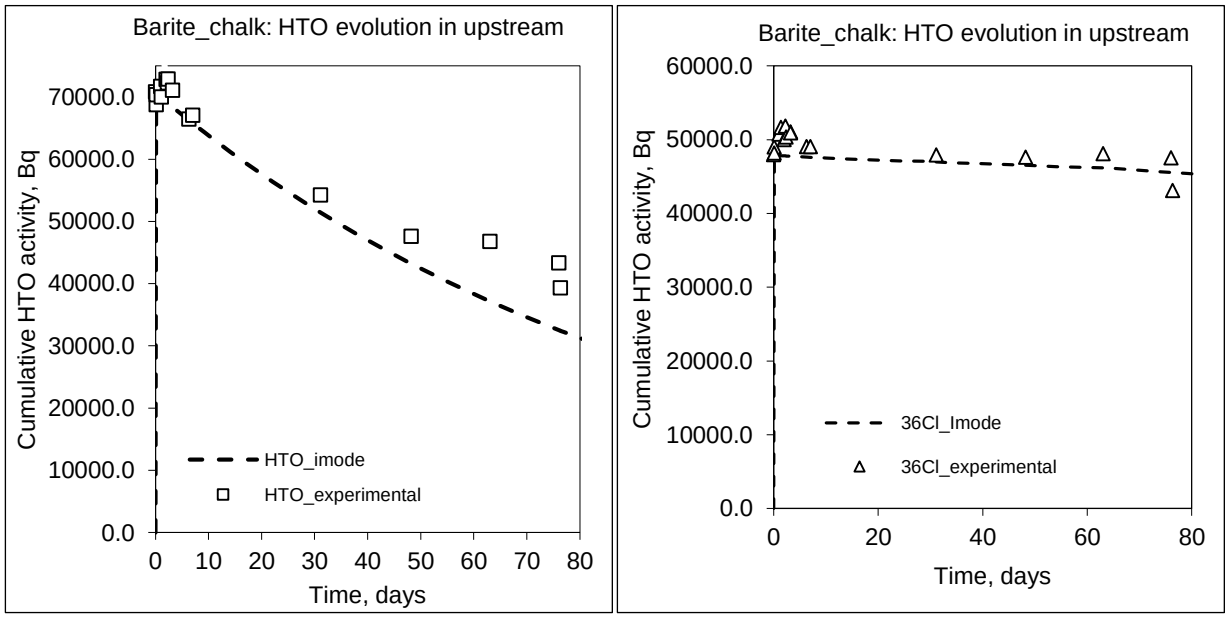

Figure S7: HTO and 36Cl evolution in upstream: HTO diffusive curve clearly shows the activity decrease in upstream, no activity decrease for 36Cl is observed after 80 days since its injection

Chapter-2.3: Barite precipitation in Compacted Illite

RÉSUMÉ

Les roches naturelles sont complexes tant au niveau de leur structure poreuse que de leur composition minéralogique, contenant et des minéraux dont les surfaces sont chargées négativement comme l'illite et la smectite, et des minéraux de surface quasi-neutre comme les quartz, les minéraux carbonatés, *etc*. Cette complexité rend de fait difficile leur étude dans une première approche. C'est pourquoi, pour évaluer de façon plus pertinente l'impact de différents paramètres sur la précipitation, différents matériaux modèles ont été utilisés ici : chacun portant une propriété des roches argileuses consolidées. Dans ce chapitre, des essais de diffusion réactive ont été réalisés en induisant une précipitation de barytine au sein d'échantillons d'illite compactée. De manière à simplifier le système et avoir un meilleur contrôle de la précipitation de barytine, l'argile a été pré-conditionnée sous forme de césium. Cette approche expérimentale a été envisagée afin de répondre à la question suivante : « Est-ce qu'un même type précipité peut conduire à un colmatage de même efficacité s'il opère dans des matériaux poreux de porosité similaire mais de charge de surface différentes ? ». En outre, les résultats des expériences sur la craie et la kaolinite ont montré que la barytine néoformée devait également avoir des charges de surface négatives eu égard au comportement distinct de HTO et de $^{36}Cl^-$. Aussi, des essais de diffusion avec ces deux traceurs ont également été réalisés pour évaluer le possible impact de la charge de surface de la barytine sur l'exclusion des anions dans l'illite.

1 Materials and Methods

1.1 Illite purification, conditioning and compaction

The compacted samples for this study were prepared using Illite du Puy located in Massif Central, France. The unpurified clay rock in its natural form contains 70 wt% of illite, 20 wt% of calcite, 5 wt% of kaolinite and 5 wt % of quartz (Poinssot, Baeyens, & Bradbury, 1999).The carbonate phases and quartz were removed from the clay by series of washing with 0.1 M HCl and passing the solution from sieve of mesh size 69 µm. The clay phase recovered from acidic solution was then washed repeatedly with MilliQ water. The final clay-water solution was centrifuged to obtain pure illite. The cation exchange capacity (CEC) for pure illite was already measured in literature and is equal to 225 meq.kg^{-1} (Altmann et al., 2015)(Poinssot et al., 1999).

In our study, the reactive diffusion experiments are carried out using a counter diffusion setup: two reactants independently diffusing from counter reservoirs meet in sample pores to generate mineral precipitation. In a sample possessing neutral pore surface, the pore network will not alter the diffusion of both cations and anions in reference to water tracer diffusive behavior. However, the pore surface of compacted illite (in pure form) possesses permanent negative surface charge. Thus, in our setup, on one surface of the sample there is strong adsorption of cations and at the counter surface there is strong exclusion of anionic species. In such situation, the anions will diffuse through the anionic accessible porosity to the zone where cations are strongly adsorbed. In this case, most of the mineral may precipitate at one surface of the sample and consequently generate uninterpretable dataset. For this reason, in the first step, the clay was conditioned with cesium in order to reduce the affinity of barium towards the clay surface. For that purpose, the protocol detailed in (Altmann et al., 2015) was used. In this protocol, a constant pH 3.5 is maintained by addition of 5×10^{-2} M Cs-formiate/formic acid buffer. Subsequently the clay is washed with 1 M CsCl (4 times; no buffer added). Finally, the conditioned clay was with MilliQ water to remove excessive CsCl. A fine grained and homogeneous dry material obtained by freeze-drying was then stored at 96% relative humidity in a closed chamber at controlled temperature of 40°C. Since illite clay has higher affinity for the monovalent cesium ion than divalent barium ion, this conditioning would reduce the adsorption extent of barium.

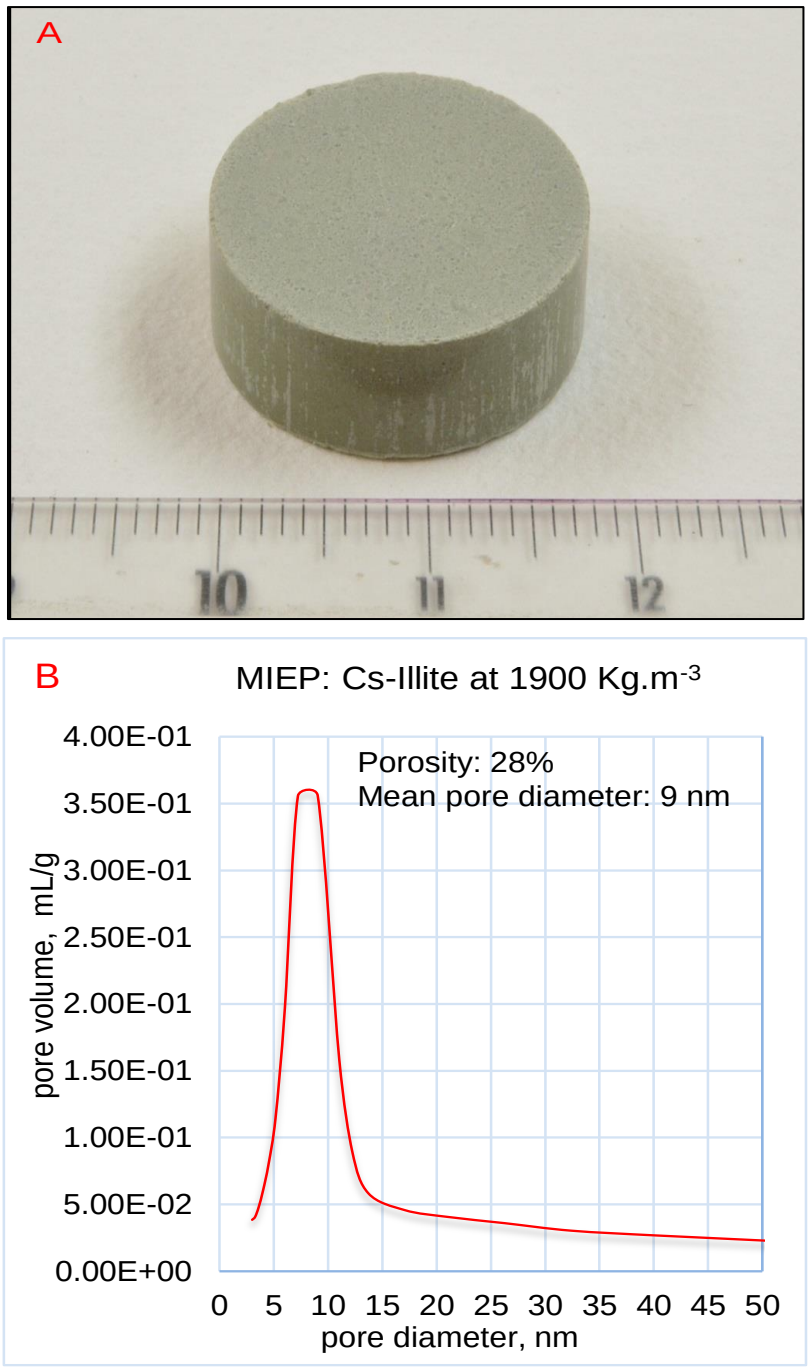

Figure 1A: compacted illite sample at dry density 1900 kg.m-3, 1B: Pore size distribution for compacted illite sample

Finally, as shown in Figure 1A, this powder was used to prepare four compacted samples at bulk dry density 1900 kg.m^{-3} for this study. Three samples were dedicated for diffusion and reactive diffusion studies and the fourth sample was dedicated for determining total accessible porosity and mean pore size. This was achieved by means of Mercury Intrusion and Extrusion Porosimetry (MIEP) characterization using a Micromeritics Autopore III 9420 apparatus. The total porosity and mean pore throat derived from this analysis are 29% and 9 nm. The pore size distribution of compacted illite sample from mercury intrusion-extrusion results is plotted in Figure 1B.

1.2 Diffusion experiments

In this study, the experiments were carried out using through-diffusion technique (Berthe, Savoye, Wittebroodt, & Michelot, 2011; Putnis & Fernandez-Diaz, 1990; S. Savoye, Beaucaire, Grenut, & Fayette, 2015). The general sequence used is as followed:

1. Determination of the diffusive parameters for tritiated water (HTO) and ^{36}Cl tracers through intact materials (i.e., before precipitation),

2. Launching of the reactive diffusion experiments by injecting barium and sulfate in the counter-diffusion reservoirs,

3. Determination of the diffusive parameters for HTO and ^{36}Cl through reacted materials, when chemical equilibrium was almost achieved, in order to assess the barite precipitate impact on their diffusive behavior.

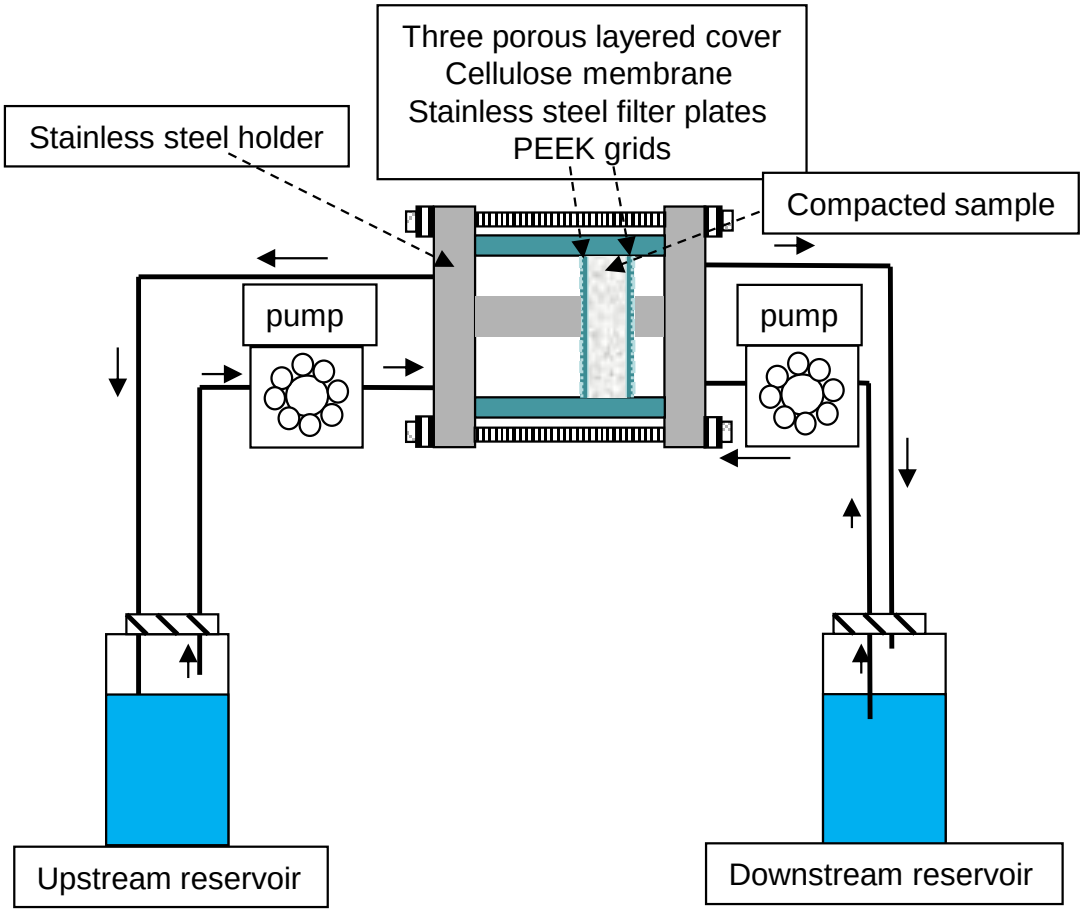

Figure 2: Through diffusion setup used for diffusion and reactive diffusion studies for compacted cesium-illite samples

The schematic diagram of diffusive cell is presented in Figure 2 **(**(Tertre et al., 2018), (Sébastien Savoye, Frasca, Grenut, & Fayette, 2012), (Glaus, Frick, Rossé, & Loon, 2010)**)**. This setup consists of a PEEK diffusion cell of inner diameter of 18.75 mm and two aqueous reservoirs (i.e., an upstream reservoir and a downstream reservoir). Using a peristaltic pump (Ismatec), the solutions of the upstream and downstreams reservoirs are homogenized. Note that the body of the diffusion cell is made of PEEK in order to allow for the characterization of the illite sample by means of X-Ray microtomography during the experiment. Three diffusion setups of this kind were prepared by directly compacting Cs-illite powder in the diffusion cell at a bulk dry density of 1900 $kg.m^{-3}$ (i.e., porosity). This is based on the dry mass of the solid placed in the cell and the volume of the cell, leading to a thickness of 6 mm. Before beginning the diffusion experiments, it is necessary to ensure homogeneous supply of solution to the surface of the sample (Tertre et al., 2018). Thus, before closing the diffusive cell with stainless steel covers, each face of the sample

is covered with three porous layers in the following order: Whatman cellulose nitrate membrane filters (manufactured by GE healthcare) of 0.8 µm mesh, then stainless-steel filter plates (pore diameter 10 µm from MOTT industrial division), and finally two grids (nominal spaces of 280 & 450 µm for monofilaments with diameters equal to 120 & 200 µm). Finally, using ascendant capillary method (Tertre et al., 2018), air from the compacted samples was removed after which the samples were equilibrated with 0.1 M CsCl solution. Due to the small size of the samples, the equilibration step was achieved in two weeks.

The first diffusive cell labelled as ILL-A was firstly used to acquire diffusion coefficients of tritiated water (HTO) and chloride-36 (^{36}Cl) for 70 days and finally to acquire the diffusive parameters of ^{133}Ba at intact conditions for 70 days. In the second and third cell labelled as ILL-B and ILL-C barite precipitation experiments were launched. ILL-B was used for chemistry monitoring in reservoirs and precipitation impact on diffusivity of HTO/^{36}Cl after 70 days of experimental time. Finally, ILL-C was used to determine the 3D-evolution of barite precipitates in illite porous space after 30 days and 140 days of precipitation step using X-ray microtomography.

1.2.1 HTO/^{36}Cl and ^{133}Ba diffusivity at intact conditions

After equilibration step, the upstream and downstream solutions of ILL-A were completely renewed by 50 mL of fresh 0.1 M CsCl solution. The upstream was spiked with 6.5 µL of tritiated water (labelled CERCA ELSB50 n°80212/D, source activity 7599 MBq.L^{-1}) and 32 µL of ^{36}Cl (labelled E&Z 1760-100-1 source activity 767.32 MBq.L^{-1}.) to obtain initial volumetric activity of 1 MBq.L^{-1} (HTO) and 0.5 MBq.L^{-1}(^{36}Cl) respectively. Evolution of HTO and ^{36}Cl activity was measured by periodic sampling in both reservoirs. After this step, out-diffusion of HTO and ^{36}Cl was carried out by completely renewing the upstream and downstream bottles with 50 mL of fresh 0.1 M CsCl solution. This step was carried out for 1 week to completely withdraw the tracers from sample pores. After out-diffusion step, the upstream solution was renewed with 50 mL of fresh 0.1 M CsCl solution. This solution was spiked with 100 µL of ^{133}Ba (ELSB45 CERCA N°5245 and source activity 1.78 MBq.L^{-1}) to obtain initial volumetric activity of 1.7 kBq.L^{-1}. Conversely, the downstream solution was renewed with 50 ml of fresh 0.1 M CsCl solution. Then, evolution of ^{133}Ba activity was measured by periodic sampling in both reservoirs.

1.2.2 Barite precipitation experiment

Barite precipitation experiment in cell ILL-B and ILL-C were launched by replacing upstream reservoir with 50 mL of fresh 0.1 M CsCl solution containing 20 mM of $BaCl_2$ (*resp* Cs_2SO_4 in

downstream at same concentration). At the beginning of experiment, the upstream reservoir of ILL-B was spiked with similar amount of ^{133}Ba from same source and initial volumetric activity used in ILL-A case. The monitoring of activity decreases of this tracer in upstream for the total time of reactive diffusion step was carried out by periodically sampling the upstream solution. From the initial conditions of upstream solution, the ratio of barium concentration (mol. L^{-1}) and ^{133}Ba specific activity (Bq. mL^{-1}) is known. Using this ratio, the measured activity at each sampling was converted into stable barium concentration. In downstream reservoir of ILL-B cell, the sulfate concentration decrease for total experimental time was measured by periodic sampling of 100 µL of downstream reservoir solution and diluting it with 1.9 mL of MilliQ water. The concentration in each of the diluted sampled solution was measured using Ionic Chromatography measurements (Metrohm 850 professional IC, equipped with ASup 7 150/4 column). At the end of experiment, by means of initial and final concentrations of each ion, the amount of barite precipitated into the porous sample was then estimated. Knowing the molar volume of barite (*i.e.* 0.019 mol.cm^{-3}) and the porous volume of the sample, the porosity reduction due to precipitation was finally calculated.

1.2.3 Precipitation impact on diffusivity

To determine precipitation impact on diffusivity, HTO and ^{36}Cl were injected in the upstream reservoir of ILL-B after 70 days of precipitation experiment. The source, volumetric activity of both tracers in upstream and the periodic sampling protocol in both reservoirs were the same as the ones used for ILL-A. The activity evolution in downstream of ILL-B was followed for 70 days. In the upstream of cell ILL-C after 140 days of reactive diffusion step, 44 µL of pure deuterated water (HDO) was injected. At each sampling time, 100 µL of solution was withdrawn from upstream and downstream reservoirs. The HDO concentration in each solution was measured using a cavity-ringdown laser absorption spectrometer (Los Gatos Research LGR 100).

1.2.4 Protocols used for determining activity of radioisotopes

For HTO/^{36}Cl activity measurement, following protocol was used: 100 µL of upstream and downstream solutions, each mixed with 900 µL of MillQ water and 4 ml of ultimagold scintillation liquid in a 5 ml scintillation bottle. The activities were measured using a liquid scintillation recorder Packard Tricarb 2500. For ^{133}Ba activity measurement following protocol was used: 100 µL of upstream solution mixed with 900 µL of MilliQ water in 5 mL gamma counting bottle. The activity measurement for each sampling was done using gamma counter (Packard 1480 WIZARD, USA).

1.2.5 Treatment of experimental diffusive results

The experimental activity dataset for both HTO and ^{36}Cl were interpreted numerically using Fick's second law for one-dimensional transport (Crank, 1975).

$$\frac{\partial C}{\partial t} = \frac{D_e}{\alpha}\frac{\partial^2 C}{\partial x^2} = \frac{D_e}{\phi + R_d \rho_{dry}}\frac{\delta^2 C}{\delta x^2} \qquad (1)$$

where C is the concentration in mol.m^{-3} (or activity Bq.m^{-3} in our case), t is the time in s, D_e is the effective diffusion coefficient in m^2.s^{-1}, $\alpha = \phi + R_d \rho_{dry}$ is the rock capacity factor, ϕ is the porosity, ρ_{app} is the bulk dry density in kg.m^{-3}, and R_d is the distribution ratio in m^3.kg^{-1}. The initial and boundary conditions for this through diffusion setup in a condition when the concentration in upstream reservoir is left free to decrease are as follows:

$$C(x,t) = 0 \text{ for } t = 0 \qquad (2)$$

$$C(x,t) = C_0 \text{ for } x = 0 \text{ at } t = 0 \qquad (3)$$

where C_0 is the initial concentration (or initial activity in Bq.m^{-3}) in the upstream reservoir at the injection time, L is the sample thickness (m) and l is the filter plate thickness (m). The total porosity and effective diffusion coefficient of these filter plates (equal to 28% and 2.3 x 10^{-10} m^2.s^{-1} for HTO and 2.0 x 10^{-10} m^2.s^{-1} for ^{36}Cl) are taken from literature (Tertre et al., 2018), (González Sánchez et al., 2008). Using the initial and boundary conditions from equation 2 and 3, the semi-analytical solutions to determine the flux in downstream reservoirs is well noted in literature (Crank, 1975), (Moridis, 1998), (Didierjean, Maillet, & Moyne, 2004), (Descostes et al., 2008). The semi-analytical solutions are implemented in CEA's tool called Interpretation Model of Diffusion Experiments (Radwan, Hanios, & Grenut, 2006) (I-Mode). Finally, using I-Mode the experimental data were reproduced numerically at certain values of effective diffusion coefficient.

For all of the tracers used in ILL-A, ILL-B and ILL-C, the associated uncertainties in cumulative activity and cumulative concentration data for downstream were calculated using the equations from Gaussian error propagation method. These equations are detailed in Appendix-I. These associated errors were then plotted with the experimental data over time. Using I-Mode, three modeled curves were reproduced: two to accommodate the minimum and maximum range of error, and third to reproduce the activity data. These three curves represent the minimum, maximum and optimum data fit using I-Mode. The effective diffusion coefficient values obtained

for minimum and maximum fit present the error range in measurements of effective diffusion coefficients.

1.3 Imaging of barite precipitates in Illite sample

The 3D evolution of barite precipitates in compacted illite was determined after 30 days and 140 days of reactive diffusion experiment in ILL-C cell. At the day of measurement, the circulation of reactants in cell was temporarily stopped. The whole diffusion cell was disconnected from reservoirs and was placed in an X-ray micro-tomograph (µCT) Skyscan 1272, Brucker apparatus. After imaging, the cell was connected back to reservoirs to continue the barite precipitation process.

1.4 Barium sorption on Cs-illite:

The adsorption of Ba^{2+} on Cs-illite was measured by means of batch experiments. This was done by firstly spiking 20 mL of solution containing 20 mM $BaCl_2$ reactant and 0.1 M CsCl as background electrolyte with 25 µL of ^{133}Ba source (source activity 1.78 $MBq.L^{-1}$ and source CERCA ELSB45 n°5245). Then in each batch tube, 1 g of Cs-illite was suspended with 5 mL of this spiked solution. After one week the solution was centrifuged at 15,000 rounds per minute from the clay and activity in the solution was measured using the same activity measurement protocol used for ILL-A. The distribution coefficient $R_{d,\,133Ba}$ in $m^3.kg^{-1}$ was determined using equation-4.

$$R_{d,133Ba} = \frac{V}{m}\frac{A_0 - A_f}{A_f} \qquad (4)$$

where A_o (Bq) is the initial activity measured in solution, A_f(Bq) is the final activity remaining in the centrifuged solution, V (m^3) is the volume of solution in centrifuge tube, and m (kg) is the mass of dried illite powder.

2 Results

2.1 HTO, ^{36}Cl and ^{133}Ba diffusive parameters at intact conditions

The evolution of the experimental activity data with associated errors for HTO, ^{36}Cl and ^{133}Ba in upstream and downstream reservoir of ILL-A are reported in Figure 3,Figure 4,and Figure 5 respectively. In each figure, experimental data are reproduced using I-Mode with diffusive parameter values given in Table 1 as the best fit values. Moreover, in Figure 3,Figure 4, and Figure

5, two additional modeled curves are reported, bracketing the experimental data and their associated error bars. These curves allowed us to have an estimation of the associated uncertainties in diffusive parameters for each tracer given in Table 1.

The analysis of Table 1 shows how the charge of the species clearly influences their diffusive behavior through a charged porous medium. Compared to the neutral species, i.e. HTO, the anionic one, i.e. ^{36}Cl, has access to only two third of the total porosity, inducing a reduction of its D_e value. Conversely, cationic species, i.e. ^{133}Ba, exhibits a quite high diffusion coefficient value, especially when converted in diffusivity, i.e. D_e over the D_0 ratio (Table 1). In that case, diffusivity value is almost twice the HTO diffusivity one, indicating the occurrence of the enhanced diffusion process, already extensively described in literature (ref…). Moreover, note that the distribution coefficient measured in dispersed illite led to a value ($R_{d,133Ba}$ = 3x10^{-3} m^3.kg^{-1}) in a very good agreement with the value estimated from diffusion experiment (Table 1).

The comparison with literature data is complicated by the fact that the current experiments are the first ones performed through illite conditioned under cesium form. Only were through-diffusion experiments for HTO and ^{36}Cl carried out through sodium and calcium conditioned illite compacted at the same dry density by (González Sánchez et al., 2008), (Glaus et al., 2010). These authors determines $D_{e\ HTO,\ Na\text{-}illite}$ 13×10^{-11} m^2.s^{-1} and $D_{e\ HTO,\ Ca\text{-}illite}$ = 9.4×10^{-11} m^2.s^{-1}. This means that, at a same dry density, the effective diffusion coefficient of water tracer for Na-illite is 1.4 time larger compared to Ca-illite, and 3.3 time larger compared to Cs-illite. Note that for ^{36}Cl, $D_{e\ Cs\text{-}illite}$ and $D_{e\ Na\text{-}illite}$ are similar ($D_{e,36Cl,Na\text{-}illite}$ = 2.8×10^{-11} m^2.s$^{-1,}$ (Glaus et al., 2010)). Such a difference in HTO diffusive behavior was explained by González Sánchez et al. (2008) by the differences in hydration or solvation of the Na and Ca cations (González Sánchez et al., 2008). In our case, cesium is known as being very weakly bonded to its hydration shell compared to calcium, and especially sodium ((Hartkamp & Coasne, 2014)). Therefore, we can assume that the status of the water interacting with the compensating cation adsorbed onto the clay surface can directly influence the diffusive rate of HTO. Nevertheless, this point is still under debate.

Table 1: Diffusion coefficients of HTO, ^{36}Cl at intact(section 2.1) and reacted(section 2.5), and ^{133}Ba (section 2.1) for intact illite conditions obtained at minimum, maximum and best fits using I-Mode

	cell	Tracer	$D_{e,best}$ $\times 10^{-11}$ $m^2.s^{-1}$	$D_{e,min}$ $\times 10^{-11}$ $m^2.s^{-1}$	$D_{e,max}$ $\times 10^{-11}$ $m^2.s^{-1}$	$D_{e,best}/D_0$ □	□□□□□□, -	R_d $kg.m^{-3}$
Intact	IIII-A	HTO	3.9	3.1	4.5	0.0195	0.28	0
	IIII-A	^{36}Cl	2.5	2	3.5	0.014	0.18	0
	IIII-A	^{133}Ba	2.8	2.5	3.2	0.037	6.2	3.1
Reacted	IIII-B	HTO	5	4	5.9			
	IIII-B	^{36}Cl	4	3	4.8			
	IIII-A	HDO	3.9	3.2	4.5			

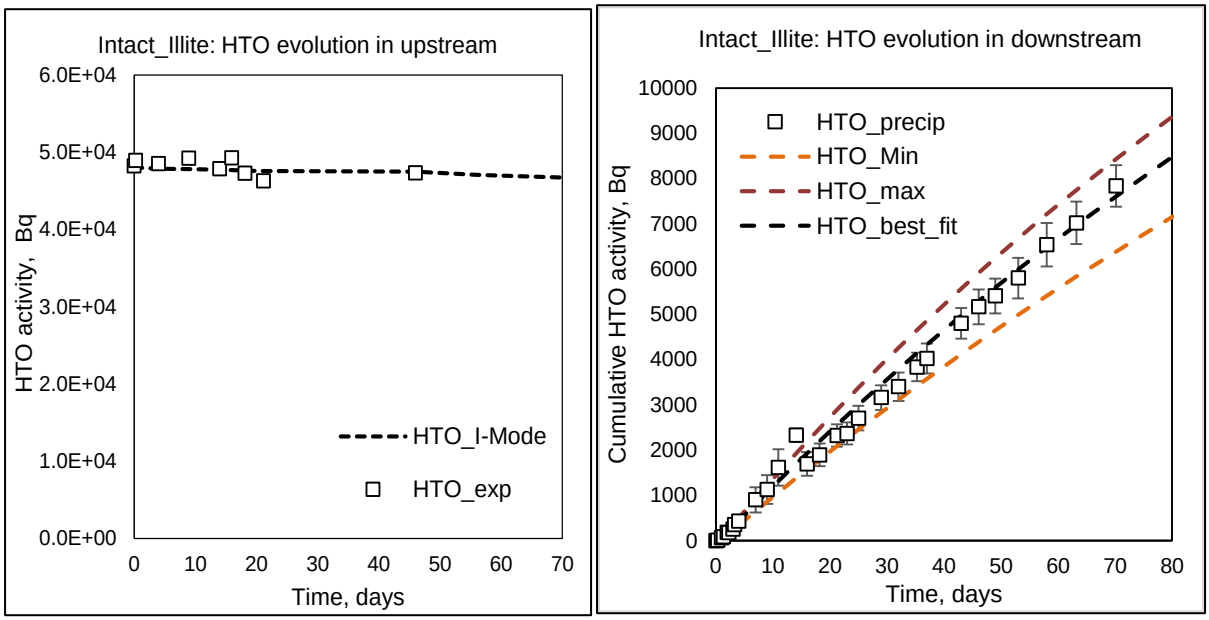

Figure 3: HTO cumulative activity evolution in upstream and downstream for intact illite. The cumulative activity values measured in downstream reservoir are reproduced using I-Mode to obtain error range in diffusion coefficients

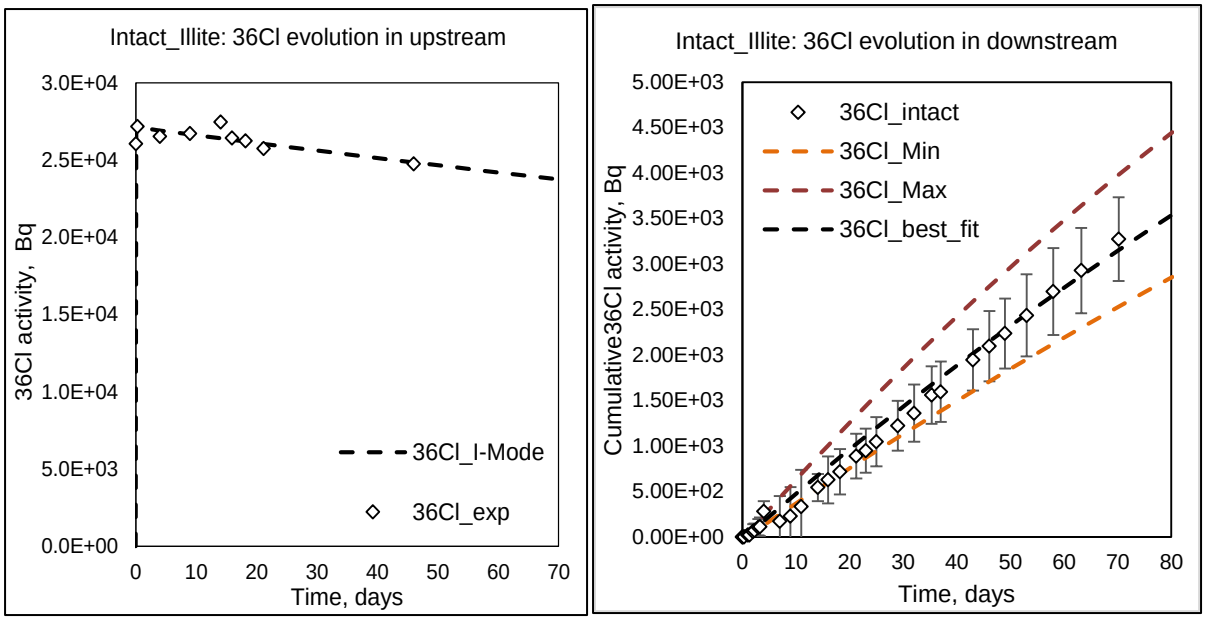

Figure 4:[36]Cl cumulative activity evolution in upstream and downstream for intact illite. The cumulative activity values measured in downstream reservoir are reproduced using I-Mode to obtain error range in diffusion coefficients

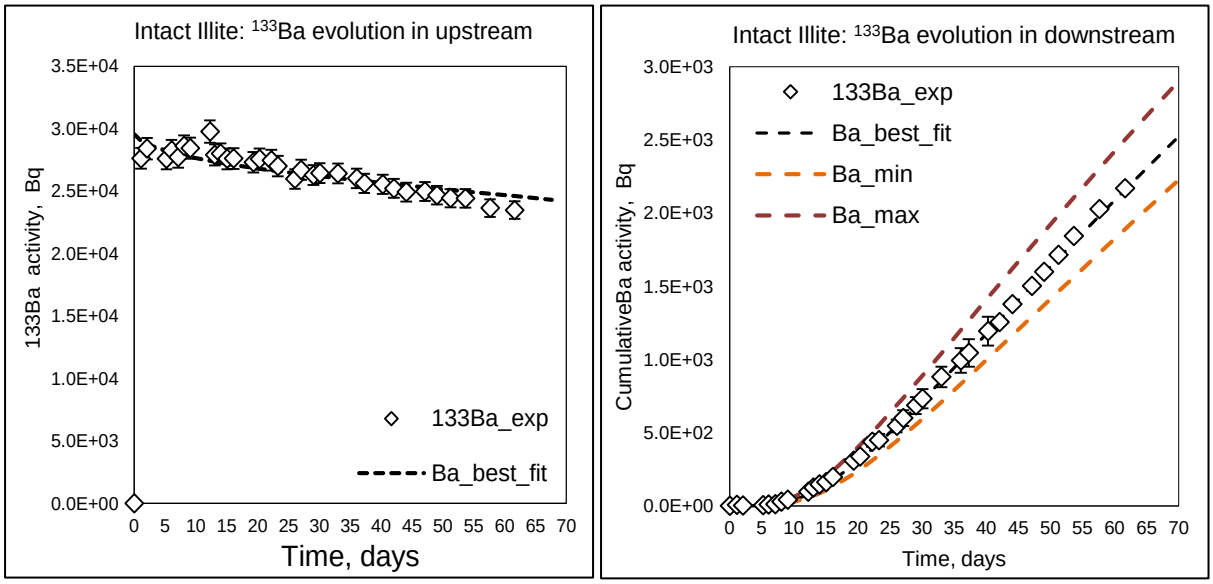

Figure 5: [133]Ba cumulative activity evolution in upstream and downstream for intact illite. The cumulative activity values measured in downstream reservoir are reproduced using I-Mode to obtain error range in diffusion coefficients

2.2 Evolution of barium and sulfate in response to precipitation

The evolution of the barium concentration in upstream reservoir of cell ILL-B is plotted in Figure 6. For comparison, a modeled curve of barium concentration decrease calculated from the intact case is also reported. This curve was obtained using the diffusion coefficient of barium for intact illite, sample thickness equal to 6 mm and the R_d value from batch experiments.

This figure shows a faster decrease in barium concentration in upstream under reactive diffusion compared to diffusion at intact illite in ILL-A. Using the R_d and $D_{e,\,^{133}Ba}$ from ILL-A study, the barium concentration decrease in Figure 6 was reproduced by I-Mode when the sample thickness was reduced to 1.2 mm instead of 6 mm. This shows that, in reactive diffusion, a zone just near the upstream surface of the sample is acting like a sink, which rapidly consumes all of the diffusing barium from upstream. The correct total amount of barium contributed to precipitation and adsorption in illite sample will be determined by abrasive peeling method. However, since this task is not performed for the moment, the amount of barium contributing to adsorption on clay surface and barite precipitation in illite sample remains unknown.

Similarly, the concentration decrease data in downstream of sulfate is also reported in Figure 6. This figure shows a lower concentration decrease compared to barium in upstream. In our study the diffusion behavior of sulfate under pure diffusive condition was not determined. Thus, a modeled curve for sulfate concentration decrease under pure diffusion was reproduced, using sample thickness equal to 6 mm and ^{36}Cl diffusion coefficient from ILL-A study. However, to model sulfate data in downstream for reactive diffusion, the D_e value was increased to $6x10^{-11}$ $m^2.s^{-1}$ and the sample thickness was decreased to 3 mm in I-Mode. Thus, compared to barium sulfate needs to diffuse across a larger distance in the sample before contributing to barite precipitation. The barium and sulfate evolution in upstream and downstream reservoirs for ILL-B clearly shows the asymmetry between their contributions to precipitation in illite experiment.

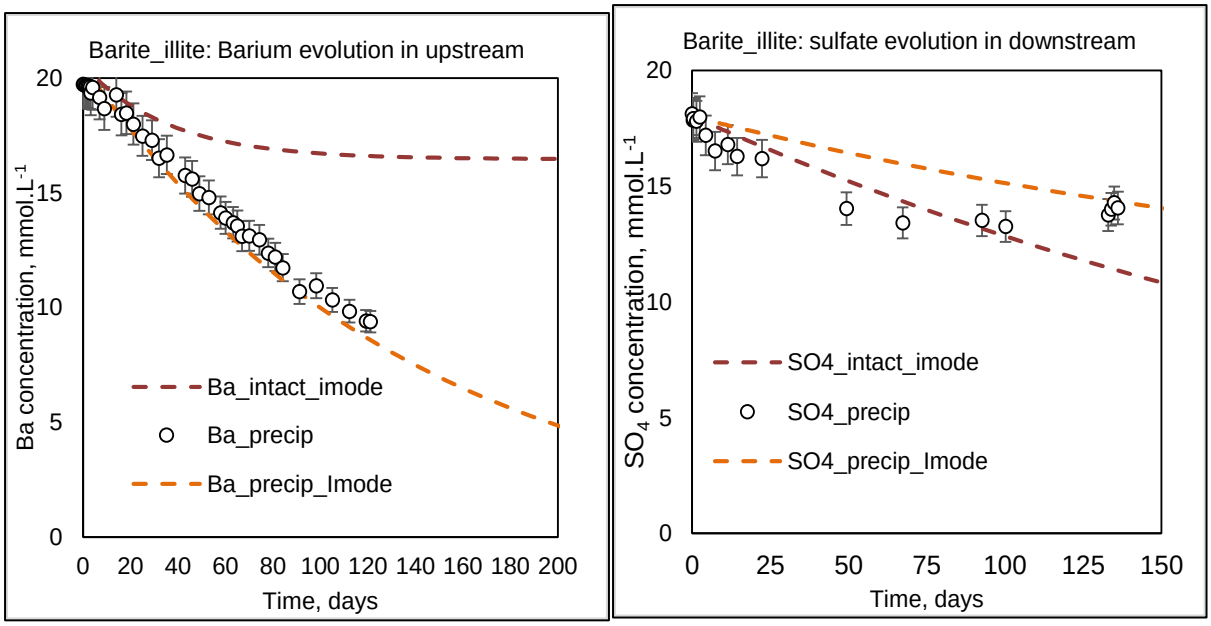

Figure 6: Ba and sulfate decrease is observed in reservoirs in response to barite precipitation in sample. The dashed lines are modeled curves obtained using I-Mode

2.3 Xray-µCT imaging

The 3D evolution of barite precipitates in illite sample of cell ILL-C after 30 days of reactive diffusion experiment are reported in Figure 7A and Figure 7C. Similarly, the evolution of these precipitates after 140 days of reactive diffusion experiment is reported in Figure 7B and Figure 7D respectively. These figures show that barite precipitated within two different zones in the cell: in precipitation plane closer to upstream (1.5 mm from the upstream surface) in the clay sample and at the interface between upstream face and PEEK filter. In our study, the compaction step was done as carefully as possible to have a homogeneous pore size distribution in the sample. However, the µCT images shows a tilted precipitation plane in the sample. In one half of precipitation plane significant amount of barite precipitation is observed, while a smaller amount of barite is observed in the other half. This means that the pore size distribution after compaction could not be totally homogeneous. Finally, the total amount of barite precipitated in both zones in illite sample cannot be quantified by means of µCT images. This is because the resolution of µCT images is 20 µm whereas barite precipitated in voids of nanometric scale size (between 9 nm and 100 nm). The acquisition after 140 days more or less shows no obvious evolution of precipitated zone located in the sample. However, a significant evolution at the interface between sample surface and filter is clearly observed. Finally, in both of the acquisitions an empty space is

observed in the reacted zone. No barite precipitation is observed in this empty space. In literature, illite du Puy contains some fraction of smectite. Thus, one of the possible explanations is that this empty space could be in fact the gel formed by the smectite mineral. Such gels are known to have very small nano-porosity thus inhibiting precipitation. However, to quantify whether this empty space is infact gel, a high-resolution scanning such as TEM, FIB-SEM are to be performed. These tasks will be carried out in future.

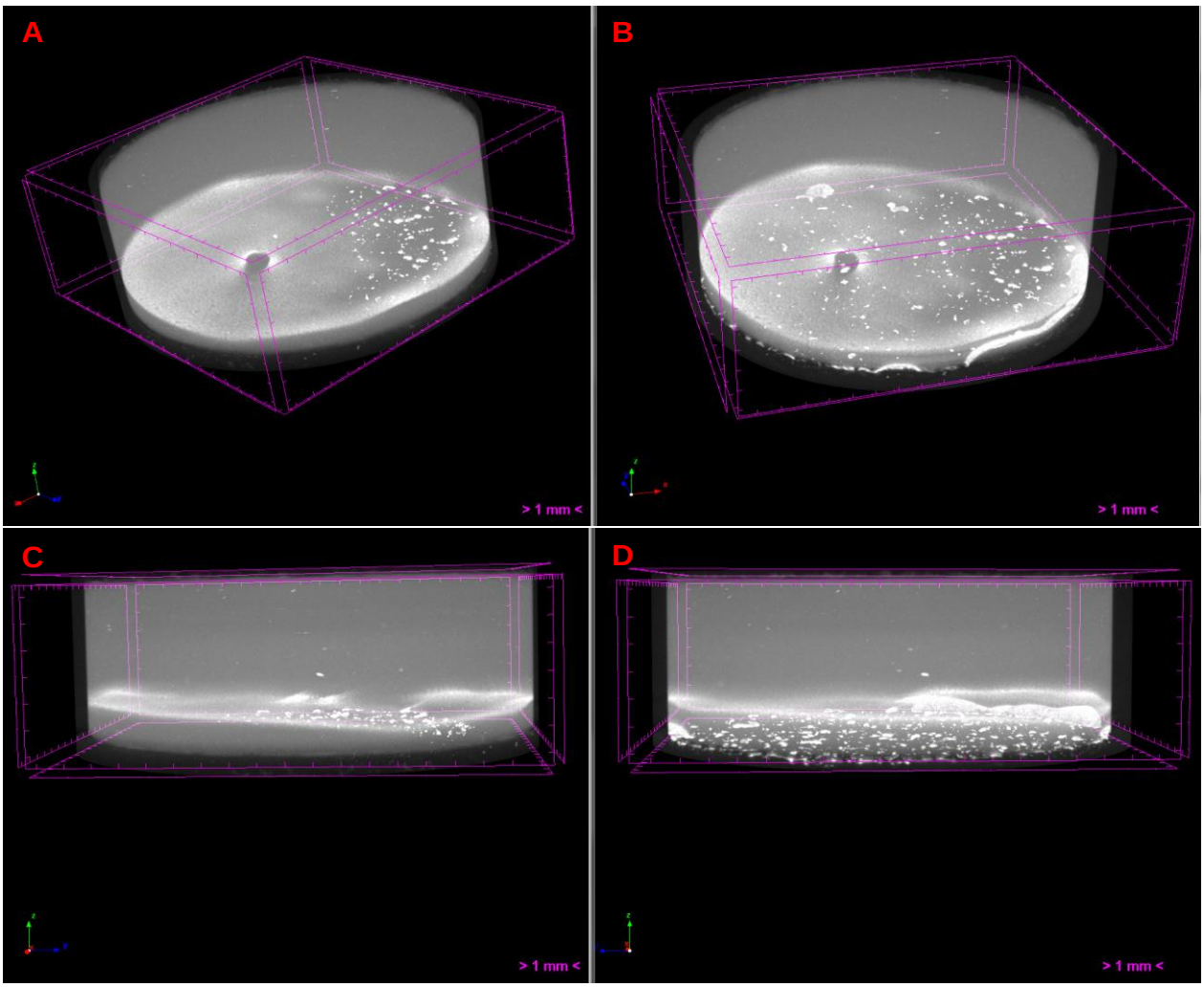

Figure 7A: Barite precipitated zone formed near the barium reservoir face of the illite sample after 30 days of precipitation; 7B: after 140 days no clear evolution in the precipitation zone is observed; 7C: At the interface between clay surface and PEEK filter, formation of barite precipitates can be observed after 30 days; 7D: At acquisition of 140 days the barite precipitates at the interface have evolved

2.4 Porosity reduction due to precipitation

In section 2.2, a clear asymmetry between barium and sulfate contribution to barite precipitation was observed. The µCT images (section 2.3) further showed barite precipitation in two zones: in illite sample and on the interface between upstream surface of sample and PEEK filter. Since the amount of barite precipitated at interface remains unknown, the porosity reduction from chemistry monitoring cannot be accurately calculated. Thus, a range of porosity decrease was calculated from initial and final concentrations of barium and sulfate. E.g. From chemistry monitoring, the total amount of barium and sulfate contribution to precipitation is equal to 0.61 mmol and 0.004 mmol respectively. Let us assume that out of these total amounts 50% of barium and sulfate contributed to precipitation in illite pores. Thus, from molar volume of barite, the total volume occupied by barite mineral is equal to 0.016 cm^3 and 0.00011 cm^3 respectively. From these volumes and sample pore volume, the residual porosity in sample is equal to 26.10 % and 27.99% respectively. A range of porosity decrease considering different percentage of barium and sulfate contribution to precipitation in sample are calculated in Table *2* respectively. These calculations show that although porosity reduction estimated by each reactant is very different, in all cases barite precipitation led to very small amount of total porosity reduction.

Table 2: Total volume of porous sample and amount of volume occupied by barite precipitates

Sample Porosity, %	***28***
Porous volume cm3	*0.46*
Barium mmol	*0.61*
Sulfate mmol	*0.004*
Molar volume cm3/mol	*52*

%Volume occupied by barite	*Barium* cm^3	*Sulfate* cm^3	*%Porosity reduction*	
			Barium	*Sulfate*
100	*0.031*	*0.00022*	*26.10*	*27.99*
75	*0.024*	*0.00016*	*26.57*	*27.99*
50	*0.016*	*0.00011*	*27.05*	*27.99*
25	*0.008*	*0.00005*	*27.52*	*27.997*
10	*0.003*	*0.00002*	*27.81*	*27.999*

2.5 *Precipitation impact on diffusivity*

The experimental activity data for HTO and ^{36}Cl in upstream and downstream of Ill-B are reported in Figure *8* and Figure 9. Similarly, the cumulative concentration data of HDO for ILL-C are reported in Figure 10. For all three cases, associated uncertainties in the cumulative activity were calculated using Gaussian error propagation equations from Appendix-I. The cumulative experimental data with associated uncertainties for downstream were modeled using I-Mode. Thus, for each tracer three modeled curves were generated: two resembling the error intervals and one resembling the best fit of the experimental data. The modeled curve at best fit was calculated by using generated an effective diffusion coefficient value for the given tracer and the modeled curves for the error range generated the error range in diffusion coefficient for each

tracer. These values for HTO, ^{36}Cl and HDO obtained using I-Mode from Figure 8, Figure 9 and Figure 10 are reported in Table 1. For HTO and HDO, the effective diffusion coefficients are similar to the HTO diffusion coefficient value obtained for intact illite case. Thus, barite precipitation shows no significant impact on diffusivity of water tracer after 70 and 140 days of precipitation experiment. For ^{36}Cl, Table 1 further shows that the effective diffusion coefficient of this tracer is closer to the value obtained at intact illite condition. Thus, barite precipitation shows no clear impact on the diffusivity of anionic tracer

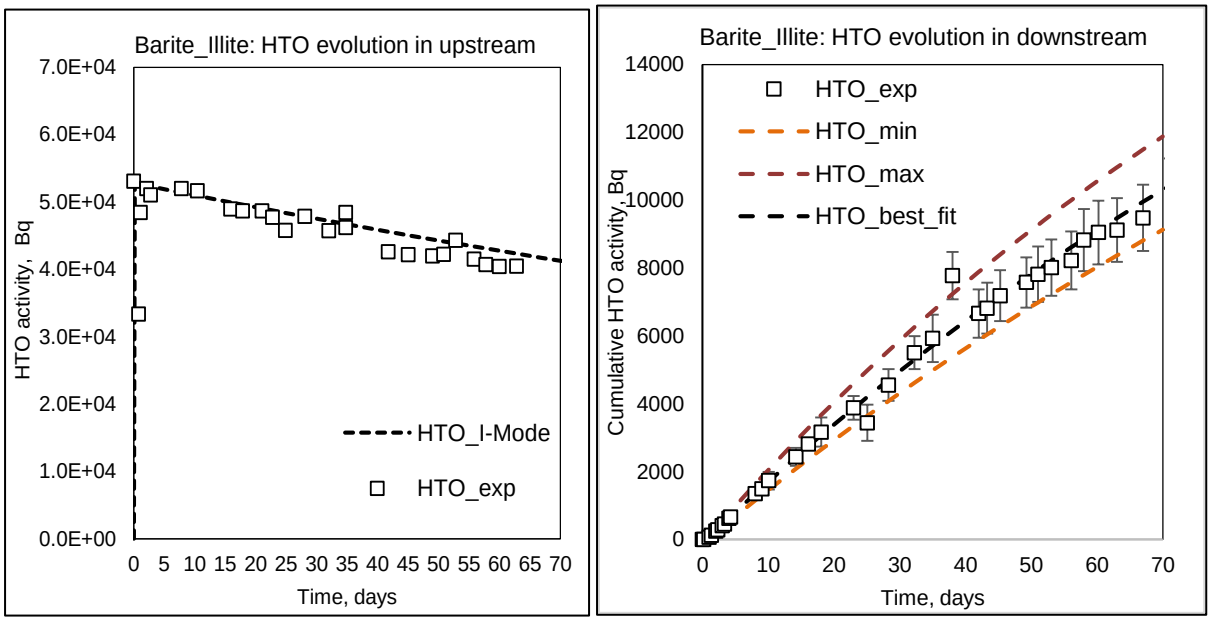

Figure 8: HTO cumulative activity evolution in upstream and downstream after 70 days of barite precipitation experiment in illite. The cumulative data of downstream are reproduced at minimum, best and maximum fits using I-Mode

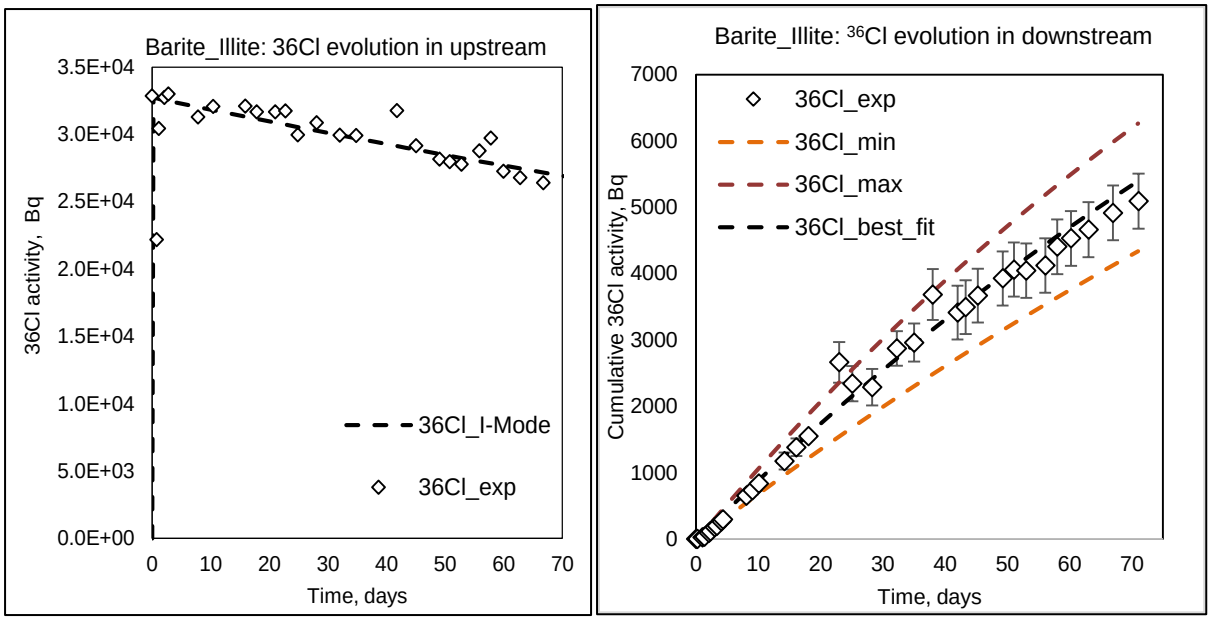

Figure 9: ^{36}Cl cumulative activity evolution in upstream and downstream after 70 days of barite precipitation experiment in ILL-B. The cumulative data of downstream are reproduced at minimum, best and maximum fits using I-Mode

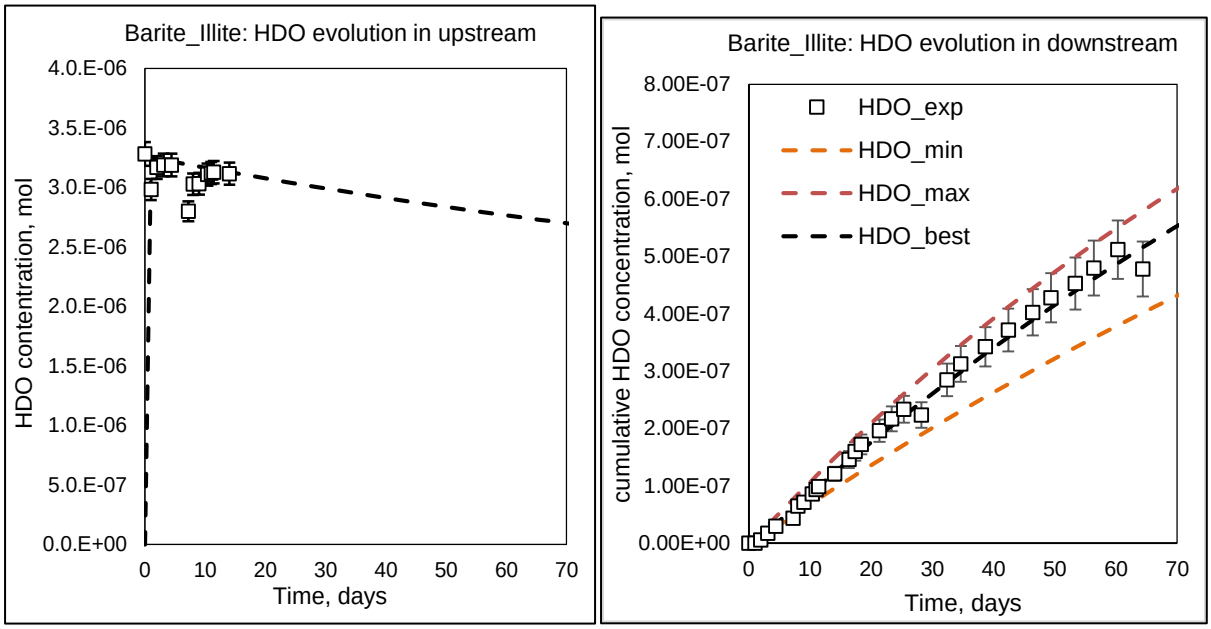

Figure 10: HDO cumulative concentration evolution in upstream and downstream after 140 days of barite precipitation experiment in ILL-C. The cumulative data of downstream are reproduced at minimum, best and maximum fits using I-Mode

3 Discussion

This study dealt with investigating the clogging impact on a proxy material that resembles a mean pore size and surface charge closer to consolidated claystones. These claystones are considered as potential host rock for radioactive waste disposal repository. Such proxy material was developed by compacting cesium-conditioned Illite du Puy at a dry density 1900 $kg.m^{-3}$. From mercury intrusion and extrusion porosimetry, the mean pore diameter and total porosity of this compacted sample was equal to 9 nm and 28%, respectively. At intact conditions, the effective diffusion coefficient of HTO was lower compared to Ca-illite and Na-illite. However, the effective diffusion coefficient for ^{36}Cl obtained in our study and the one obtained in literature on Na-illite are similar.

To study the evolution of barite precipitate in illite sample and to evaluate its impact on diffusivity, precipitation experiments were launched in two cells. The chemistry of reactants, sample geometry and volume of reservoirs were same for both cases. In one cell (ILL-B), the chemistry monitoring clearly showed asymmetry between the evolution of the two reactants, barium and sulfate in upstream and downstream reservoirs, and their contribution to precipitation in illite sample. Barium is involved both in barite precipitation process and adsorbed on the illite surface, contrary to sulfate, only contributing to barite precipitation. Nevertheless, the mass balance calculations showed a very small amount of anionic porosity decrease due to barite precipitation in illite sample: from 18% (intact anionic porosity) to 14%, calculated from sulfate evolution, when assuming (i) 1 mm as the barite precipitation thickness, as indicated by µCT images and (ii) no precipitation outside the sample. However, the µCT images obtained after 30 days showed that barite precipitated in two distinct zones: the ca. 1-mm thick front, located within the sample, near the upstream side and a second one, located at the interface between sample upstream face and filter plate. The µCT images obtained after 140 days showed no clear evolution within sample, but a significant increase of the amount of precipitated barite outside the sample. These observations indicate that the mass balance calculation overestimates the sulfate actually involved in barite precipitating within sample because some sulfate ions are able to diffuse across illite so as to precipitate in the counter reservoir with barium. Note that such barite precipitation outside the sample was never observed in the barite experiments performed into chalk and kaolinite. The fact that sulfate is able to cross illite sample without precipitating indicates that either barium species are not accessible anymore or barite precipitation is partially inhibited into the small pores of illite. The first hypothesis contradicts the fact that cation exchange process is instantaneous and

reversible and that there is still barium in solution, capable of being involved in precipitation. Therefore, it seems that the inhibition of barite precipitation has to be considered.

After 70 days of barite precipitation experiment, HTO and ^{36}Cl tracer were injected in upstream reservoirs and their activity evolution was followed in the downstream one. The effective diffusion coefficient values obtained after fitting cumulative activity data for each tracer showed no clear impact of barite precipitation on their diffusivity. In the second cell (ILL-C), HDO was injected in upstream after 140 days of barite precipitation and its cumulative concentration evolution was measured in downstream reservoir. The effective diffusion coefficient value obtained after fitting the cumulative concentration curve further showed no clear impact of barite precipitation in diffusion of this water tracer. These two results are consistent with the fact that only a small amount barite would have precipitated within sample through a quite large thickness.

Inhibition of barite precipitation within illite sample

The bulk solubility of a given mineral may change in confined media. This is due to the tension applied by the pore space onto the forming mineral. One such study showed that sodium carbonate in 30 nm pores possess solubility similar to bulk conditions. However, when the pore size is decreased to 10 nm and 7 nm, the solubility of the same mineral increased by a factor of 2 and 3 respectively(Rijniers, Huinink, Pel, & Kopinga, 2005). Such increase in solubility may decrease the precipitation probability in nanometer size pores. In another study, evolution of a pore size distribution in response to precipitation using constant solubility and pore scale pore size on the solubility in response to quartz precipitation was investigated (Emmanuel & Berkowitz, 2007). In literature, the solubility product of a given mineral is equal to ratio of ion activity product and thermodynamic solubility (Stumm & Morgan, 2012). However, the pore scale solubility is controlled by the diameter of the pore and the interfacial energy to initial precipitation. The interfacial energy is the energy barrier that a cluster of instable mineral nuclei needs to overcome to form stable nuclei and precipitate(Prieto, 2014), (Kashchiev & van Rosmalen, 2003). The end works of this study showed evolution of pore size distribution for pores of size ranging in between 10^{-4} m to 10^{-8} m. The constant solubility model showed evolution of very small porosities and macroporosities were less impacted. However, pore scale solubility model showed no precipitation of quartz in smallest pores, but, intermediate pores and macro pores were significantly impacted.

In our study, the µCT images obtained after 30 days and 140 days indicated that barite precipitate continued to evolve at the interface between sample upstream face and filter plate. However, more

or less no clear evolution in the illite sample was observed at the resolution given by µCT. This means that in some pore voids, barite precipitated for initial 30 days after which the residual pore voids could inhibit barite precipitation. Such inhibition could take place in pores of size less than or equal to mean pore diameter of the sample.

Moreover, no change in diffusive behavior of water tracer and ^{36}Cl and was observed through barite precipitated illite samples. Thus, there is significant amount of connectivity still present in the reacted zone. From works of (Emmanuel & Berkowitz, 2007) and (Rijniers et al., 2005) and diffusion results of water tracer after 70 and 140 days, we suspect that due to very small size of these pores (<9 nm), barite precipitation might be limited in these pores so as to let tracer diffuse.

Barite precipitation impact on ^{36}Cl diffusion

The precipitation impact on containment properties of a porous sample is generally estimated by using water tracer. However, several studies have shown that sulfate alkali minerals such as barite and celestite at equilibrated conditions are negatively surface charged (Bokern, Hunter, & McGrath, 2003),(González-Caballero, Cabrerizo, Bruque, & Delgado, 1988).

In one of such studies, celestite precipitation in compacted Na-illite at dry density 1700 $kg.m^{-3}$ resulted in complete clogging of ^{36}Cl tracer (Chagneau et al., 2015). From their observations, two conclusions were outlined:1) celestite precipitated in larger pores and was inhibited in the smaller pores, 2) newly formed celestite mineral possessed negative surface charge. In the first case, the pores that inhibited celestite precipitation were also inaccessible for diffusion of anions such as sulfate and ^{36}Cl. This is because in these pores there is overlapping of electric double layer and no bulk water is available for these ions to diffuse. Thus, as the big pores were filled by celestite and as in small pores there was anionic exclusion, total clogging of ^{36}Cl was observed. In the second case, the negative surface charge of celestite with the anionic accessible porosity altogether led to complete exclusion of ^{36}Cl.

In our study dealing with barite precipitation in two porous media namely chalk and kaolinite, barite mineral at equilibrated conditions possessed negative surface charge. In this study barite precipitation had strong impact on diffusive behavior of ^{36}Cl through barite precipitated zone. However, in present work although µCT image showed some barite precipitation in the illite pores, the diffusive measurements showed no impact on ^{36}Cl diffusivity. One must note that, in chalk and kaolinite barite clogging experiments, we saw clear impact of negative surface charge of barite on diffusion of ^{36}Cl. But in illite we cannot confirm whether barite mineral formed on negatively surface

charged illite surface also has negative surface charge. The contribution of barium to sorption and precipitation in illite case remains unknown.

Future Scope of Work:

The contribution of reactants to precipitation in illite sample cannot be quantified since, there is sorption of barium on illite pores and barite precipitation at interface. For this investigation, we will perform some abrasive peeling to investigate the barium activity in the unreacted and reacted zone of illite.

The morphology of barite in illite pores remains unknown. Thus, in future high-resolution scanning such as X-ray Synchrotron tomography, FIB-SEM imaging would be carried on illite samples. Finally, the empty space observed in the reacted zone will also be quantified using imaging techniques.

4 References

Altmann, S., Aertsens, M., Appelo, T., Bruggeman, C., Gaboreau, S., Glaus, M., … Gaboreau, S. (2015). Processes of cation migration in clayrocks : Final Scientific Report of the CatClay European Project HAL Id : cea-01223753.

Berthe, G., Savoye, S., Wittebroodt, C., & Michelot, J. L. (2011). Changes in containment properties of claystone caprocks induced by dissolved CO2seepage. *Energy Procedia*, *4*, 5314–5319. https://doi.org/10.1016/j.egypro.2011.02.512

Bokern, D. G., Hunter, K. A., & McGrath, K. M. (2003). Charged Barite - Aqueous Solution Interface: Surface Potential and Atomically Resolved Visualization. *Langmuir*, *19*(24), 10019–10027. https://doi.org/10.1021/la0269255

Chagneau, A., Tournassat, C., Steefel, C. I., Bourg, I. C., Gaboreau, S., Esteve, I., … Schäfer, T. (2015). Complete restriction of36Cl-diffusion by celestite precipitation in densely compacted illite. *Environmental Science and Technology Letters*, *2*(5), 139–143. https://doi.org/10.1021/acs.estlett.5b00080

Crank, J. (1975). *The Mathematics of Diffusion*. (C. Press, Ed.) (2nd ed.). Oxford.

Descostes, M., Blin, V., Bazer-Bachi, F., Meier, P., Grenut, B., Radwan, J., … Tevissen, E. (2008). Diffusion of anionic species in Callovo-Oxfordian argillites and Oxfordian limestones (Meuse/Haute-Marne, France). *Applied Geochemistry*, *23*(4), 655–677. https://doi.org/10.1016/j.apgeochem.2007.11.003

Didierjean, S., Maillet, D., & Moyne, C. (2004). Analytical solutions of one-dimensional macrodispersion in stratified porous media by the quadrupole method: Convergence to an equivalent homogeneous porous medium. *Advances in Water Resources*, *27*(6), 657–667. https://doi.org/10.1016/j.advwatres.2004.02.022

Emmanuel, S., & Berkowitz, B. (2007). Effects of pore-size controlled solubility on reactive transport in heterogeneous rock. *Geophysical Research Letters*, *34*(6), 1–5. https://doi.org/10.1029/2006GL028962

Glaus, M. A., Frick, S., Rossé, R., & Loon, L. R. V. (2010). Comparative study of tracer diffusion of HTO,22Na+and36Cl-in compacted kaolinite, illite and montmorillonite. *Geochimica et Cosmochimica Acta*, *74*(7), 1999–2010. https://doi.org/10.1016/j.gca.2010.01.010

González-Caballero, F., Cabrerizo, M. A., Bruque, J. M., & Delgado, A. (1988). The zeta potential of celestite in aqueous electrolyte and surfactant solutions. *Journal of Colloid And Interface Science*, *126*(1), 367–370. https://doi.org/10.1016/0021-9797(88)90131-2

González Sánchez, F., Van Loon, L. R., Gimmi, T., Jakob, A., Glaus, M. A., & Diamond, L. W. (2008). Self-diffusion of water and its dependence on temperature and ionic strength in highly compacted montmorillonite, illite and kaolinite. *Applied Geochemistry*, *23*(12), 3840–3851. https://doi.org/10.1016/j.apgeochem.2008.08.008

Hartkamp, R., & Coasne, B. (2014). Structure and transport of aqueous electrolytes: From simple halides to radionuclide ions. *Journal of Chemical Physics*, *141*(12). https://doi.org/10.1063/1.4896380

Kashchiev, D., & van Rosmalen, G. M. (2003). Review: Nucleation in solutions revisited. *Crystal Research and Technology*, *38*(78), 555–574. https://doi.org/10.1002/crat.200310070

Moridis, G. J. (1998). A SET OF SEMIANALYTICAL SOLUTIONS FOR PARAMETER ESTIMATION IN DIFFUSION CELL EXPERIMENTS. *Sciences-New York*, (June).

Poinssot, C., Baeyens, B., & Bradbury, M. H. (1999). Experimental and modelling studies of caesium sorption on illite. *Geochimica et Cosmochimica Acta*, *63*(19–20), 3217–3227. https://doi.org/10.1016/S0016-7037(99)00246-X

Prieto, M. (2014). Nucleation and supersaturation in porous media (revisited). *Mineralogical Magazine*, *78*(6), 1437–1447. https://doi.org/10.1180/minmag.2014.078.6.11

Putnis, A., & Fernandez-Diaz, L. (1990). Factors controlling the kinetics of crystallization: Supersaturation evolution in a porous medium. Application to barite crystallization. *Geological Magazine*, *127*(6), 485–495. https://doi.org/10.1017/S0016756800015417

Radwan, J., Hanios, D., & Grenut, B. (2006). *Qualification expérimentale de la plate-forme ALLIANCES . 1 ère Partie : Calculs préliminaires .* GIF SUR YVETTE. https://doi.org/NT DPC / SECR 06-051 indice A DO 190

Rijniers, L. A., Huinink, H. P., Pel, L., & Kopinga, K. (2005). Experimental evidence of crystallization pressure inside porous media. *Physical Review Letters*, *94*(7), 23–26. https://doi.org/10.1103/PhysRevLett.94.075503

Savoye, S., Beaucaire, C., Grenut, B., & Fayette, A. (2015). Impact of the solution ionic strength on strontium diffusion through the Callovo-Oxfordian clayrocks: An experimental and modeling study. *Applied Geochemistry*, *61*, 41–52. https://doi.org/10.1016/j.apgeochem.2015.05.011

Savoye, S., Frasca, B., Grenut, B., & Fayette, A. (2012). How mobile is iodide in the Callovo-Oxfordian claystones under experimental conditions close to the in situ ones? *Journal of Contaminant Hydrology*, *142–143*, 82–92. https://doi.org/10.1016/j.jconhyd.2012.10.003

Stumm, W., & Morgan, J. J. (2012). *Aquatic chemistry: chemical equilibria and rates in natural waters* (Vol. 126). John Wiley & Sons.

Tertre, E., Savoye, S., Hubert, F., Prêt, D., Dabat, T., & Ferrage, E. (2018). Diffusion of Water through the Dual-Porosity Swelling Clay Mineral Vermiculite. *Environmental Science and Technology*, *52*(4), 1899–1907. https://doi.org/10.1021/acs.est.7b05343

s, M. A., & Diamond, L. W. (2008). Self-diffusion of water and its dependence on temperature and ionic strength in highly compacted montmorillonite, illite and kaolinite. *Applied Geochemistry*, *23*(12), 3840–3851. https://doi.org/10.1016/j.apgeochem.2008.08.008

Hartkamp, R., & Coasne, B. (2014). Structure and transport of aqueous electrolytes: From simple halides to radionuclide ions. *Journal of Chemical Physics*, *141*(12). https://doi.org/10.1063/1.4896380

Kashchiev, D., & van Rosmalen, G. M. (2003). Review: Nucleation in solutions revisited. *Crystal Research and Technology*, *38*(78), 555–574. https://doi.org/10.1002/crat.200310070

Moridis, G. J. (1998). A SET OF SEMIANALYTICAL SOLUTIONS FOR PARAMETER ESTIMATION IN DIFFUSION CELL EXPERIMENTS. *Sciences-New York*, (June).

Poinssot, C., Baeyens, B., & Bradbury, M. H. (1999). Experimental and modelling studies of caesium sorption on illite. *Geochimica et Cosmochimica Acta*, *63*(19–20), 3217–3227. https://doi.org/10.1016/S0016-7037(99)00246-X

Prieto, M. (2014). Nucleation and supersaturation in porous media (revisited). *Mineralogical Magazine*, *78*(6), 1437–1447. https://doi.org/10.1180/minmag.2014.078.6.11

Putnis, A., & Fernandez-Diaz, L. (1990). Factors controlling the kinetics of crystallization: Supersaturation evolution in a porous medium. Application to barite crystallization. *Geological Magazine*, *127*(6), 485–495. https://doi.org/10.1017/S0016756800015417

Radwan, J., Hanios, D., & Grenut, B. (2006). *Qualification expérimentale de la plate-forme ALLIANCES . 1 ère Partie : Calculs préliminaires .* GIF SUR YVETTE. https://doi.org/NT DPC / SECR 06-051 indice A DO 190

Rijniers, L. A., Huinink, H. P., Pel, L., & Kopinga, K. (2005). Experimental evidence of crystallization pressure inside porous media. *Physical Review Letters*, *94*(7), 23–26. https://doi.org/10.1103/PhysRevLett.94.075503

Savoye, S., Beaucaire, C., Grenut, B., & Fayette, A. (2015). Impact of the solution ionic strength on strontium diffusion through the Callovo-Oxfordian clayrocks: An experimental and modeling study. *Applied Geochemistry*, *61*, 41–52. https://doi.org/10.1016/j.apgeochem.2015.05.011

Savoye, S., Frasca, B., Grenut, B., & Fayette, A. (2012). How mobile is iodide in the Callovo-Oxfordian claystones under experimental conditions close to the in situ ones? *Journal of Contaminant Hydrology*, *142–143*, 82–92. https://doi.org/10.1016/j.jconhyd.2012.10.003

Stumm, W., & Morgan, J. J. (2012). *Aquatic chemistry: chemical equilibria and rates in natural waters* (Vol. 126). John Wiley & Sons.

Tertre, E., Savoye, S., Hubert, F., Prêt, D., Dabat, T., & Ferrage, E. (2018). Diffusion of Water through the Dual-Porosity Swelling Clay Mineral Vermiculite. *Environmental Science and Technology*, *52*(4), 1899–1907. https://doi.org/10.1021/acs.est.7b05343

.

Chapter-2.4: Discussion of Precipitation Experiments

RÉSUMÉ

Ce chapitre fait le point sur les principaux résultats expérimentaux acquis dans ce travail : des expériences de contre-diffusion réactive testant l'effet du minéral précipité (gypse ou barytine) ainsi que le milieu poreux initial (craie micritique, kaolinite compactée ou illite compactée conditionnée au césium). Les différences de propriétés chimiques des minéraux précipités (barytine et gypse) mènent à des comportements très différents sur le même type de matériau (craie micritique). La distribution spatiale des précipités et donc l'impact sur les propriétés de transport sont radicalement différents. Les résultats obtenus pour la précipitation du même minéral (barytine) dans deux matériaux (craie et kaolinite compactée) de porosité et diffusivité initiale différentes mènent également à une évolution très différente des propriétés de transport. Ainsi, l'analyse du colmatage induit par la précipitation d'un minéral dans un matériau ne peut pas être directement extrapolée à d'autres matériaux. Les résultats obtenus avec l'illite compactée montrent des effets d'inhibition de la précipitation. Il est ainsi montré l'importance de prendre en compte l'effet de taille de pore et de charge de surface du milieu poreux et des minéraux précipités.

The final goal of precipitation experiments was to demonstrate “whether Archie relationship can be generalized for clogging phenomena on any porous media.” For such demonstration, following three questions need to be answered:

- Can clogging phenomena be generalized for materials with same porosity but different pore size distributions?
- Will a same precipitating mineral lead to same effectiveness of clogging on two materials with different pore size distributions and different surface charge properties?
- Will precipitating minerals of very different intrinsic properties, such as solubility or kinetic rate of precipitation, leads to same impact on diffusivity of a single porous material?

To find possible answer of the first two questions barite precipitation experiments were carried in chalk, illite and kaolinite materials and, for the final question, barite and gypsum precipitation in chalk were carried out. These sulfate alkali mineral (i.e., barite and gypsum) were selected as they present two extremities in reference to their kinetic rate of precipitation and solubility. For each individual case, the experimental results are explained in length in their respective sections in this manuscript. However, for general discussion the principal end results are briefly recalled in this section.

1 Barite precipitation in chalk, kaolinite and illite

1.1 Precipitation behavior from chemistry monitoring

The intact properties for the three proxy porous materials are presented in Table 1. The chalk porous matrix is composed of calcite and kaolinite pore surface possess weak negative surface charge. Thus, both water tracer (HTO) and anionic tracer (^{36}Cl) have similar accessible porosity for diffusion. Thus Table 1 shows that HTO and ^{36}Cl have similar diffusion behavior in each porous material. However, illite pore surface possess permanent negative charge. Therefore, the anionic accessible porosity and effective diffusion coefficient of ^{36}Cl is lower than HTO. For these three porous materials, barite precipitation experiments were performed using counter diffusion of barium and sulfate ions from their respective reservoirs into the porous sample. At certain time, these ions will meet in sample pores and generate supersaturated solution with respect to barite. As the experiments progress, the pore solution will overcome the threshold supersaturation and form stable barite nuclei. Thus, barite precipitation removes some barium and sulfate from the pore solution so that supersaturation is reduced to saturation with respect to barite. Moreover, the

stable nuclei will provide additional barite surface on which incoming barium and sulfate ions will allow further barite growth over time. However, due to very different pore structure and pore surface properties, the distribution of these first points of precipitation are expected to be different for each porous material. The difference in precipitation impact on diffusivity in function of these materials was demonstrated from water tracer diffusivity measurements after 70 days of precipitation.

*Table 1: Intact properties such as accessible porosity and effective diffusion coefficients of water tracers and ^{36}Cl for the three porous materials. * ^{36}Cl diffusive coefficient for chalk was determined by fitting HTO experimental data (since diffusion of water tracer and chloride ion until infinite dilution in pure water are similar and since there are no charge surface in chalk material)*

Intact Properties				
Porous sample	Total Porosity %	$D_{e,HTO}$ $x10^{-10}$ $m^2.s^{-1}$	Anionic accessible Porosity %	$D_{e,36Cl}$ $x10^{-10}$ $m^2.s^{-1}$
Chalk	45	4.15	45	4.05*
Kaolinite	36	2.9	36	2.3
Illite	29	0.5	19	0.27

However, prior to this step, the behavior of barium and sulfate concentration decrease in reservoirs were determined using reservoir monitoring step. In this section, barium ion behavior in response to barite precipitation in chalk, kaolinite and illite is presented. This was done by reproducing two barium concentration curves using I-mode. The first curve presented the barium evolution in upstream under pure diffusion for intact sample case. The second diffusion curve presents barium evolution in upstream in response to barite precipitation in the sample. To model these curves the necessary input parameters for I-mode are geometry of the experimental cell: reservoir volumes, barium concentration in reservoir, sample surface and thickness and sample porosity.

The final input parameter is barium diffusion coefficient which was determined using relationship $D_{e,Ba} = \phi \times (D_{o,Ba}/D_{o,HTO})$, for chalk and kaolinite case (the bulk diffusion coefficients for barium is $D_{o,Ba} = 8.5 \times 10^{-10}\ m^2.s^{-1}$ and for HTO is $D_{o,HTO} = 2 \times 10^{-9}\ m^2.s^{-1}$ are taken from literature [1]). In the first step, using input parameters from Table 2 in I-mode, the modeled barium concentration curve for pure diffusion transport through intact sample is determined. This modeled curve for chalk is presented in Figure 1A. In the second step the experimental data points of barium concentration

decrease in response to barite precipitation in chalk were modeled using I-mode. In chalk experiment, all the barium lost in reservoir was consumed for barite precipitation in sample (no barium diffusion in counter reservoir). Thus, for the second step modeling a zero-concentration boundary condition was imposed by considering very large counter reservoir volume. Finally, to reproduce the experimental data points the barium effective diffusion was increased (value presented in Table 2).The resulting modeled curve is presented in Figure 1A. The two modeled curves for pure diffusion and reactive diffusion shows clear difference in barium concentration decrease in the reservoir.

In precip_I_mode case a rapid barium concentration decrease is observed for initial 30 days of the experiment. This means that, at the very initial stage of experiment, first points of precipitation were formed in the chalk sample. These first points then acted as sink and rapidly consumed incoming barium to allow barite growth. After 30 days, I-mode showed a progressive barium concentration decrease. However, experimental data points showed that after this time barium concentration moved towards quasi-equilibrium stage. This means that after 30 days clogging as started to become effective enough to prevent barium ions to diffusion through the precipitated zone. Similar to chalk case for kaolinite, using the input parameters from Table 2 modeled curve for barium concentration decrease under pure diffusion is presented in Figure 1B. In chalk experiments, the barium concentration evolution in upstream reservoir for reactive diffusion step was reproduced by I-mode when $D_{e,Ba}$ was increased. However, in kaolinite experiment, $D_{e,Ba}$ was same as pure diffusion case but, to model the experimental data points, the sample thickness was decreased to 5 mm from initial thickness of 10 mm. Thus, in kaolinite the initial first points of precipitation were enough to block diffusion of barium through the precipitated zone. For this reason, a slow concentration decrease was observed in reservoir and the data-points reached quasi-equilibrium after 100 days of precipitation.

For illite experiment, the effective diffusion coefficient and modeled curve for barium under pure diffusion case were obtained from experiments. The input parameters used to obtain the modeled curve of barium pure diffusion through illite sample (Figure 1)are presented in Table 2. Like chalk and kaolinite case, the experimental data points and modeled curve for barium concentration decrease in response to barite precipitation are presented in Figure 1C. As shown in Table 2 to reproduce the experimental data points in this figure the thickness of the illite sample was decreased from 6 mm to 1 mm. This means that a barite precipitation is rapidly consuming barium in a zone near the barium face of the sample. From reservoir monitoring, the precipitation impact

on diffusivity of water tracer and distribution of first points of precipitation remains unknown. Thus, barium behavior modelling using I-mode for chalk, kaolinite and illite shows the difference in clogging behavior of same mineral in three different porous materials.

Table 2: Effective diffusion coefficients, sample thickness and counter reservoir volume/conditions considered to model barium diffusion under pure diffusion and reactive diffusion conditions for each sample

Barium Pure diffusion case			Barium under barite precipitation case			
	$D_{e,Ba}$ $x10^{-10}$ $m^2.s^{-1}$	Thickness of sample, mm	Counter reservoir volume ml	$D_{e,Ba}$ $x10^{-10}$ $m^2.s^{-1}$	Thickness of sample, mm	Counter reservoir condition
Chalk	19.1	6.7	138	25	6.7	Zero boundary condition
Kaolinite	15.68	10	20	15.68	5	
Illite	0.32	6	50	0.32	1	

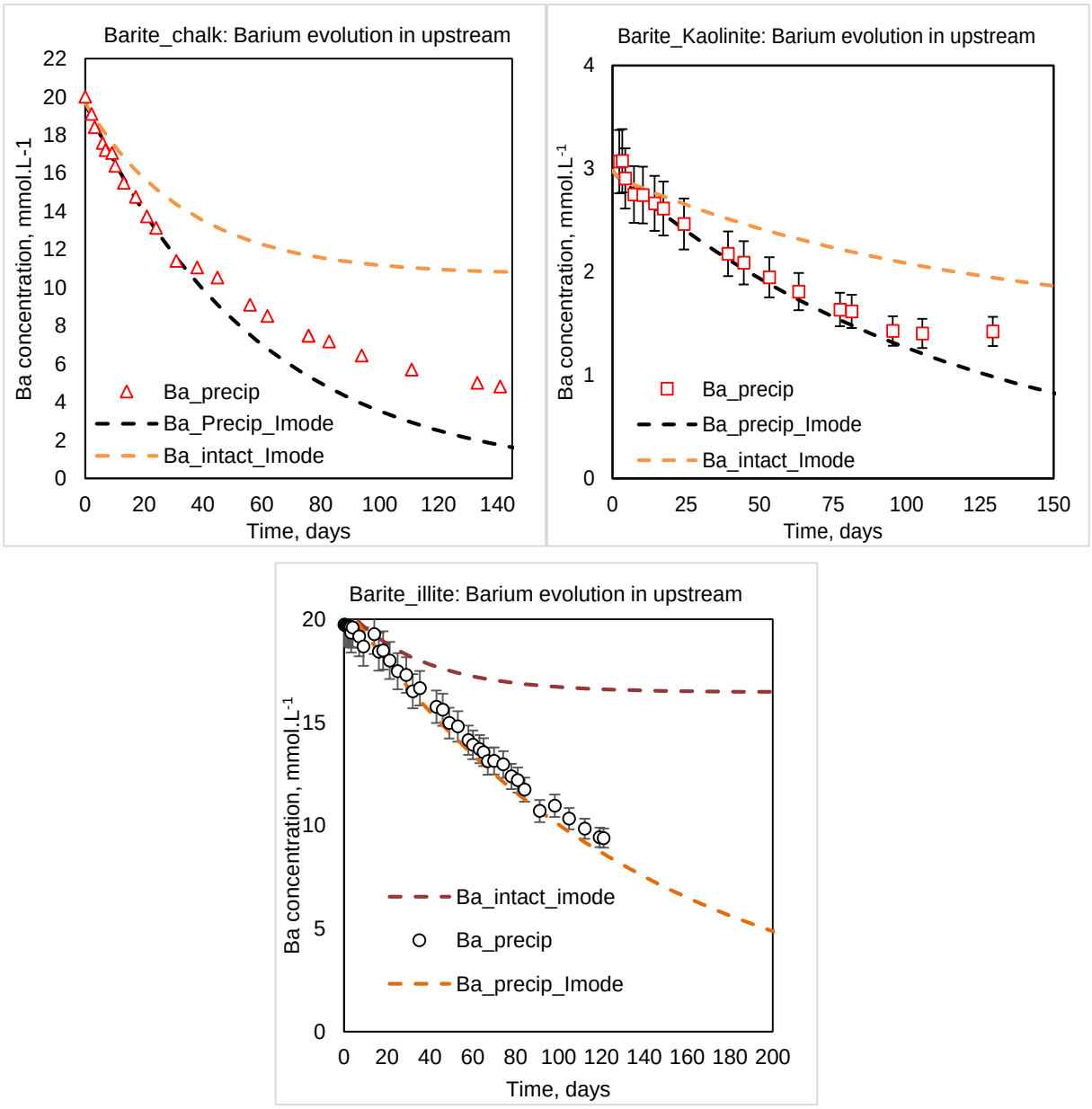

Figure 1: The experimental points presents barium concentration decrease in response to barite precipitation in chalk, illite and kaolinite sample. The dashed liners present the modeled concentration curves obtained using I-Mode for pure diffusion and reactive diffusion case.

1.2 *Evolution of barite in chalk, kaolinite and illite samples*

The barite precipitated zones in 3D using µCT imaging in chalk, kaolinite and illite are presented in Figure 2. This figure shows that barite precipitated in a thin zone in the center of the chalk sample. For kaolinite, barite precipitates are distributed near the center of the sample (with a slight offset towards the barium face of the sample) . For illite, a thin precipitated zone was formed near the barium face of the sample.

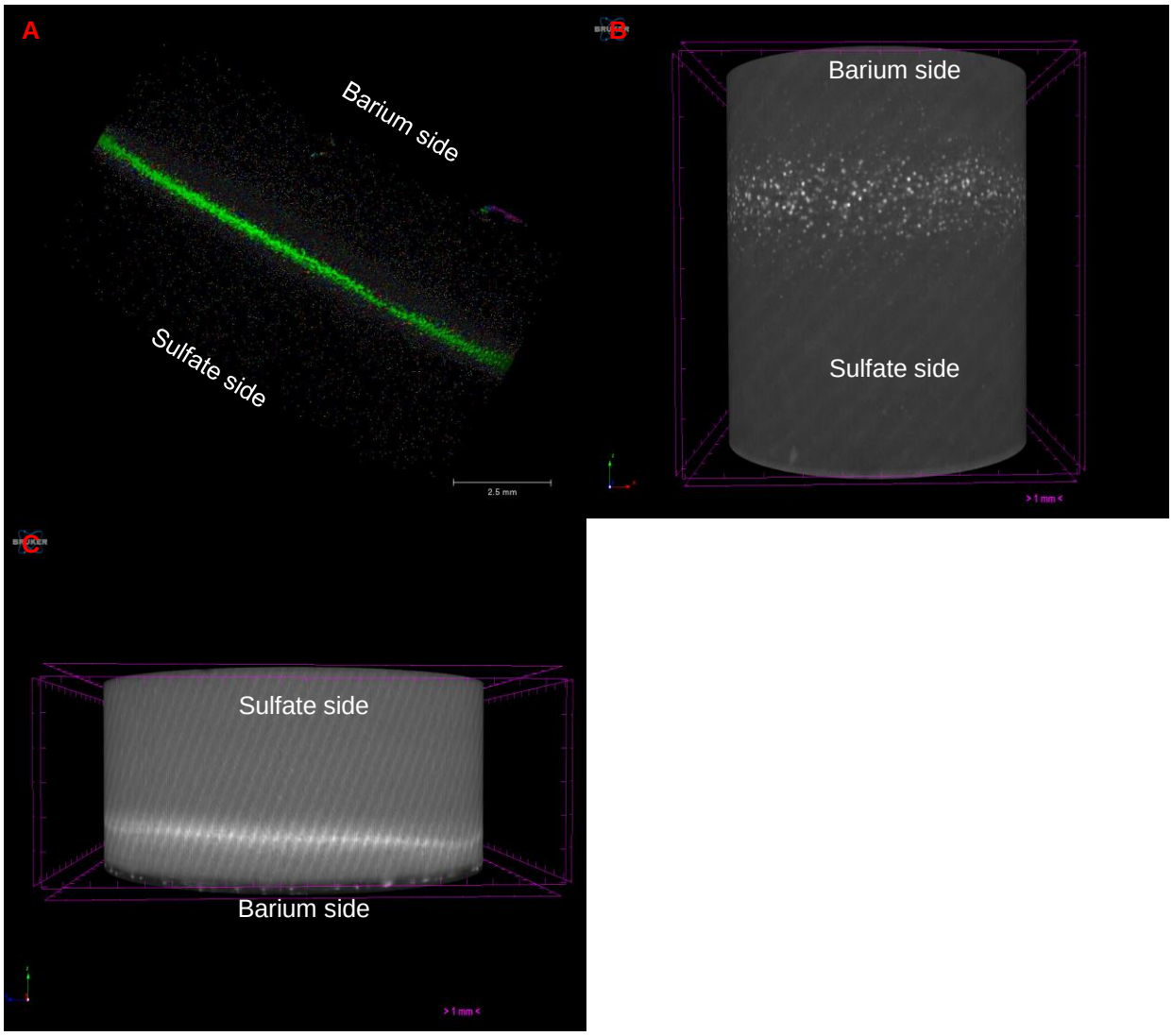

Figure 2: Evolution of barite precipitates in A: chalk, B: kaolinite and C: illite samples

The µCT images were obtained at resolution 5.5 µm for chalk, 10 µm for kaolinite and 20 µm for illite respectively. To locally characterize the barite precipitates, SEM imaging was performed on small samples of chalk and kaolinite on a small sample the barite precipitates. For both samples, these SEM images are presented in Figure 3. For chalk, the SEM imaging showed a quasi-continuous line precipitated in the center of the sample (Figure 3A). Around this line some isolated barite precipitates were also observed. At a higher resolution two distinct barite morphologies were observed. In coccoliths big crystals of barite precipitated and, in pores of size less than or equal to mean pore diameter, barite overgrowth was observed (Figure 3C). In kaolinite, the SEM images shows that the distributed big barite spheres in µCT image are in fact barite clusters of small barite formed in pores of size less than or equal to mean pore size of kaolinite (Figure 3B and D).

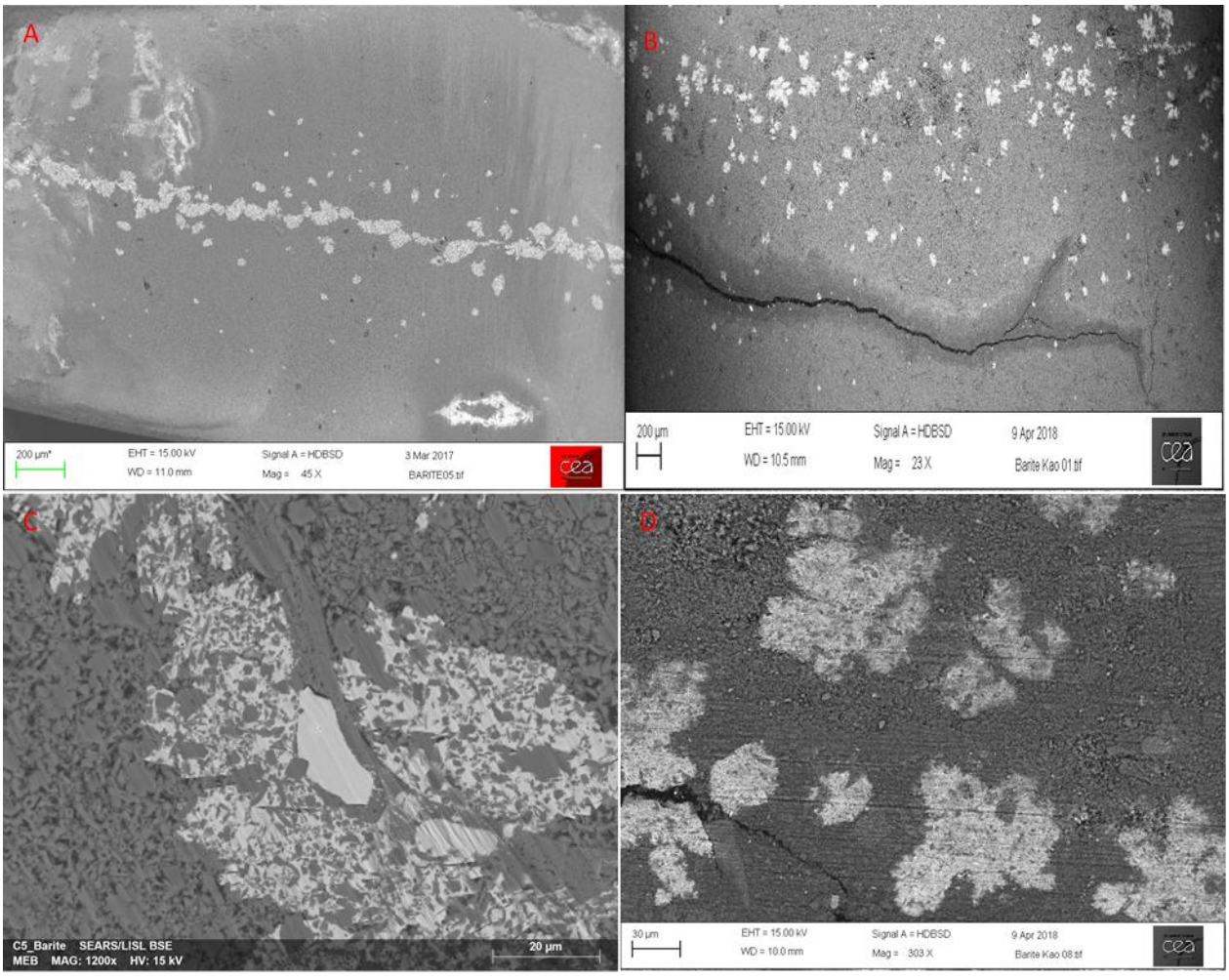

Figure 3: SEM observations for barite precipitates in chalk (A and C) and kaolinite samples (Band D).

As described earlier in the section 1.1, the experiments were performed using counter-diffusing technique where barium and sulfate diffuse into the sample and supersaturate the pore solution with respect to barite. The pores in which supersaturation to initiate precipitation is firstly achieved allows formation of stable barite seeds and the precipitation kinetics is locally enhanced. These pores are called first points of precipitation. In chalk, the final barite precipitated zone from SEM images shows that these first points of precipitation fall in a single line at the center of the sample. However, in kaolinite these first points of precipitation are distributed near the center of the sample. This difference in distribution is due to the difference in the mean pore size and pore size distribution. In each sample, due to orientation of pores or random distribution of connectivity, there is heterogeneity present in the system. Thus, there is local variation in diffusion of counter diffusing barium and sulfate ions. Consequently, the pore located in the precipitated zone first points where these ions will meet, the rate of supersaturation of pore solution with respect to barite will vary. However, the zone where precipitation took place in chalk contains simultaneously pore of size less than or equal to means pore size and coccoliths as macro porosities. The low solubility of barite and the pores (pore of size less than or equal to 660 nm and coccoliths) size will thus compensate the local variation in rate of supersaturation. For this reason, the first points of precipitation fell in the single line in the center of the sample from which barite eventually grew over the experimental time. On another hand, in kaolinite, the mean pore size is 20 times smaller than in chalk. Thus, the local variation in supersaturation seems to be significant as first points of precipitation are distributed, and they do not fall in single line. In this case once stable seeds of barite were formed in the first points, saturation was drained down to vicinity. Due to small volume of pores, barite precipitation was inhibited in the surrounding pores. Finally, as experiment progressed barite precipitates grew on this stable barite and formed clusters.

In illite case, a very different evolution was observed. The µCT image shows that barite precipitated in a zone located close to the face of barium inlet reservoir. Barite also precipitated at an interface between barium inlet face of sample and filters (images already presented in illite experimental section). The µCT images taken after 30 days and 140 days of precipitation showed significant barite growth at the interface and no significant evolution in the illite sample. Several possibilities can explain the observed inhibition of barite precipitation in the illite sample. The first hypothesis is that illite sample possesses mean pore size 66 times smaller than chalk. Some works have shown that in such small confined volumes, due to the tension applied by the pore space onto the forming mineral, its bulk solubility may change [2]. Such increase in solubility may decrease the precipitation probability in nanometer size pores. A numerical work using pore scale

solubility model showed that precipitation of quartz mineral of very low solubility was inhibited in pores of size 10^{-4} m to 10^{-8} m [3]. The second hypothesis is that illite mineral contains permanent negative surface charge on the pore surface. In very small pores (of size few nanometers) there is overlapping of electric double layers. Thus, there is exclusion of sulfate anion from these pores and this will prevent barite formation in these pores. This means that barite might have initially precipitated in the pores of size greater than mean pore diameter. This was captured after 30 days of µCT imaging. But, since the two aforementioned cases have prevented barite precipitation in other pores, no evolution of precipitation zone in µCT of 140 days was observed.

The chemistry monitoring and post-treatment imaging thus show that, in chalk and kaolinite samples of similar total porosity but very different pore size distributions and mean pore size, the distribution of barite precipitates is not same. Barite precipitation in illite shows a very different impact of pore size on precipitation process.

1.3 Impact of barite precipitation on HTO diffusivity.

The impact of different distribution of barite mineral in chalk, kaolinite and illite was determined by injecting HTO in one reservoir, after 70 days of precipitation process. The tracer was then allowed to diffuse into counter reservoir through the sample mineral precipitated zone. After next 70 days of acquisition, the tracer behavior through intact and mineral precipitated material were compared to determine precipitation impact on diffusivity. The HTO diffusivity obtained by fitting the HTO activity data points using I-mode for intact and barite precipitated samples are presented in Table 3, respectively. These tables show that barite precipitation had higher impact on HTO diffusivity for kaolinite than chalk. For illite no visible impact on diffusivity was observed.

Table 3: Diffusion coefficients for HTO and ^{36}Cl obtained after fitting the HTO and ^{36}Cl activity data after 70 days of precipitation experiment

Precipitation impact on diffusivity		
Porous Sample	$D_{e,HTO}$ $x10^{-10}$ $m^2.s^{-1}$	$D_{e,36Cl}$ $x10^{-10}$ $m^2.s^{-1}$
Chalk	1.3	0.015
Kaolinite	0.11	Total clogging
Illite	0.5	0.4

These observations thus suggest that distribution of barite precipitates had very different impact on blocking the important connectivity in the precipitated zone for each sample. The diffusivity results for kaolinite shows that the clusters of barite precipitates have significantly reduced the connectivity in the precipitated zone. In chalk, barite has significantly consumed pores in the very thin precipitation zone. However, the diffusivity data shows significant presence of empty pores that still allowed HTO diffusion. In illite, it seems that the connectivity of pore network is dominated by pores that inhibited barite precipitation. Thus, even after precipitation since most of the pores allowed HTO diffusion, no impact of barite precipitation was observed.

2 *Gypsum precipitation in chalk sample*

The µCT imaging showed formation of large isolated spherical gypsum precipitates around the center of the chalk sample (Figure 4A). A scan at higher resolution on a smaller sample showed very high porosity reduction in these spheres (Figure 4B). However, around each sphere significant intact macro-porosity was observed (Figure 4C). Such selective precipitation in isolated zones showed that contrary to barite, the spatial variability in properties, such as heterogeneous diffusive pathways of reactive surface, for precipitation along with solubility of gypsum has governed the precipitation phenomena. In our study, gypsum precipitation was largely driven by heterogeneous nucleation phenomena. In this case, gypsum growth takes place on the pore surface. Since chalk contains calcite grains and coccoliths, there is significant variation in surface roughness and active surface area (acting as substrate). Thus, the variability of surface area available for gypsum growth will control nucleation distribution and kinetics at the center of sample even though the counter diffusing calcium and sulfate would equally saturate the pore volumes over time. These nuclei would then follow the similar positive feedback phenomena as barite case and locally enhance precipitation. They will evolve as isolated more or less spherical clusters because they are initially irregularly distributed at the center of sample. Similarly, the randomly orientated coccoliths within carbonate grains mixture will also generate a heterogeneous pore network. Similar to barite case, these heterogeneous diffusive pathways will generate variation in rate of saturation in the precipitation zone. Since gypsum precipitation occurs close to equilibrium conditions, small differences in saturation index may enhance or delay precipitation locally. Thus, there is selective precipitation in points where saturation is slightly higher than the neighboring point. Once stable gypsum is formed in these first points, there is positive feedback which prevents precipitation in neighboring pores. As gypsum will grow from this initial point, they will finally form isolated spherical clusters in the center of the sample. To determine the impact of these isolated

spheres evolution in chalk on the diffusivity, water tracer was injected after 70 days of precipitation. Similar to barite case in chalk the experimental data points were reproduced using I-mode to obtain the diffusion coefficient. This fitting showed that gypsum precipitation reduced the intact water tracer diffusivity from 4.15×10^{-10} $m^2.s^{-1}$ to 2.5×10^{-10} $m^2.s^{-1}$ respectively. Thus, gypsum precipitation in chalk led to lower impact on diffusivity than barite. This lower impact is due to the fact that although gypsum significantly reduced the porosity in the isolated clusters, but around these cluster there was still intact porosity remaining. Since, this intact porosity allowed significant water tracer to diffuse through precipitated zone, a lower impact was observed.

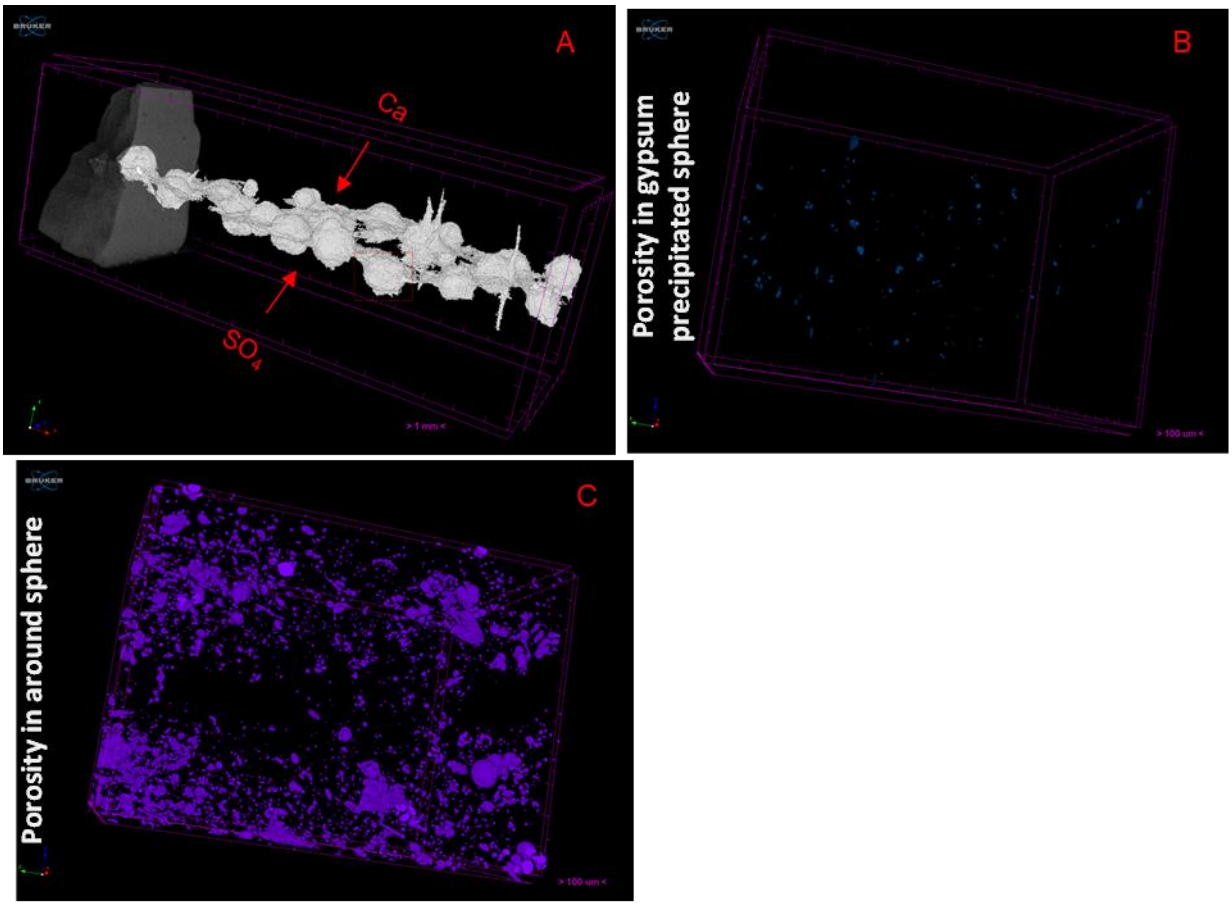

Figure 4A: Gypsum precipitated spheres distributed in the chalk sample; 4B: Each sphere is cluster of gypsum precipitates in which porosity is significantly reduced; 4C: Around each sphere intact porosity can be clearly observed

3 Conclusion from reactive diffusion experiments

The reactive diffusion experiments were carried out in view of finding possible answers to the following questions:

1. Can clogging phenomena be generalized for materials with same porosity but different pore size distributions?
2. Will a same precipitating mineral lead to same effectiveness of clogging on two materials with different pore size distributions and different surface charge properties?
3. Will precipitating minerals of very different intrinsic properties such as solubility, kinetic rate of precipitation leads to same impact on diffusivity of a single porous material?

From the end results of all the experiments following answers can thus be concluded:

1. Barite precipitation in chalk and kaolinite showed that different pore size distributions led to very different impact on evolution for the same mineral precipitation (barite) and consequently a different impact on diffusivity of water tracer. Thus, barite precipitation results for one porous material cannot be used to predict the possible impact of precipitation on another porous material.
2. The same experiment carried out in illite with the same reactants showed an inhibition of mineral precipitation (again barite). As a result, no evolution of the diffusivity was observed. Thus, the experimental results derived on materials with big pores and neutral surface cannot be used to predict possible impacts of precipitation on material with very small pores containing negative surface charge.
3. An experiment carried out with the same substratum (chalk) and two different reactants (leading to barite or gypsum precipitation) showed that the intrinsic property of each mineral along with spatial variability in properties led to very distinct evolution of each mineral. This distinct evolution then led to very different impact on water tracer diffusivity.

Finally, barite precipitation in chalk, kaolinite and illite experiments had very different impact on diffusivity of ^{36}Cl (see Table 3). In chalk and kaolinite, barite mineral possessed negative surface charge due to which a strong impact on ^{36}Cl diffusivity was observed. However, in illite no impact on diffusivity of this tracer was observed. Thus, these experiments show that barite mineral forming on neutral pore surface will have negative surface charge. However, the surface charge of barite forming on negative surface charged clayey mineral still remains unknown.

Out of all of these results, the barite and gypsum in chalk results will be used in next chapter to demonstrate if such distinct evolution can be reproduced at REV scale in 1D. Already from the experiment results, it can be expected that some kind of information on the intrinsic differences of reactivity for barite and gypsum have to be incorporated in the model so there can be a chance to simulate different behaviors. Then 2D modeling will be used to determine if numerically spatial variability in chalk properties along with intrinsic mineral properties can be quantified or not. Finally, the 1D modeling will be used to demonstrate if Archie's relationship can be used as predictive model to determine very different chemistry feedback on diffusion in same porous material.

4 References

(1) Li, Y.-H.; Gregory, S. Diffusion of Ions in Sea Water and in Deep Sea Sediments. *Geochimica et Cosmochimica Acta, 1974* **1973**, *38* (2), 703–714.

(2) Rijniers, L. A.; Huinink, H. P.; Pel, L.; Kopinga, K. Experimental Evidence of Crystallization Pressure inside Porous Media. *Physical Review Letters* **2005**, *94* (7), 23–26.

(3) Emmanuel, S.; Berkowitz, B. Effects of Pore-Size Controlled Solubility on Reactive Transport in Heterogeneous Rock. *Geophysical Research Letters* **2007**, *34* (6), 1–5..

CHAPTER-3: NUMERICAL SIMULATIONS OF BARITE AND GYPSUM PRECIPITATION IN CHALK

RÉSUMÉ

Les chapitres précédents ont mis en évidence l'importance du type de milieu et des minéraux précipités sur la trajectoire d'évolution du milieu, en termes d'évolution de la structure poreuse du milieu et de ses propriétés de transport diffusif. Ces résultats sont utilisés pour tester les approches de modélisation transport réactif, ici à l'échelle du laboratoire. L'impact de la précipitation et de la dissolution sur les propriétés de la structure poreuse (perméabilité, porosité, diffusivité) est généralement prédit en utilisant des codes de chimie-transport s'appuyant sur une approche continue macroscopique. L'avantage de ce type de codes est qu'il permet de représenter le volume d'intérêt comme étant constitué d'éléments de volume qui caractérisent localement les propriétés du matériau, telles que la porosité, la perméabilité, *etc*. Dans la plupart des codes de chimie-transport actuels, la géométrie naturelle mais complexe du matériau est de ce fait simplifiée (homogénéisée) pour permettre l'acquisition de simulations réalisées à de larges échelles de temps et d'espace. En l'absence de représentation phénoménologique de la structure du milieu poreux et de son évolution, les changements de perméabilité et de diffusivité en réponse à une dissolution/précipitation s'appuient sur des relations empiriques comme les lois de Kozeny-Carman et d'Archie. Connaissant la nature empirique de ces lois, il apparaît alors nécessaire d'en tester leurs capacités prédictives. Dans cette perspective, les résultats expérimentaux obtenus à l'aide d'expériences de précipitation/diffusion du gypse et de la barytine dans une craie micritique ont été modélisés en 1D et en 2D en utilisant deux codes de chimie-transport, HYTEC et CrunchTope. Pour rappel, les résultats expérimentaux avaient montré deux phénomènes distincts responsables de la distribution et de la morphologie des précipités de barytine et de gypse. Pour la barytine, il apparaissait que le phénomène de nucléation dépendait de la taille des pores, alors que pour le gypse, la distribution et la morphologie des précipités étaient gouvernées par la variabilité spatiale de la structure des pores de la craie. Dans l'approche classique 1D, le facteur de cimentation de la loi d'Archie (l'intensité de la dépendance du coefficient de diffusion à la porosité) a dû être calé sur chaque expérience. Les codes n'ont ainsi pas permis de modéliser à la fois, avec un jeu de paramètres cohérents, l'impact de la précipitation sur la diffusivité et la contribution des réactifs sur la précipitation. En outre, une analyse de sensibilité rigoureuse a été également réalisée sur des paramètres comme la surface réactive, la cinétique, le facteur de cimentation, et la sursaturation. Bien que ces étapes montrent un changement significatif du front de précipitation, et un impact sur la diffusivité et sur la quantité de réactifs contribuant à la précipitation, les codes n'ont toujours pas pu représenter les résultats expérimentaux obtenus. L'influence de la variabilité spatiale du milieu pointée lors du dépouillement des expériences a ensuite incité à prolonger les simulations vers des simulations 2D en présence d'une distribution de porosité hétérogène. Pour le gypse, deux cas furent considérés : une précipitation homogène et une autre hétérogène induite par le phénomène de nucléation. Le premier a montré que la précipitation du gypse était gouvernée par les

surfaces réactives alors que le second montrait qu'un phénomène de diffusion hétérogène régissait la précipitation. Les deux simulations ont montré la formation de nodules isolées au centre de l'échantillon, mais dans le cas hétérogène, la structure des nodules de gypse était plus proche de celles observées expérimentalement. L'utilisation du même ensemble de paramètres pour la modélisation numérique de la précipitation de la barytine a montré l'apparition d'une mince zone de précipité au centre de l'échantillon, compatible avec la réalité. Un résultat majeur est la possibilité de représenter deux expériences aux comportements si différents avec un jeu homogène de paramètres pour les modèles, ces paramètres étant en outre directement issus de l'observation ou de la littérature. Les résultats des modélisations numériques présentés dans ce chapitre montrent donc la nécessité d'une approche en deux temps : dans un premier temps, il s'agit de déterminer les différents facteurs gouvernant la distribution et la morphologie des précipités, et dans un second temps, d'incorporer ces facteurs prépondérants dans les codes, afin d'en améliorer la capacité prédictive.

1 Introduction to clogging experiments in chalk

Numerical modelling using reactive transport codes was carried out based on the experimental results from study Rajyaguru et al. (under review). A brief description of the experimental setup, which is important for such modelling, is provided here. The experiments were conducted using a static diffusion cell, which consists of two reservoirs sandwiching a porous sample. The first reservoir is named upstream and the counter reservoir downstream. The porous sample used in this study is a chalk sample of micritic family (diameter 33 mm and thickness 6.5 mm). The volume of upstream reservoir and downstream reservoir is equal to 178 ml and 138 ml, respectively. The schematic view of the through diffusion cell is presented in Figure 1.

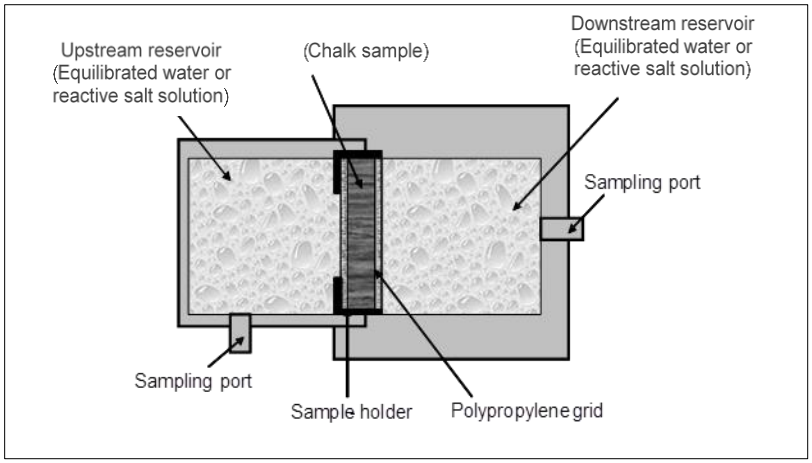

Figure 1: Static through diffusion cell comprised of two reservoirs sandwiching a chalk sample and used for barite and gypsum precipitation experiments

1.1 Choice of porous material and precipitating minerals for clogging experiments

The total porosity of chalk is 45%, with mean pore throat of 660 nm and randomly distributed coccoliths as macropores. The coccoliths with grain matrix add spatial variability in properties such as reactive surface and heterogeneous pore structure (local variation in diffusion of ionic species). The impacts of such spatial variability on evolution of two sulfate alkali mineral were determined by studying precipitation of barite and gypsum in chalk. This step is important as it allowed us to demonstrate that barite and gypsum evolution to very different impacts on chalk properties (porosity, water tracer diffusivity). These minerals were selected due to their difference in intrinsic properties such as solubility and kinetic rate of precipitation. Barite is a sparingly soluble mineral

with slow kinetics of precipitation. The morphology and evolution of barite is also dependent upon the governing nucleation phenomena (Kashchiev and van Rosmalen, 2003; Prieto, 2014). Gypsum is a fairly soluble mineral compared to barite and it precipitates with fast kinetics. Contrary to barite, at solution saturation index values close to equilibrium with respect to gypsum, the precipitation of this mineral is governed by heterogeneous nucleation phenomena (Alimi et al., 2003).

1.2 Clogging experiments

1.2.1 Chemistry of reservoirs

For reactive diffusion experiments, the upstream reservoir and downstream reservoir were firstly filled with equilibrated solution. Then, $BaCl_2$ (resp $CaCl_2$ for gypsum case) was added to the upstream solution and Na_2SO_4 (same for gypsum case) to downstream solution. The detailed ion concentration for equilibrated solution and reactants injection is detailed in Table 1.

Table 1: Chemical composition of the equilibrated solutions with reactants used for the barite and gypsum experiments

Ions	Rock-equilibrated Solution mmol. L^{-1}	Barite experiment		Gypsum experiment	
		Upstream mmol. L^{-1}	Downstream mmol. L^{-1}	Upstream mmol. L^{-1}	Downstream mmol. L^{-1}
Na	159.40	119.40	159.40	0.50	0.89
K	-	-	40.00	-	160.20
Ca	20.62	20.62	20.62	80.50	1.25
Mg	0.07	0.07	0.07	0.07	0.07
Ba	-	20.00	-	-	-
Cl	200.20	200.39	200.20	161.30	1.34
SO4	-	-	20.00	-	80.10
HCO3	0.39	0.39	0.39	0.23	2.12
Log(pCO_2) (atm)	-3.5	-3.5	-3.5	-3.5	-3.5

1.1 Chemistry monitoring in reservoirs

The evolution of reactant concentration in upstream and downstream reservoirs were followed using reservoir monitoring method for the total experimental time of 140 days (the method is detailed in chalk chapter). To evaluate the barite clogging impact on diffusivity, at the very beginning of experiment upstream solution was spiked with tritiated water. The evolution of activity in downstream was then followed for 140 days. A similar barite cell was prepared in which barite precipitation was carried out for 70 days after which HTO was injected in upstream and its activity was followed for the next 70 days. For gypsum, pure deuterated water (HDO) was injected in upstream and its downstream after which concentration evolution was followed for 70 days. On the 70th day, respecting the chemistry of equilibrated solution and reactants in upstream and downstream, both reservoirs solutions were replaced with HDO free solutions after which HDO was reinjected in upstream.

2 Summary of results from chalk experiments

2.1 Chemistry monitoring in reservoirs

From initial and final reactant concentration in reservoirs both minerals led to similar total porosity decrease of chalk sample. However, reservoir monitoring step showed a distinct evolution of reactant in reservoir for both cases. In barite case, the concentrations of reactants in counter reservoir stayed below detection. This is because the solubility of barite is very low ($K_{sp(barite)}=10^{-9.97}$) so that saturation (and even supersaturation to initiate precipitation) is reached easily. Consequently, barite precipitation buffers barium and sulfate concentrations at very low levels (around 10^{-5} mol. L^{-1} if barium and sulfate have similar concentrations).Thus, all of the barium diffusing from upstream (resp. sulfate) into sample will contribute to barite precipitation in chalk.

For gypsum case, an accumulation of calcium and sulfate in the counter reservoirs was observed. Since, gypsum is a fairly soluble mineral ($K_{sp(gypsum)} = 10^{-4.58}$) so that (with equal concentration boundary conditions) calcium and sulfate concentrations increase in the reservoirs, until the equilibrium value is reached. Indeed, some evidence of gypsum precipitation was even found (although not quantified) in the reservoirs. After 20 days, calcium and sulfate concentrations are buffered by gypsum, and stay on a plateau throughout the experiment.

2.2 Clogging impacts on water tracer diffusivity

For the tracer test at initial time, the water tracers injected in the upstream of barite and gypsum cell showed little and no significant impact of precipitation on their diffusivity. However, for the test at 70 days, a significant difference was observed. Barite precipitation decreased tritiated water diffusivity by a factor 3.7, whereas gypsum precipitation decreased deuterated water diffusivity by a factor of 1.6. These experimental acquisitions for tracer behavior under pure diffusion case for intact chalk and under reactive diffusion case for barite and gypsum clogging are explained in length in Rajyaguru et al (under revision, Chemical Geology, 2018, Chapter-2.1 on this manuscript).

2.3 Evolution of barite and gypsum minerals in chalk sample

The post treatment imaging of reacted chalk samples was carried out by means of X-ray microtomography and back scattering electron scanning electron microscopy (BSE-SEM). The 3D images from µCT clearly showed two distinct evolutions of barite and gypsum precipitated zones in the chalk sample. Barite precipitates were distributed in a thin zone located at the center of the sample. The BSE-SEM images further showed that barite precipitated with two different morphologies in this zone. 1) In pores of size less than or equal to mean pore throat of chalk barite grew on the pore surface due to heterogeneous nucleation phenomena. 2) In macro pores such as coccoliths barite precipitated from pore solution due to homogeneous nucleation phenomena. Finally, as barite precipitates resulting from each nucleation phenomena occupied most of the pores in the center of the sample, its precipitation had significant impact on diffusivity.

For gypsum, 3D imaging showed isolated spherical clusters of gypsum precipitates distributed along the center of the sample. To determine gypsum precipitation impact on blocking the diffusive pathways a scan at higher resolution was carried out. From this scan residual porosity in spherical clusters and in matrix around these clusters was obtained by image processing. In spherical clusters, presence of very small amount of residual porosity and in surrounding matrix significant residual porosity were observed. Moreover, BSE-SEM images no distinct morphology of gypsum mineral was observed. Finally, as gypsum precipitates occupied the pores located only in each isolated spherical zone, the intact matrix surrounding each sphere allowed tracer to diffuse through the precipitated zone. Thus, a lower impact on diffusivity compared to barite case was observed for gypsum case

2.4 Conclusions from barite and gypsum experiments

The barite precipitation in different pore volumes of chalk sample was governed by homogeneous and heterogeneous nucleation phenomena. The two distinct morphologies of barite precipitate were observed in the reacted zone, depending upon each phenomenon. Barite mineral would precipitate in this zone at saturation index around 4, as indicated by (Prasianakis et al., 2017). However, due to low solubility of mineral, such high saturation was easily reached and most of the barite precipitated in the first line of precipitation which is located in the center of the sample.

For gypsum, isolated spheres distributed in the center of the sample were observed. Each sphere resembles a cluster of gypsum precipitates in the chalk pores. These spheres further demonstrate selective gypsum precipitation. Moreover, gypsum mineral in chalk precipitated at saturation index near to equilibrium. In literature at this saturation gypsum precipitation is governed by heterogeneous nucleation phenomena (Alimi et al., 2003). This means that gypsum mineral growth on pore surface controlled the precipitation phenomena. In this case reactive surface for precipitation can be the deciding parameter for selective gypsum precipitation. In our study, the chalk sample has a spatially variable distribution of the surface roughness since chalk matrix is composed of a mixture of grains and coccoliths. In this case although counter diffusing calcium and sulfate will equally saturate pore solution in the precipitation zone, some of the pores may provide higher surfaces for early formation gypsum nuclei, where further precipitation is then enhanced. Thus, these pores will control the distribution of gypsum nuclei and these nuclei will control kinetics of gypsum precipitation. Moreover, as these pores are randomly distributed in the precipitation zone, the precipitation controlling nuclei are also randomly distributed. As experiment progresses, these nuclei will grow and form isolated gypsum clusters.

However, the variable distribution of grain porosity in chalk with coccoliths can also provide a heterogeneous pore network, i.e. varying tortuous diffusive pathways. In counter diffusion setup, these tortuous pathways will trigger either faster or slower meeting of calcium and sulfate ions in the pore solutions located in the precipitated zone. Consequently, the local rate of saturation with respect to gypsum will vary in each pore in the precipitation zone. Since, gypsum precipitates at saturation near to equilibrium, this variation may either enhance or delay precipitation. In this case, the pores in which saturation rate is higher will allow formation of first gypsum nuclei. The consequence is the same: these nuclei will locally enhance precipitation and generate isolated spherical clusters similarly to the previous scenario of surface roughness.

2.5 Motivation of Numerical Modelling

The barite and gypsum experiments showed very different chemistry evolution in reservoirs, impact on diffusivity and evolution in the similar chalk porous matrix. It is clear then that the model needs to incorporate some information to describe the intrinsic differences in the reactivity of both minerals. Also, these experiments show that spatial variability with intrinsic property such as kinetic rate of precipitation and solubility can lead to very different evolution of similar pore structure. An accurate simulation strategy then needs to incorporate some level of initial spatial variability. In this work, the simulations are carried out at the representative elementary volume (REV) scale using two coupled chemistry transport codes: HYTEC and CrunchTope[11].

3 Description of the models

3.1 Reactive transport codes

Two chemistry transport codes were used for numerical analysis of barite and gypsum clogging experiments in chalk: HYTEC and CrunchTope. The generalized equation at representative elementary volume scale (REV) for HYTEC and CrunchTope codes are well described in (Lagneau, 2013; Lagneau and van der Lee, 2010; van der Lee et al., 2003) and (Steefel, 2009), respectively. For the numerical analysis of clogging experiments, these equations for mineral precipitation rate and feedback impact on porosity for both codes are presented in Table 2, (Cochepin et al., 2008).

[11] The REV scale model and continuum theory is well described in (Lichtner, 1996; Steefel and MacQuarrie, 1996)

Table 2: Formulations of Archie's law, kinetics and reactive surface area for HYTEC and CrunchTope (Cochepin et al., 2008)

Clogging impact on diffusion	**HYTEC: Modified Archie's law** $D_e(\omega) = D_e(\phi_0)\left(\frac{\phi-\phi_c}{\phi_0-\phi_c}\right)^{\alpha}$ **D_e: effective diffusion coefficient** **ϕ_c: percolation threshold** **α: cementation factor**	**CrunchTope: Archie's Law** $D(\phi) = D_0\phi^m$ **D_e: effective diffusion coefficient** **m: cementation coefficient** **D_o: molecular diffusion coefficient**
Kinetic rate for precipitaiton $r_s = -A_s k_{rate}\left[1-\left(\frac{Q_s}{K}\right)\right]$ **Q_s: ion activity product** **K: mineral equilibrium constant** **A_s: specific surface area**	HYTEC $-A_{bulk}(m^2.m^{-3}_{solution}) = A_s C$ $A_s = 3/\rho r$ ρ: particle density *r:* radius of spherical particle *C:* Particle concentration	CrunchTope[12] $-A_{bulk}(m^2.m^{-3}_{porous\ medium})$ $= \left[\frac{\phi}{\phi_0}\right]^{2/3}$ ϕ_0: porosity

3.2 1D Numerical Modeling

3.2.1 Geometry and Boundary conditions

The barite and gypsum experiments are represented by a 1D closed system in both HYTEC and CrunchTope. This was done by maintaining zero gradient boundary conditions i.e. no transport of ions outside the discretized box in x. E.g. in CrunchTope, at the beginning and end of discretization in x (from upstream to downstream) the boundary condition was zero flux.

In HYTEC, the system is represented by a 1D chalk sample of length 6.7 mm. On each side of the sample, 1D reservoirs of length 1 mm are set. To account the larger volume of reservoirs used in experiments (i.e. upstream of 178 ml and downstream of 138 ml) a bypass technique was used: porosities in 1 mm reservoirs contained porosities equal to 18700 % for upstream and 14500 %

[12] In our calculations, the initial surface area used is 100 $m^2.m^{-3}$ until the volume fraction reaches the value defined by the user (*e.g.* 0.01% in input file in Appendix-3 and Appendix-4). Afterwards it evolves as $A=A_o(\phi/\phi_o)^{2/3}$

for downstream. This trick yields the correct volume (and contents in solutes) while maintaining a short distance and maximizing diffusion between the reservoirs and the chalk sample. Thus, for the total simulation time the homogenization of the solutes in each reservoir is ensured. The discretization at dx = 100 µm and a sensitivity analysis by reducing the length down to 25 µm was performed. In CrunchTope, the reservoir size (in x) was increased to account for the relative volume of the reservoir and chalk sample. The discretization is chosen at dx = 10 µm in the chalk sample, and larger cells are used in the reservoir. A progressive refinement of meshes allowed us to avoid too strong difference in the mesh sizes. The solute homogenization in the reservoir was ensured by increasing the molecular diffusion coefficients of solutes by factor of 1000 in both reservoirs.

3.2.2 Chemistry

The chemistry of reactants in upstream and downstream reservoirs for both experiments is taken from Table 1. Although calcite is present in the chalk minerals, it is non-reactive under the conditions of the experiment, so that it was only considered for its surface area and its impact on heterogeneous precipitation of barite and gypsum. The kinetics constant for barite and gypsum precipitation (listed in Table 3) are directly obtained from literature. For gypsum, the simulation is performed using the kinetic rate equation from Table 2. The kinetic rate law is set to represent homogeneous nucleation. In HYTEC, this is achieved by spraying the system with a fake mineral "nucleus" of low reactive surface area. This surface will then allow gypsum to precipitate over it. When the precipitation starts, gypsum will then use its own surface area to advance the precipitation. After the first nucleation, the precipitation occurs mostly on the gypsum surface, to the relative surface area and kinetic rate for nucleus and gypsum.

Table 3: Kinetic rate of precipitation and specific surface area for barite and gypsum mineral obtained from literature (Nagaraja, Abimanyu, Jung, & Yoo, 2007; Potgieter & Strydom, 1996; Zhang & Nancollas, 1992)

Mineral properties	k_{rate} mol m^{-2} s^{-1}	specific surface area (S_{sp}) m^2 g^{-1}
Barite	1 x 10^{-11}	0.32
Gypsum	1.5 x 10^{-6}	1.65

Both codes are able to take into account supersaturation criterion. When a mineral is present in a system, precipitation will occur (possibly under kinetic control) as soon a saturation is reached (saturation index ≥ 0). However, the first precipitate (initiation) can only occur if a supersaturation

in the solution can allow for the formation of first stable nuclei of mineral. These nuclei have to overcome the interfacial energy to achieve the stable form (Kashchiev and van Rosmalen, 2003; Prieto, 2014). Experimentally, the supersaturation state required for formation of such nuclei is 4.0 for barite (Prasianakis et al., 2017) and 0.1 for gypsum.

For CrunchTope, the following experimental data were numerically reproduced:

(1) The evolution of cumulative activity or concentration of the water tracers (tritiated or deuterated water) in the reservoirs as a function of time,

(2) The evolution of the reactant concentration (Ba, Ca and SO_4) in the reservoirs as a function of time,

(3) The change in porosity triggered by the reactions,

(4) The thickness of the precipitate front and its localization within the samples.

The CrunchTope simulations were performed using multicomponent diffusion. The diffusion coefficient values in bulk water of the water tracers (HTO and HDO) and ionic species at 21°C

Table 4: Input parameters obtained from literature for numerical simulations, (Barbier et al., 2009; Berthe, Savoye, Wittebroodt, & Michelot, 2011; Descostes et al., 2008; Li & Gregory, 1973)

Diffusion coefficients in bulk water $x10^{-9}$ m^2 s^{-1}	$D_0^{(HTO)}$ or $D_0^{(HDO)}$	$D_0^{(Ba2+)}$	$D_0^{(Ca2+)}$	$D_0^{(SO4--)}$	$D_0^{(Cl-)}$	$D_0^{(Na+)}$	$D_0^{(K+)}$	$D_0^{(HCO3-)}$
	2	0.85	0.79	1.07	1.77	1.18	1.96	1.18

For Hytec, the following experimental data were used for being numerically reproduced:

(1) The evolution of cumulative activity or concentration of water tracers (deuterated or tritiated water) in the reservoirs as a function of time,

(2) The evolution of the reactant concentration (Ba, Ca and SO_4) in the reservoirs as a function of time,

(3) The change in porosity and associated diffusion coefficient triggered by the reactions,

(4) The thickness of the precipitation front and its localization within the samples,

A unique diffusion coefficient value was used for all the species. The mineral phases considered in the two codes were calcite as the porous material, and either gypsum or barite as the precipitating phase with precipitation rates (k_{rate}) and specific surface areas listed in Table 3

3.2.3 Sensitivity Analysis

The experimental results showed different evolution of reactants in reservoirs in barite and gypsum case. These experiments also showed different saturation at which each mineral precipitated. Finally, two distinct impacts on diffusivity of water tracers were also observed. Thus, to properly reproduce the end experimental results, different sensitivity analyses were performed using HYTEC or CrunchTope.

These analyses included: (1) impact of the mesh size, by decreasing it from 100, 50 to 25 µm, (2) variation of the cementation factor with values varying from 1.5 to 2.1 and (3) test of the supersaturation values used to initiate the gypsum or barite precipitations, (4) progressive increase of $k_{rate,barite}$ to decrease the thickness of precipitate front in order to have a greater impact on diffusivity of HTO, (5) progressive increase of bulk surface area in reservoirs (from 0.0.0001 to 50,000 ($m^2_{mineral}$).($m^{-3}_{porous\ medium}$)) at constant $k_{rate,gypsum}$ (6) progressive decrease of $k_{rate,gypsum}$ at constant bulk surface area in reservoirs. Note that the base simulation for gypsum is not the best estimate: test of additional criteria (like the possibility for gypsum to precipitate in the reservoirs) finally lead to a correct simulation.

3.3 2D Numerical Modeling

The experimental results showed a spatial variability for the gypsum precipitated: isolated clusters roughly along the central plane. This obviously cannot be reproduced by a 1D simulation. Thus, 2D simulations were carried out including an initial spatial variability in the system. Thus, 2D numerical modeling was performed based upon the observations derived from the chalk experiments:

1. Barite precipitates were uniformly distributed along the center line of chalk sample;
2. Isolated pods of gypsum were formed along the center-line of chalk sample.

For gypsum, two hypotheses were then proposed to explain such a pattern:

1. A local variation in diffusion resulting from heterogeneous pore structure led to selective precipitation of gypsum;

2. A local variation in reactive surface area resulting from pores in grain matrix and coccoliths allowed additional surface for first points of precipitation.

In both cases, gypsum can then evolve from these first nuclei to form isolated pods.

3.3.1 Geometry

The initial and boundary conditions are kept identical to the 1D base simulations for barite and gypsum. However, the system in y-direction is increased up to 8 mm high. This constitutes a 2D system with discretization as 100 µm along x axis and y axis. Like the 1D simulations, the reservoirs are described with porosity greater than unit, to account for a larger volume, without having to resort to a too high number of nodes. Two types of heterogeneity were investigated:

- a heterogeneous initial “nucleus” surface area;

- a local variation in diffusion from initial heterogeneous porosity field in chalk sample

Table 5: Input parameters for gypsum growth in subset nucleus and subtest growth

	supersaturation	nucleus		Growth		Diffusion
		k_{rate} mol.m^{-2}.s^{-1}	S m^2.g^{-1}	k mol.m^{-2}.s^{-1}	S m^2.g^{-1}	D_e x10^{-10} m^2.s^{-1}
simulation nucleus	0.3	10^{-6}	100	10^{-6}	10	1.35
simulation growth	0.3	10^{-6}	1	10^{-6}	500	1.35

A random porosity field, without spatial structure, was generated with a normal distribution centered on 0.45, with a standard deviation 0.05. The diffusion was altered accordingly, using Archie’s law.

3.3.2 Geochemistry

The conditions are identical to the base 1D simulations used for barite and gypsum experiments.

4 Results

4.1 Base Simulations using HYTEC and CrunchTope

4.1.1 Barite Base Simulation

The 1D base scripts for barite case using HYTEC and CrunchTope simulation is reported in appendix S1 and appendix S3 respectively. The simulation results are presented in Figure 2 and Figure 3 respectively. As the numerical simulation starts, the reactants from their respective reservoirs diffuse into the chalk sample. As a result, the reactant concentration decreases in each reservoirs (Figure 2A and 2B, Figure 3B and 3C). Consequently, a diffusion profile can be observed for Ba^{2+} and SO_4^{2+} (Figure 2C). As more and more reactants meet in the sample, the saturation of pore solution in the center with respect to barite increases (Figure 2D). At one point, first nuclei of stable barite precipitate from this solution and the saturation falls below equilibrium. This allows for barite precipitation in a thin zone (Figure 2E) (inhibiting precipitation from first line of precipitation (Figure 2C)), with a resulting porosity loss (Figure 2F and Figure 3A). Consequently, a progressive decrease in diffusivity is observed in this thin precipitation zone (Figure 2F). The impact of decrease in porosity and diffusivity can be observed on the evolution of reactants in the reservoirs in response to precipitation over time. The concentration curves show a progressive concentration decrease of barium in upstream. After 60 days, gradually, barium concentration reaches quasi-equilibrium state showing that barite precipitates have filled most of the pores in the precipitated zone.

The total amount of barite precipitated in this zone was deduced from concentration evolution of reactants in the reservoirs. The base simulations shows that the code reproduces correctly the experimental data for chemistry evolution of both reactants (Figure 2A and 2B Figure 3B and 3C), and the thickness of precipitated zone obtained from SEM images in chalk paper is approximately equal to ~500µm, the 1D code reproduce similar width of precipitation zone) and amount of barite precipitated in this zone (Figure 2E). In the base simulation, the tracer behavior in downstream in response to barite precipitation were also estimated for injection at 0 days and 70 days after beginning of precipitation. The experimentally and numerically derived tracer behavior are compared (Figure 2G, 2H) at cementation factor 1.8 and at cementation factor 1.97 (Figure 3D, 3E) respectively. At cementation factor equal to 1.8 HYTEC fairly reproduced the water tracer behavior for injection at 0 days. The code well reproduced the water tracer behavior for injection at 70 days. But at cementation factor equal to 1.97, CrunchTope underestimated the impact of precipitation on the diffusivity of water tracers for both 0 to 70 days and 70 to 140 days.

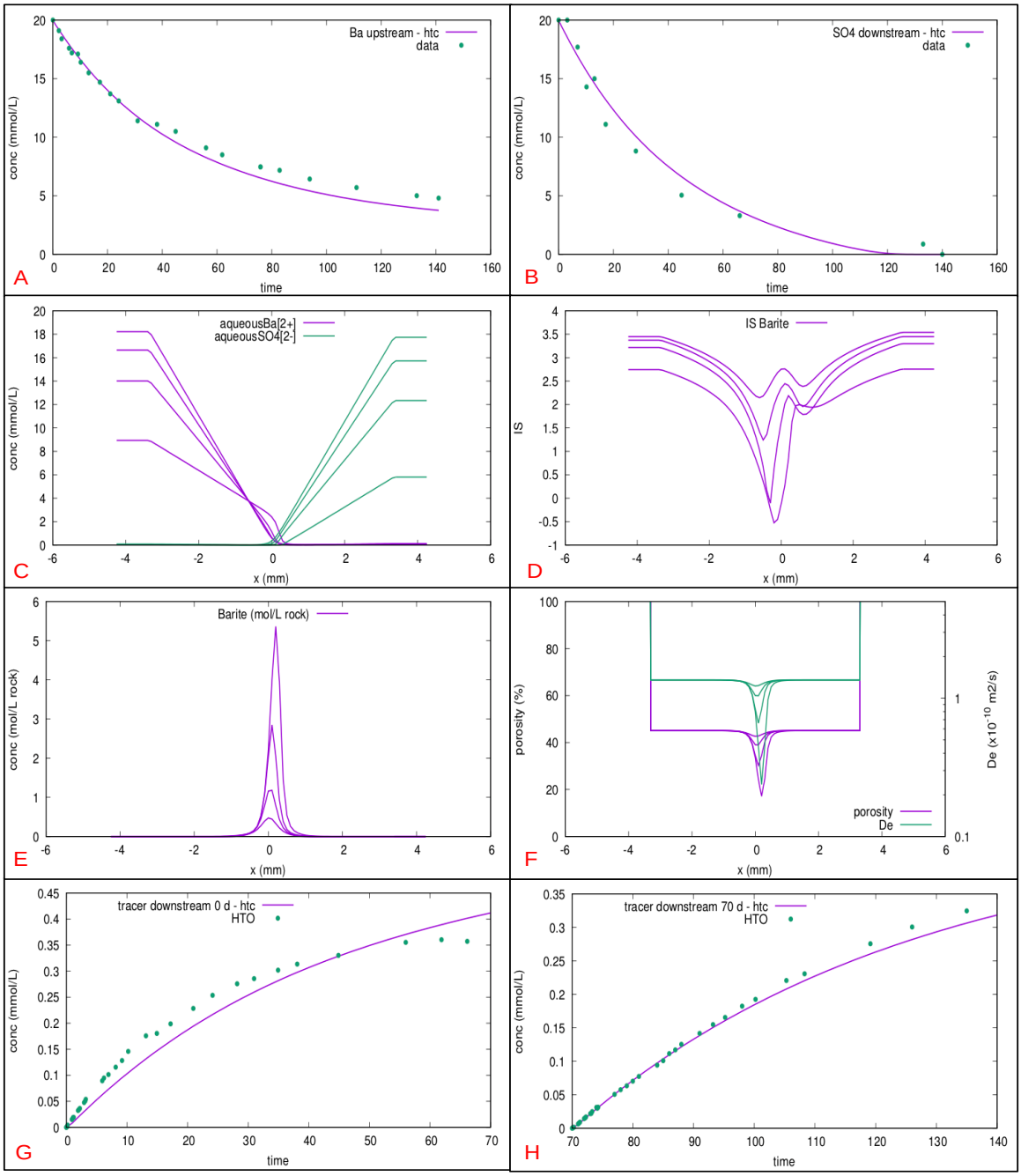

*Figure 2:comparison between HYTEC and experimental data for basic chalk barite simulation, concentration profiles for Ba^{2+} and SO_4^{2-} at 5, 10, 20 and 50 days, **A**: Ba^{2+} evolution in upstream reservoir, **B**: SO_4^{2-} evolution in downstream reservoir, **C**: concentration profiles for Ba^{2+} and SO_4^{2-} in the center of the sample at 5, 10, 20 and 50 days **D**: barite saturation index at 5, 10, 20 and 50 days in the precipitation zone, **E**: barite concentration evolution at 5, 10, 20 and 50 days after precipitation in thin zone in the center of the sample, **F**: evolution of barite has led to a progressive porosity decrease in the center of the sample , consequently decrease of diffusivity of water tracer in this zone is observed at each time step, **G,H**: Experimental (green circles) and numerical(continuous line) water tracer evolution in downstream reservoirs for water tracer injected at 0 days and 70 days after barite precipitation.*

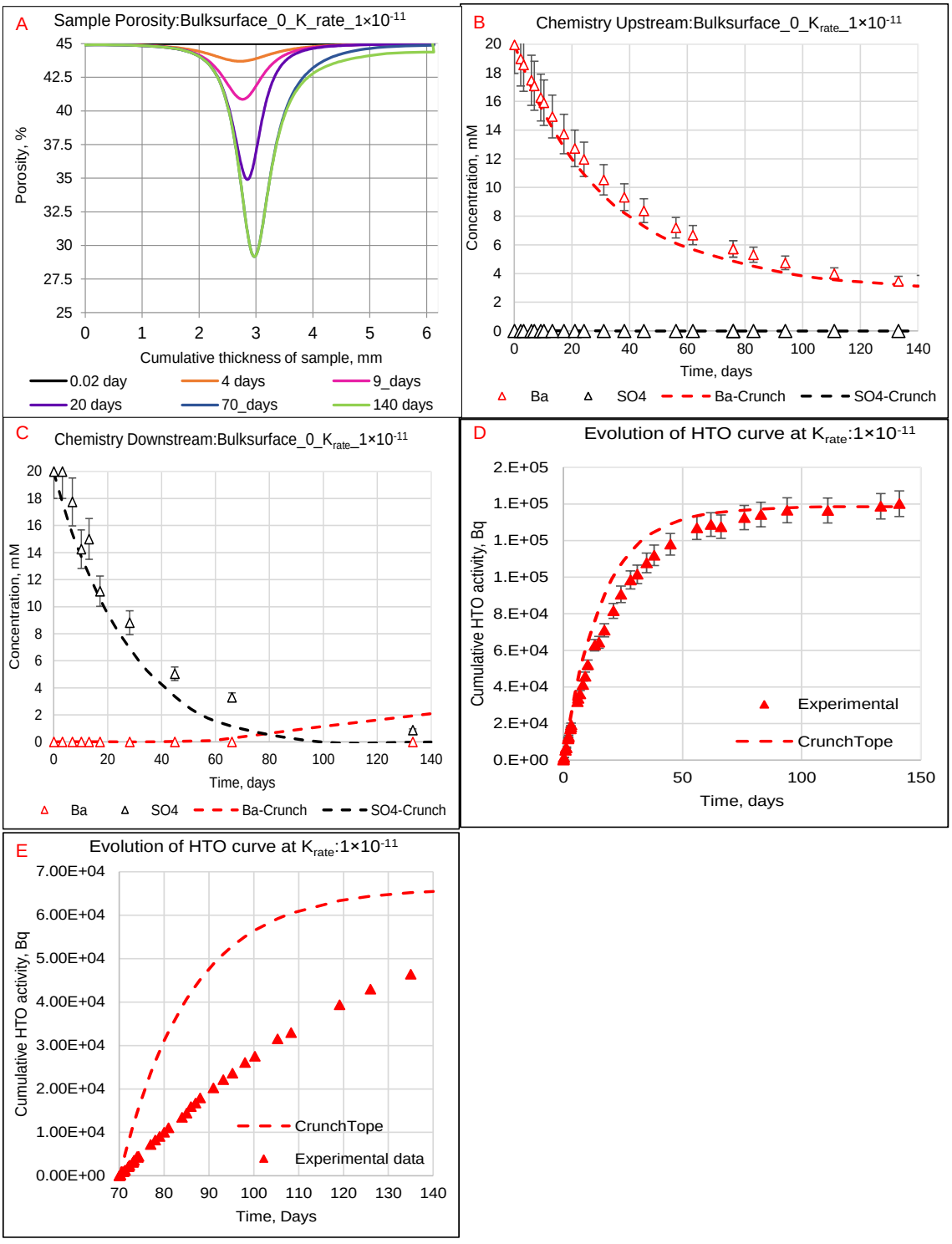

Figure 3: comparison between CrunchTope and experimental data for basic chalk barite simulation, ***A:*** *Porosity reduction at times 0.02, 4, 9, 20 70 and 140 days due to barite center of chalk sample,* ***B****: Numerical and experimental evolution of barium and sulfate data points in upstream reservoir,* ***C****: Numerical and experimental evolution of barium and sulfate data points in downstream reservoir,* ***D****: numerical simulation of HTO activity for 0-70 days,* ***E****: numerical simulation of HTO activity for 70-140 days*

4.1.2 Gypsum Base Simulation

The 1D base scripts for modeling gypsum experiment using HYTEC and CrunchTope are reported in appendix S2 and appendix S4 respectively. The gypsum experiments showed that precipitation had little impact on diffusivity of tracers injected after 0 days and 70 days of precipitation. Thus, the base simulation for HYTEC was performed without feedback, i.e cementation factor equal to 0. But for CrunchTope, the simulations were performed at cementation factor equal to 1.97, with feedback effect.

The numerical simulations show that counter diffusing calcium and gypsum meet in the center of the sample (Figure 4B). At the beginning of experiment the saturation increases up to zero (Figure 4A and Figure 5A). As the experiment further progresses in the center of the sample, more and more Ca^{2+} and SO_4^{2-} form gypsum and saturation index (SI) increase up to 0.1 is observed. Indeed, due to this process, precipitation is forbidden until the correct supersaturation is reached; after that, precipitation occurs rapidly (fast kinetics), locally, down to SI = 0. As a result, when this supersaturation is reached, gypsum starts precipitating and locally decreases the SI; diffusion propagates this lowered SI, preventing precipitation further form this point (the reactants are pumped in towards the first grains). This effect is highlighted on the sensitivity analysis on supersaturation (see next section). Moreover, once gypsum precipitation is initiated a progressive increase of gypsum mineral in the chalk sample takes place at each time step (evolution of two adjacent peaks in Figure 4C and a broadened peak in Figure 5C).

However, a delay in time to achieve saturation to initiate precipitation was observed. This delay in gypsum precipitation is due to its higher solubility than barite. Thus, the saturation index to initiate precipitation is achieved at longer times (as $K_{sp}^{gypsum} = 10^{-4.58}$, more calcium and sulfate ions are needed to achieve ion activity product (IAP) = K_{sp} or SI=0). Consequently, the formation of first stable nuclei to initiate precipitation is delayed compared to barite case (see time at which first gypsum precipitates in Figure 5C). This delay further allowed diffusion of reactants in the counter reservoirs until no precipitation takes place (Figure 4D, 4E and Figure 5E, 5F). Once precipitation is initiated the reactants are consumed and no further evolution in counter reservoirs is observed (after 20 days the reactants reach a plateau at 13 mmol and their concentration remains around this value in the counter reservoir).

For HYTEC, the evolution of reactants in their respective reservoirs were well reproduced (Figure 4D). But their evolution in counter reservoirs was overestimated (Figure 4E). On the contrary, for CrunchTope the evolution of calcium in upstream was well reproduced and the evolution of sulfate in downstream was overestimated. Finally, when chemistry feedback is taken into account, the

evolution of reactants in counter reservoirs was better reproduced compared to HYTEC simulation. This discrepancy between chemistry evolutions observed experimentally and numerically can be due to gypsum precipitation in reservoirs. Indeed, some experimental evidence of gypsum precipitation in both reservoirs were found which is bound to decrease the reactant concentrations. Since the model did not allow for gypsum precipitation in the reservoirs, no precipitation could occur (Figure 4C and Figure 5B and 5D). This difference can account for the discrepancy between simulation and observation: it will be addressed in 4.1.4.1. The tracer behavior for injection at 0 days and 70 days after gypsum precipitation were numerically reproduced in the base simulation (CrunchTope). At cementation factor 1.97, the code well reproduced the experimentally derived precipitation impact on diffusivity of water tracer for both cases (refer Figure 4G & 4H).

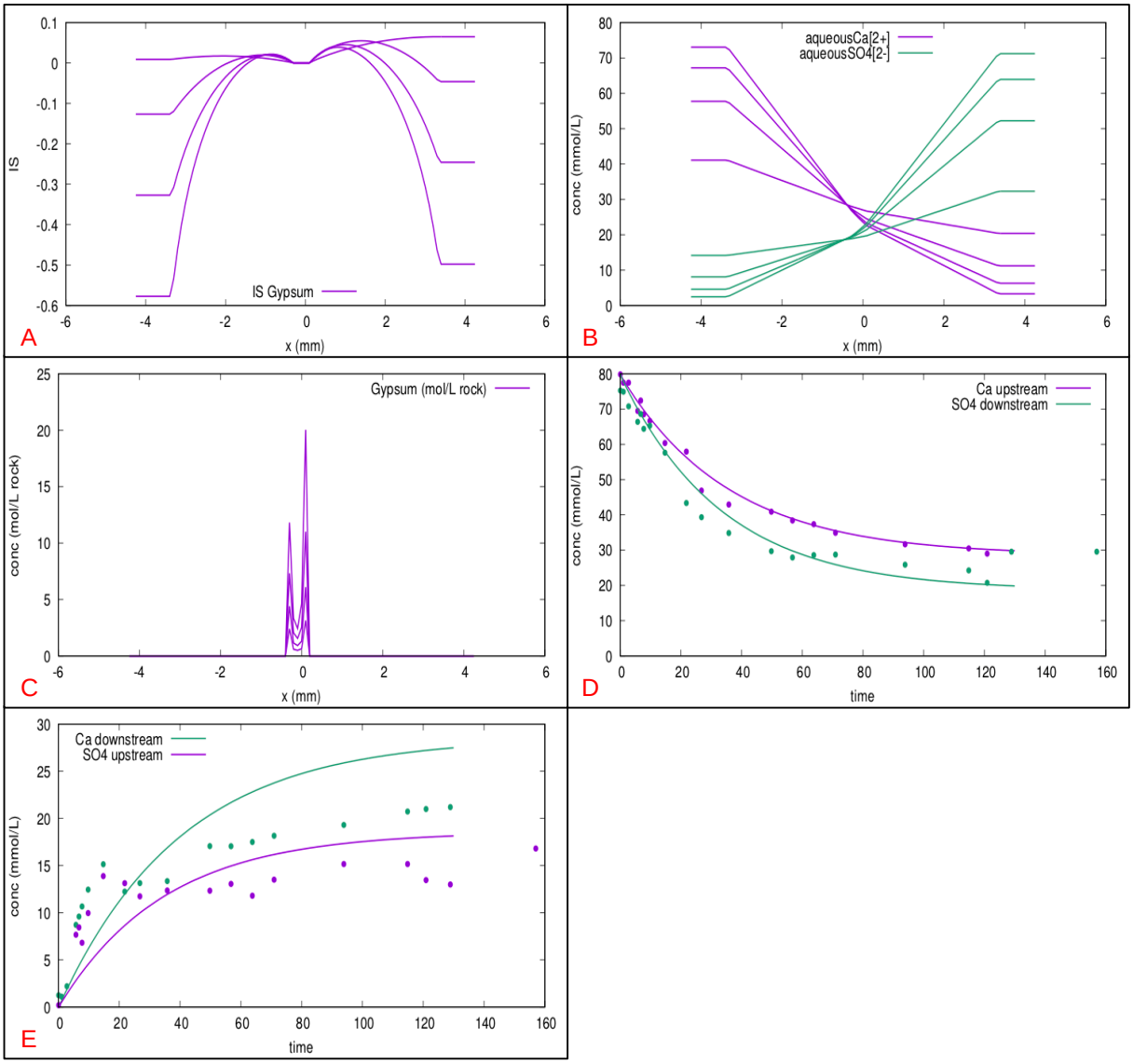

Figure 4: comparison between HYTEC and experimental data for basic chalk gypsum simulation, ***A****: gypsum saturation index at 5, 10, 20 and 50 days in the precipitation zone,* ***B:*** *concentration profiles for* Ca^{2+} *and* SO_4^{2-} *at 5, 10, 20 and 50 days,* ***C:*** *gypsum concentration profile in the center of the sample at 5, 10, 20 and 50 days,* ***D****: evolution of* Ca^{2+} *in upstream reservoir and* SO_4^{2-} *in downstream reservoir,* ***E****: evolution of* SO_4^{2-} *in upstream reservoir and* Ca^{2+} *in downstream reservoir*

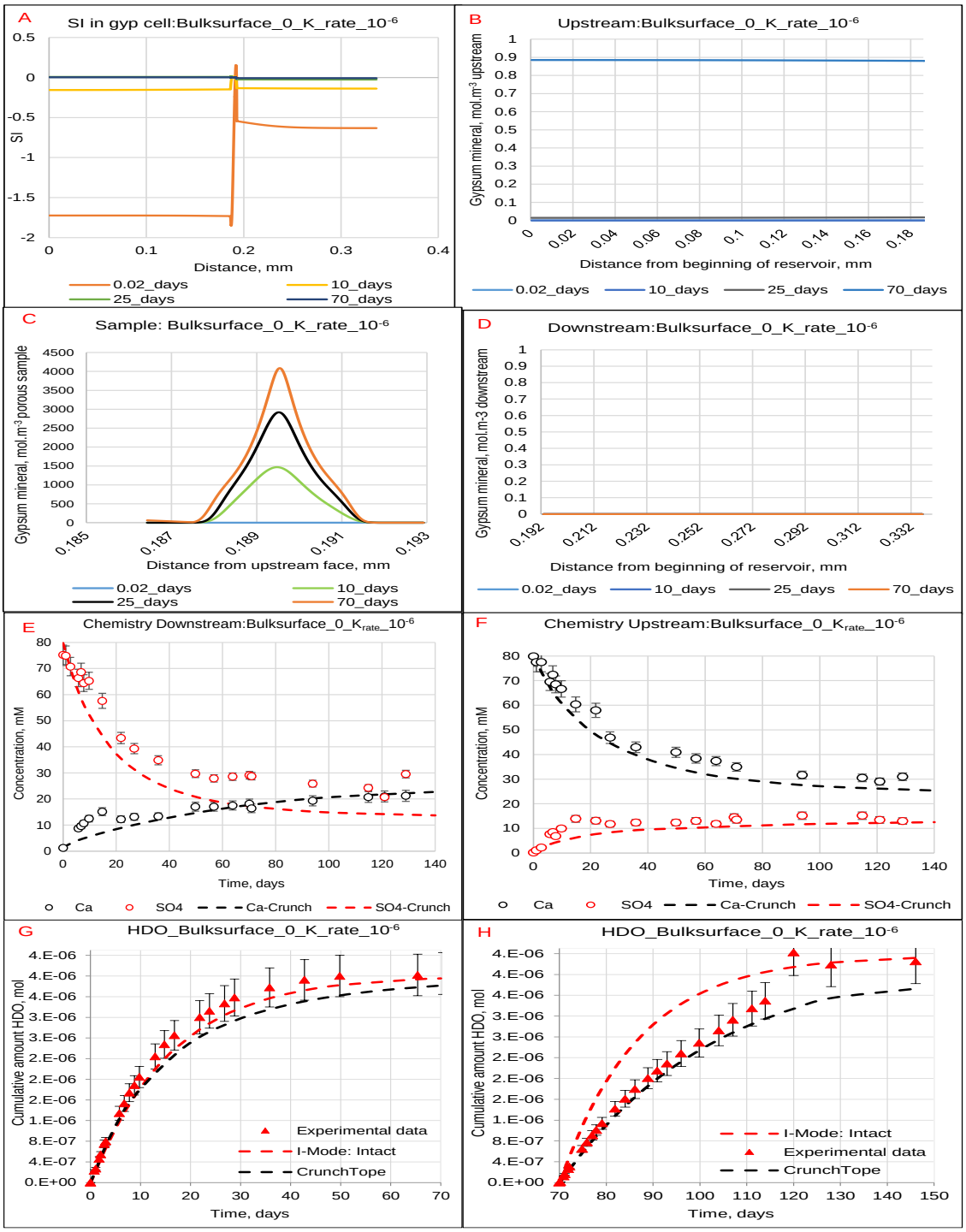

Figure 5: comparison between CrunchTope and experimental data for basic chalk gypsum simulation, ***A:*** *Saturation index of gypsum mineral in two reservoirs and chalk sample,* ***B****: Very small amount of gypsum mineral precipitating in upstream,* ***C****: Gypsum precipitation zone in the center of the sample,* ***D****: No gypsum precipitation in downstream,* ***E****: numerical simulation of* Ca^{2+} *&* SO_4^{2-} *in downstream reservoir,* ***F****: numerical simulation of* Ca^{2+} *&* SO_4^{2-} *in upstream reservoir,* ***G****: numerical simulation of HDO concentration for 0-70 days,* ***H****: numerical simulation of HDO concentration for 70-140 days*

4.1.3 Sensitivity analysis for barite

4.1.3.1 Effect of the mesh size

A sensitivity analysis was performed by changing the mesh size from 100 µm (base simulation) to 50 µm and 25 µm respectively. The impact of mesh size on evolution of reactants in reservoirs and on the evolution of precipitation front in the center of the sample is presented in Figure 6(A to F). Figure 6D shows that the difference in impact of decrease in mesh size from 100µm to 50µm on the width of the precipitation front is small. Moreover, Figure 6D shows that the decrease in porosity and diffusivity in the precipitated zone for 100µm and 50µm case are similar. Thus, for these two mesh sizes the reactants evolution in reservoirs estimated by code are similar (Figure 6A & 6B). However for 25 µm, as shown in Figure 6D an entailed (small) re-concentration of the solid on a thinner area in the center of the sample has significant impact on diffusivity and porosity decrease in Figure 6C. Consequently, after 60 days, total clogging is reached and no further evolution the system occurs for 25 µm case (Figure 6A and 6B).

Moreover, at the same cementation factor the grid size showed similar tracer behavior for injection at 0 days after precipitation (Figure 6E). However, for injection after 70 days of precipitation, the grid size had very different impact the tracer behavior (Figure 6F). At grid size 100µm and 50µm a small difference in tracer behavior was observed and at 25µm the code showed no tracer behavior (resembling total clogging). Finally, for all cases the code underestimated the precipitation impact on diffusivity for each mesh size.

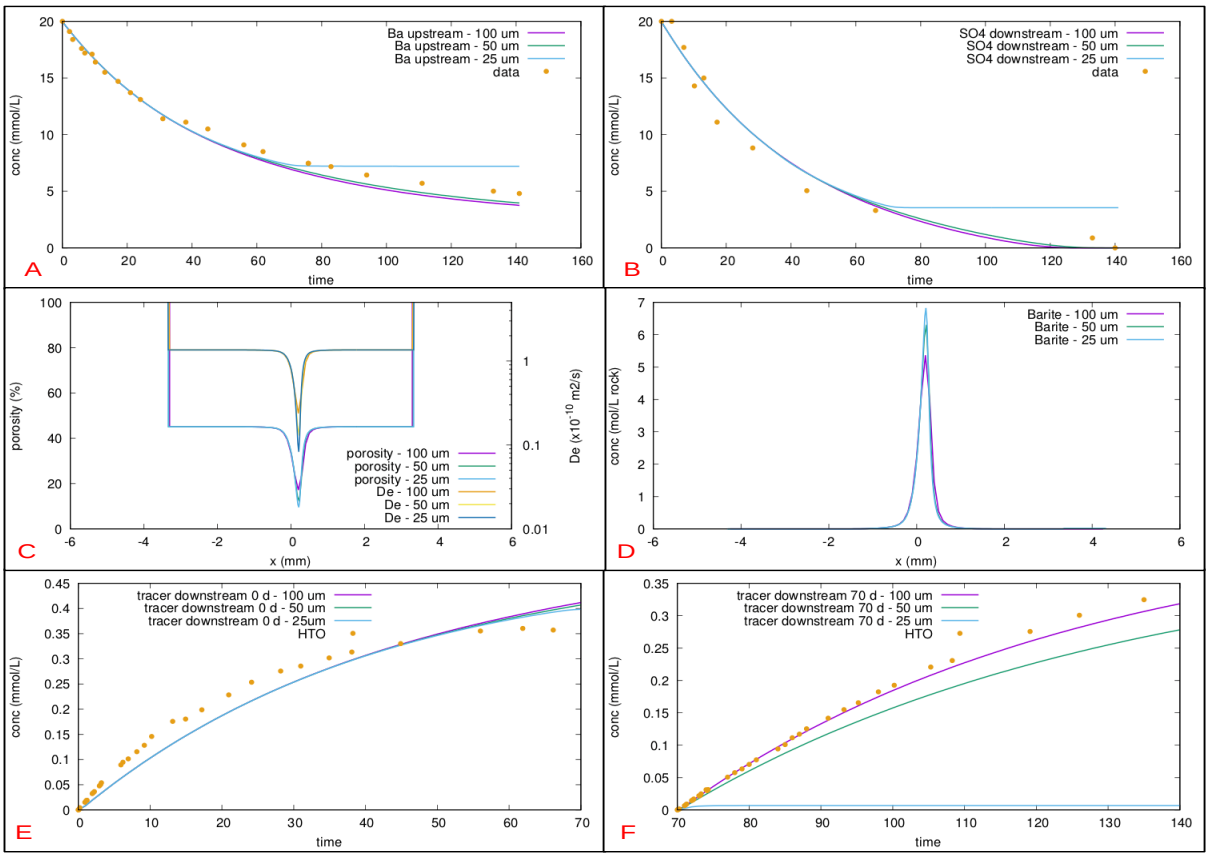

Figure 6: Sensitivity analyses at different mesh size on basic chalk barite simulation, ***A****: Ba^{2+} evolution in upstream reservoir at different mesh sizes,* ***B****: SO_4^{2-} evolution in downstream reservoir at different mesh sizes,* ***C****: concentration profiles for Ba^{2+} and SO_4^{2-} at 5, 10, 20 and 50 days shows small entailed reconcentration of mineral for 25µm mesh size,* ***D****: simulations at 100µm and 50µm shows a similar progressive porosity decrease at times 5, 10, 20 and 50 days in the center of the sample, at 25µm higher porosity and diffusivity decrease are observed,* ***E****: numerical(full lines) simulations show no impact of mesh size on tracer behavior for injection at 0 days of precipitation,* ***F****: numerical(full lines) simulations show significant impact of mesh size on tracer behavior for injection at 70 days of precipitation*

4.1.3.2 Effect of the cementation factor

In barite experiments the chemistry monitoring showed a gradual barium concentration decrease for initial 60 days in upstream. At this time as the precipitated zone contains mostly empty or partially filled pores the barium ion can diffuse through the precipitated zone. This ion will then contribute to precipitation around the main precipitation line (the SEM images in chalk paper shows formation of isolated barite precipitates around main precipitated line). The impact of barite precipitation for initial times was captured by injecting the water tracer at beginning of experiment. In this step water tracer was injected in upstream at 0 days of precipitation and its activity evolution

was measured in downstream for 70 days. The data points in downstream were then fitted using I-mode to obtain water tracer diffusivity equal to 2.5×10^{-10} $m^2.s^{-1}$. Thus, using Archie's law the change in cementation factor compared to intact case (1.97) is equal to 2.08. This observation shows that the partially filled or empty pores at initial that allowed barium diffusion at initial times also allowed water tracer to diffuse. Since diffusion of water tracer is faster than precipitation kinetics of barite, the water tracer achieved equilibrium in downstream before most of the pores were filled by barite in the precipitation zone.

However, the chemistry monitoring further showed that after 60 days a gradual plateau was achieved in barium concentration in the upstream reservoir. This change from gradual concentration decrease to attainment of concentration plateau shows that most of the partially and unfilled pores are now filled with barite which can now effectively block important diffusive pathways. This change in barium ion behavior in response to precipitation was well captured by water tracer injection after 70 days of precipitation. Similar to injection at beginning of experiment case, the experimental data points of water tracer were reproduced using I-mode. The resulting water tracer diffusivity was equal to 1.1×10^{-10} $m^2.s^{-1}$ and using Archie's law the new cementation factor was equal to 3.6. These observations show that after 60 days most of the pores in the center of the sample were filled with barite. These pores significantly blocked barium ion diffusion and water tracer diffusion through the precipitation zone. Thus, barium ion plateau in upstream and significant impact on diffusivity was observed. The chemistry monitoring and water tracer behavior thus shows two different evolution of chalk cementation factor in response to precipitation.

To capture these aforementioned process (evolution of chemistry in reservoirs, thickness of precipitation front and consequently on diffusivity of water tracers) numerically a sensitivity analysis was performed on cementation factor. Based on the base simulation, the cementation factor varied from 1.8 (base) down to 1.5 and up to 2.1. Figure 7A and 7B shows that for values between 1.5 and 2, a very small difference in the impact on evolution of reactants evolution in reservoir is observed. However, at cementation factor value 2.1, total clogging is reached around 80 days, with no further evolution of the system.

Figure 7C shows that as the cementation increases, the entailed re-concentration in very thin zone increases in the center of the sample. Consequently, a sharp decrease in porosity and diffusivity is observed in this zone (Figure 7D). The change in cementation factor from 1.5 to 2.1 has no significant impact on modeled diffusive curves for 0 to 70 days (Figure 7E). However, at cementation factor 2 and 2.1, a sharp change is observed in the modeled diffusive curve for and 70 to 140 days case (Figure 7F). The increase in the sensitivity of cementation factor in the latter

case can be explained from experimental observations. The codes showed porosity evolution for first 70 days of precipitation. Thus, for this period the grids in the precipitation zone are either partially filled or completely unfilled. Since numerically no impact on diffusivity was observed the change in cementation factor had no influence on the water tracer behavior. But, at 70 days different entailed (re)concentration of barite in thin zone was observed for each cementation factor. This means that at higher cementation factor more barite has precipitated in the thin zone and led to higher porosity and diffusivity decrease in this thin zone. In this case the change in cementation factor can drastically change the properties of barite precipitated chalk. For this reason, a small change of cementation factor and generated different water tracer behavior.

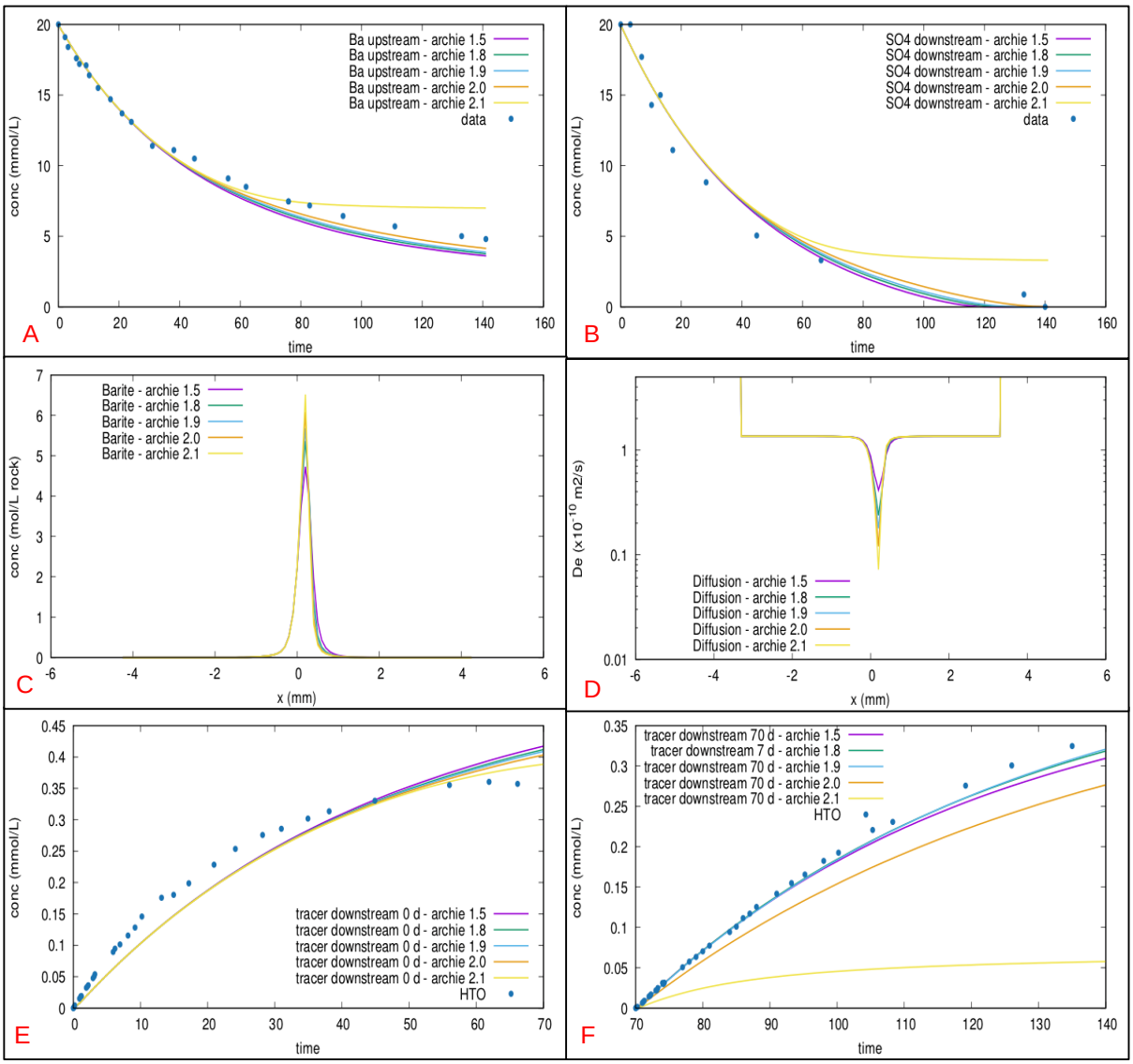

Figure 7: Sensitivity analyses at different cementation factors on basic chalk barite simulation, ***A****: Ba^{2+} evolution in upstream reservoir,* ***B****: SO_4^{2-} evolution in downstream reservoir,* ***C****: concentration profiles for Ba^{2+} and SO_4^{2-} at 5, 10, 20 and 50 days shows small entailed reconcentration of mineral at cementation factor equal to 2.1for 25µm mesh size,* ***D****: simulations at cementation factor values between 1.5 and 2 show a similar progressive porosity decrease at times 5, 10, 20 and 50 days in the center of the sample, at cementation factor equal to 2 higher porosity and diffusivity decrease are observed,* ***E****: numerical(full lines) simulations show no impact of cementation factor on tracer behavior for injection at 0 days of precipitation,* ***F****: numerical(full lines) simulations show significant impact of cementation factor on tracer behavior for injection at 70 days of precipitation*

4.1.3.3 Effect of Supersaturation

The third sensitivity analyses for barite case was impact of supersaturation on precipitation. For this purpose, two simulations were launched: supersaturation was equal to zero in the first and four in the second. Figure 8A shows that supersaturation has no impact on the evolution barite mineral in the center of the sample. Consequently, no impact on porosity and diffusivity decrease was observed in this zone (Figure 8B). Similarly, the evolution of barium in upstream in response to supersaturation is the same for both cases (Figure 8C and 8D). Thus, no change in modeled water tracer curve in downstream for 0 to 70 days case is observed. (Figure 8E).

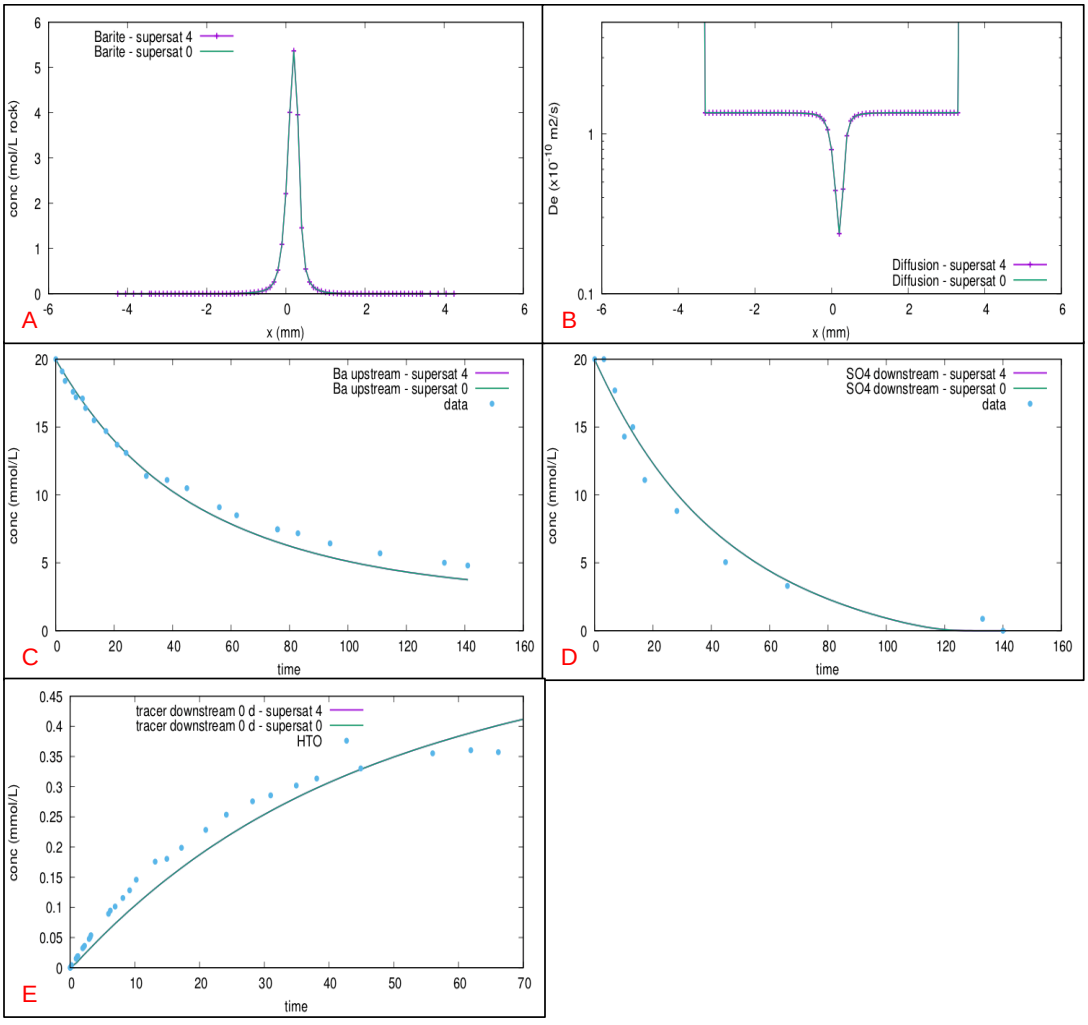

*Figure 8: supersaturation sensitivity analysis, **A**: concentration profiles for barite in the center of the sample at 50 days for the two supersaturation values, **B**: decrease in diffusion coefficient in center of the sample for 50 days, **C**: evolution of Ba^{2+} in upstream reservoir, **D**: evolution of SO_4^{2-} in downstream reservoir **E**: evolution of water tracer in downstream for time 0 to 70 days since beginning of experiment, **F**: numerical(full lines) simulations show no impact of supersaturation on tracer behavior for injection at 0 days of precipitation*

4.1.3.4 *Effect of mineral precipitation rate value*

In the base simulation (see section 4.1.1), CrunchTope well reproduced the chemistry evolution in reservoirs but underestimated the impact of clogging on diffusion. In section 4.1.3.2 to properly fit the diffusive curves a sensitivity analysis in HYTEC was launched by changing cementation factors. These simulations showed that at higher cementation factor, an entailed re-concentration in very small area can lead to significant impact on diffusivity.

Another way to generate such entailed re-concentration of barite in precipitation zone is by slightly increasing the $k_{\_rate}$ (or mathematically equivalently the specific surface area). Thus, CrunchTope simulations were launched for different k_{rates} in an interval between $k_{rate} = 10^{-11}$ and $k_{\_rate}$ 10^{-10} $mol.m^{-2}.s^{-1}$ respectively. The results for k_{rate} equal to 10^{-10} shows a progressive porosity decrease for initial numerical times (Figure 9A). However, on 70th day the entailed re-concentration of barite has led to total clogging in a very thin zone in the center of the sample. This effect is observed in chemistry evolution in reservoirs (Figure 9B and 10C). For the initial time until 30 days, barium and sulfate concentration decrease is observed in their respective reservoirs. From 30th day until end of simulations no further reactants concentration decrease is observed in their respective reservoirs showing total clogging effect. Moreover, for initial 30 days, the code underestimates the precipitation impact on water tracer behavior (Figure 9D), after which no tracer diffusion is observed in the downstream reservoir. Finally, at different k_{rates}, for 70 to 140 days, the code failed to reproduce the tracer behavior determined experimentally (Figure 9E).

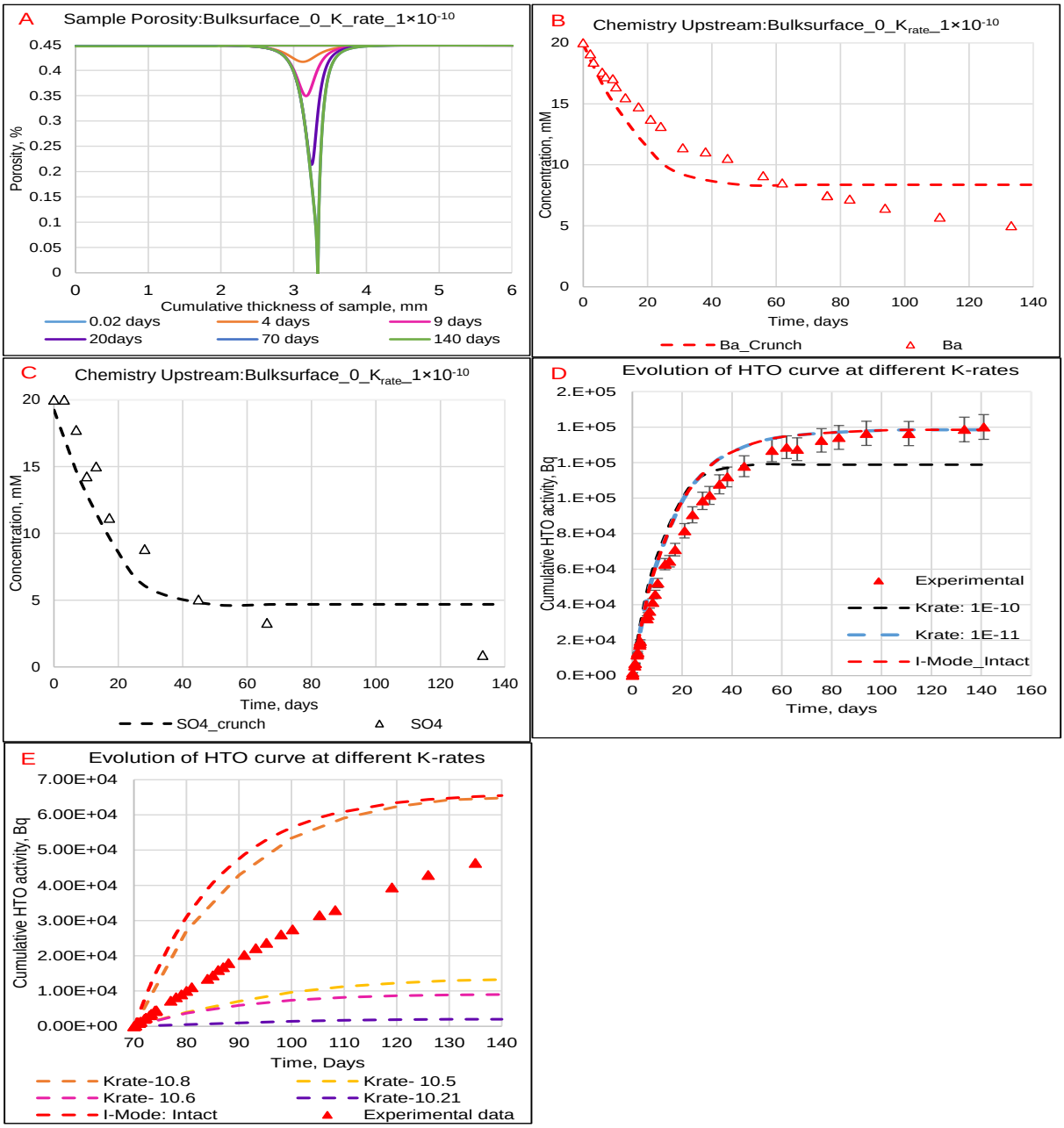

*Figure 9: Mineral precipitation rate sensitivity analysis, **A**: Total clogging due to barite precipitation in the center of chalk sample at higher k_{rate}, **B**: Numerical and experimental evolution of barium concentration in upstream reservoir, **C**: Numerical and experimental evolution of sulfate concentration in downstream reservoir, **D**: numerical simulation of HTO activity for 0-70 days at two different k_{rates}, **E**: numerical simulation of HTO activity for 70-140 days at different k_{rates}*

4.1.4 Sensitivity analysis for gypsum

4.1.4.1 Effect of supersaturation

To test the impact of supersaturation on precipitation, the base simulation was carried out without supersaturation effect. The evolution of saturation index and gypsum precipitation front in the center of the sample is presented in Figure 10(A to E) respectively. Figure 10A shows a gradual increase in saturation index in the chalk sample. However, throughout the simulation the saturation index neither increases nor decreases but remains at equilibrium (SI=0). This means that without supersaturation gypsum can start precipitating as soon as SI=0. In this case, there is “no pumping in effect,” so that the reaction front is much larger (Figure 10C). The simulation is very sensitive to the value of supersaturation: indeed, for supersaturation SI=0.6, the system fails to reach this saturation so that no precipitation occurs at all (not shown). Finally, the simulations without supersaturation effect led to similar evolution of calcium and sulfate concentration evolution in precipitation zone, in respective and counter reservoirs (Figure 10B, 10D and 10E)..

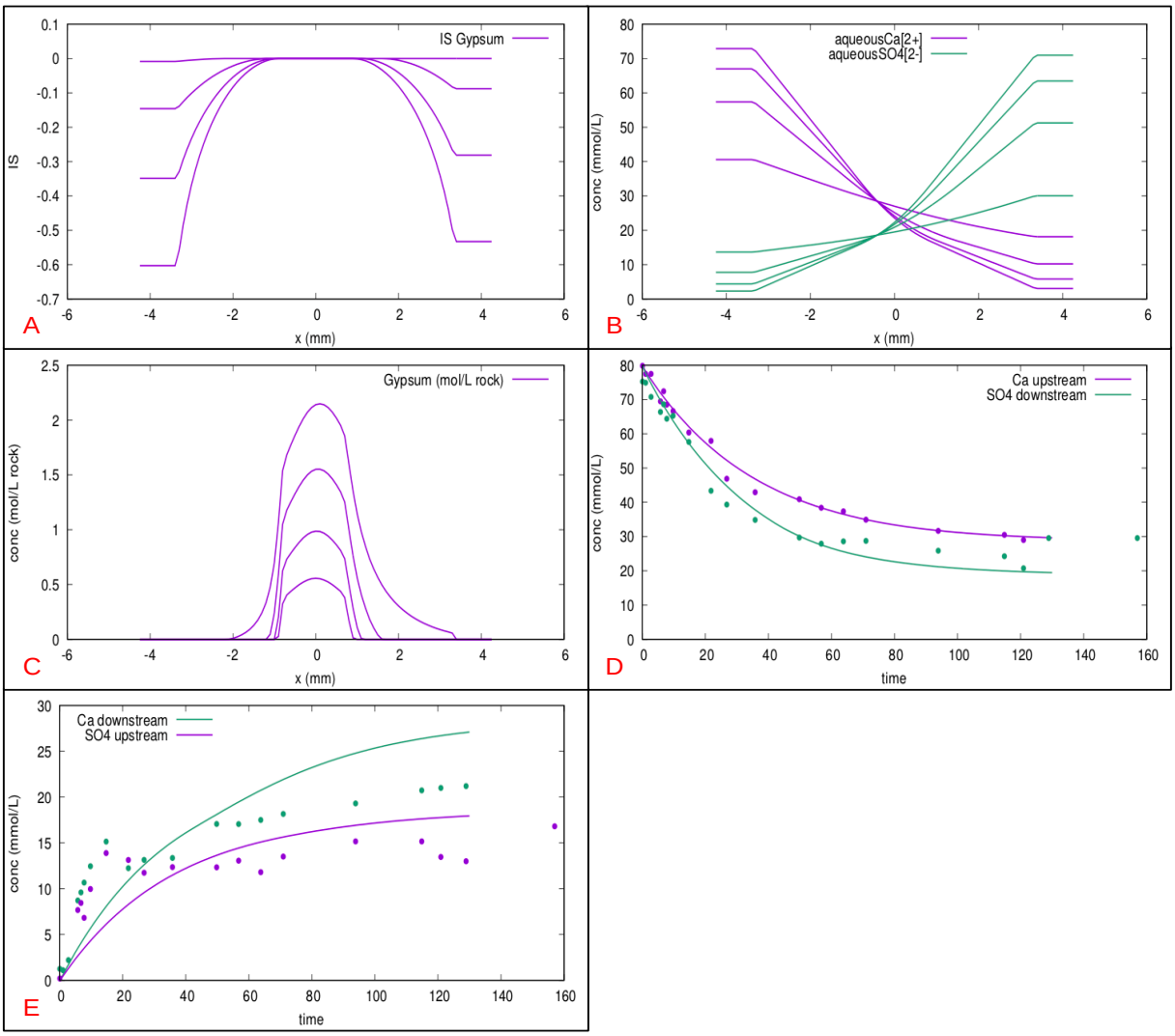

*Figure 10: supersaturation sensitivity analysis, **A**: Gypsum simulation without supersaturation shows that gypsum can precipitate as soon as saturation is reached (hence SI<=0 everywhere), **B**: concentration profiles for Ca^{2+} and SO_4^{2-} at 5, 10, 20 and 50 days, C:Gypsum concentration profiles at 5, 10, 20 and 50 days shows broadening of precipitation zone in the center of the sample, **D**: evolution of Ca^{2+} in upstream reservoir and SO_4^{2-} in downstream reservoir, **E**: evolution of SO_4^{2-} in upstream reservoir and Ca^{2+} in downstream reservoir*

4.1.4.2 Precipitation in reservoirs

In section 4.1.2, the base simulations with no feedback well reproduced the evolution of reactants in their respective reservoirs. However, the code overestimated their evolution in counter reservoirs. This is because experimentally gypsum precipitated in the reservoirs, but numerically no such precipitation was observed. Thus, a simulation using the base simulation is carried out in this section to allow precipitation in the reservoirs. This is achieved by adding some reactive surface area favorable to gypsum precipitation in the reservoirs.

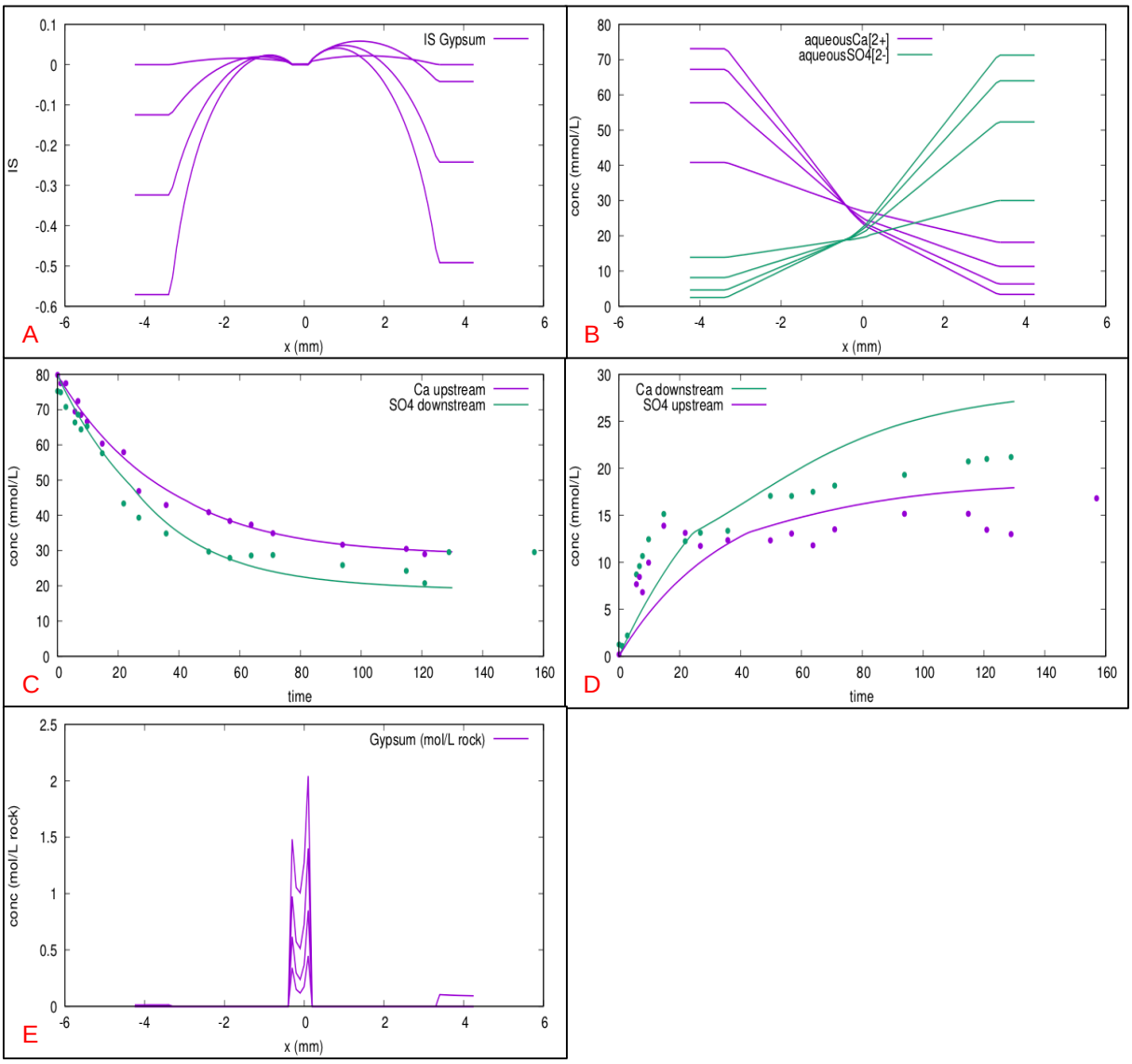

Figure 11: gypsum precipitation allowed in the reservoirs. ***A****: gypsum saturation index at 5, 10, 20 and 50 days in the precipitation zone,* ***B****: concentration profiles for Ca^{2+} and SO_4^{2-} at 5, 10, 20 and 50 days,* ***C****: evolution of Ca^{2+} and SO_4^{2-} diffusing in the sample,* ***D****: evolution of Ca^{2+} and SO_4^{2-} diffusing out of the sample,* ***E****: gypsum concentration profiles at 5, 10, 20, 50 days*

Figure 11A, shows that the added reactive surface has no impact on the evolution of saturation with respect to gypsum in the precipitation zone. Similarly, Figure 11E shows that due to presence of this reactive surface area some precipitation is indeed achieved in the reservoirs. It is difficult to calibrate the simulation due to the lack of experimental data (e.g. amount of gypsum precipitated in the reservoir). Although the Ca^{2+} and SO_4^{2-} evolution is still not perfectly represented in their respective outlet reservoirs. It is interesting to note that this process leads to discontinuity in the slope which has been observed in the experiments after 20 and 40 days (Figure 11D).

Similar to former case, bulk surface area ranging from 0.00001 to 50,000 ($m^2_{mineral}.m^{-3}_{porous\ medium}$) were added in the upstream and downstream reservoirs to achieve precipitation in reservoirs. In this report the chemistry evolution, gypsum mineral evolution in samples and reservoirs for bulk surface area 50,000 ($m^2_{mineral}.m^{-3}_{porous\ medium}$) are presented in Figure 12. These figures show very small amount of gypsum precipitation in upstream and no precipitation in downstream. The gypsum mineral evolution in chalk sample remains the same as in the base simulation. Thus, HYTEC and CrunchTope simulations show that by only adding reactive surface area in the reservoirs significant precipitation cannot be achieved. Although delay in gypsum precipitation led to diffusion of reactants in counter reservoirs, but once gypsum precipitation is initiated in the chalk sample, the fast kinetics of gypsum pumps in all the reactants in the precipitation zone. Thus, precipitation further stops enough ions to diffuse into the counter reservoirs which can allow higher amount of gypsum precipitation.

This can be achieved by gradually decreasing the theoretical kinetic rate (10^{-6} $mol.m^{-2}.s^{-1}$) in base simulation until significant precipitation in reservoirs is achieved. This main idea behind this approach was to slow down formation of gypsum in chalk sample. This would then allow more reactants to diffuse into counter reservoir. Finally, using the bulk surface area these reactants can allow higher gypsum precipitation in reservoirs. The numerical results for gypsum experiment at the kinetic rate of precipitation $10^{-7.7}$ $mol.m^{-2}.s^{-1}$ and bulk surface area 300 ($m^2_{mineral}$).($m^{-3}_{porous\ medium}$)are presented in Figure 13. Figure 13A shows that decrease in k_{rate} has no impact on the saturation index of gypsum precipitation. Figure 13B and 13D shows that at lower k_{rate} the bulk surface area is now sensitive and significant gypsum precipitated in reservoirs. However, Figure 13C shows that the thickness of gypsum precipitation zone is broadened in the chalk sample. Moreover, Figure 13E and 13F shows that the code well reproduced calcium evolution in upstream, but it overestimated the sulfate evolution in downstream. The code well reproduced the reactants evolution in counter reservoirs. Thus, tracers were injected in upstream at 0 days and 70 days after precipitation. The water tracer behavior in downstream is presented in Figure 13G and 13H respectively. Figure 13G shows that the code well reproduced the precipitation impact on diffusivity for 0 to 70 days. However, Figure 13H shows that the code underestimated the precipitation impact on diffusivity for 70 to 140 days. The latter observation contradicts the tracer behavior observed in Figure 5H for the base simulation.

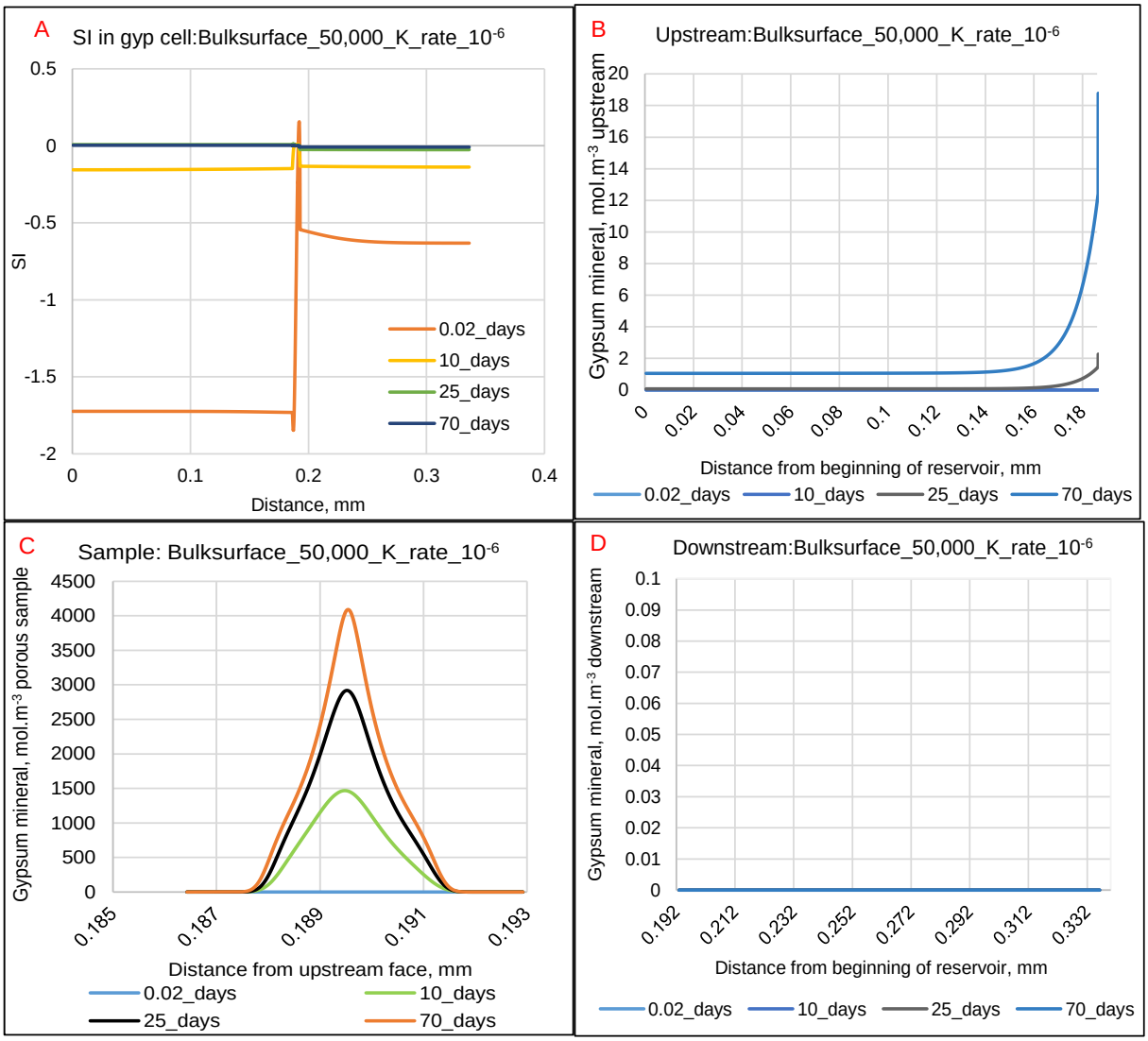

*Figure 12: bulk surface sensitivity in reservoirs, **A**: Saturation index of gypsum mineral in two reservoirs and chalk sample; **B**: Very small amount of gypsum mineral precipitating in upstream at very high bulk surface area; **C**: Gypsum precipitation zone in the center of the sample; **D**: No gypsum precipitation in downstream*

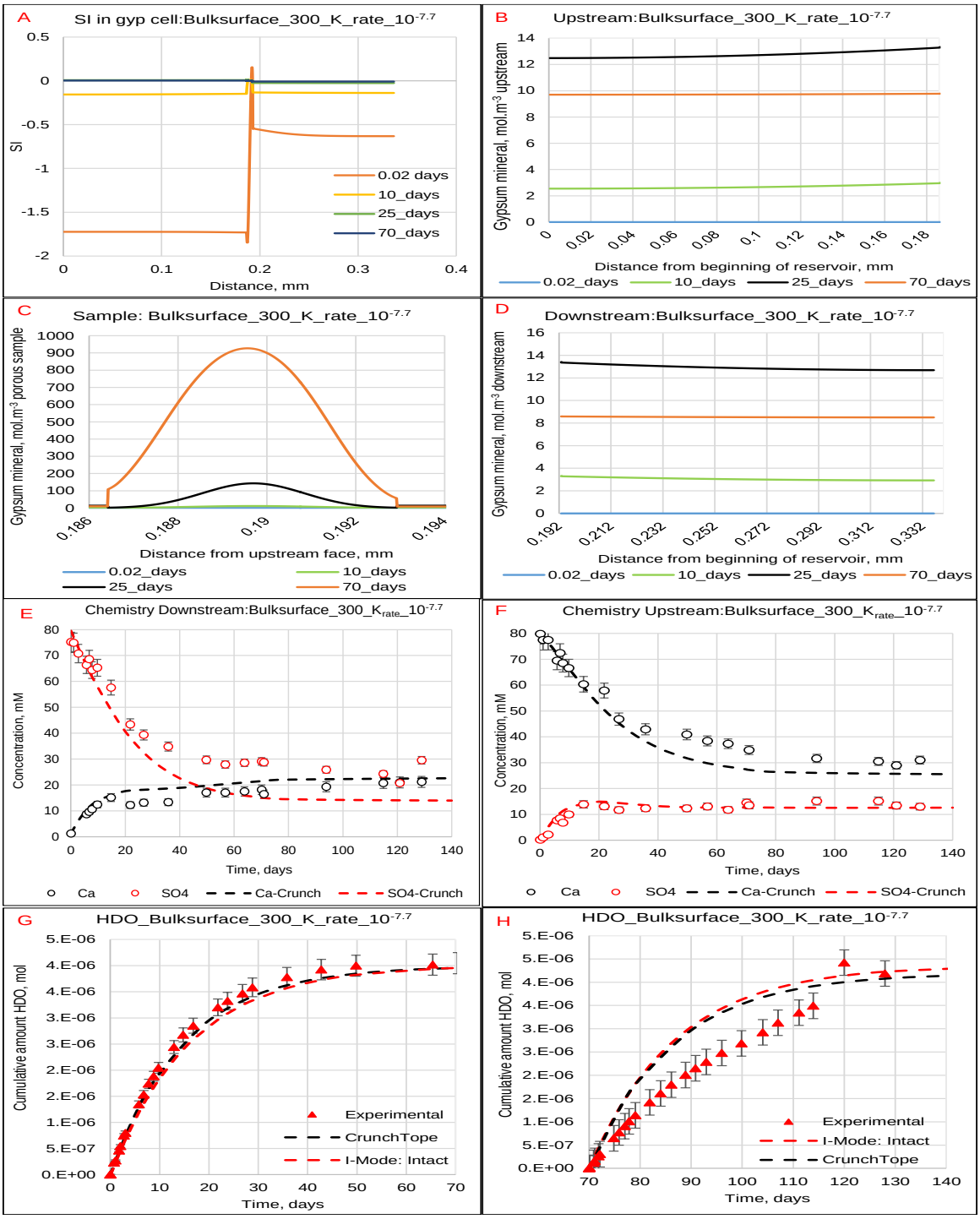

*Figure 13: Mineral precipitation rate sensitivity, **A**: Saturation index of gypsum mineral in two reservoirs and chalk sample, **B**: Significant amount of gypsum mineral precipitating in upstream, **C**: Expansion of gypsum precipitation zone in the center of the sample, **D**: Significant amount of gypsum precipitation in downstream; **E**: numerical simulation of Ca^{2+}; SO_4^{2-} in upstream reservoir, **F**: numerical simulation of Ca^{2+}; SO_4^{2-} in downstream reservoir, **G**: numerical simulation of HDO concentration for 0-70 days, **H**: numerical simulation of HDO concentration for 70-140 days*

4.2 2D simulations

4.2.1 Chalk Gypsum

Gypsum experiments showed that selective evolution of gypsum in isolated zone originated from spatial variability in properties such as heterogeneous pore structure and reactive surface area in chalk. However, at 1D, the code uses porosity equal to 45% in all the meshes and thus such impacts of pore structure are compensated.

Moreover, the sensitivity analysis on base simulations showed that “evolution of diffusion first depends on pore structure rather than overall porosity”. Since, at 1D experimentally observed microstructure evolution cannot be quantified, 2D simulations were launched in HYTEC. A random porosity field is prepared using a normal law, centered on 0.45 and with a standard deviation of 0.05. Note that no specific structure was constrained on the porosity field. For gypsum precipitation two subtests were carried out to determine the “nucleus” and “growth” governed gypsum growth. These subtests were carried out to demonstrate the change in gypsum precipitation front under competition between kinetic of (homogeneous) nucleation, kinetic of growth (heterogeneous) and diffusion. The input parameters for these tests are listed in Table 5.

Figure 14 presents the cross-section view of 2D gypsum simulation for “nucleus” case. This simulation shows that the concentration decrease of reactants from inlet face to the center of the sample is not strictly linear (see Figure 14D for comparison between concentration evolution in homogeneous and heterogeneous diffusivity field). This means that there is small local variation in the diffusion of reactants towards the center of the sample. As more and more of reactants meet in the center of the sample the saturation index with respect to gypsum increases up to 0.3 (0.46 days in Figure 14C). Moreover, to allow nucleus driven growth, in the center of the sample gypsum nucleus of varying concentration are distributed. The numerical simulations showed that some of these nuclei of highest concentration firstly allowed gypsum growth onto their surface (see Figure 16 for nucleus driven growth at different time steps). Consequently, at these first points of precipitation the saturation index locally falls near to equilibrium (sharp point decrease in Figure 14C and Figure 15A and 15B). This effect is shown in Figure 14A and 14B where after 0.46 days the nucleus pumps in the reactants and a sharp decrease in their concentration is observed locally. As the simulation proceeds, gypsum grows over these nuclei in form of 100 µm pods (Figure 16). Since these nuclei are randomly distributed at the central line of the sample these pods are isolated in reference to each other.

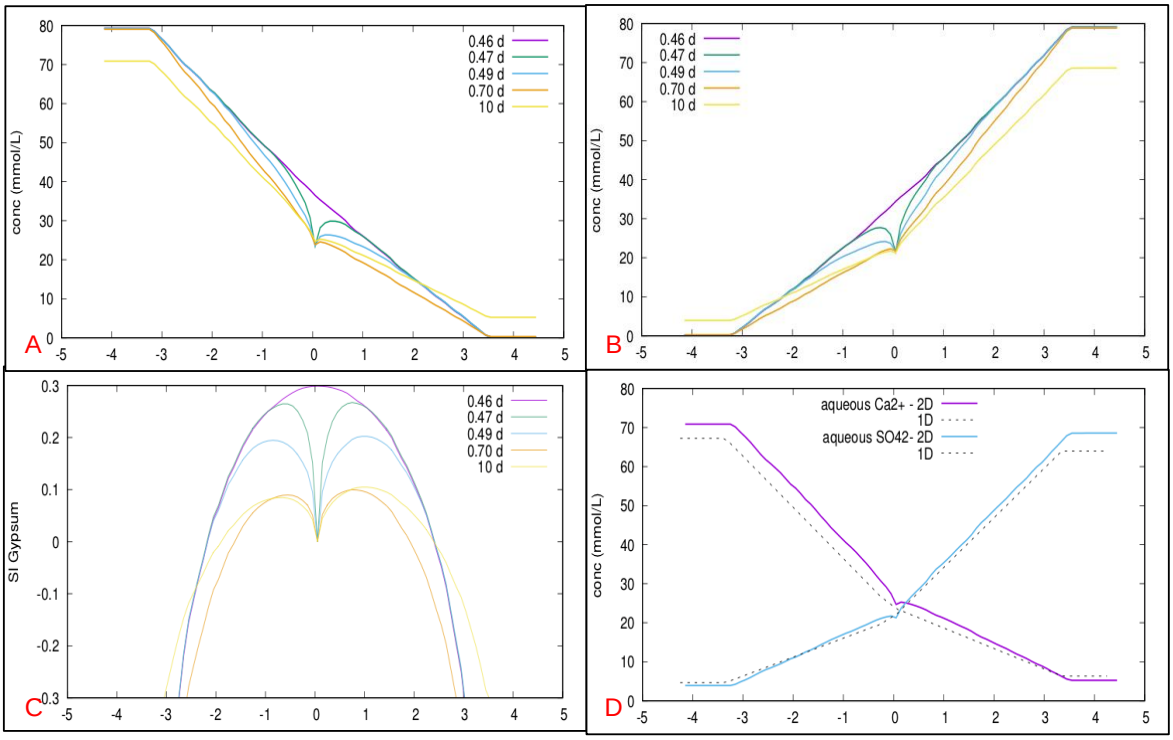

*Figure 14: 2D simulations with spatial variability for "nucleus", **A**: Evolution of Ca^{2+} at different times in chalk sample, **B**: Evolution of SO_4^{2-} at different times in chalk sample, **C**: Evolution of saturation index in the center of the sample at different times, **D**: comparison between Ca^{2+} and SO_4^{2-} at 1Dfor homogeneous diffusion (dashed lines) and 2D for heterogeneous diffusion field (continuous lines) in sample*

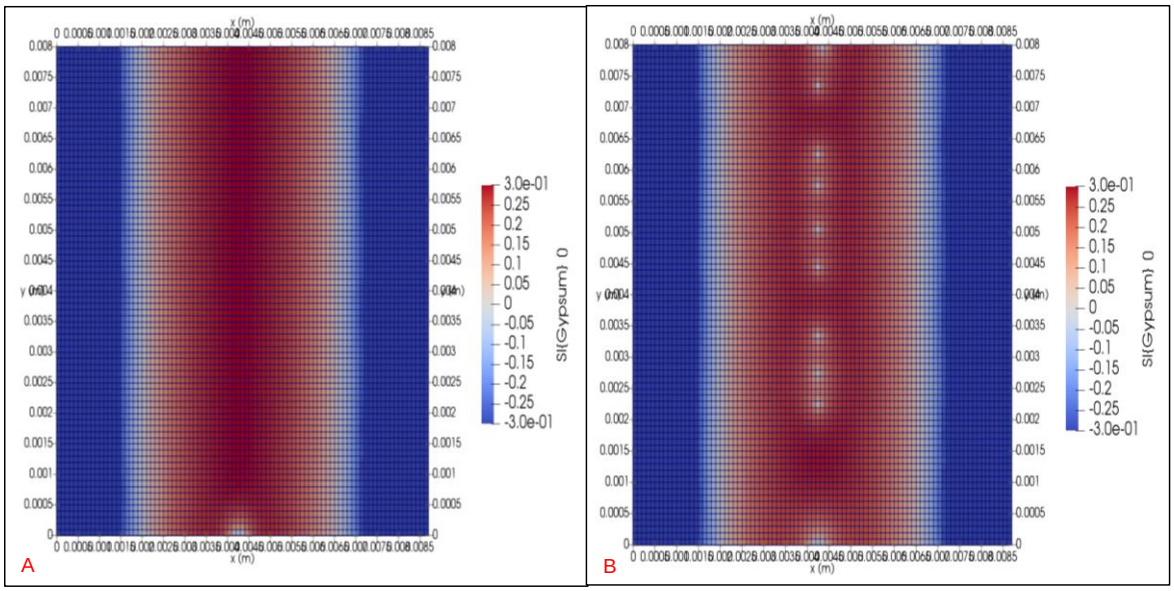

*Figure 15: 2D simulations with spatial variability for "nucleus", **A**: Saturation index evolution in the center of the sample at 0.46 days, **B**: Saturation index evolution in the center of the sample when nucleus pumps in reactants to from first stable gypsum precipitates.*

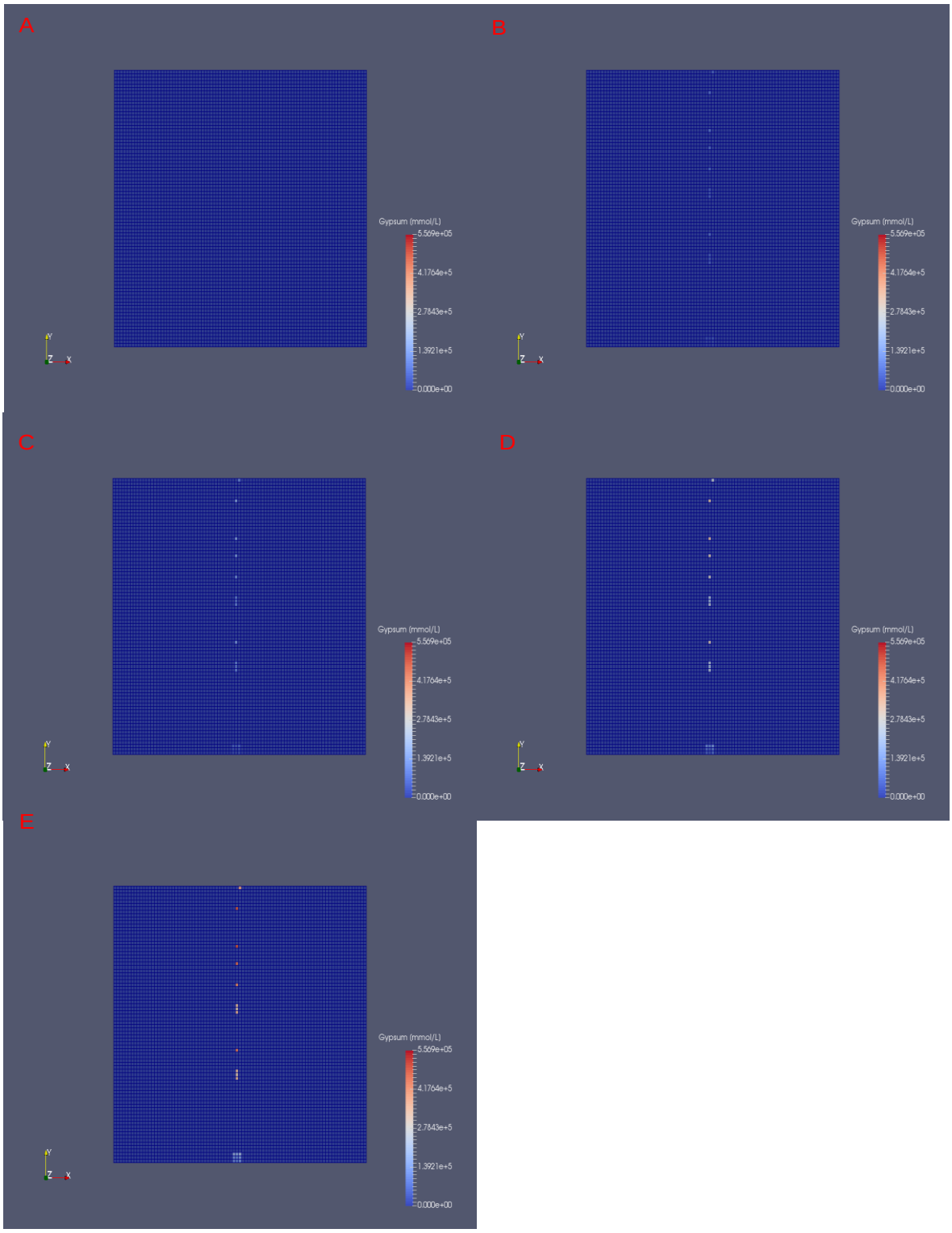

Figure 16: evolution of gypsum mineral in for subtest "nucleus" at time 1 day (A), 5 days (B), 10 days (C), 30 days (D), and 70 days (E)

Figure 17 presents the cross-section view of 2D gypsum simulation for “growth” case. Similar to previous case in this case too spatial variability has allowed a small local variation in the diffusion of reactants towards the center of the sample (see Figure 17D for comparison between concentration evolution in homogeneous and heterogeneous diffusivity field). Figure 17C shows that as more and more of reactants meet in the center of the sample the saturation index with respect to gypsum increases up to 0.3 (0.46 days in Figure 17C). As the simulations proceeds until 0.47days there is a saturation index decrease in approximately in a broad zone in the center of the sample (Figure 17C). This effect is also represented in Figure 17A Figure 17B where a flat concentration decrease is observed in the center of the sample.

At 2D this broad zone in fact contains isolated spheres each containing grids in which saturation has fallen from 0.3 to equilibrium (Figure 18). These sharp decrease in saturation index shows formation of first clusters of gypsum nuclei in these isolated spherical zones (Figure 19B). As simulation proceeds, these first nuclei then allowed gypsum growth onto their surface. The end results of simulation thus showed formation of isolated gypsum spheres distributed in the center of the sample (Figure 19C, 19D and 19E). This surface growth case shows gypsum evolution seen in the experiments.

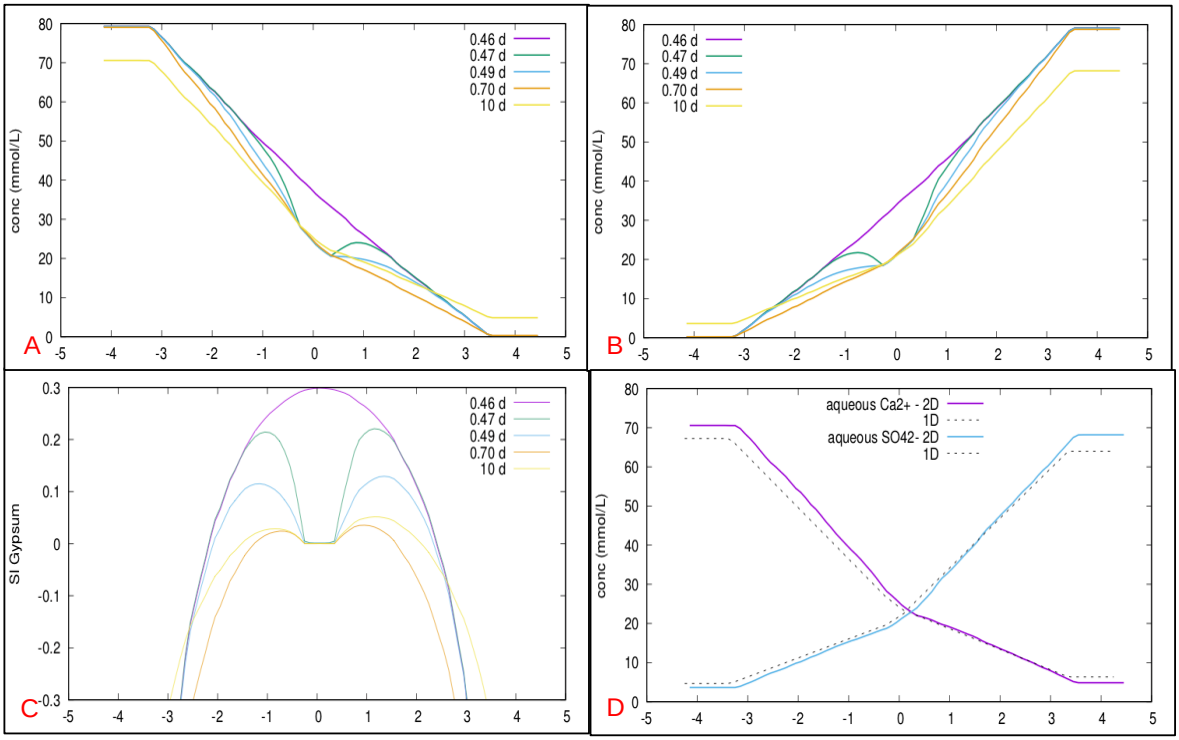

*Figure 17: 2D simulations with spatial variability for "growth", **A**: Evolution of Ca^{2+} at different times in chalk sample, **B**: Evolution of SO_4^{2-} at different times in chalk sample, **C**: Evolution of saturation index in the center of the sample at different times, **D**: comparison between Ca^{2+} and SO_4^{2-} at 1Dfor homogeneous diffusion (dashed lines) and 2D for heterogeneous diffusion field (continuous lines) in sample*

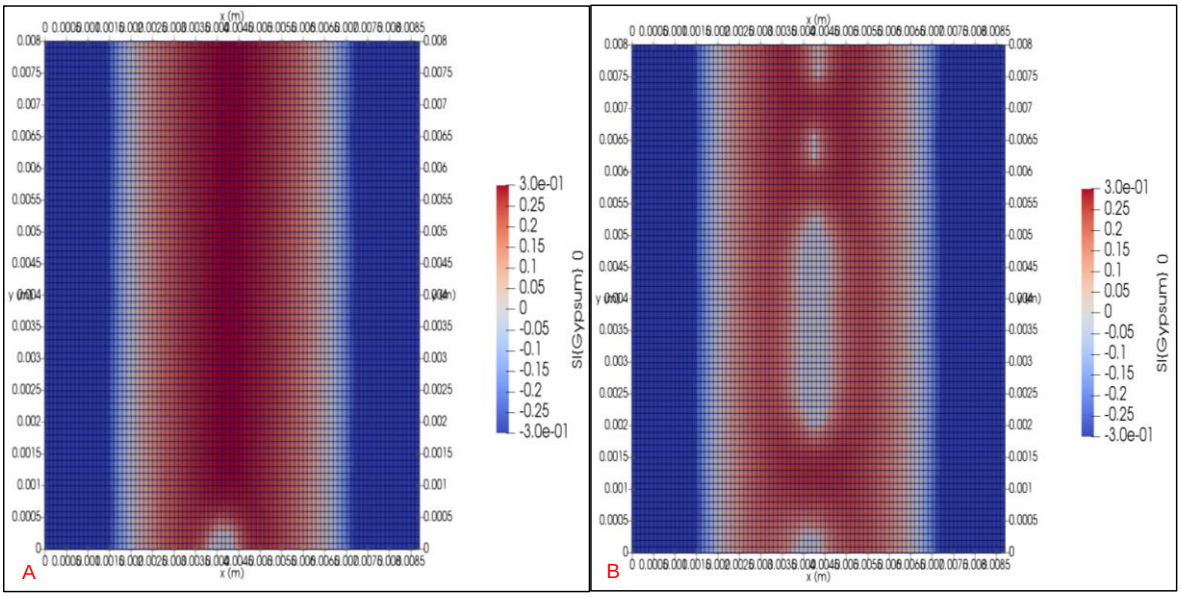

*Figure 18: 2D simulations with spatial variability for "growth", **A**: Saturation index evolution in the center of the sample at 0.46 days, **B**: Saturation index evolution in the center of the sample when nucleus pumps in reactants to from first stable gypsum precipitates.*

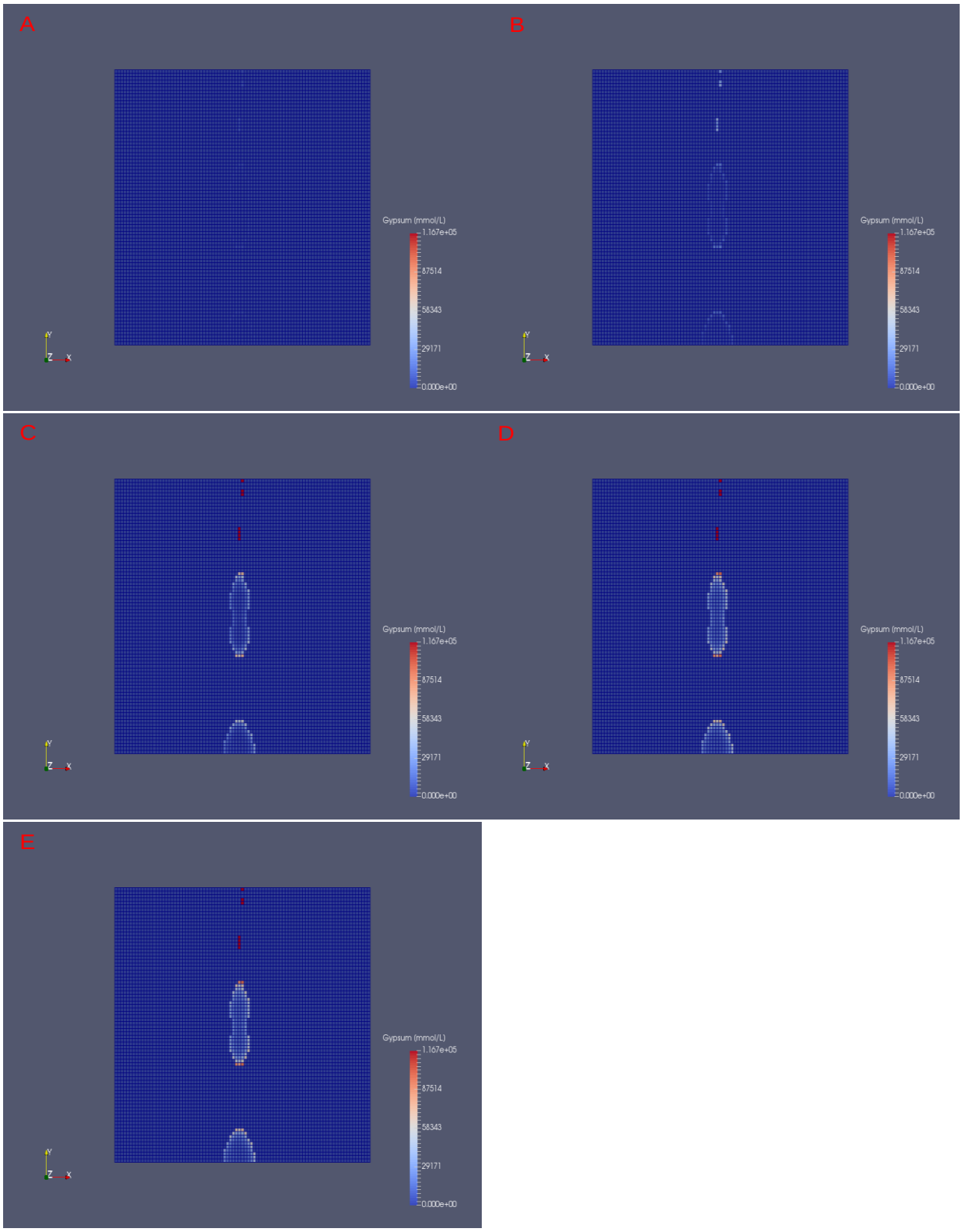

Figure 19: evolution of gypsum mineral in for subtest "growth" at time 1 day (A), 5 days (B), 10 days (C), 30 days (D), and 70 days (E)

4.2.2 Chalk-Barite

The impact of spatial variability in diffusion on the evolution of barite at 2D was also tested using HYTEC. Figure 20 presents the cross-section view of 2D barite simulation. This figure shows that spatial variability has allowed a small local variation in the diffusion of reactants towards the center of the sample. However, despite the spatial variability, the simulations results are remarkably similar to the 1D simulation. The faster diffusion compared to kinetics prevents the formation of “spheres of influence”, and thus evenly distributes the precipitates along the central thin precipitation front. As simulations proceeds, barite grows at this first points of precipitates in the center of the sample (see barite evolution in 2D in figures Figure 21A to 21E). The end result is a thin barite precipitated front in the center of the sample. One must note that in experiments barite growth took place due to homogeneous and heterogeneous nucleation phenomena. However, in this simulation this part has not been tested.

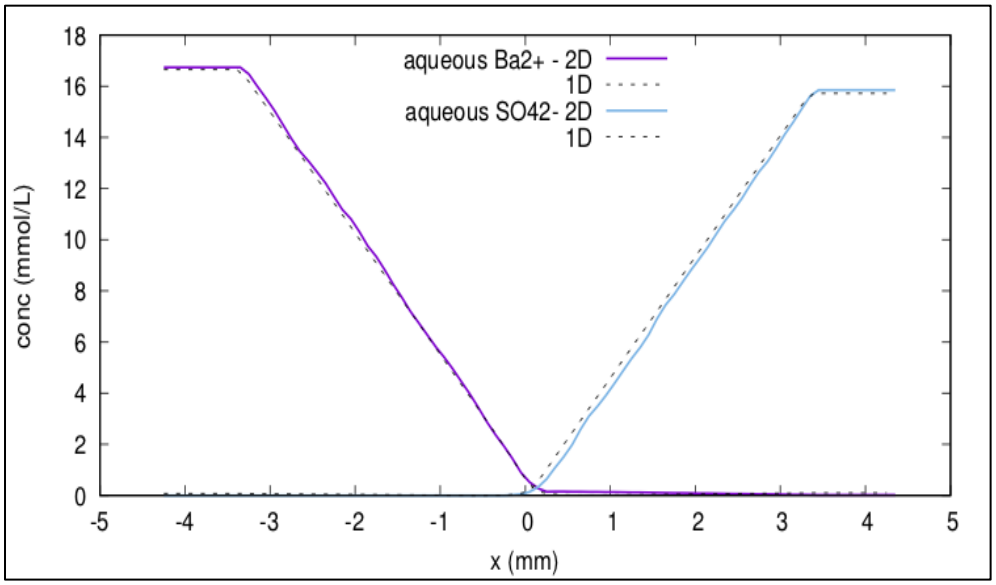

Figure 20: evolution of barite mineral using HYTEC at time 1 day (A), 5 days (B), 10 days (C), 30 days (D), and 70 days (E)

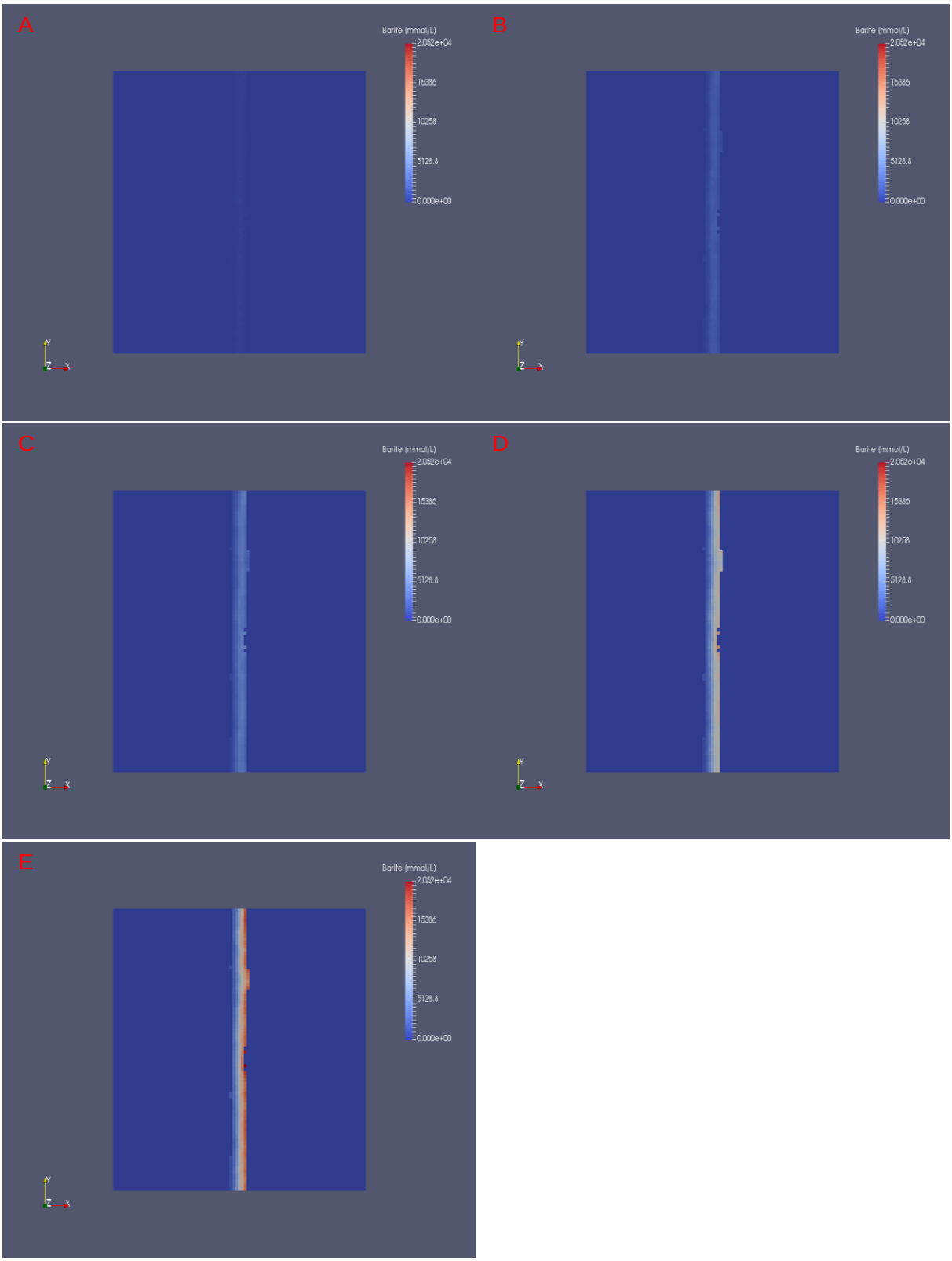

Figure 21: evolution of barite mineral using HYTEC at time 1 day (A), 5 days (B), 10 days (C), 30 days (D), and 70 days (E)

CrunchTope simulations are still running. Results will be incorporated in a future paper focusing on the simulation results.

5 Conclusion

Barite and gypsum clogging experiments in chalk showed different evolution of reactants in reservoirs. The experimental data set of water tracers after 0 days and 70 days of precipitation experiments showed distinct impact for both cases: barite impacted more on diffusivity than gypsum. Based upon these experimental results, the numerical simulations were carried out in 1D and 2D. Finally, the experimental and numerical results were used to demonstrate the predictive limit of Archie's relationship and kinetic rate equation.

For barite experiments, the base simulations in 1D well reproduced the chemistry evolution in reservoirs. Moreover, HYTEC code well reproduced tracer behavior in response to precipitation for injection at 0 days and after 70 days since the beginning of experiment. But, CrunchTope failed to reproduce the water tracer behavior at both injections. The sensitivity analysis on cementation factor within reasonable limits well captured the chemistry behavior in response to precipitation. However, in each case the fitting did not properly reproduce the tracer behavior in response to precipitation.

These results thus show that with proper adjustment of parameters barite precipitation can be well described in 1D for systems like chalk.

However, 1D simulations are unable to describe the gypsum precipitation in chalk. This is because for gypsum structural information (spatial variability in properties of pore structure plus kinetics of precipitation and supersaturation) is necessity. From these experiments such information on structural properties can be used to carry 2D simulations. Using such information HYTEC well reproduced the isolated clustered evolution of gypsum in chalk.

Standard simulation habits on such a system would go to 1D, which in our case not fully representative.

On the contrary, barite and gypsum in 2D were simulated with the same model, despite large differences in behavior of precipitation (solubility, supersaturation, kinetics of precipitation, growth). All these differences stem from different chemical behavior, which are precisely represented in the models. The consistent model to represent both behaviors gives strength to the REV modeling approach. Still, we need to be very careful: experiments are needed to ensure that we identify all the key processes.

6 References

Alimi, F., Elfil, H., Gadri, A., 2003. Kinetics of the precipitation of calcium sulfate dihydratein a desalination unit. Desalination 157, 9–16.

Barbier, E., Coste, M., Genin, A., Jung, D., Lemoine, C., Logette, S., Muhr, H., 2009. Simultaneous determination of nucleation and crystal growth kinetics of gypsum. Chemical Engineering Science 64, 363–369. https://doi.org/10.1016/j.ces.2008.10.036

Berthe, G., Savoye, S., Wittebroodt, C., Michelot, J.L., 2011. Changes in containment properties of claystone caprocks induced by dissolved CO2seepage. Energy Procedia 4, 5314–5319. https://doi.org/10.1016/j.egypro.2011.02.512

Cochepin, B., Trotignon, L., Bildstein, O., Steefel, C.I., Lagneau, V., Van der lee, J., 2008. Approaches to modelling coupled flow and reaction in a 2D cementation experiment. Advances in Water Resources 31, 1540–1551. https://doi.org/10.1016/j.advwatres.2008.05.007

Descostes, M., Blin, V., Bazer-Bachi, F., Meier, P., Grenut, B., Radwan, J., Schlegel, M.L., Buschaert, S., Coelho, D., Tevissen, E., 2008. Diffusion of anionic species in Callovo-Oxfordian argillites and Oxfordian limestones (Meuse/Haute-Marne, France). Applied Geochemistry 23, 655–677. https://doi.org/10.1016/j.apgeochem.2007.11.003

Descostes, M., Pili, E., Felix, O., Frasca, B., Radwan, J., Juery, A., 2012. Diffusive parameters of tritiated water and uranium in chalk. Journal of Hydrology 452–453, 40–50. https://doi.org/10.1016/j.jhydrol.2012.05.018

Emmanuel, S., Berkowitz, B., 2007. Effects of pore-size controlled solubility on reactive transport in heterogeneous rock. Geophysical Research Letters 34, 1–5. https://doi.org/10.1029/2006GL028962

González-Caballero, F., Cabrerizo, M.A., Bruque, J.M., Delgado, A., 1988. The zeta potential of celestite in aqueous electrolyte and surfactant solutions. Journal of Colloid And Interface Science 126, 367–370. https://doi.org/10.1016/0021-9797(88)90131-2

Hang, J., Shi, L., Feng, X., Xiao, L., 2009. Electrostatic and electrosteric stabilization of aqueous suspensions of barite nanoparticles. Powder Technology 192, 166–170. https://doi.org/10.1016/j.powtec.2008.12.010

Kashchiev, D., van Rosmalen, G.M., 2003. Review: Nucleation in solutions revisited. Crystal Research and Technology 38, 555–574. https://doi.org/10.1002/crat.200310070

Lagneau, V., 2013. Modélisation des couplages entre réactions géochimiques et processus hydrodynamiques en milieu poreux – applications au stockage de CO 2 et à l'exploitation d'uranium 200.

Lagneau, V., van der Lee, J., 2010. Operator-splitting-based reactive transport models in strong feedback of porosity change: The contribution of analytical solutions for accuracy validation and estimator improvement. Journal of Contaminant Hydrology 112, 118–129. https://doi.org/10.1016/j.jconhyd.2009.11.005

Li, Y.-H., Gregory, S., 1973. Diffusion of Ions in Sea Water and in Deep Sea Sediments. Geochimica et Cosmochimica Acta, 1974 38, 703–714. https://doi.org/10.1016/0016-7037(74)90145-8

Lichtner, P.C., 1996. Continuum formulation of multicomponent-multiphase reactive transport. Reviews in Mineralogy and Geochemistry 34, 1–81.

Mallon, A.J., Swarbrick, R.E., 2008. Diagenetic characteristics of low permeability, non-reservoir chalks from the Central North Sea. Marine and Petroleum Geology 25, 1097–1108. https://doi.org/10.1016/j.marpetgeo.2007.12.001

Nagaraja, B.M., Abimanyu, H., Jung, K.D., Yoo, K.S., 2007. Preparation of mesostructured barium sulfate with high surface area by dispersion method and its characterization. Journal of Colloid and Interface Science 316, 645–651. https://doi.org/10.1016/j.jcis.2007.09.004

Poonoosamy, J., Curti, E., Kosakowski, G., Grolimund, D., Van Loon, L.R., Mäder, U., 2016. Barite precipitation following celestite dissolution in a porous medium: A SEM/BSE and μ-XRD/XRF study. Geochimica et Cosmochimica Acta 182, 131–144. https://doi.org/10.1016/j.gca.2016.03.011

Potgieter, J.H., Strydom, C.A., 1996. An investigation into the correlation between different surface area determination techniques applied to various limestone-related compounds. Cement and Concrete Research 26, 1613–1617. https://doi.org/10.1016/S0008-8846(96)00159-7

Prasianakis, N.I., Curti, E., Kosakowski, G., Poonoosamy, J., Churakov, S. V., 2017. Deciphering pore-level precipitation mechanisms. Scientific Reports 7, 1–9. https://doi.org/10.1038/s41598-017-14142-0

Prieto, M., 2014. Nucleation and supersaturation in porous media (revisited). Mineralogical Magazine 78, 1437–1447. https://doi.org/10.1180/minmag.2014.078.6.11

Steefel, C.I., 2009. CrunchFlow software for modeling multicomponent reactive flow and transport. User's manual. Earth Sciences Division. Lawrence Berkeley, National Laboratory, Berkeley, CA. October 12–91.

Steefel, C.I., MacQuarrie, K.T.B., 1996. Approaches to modeling of reactive transport in porous media. Reviews in Mineralogy and Geochemistry 34, 85–129.

van der Lee, J., De Windt, L., Lagneau, V., Goblet, P., 2003. Module-oriented modeling of reactive transport with HYTEC. Computers and Geosciences 29, 265–275. https://doi.org/10.1016/S0098-3004(03)00004-9

Zhang, J., Nancollas, G.H., 1992. Influence of calcium/sulfate molar ratio on the growth rate of calcium sulfate dihydrate at constant supersaturation. Journal of Crystal Growth 118, 287–294. https://doi.org/10.1016/0022-0248(92)90073-R

7 APPENDIX

S1: 1D base simulation script for barite using HYTEC

```
# CHALK 1D - barite
# VLagneau - June 2018
database = /home/vlagneau/bin/ctdp/chess.tdb
permeability = 1e-20 m/s
storage = 0.1
flow-regime = stationary
porosity = variable
# Geometry
# domain defines the global system
# zone is the keyword for a specific area
# --------------
domain = -4.35,-0.5 4.35,-0.5 4.35,0.5 -4.35,0.5 mm
zone res_left {
  geometry = rectangle -3.85,0 1,1 mm, nodes = 5,1
  porosity = variable {
    start = 187.09
          archie = 1.8
  }
  diff.coeff = 1e-8 m2/s  #### PORE DIFFUSION
  geochemistry = ch_left
  modify at 70 d, source = 0.025e-6 m3/d using ch_inject
```

```
  modify at 70.01 d, source = 0
}
zone res_right {
  geometry = rectangle 3.85,0 1,1 mm, nodes = 5,1
  porosity = variable {
    start = 145.51
          archie = 1.8
  }
  diff.coeff = 1e-8 m2/s
  geochem = ch_right
}
zone chalk {
  geometry = rectangle 0,0 6.7,1 mm, nodes = 67,1
  porosity = variable {
    start = 0.45
          archie = 1.8
  }
#  diff.coeff = 9.333e-10 m2/s
  diff.coeff = 3.00e-10 m2/s
  geochem = ch_initial
}
# Boundary conditions
# ------------------------------
# Geochemistry
```

```
# unit is keyword for a "geochemical unit"
# --------------
unit ch_initial {
        mineral Calcite = 20 mol/L, surface = 0.55 m2/g ## mineral defined by mass/L of water!!!
        mineral Barite = 0 mol/L, surface = 1.65 m2/g
}
unit ch_left {
  total HDO = 1 umol/L
  total BA = 20 mmol/L
    total Ba[2+] = 20 mmol/L
    total  Cl[-] = 40 mmol/L
        mineral Calcite = 0 mol/L, surface = 0.55 m2/g ## surface is 0 because conc = 0
        mineral Barite = 0 mol/L, surface = 1.65 m2/g
}
unit ch_right {
    tot K[+] = 40 mmol/L
    tot SO4[2-] = 20 mmol/L
    tot SO4 = 20 mmol/L
        mineral Calcite = 0 mol/L, surface = 0.55 m2/g
        mineral Barite = 0 mol/L, surface = 1.65 m2/g
}
unit ch_inject {
  total HDO2 = 1 umol/L
        mineral Calcite = 0 mol/L, surface = 0.55 m2/g ## surface is 0 because conc = 0
```

```
        mineral Barite = 0 mol/L, surface = 1.65 m2/g
}
# Time criteria
# ------------------------
duration = 141 day
timestep = variable {
    start = 1 min
        maximum = 0.1 d
}
# Output parameters
# ----------------------------
output-format = res, vtk
sampling = 141
## selections
select aqueous{Ba[2+]}, aqueous{SO4[2-]} in mmol/l
select Barite in mmol/L
select SI{Barite}  ## saturation index
select porosity
select min-volume in L
select diffusion in m2/s ### EFFECTIVE DIFFUSION
select node
select BA, SO4 in mmol/L
select HDO, HDO2 in umol/L
# DATABASE
```

```
# --------
exclude minerals
include Calcite, Barite
define base HDO
define base HDO2


extend mineral Barite {
        kinetics { # prec
                rate = 1.5e-11 mol/m2/s
                y-term {
                        species = Barite
                        saturation-index = 1e4
                }
                area = Calcite
        }
        kinetics { # diss
                rate = -1.5e-11 mol/m2/s
                y-term, species = Barite
                area = Barite
        }
}
extend mineral Calcite {
  logK = 100
}
```

define base BA

define base SO4

S2: 1D base simulation script for gypsum using HYTEC

CHALK 1D - Gypsum

VLagneau - June 2018

database = /home/vlagneau/bin/ctdp/chess.tdb

Geometry

domain defines the global system

zone is the keyword for a specific area

----

domain = -4.35,-0.5 4.35,-0.5 4.35,0.5 -4.35,0.5 mm

zone res_left {

geometry = rectangle -3.85,0 1,1 mm, nodes = 5,1

porosity = 187.09

diff.coeff = 1e-8 m2/s #### PORE DIFFUSION

geochemistry = ch_left

}

zone res_right {

geometry = rectangle 3.85,0 1,1 mm, nodes = 5,1

porosity = 145.51

diff.coeff = 1e-8 m2/s

geochem = ch_right

```
}
zone chalk {
geometry = rectangle 0,0 6.7,1 mm, nodes = 67,1
porosity = 0.45
diff.coeff = 4e-10 m2/s
geochem = ch_initial
}
# Boundary conditions
# ------------------------------
# Geochimistry
# unit is keyword for a "geochemical unit"
# --------------
unit ch_initial {
mineral Nucleus = 1 g/L, surface = 100 cm2/g
mineral Gypsum = 0 g/L, surface = 1000. m2/g
}
unit ch_left {
total Ca[2+] = 80 mmol/L
total Cl[-] = 160 mmol/L
mineral Nucleus = 0 g/L, surface = 1 cm2/g
mineral Gypsum = 0 g/L, surface = 0. m2/g
}
unit ch_right {
tot K[+] = 160 mmol/L
```

```
tot SO4[2-] = 80 mmol/L

mineral Nucleus = 0 g/L, surface = 1 cm2/g

mineral Gypsum = 0 g/L, surface = 0. m2/g

}

# Time criteria

# ------------------------

duration = 130 day

timestep = variable {

start = 1 min

maximum = 0.05 d

}

# Output parameters

# ----------------------------

output-format = res, vtk

sampling = 130

## selections

select aqueous{Ca[2+]}, aqueous{SO4[2-]} in mmol/l

select Gypsum in mmol/L

select SI{Gypsum} ## saturation index

select porosity

select min-volume in L

select diffusion in m2/s ### EFFECTIVE DIFFUSION

select node

# DATABASE
```

```
# --------
exclude minerals
include Calcite, Gypsum
extend mineral Gypsum {
### precipitation
kinetics {
rate = 1e-2 mol/m2/s
y-term {
species = Gypsum
}
area = Gypsum
}
### precipitation
kinetics {
rate = 1e-4 mol/m2/s
y-term {
saturation-index = 1
species = Gypsum
}
area = Nucleus
}
### dissolution
kinetics {
rate = -1e-16 mol/m2/s
```

y-term, species = Gypsum

area = Gypsum

}

}

define mineral Nucleus {

surface = 1 cm2/L

}

S3: 1D base simulation script for barite using CrunchTope

TITLE

Manipe.in: C6-Clogging - Crunchdiff

END

RUNTIME

time_units days

timestep_max 0.01

timestep_init 0.001

time_tolerance 0.1

hindmarsh false

correction_max 10.0

debye-huckel true

database_sweep false

speciate_only false

graphics kaleidagraph

gimrt true

```
solver            gmres
pc                ilu
pclevel           2
database          ./datacom_ikram.dbs
coordinates       rectangular
screen_output     10
restart           crunchdiff.rst append
save_restart      crunchdiff.rst
END


OUTPUT
time_units           days
time_series_interval  1
!spatial_profile 0.02 1. 2. 3. 4. 5. 6. 7. 8. 9. 10. 11. 12. 13. 14. 15. 16. 17. 18. 19. 20. 21. 22. 23. 24. 25. 26. 27. 28. 29. &
!          30. 31. 32. 33. 34. 35. 36. 37. 38. 39. 40. 41. 42. 43. 44. 45. 46. 47. 48. 49. 50. 51. 52. 53. 54. 55. 56. 57. 58. &
!          59. 60. 62. 64. 66. 68. 70.
spatial_profile 70.1 72. 74. 76. 80. 82. 84. 86. 88. 90. 92. 94. 96. 98. 100. 102. 104. 106. 108. 110. &
         112. 114. 116. 118. 120. 122. 124. 126. 128. 130. 132. 134. 136. 138. 140.
time_series_print    Tracer  Na+  Cl-  Ca++  Mg++  K+  HCO3-  SO4--  H+  Ba++
END
```

TRANSPORT

distance_units meters

time_units second

calculate_diffusion 2.E-9

!calculate_diffusion 1.E-9

dispersivity 0.0 0.0

cementation_exponent 1.97

D_25 Ca++ 7.93e-10

D_25 K+ 19.6e-10

D_25 Ba++ 8.48e-10

D_25 SO4-- 10.7e-10

D_25 Na+ 13.3e-10

D_25 Cl- 20.3e-10

D_25 HCO3- 11.8e-10

END

BOUNDARY_CONDITIONS

x_begin amont flux

x_end aval flux

END

DISCRETIZATION

xzones 182 1.00768E-03 7 220E-06 6 84E-06 12 42E-06 24 20E-06 651 9.98E-06 24 20E-06
&

12 42E-06 6 84E-06 7 220E-06 140 1.00577E-03

END

INITIAL_CONDITIONS

amont 1-231

calcaire 232-882

aval 883-1071

END

Condition amont

units mol/kg

temperature 25.0

pH 7.37

Cl- 0.20039

SO4-- 0.0000

Ca++ 0.02062

Mg++ 0.00007

Na+ charge

K+ 0.00

HCO3- 0.00039

Ba++ 0.0200

Tracer 1

Barite 0.0 bulk_surface_area 0

Calcite 0.0 bulk_surface_area 0

END

Condition aval

units mol/kg

temperature 25.0

pH 7.69

Cl- 0.1600

SO4-- 0.0200

Ca++ 0.02062

Mg++ 0.00007

Na+ charge

K+ 0.0400

HCO3- 0.00039

Ba++ 0.000

Tracer 0.0

Barite 0.0 bulk_surface_area 0

Calcite 0.0 bulk_surface_area 0

END

Condition calcaire

units mol/kg

temperature 25.0

pH 7.69

```
Cl-             0.2002
SO4--           0.0000
Ca++            0.02062
Mg++            0.00007
Na+             charge
K+               0.0
HCO3-           0.00039
Ba++            0.0000
Tracer           0.0
Calcite  0.55  bulk_surface_area    0
Barite  0.0    specific_surface_area  1.65  0.0001
End

FLOW
time_units      second
distance_units  meters
constant_flow      0.0   0.0   0.0
END

POROSITY
porosity_update  true
minimum_porosity  0.00000000001
END
```

PRIMARY_SPECIES

Cl-

SO4--

Mg++

Na+

K+

Ba++

Tracer

Ca++

HCO3-

H+

END

Minerals

Barite -label default -rate -10.8239

Calcite -label default

End

S2: 1D base simulation script for gypsum using CrunchTope

TITLE

Manipe.C1 in: sans Clogging en 1D

END

```
RUNTIME
time_units         days
timestep_max       0.01
timestep_init      0.001
time_tolerance     0.1
hindmarsh          false
correction_max     10.0
debye-huckel       true
database_sweep     false
speciate_only      false
graphics           kaleidagraph
gimrt              true
solver             gmres
pc                 ilu
pclevel            2
database           ./datacom_ikram.dbs
coordinates        rectangular
screen_output      10
!restart           crunchdiff.rst append
save_restart       crunchdiff.rst
END
```

```
OUTPUT

time_units          days

time_series_interval 1

spatial_profile 0.02 1. 2. 3. 4. 5. 6. 7. 8. 9. 10. 11. 12. 13. 14. 15. 16. 17. 18. 19. 20. 21. 22. 23. 24. 25. 26. 27. 28. 29. &

        30. 31. 32. 33. 34. 35. 36. 37. 38. 39. 40. 41. 42. 43. 44. 45. 46. 47. 48. 49. 50. 51. 52. 53. 54. 55. 56. 57. 58. &

        59. 60. 62. 64. 66. 68. 70.

!spatial_profile 70.1 72. 74. 76. 80. 82. 84. 86. 88. 90. 92. 94. 96. 98. 100. 102. 104. 106. 108. 110. &

!           112. 114. 116. 118. 120. 122. 124. 126. 128. 130. 132. 134. 136. 138. 140.

time_series_print    Tracer  Na+ Cl- Ca++  Mg++  K+  HCO3-  SO4--  H+

END


TRANSPORT

distance_units meters

time_units  second

calculate_diffusion  2.E-9

dispersivity         0.0

cementation_exponent 1.97

D_25    Ca++     7.93e-10

D_25    K+       19.6e-10

D_25    SO4--    10.7e-10

D_25    Na+      13.3e-10

D_25    Cl-      20.3e-10
```

D_25 HCO3- 11.8e-10

END

BOUNDARY_CONDITIONS

x_begin amont flux

x_end aval flux

END

DISCRETIZATION

xzones 182 1.00768E-03 7 220E-06 6 84E-06 12 42E-06 24 20E-06 651 9.98E-06 24 20E-06 &

12 42E-06 6 84E-06 7 220E-06 140 1.00577E-03

END

INITIAL_CONDITIONS

amont 1-231

calcaire 232-882

aval 883-1071

END

Condition amont

units mol/kg

temperature 25.0

pH 7.37

Cl- 0.1613

SO4-- 0.0001

Ca++ 0.0805

Mg++ 0.00007

Na+ charge

K+ 0.00

HCO3- 0.00023

Tracer 0.0678

Gypsum 0.0 bulk_surface_area 0

Calcite 0.0 bulk_surface_area 0.

END

Condition aval

units mol/kg

Temperature 25.0

pH 7.69

Cl- 0.00134

SO4-- 0.0801

Ca++ 0.00125

Mg++ 0.00007

Na+ charge

K+ 0.1602

HCO3- 0.00212

Tracer 0.016

Gypsum 0.0 bulk_surface_area 0

Calcite 0.0 bulk_surface_area 0.

END

Condition calcaire

units mol/kg

temperature 25.0

pH 7.69

Cl- 0.2002

SO4-- 0.0000

Ca++ 0.02062

Mg++ 0.00007

Na+ charge

K+ 0.0

HCO3- 0.00039

Tracer 0.016

Calcite 0.55 bulk_surface_area 0

Gypsum 0.0 specific_surface_area 0.32 0.0001

END

FLOW

time_units second

distance_units meters

constant_flow 0.0

END

```
POROSITY
porosity_update  true
minimum_porosity  0.00000000001
END

PRIMARY_SPECIES
Tracer
Cl-
SO4--
Ca++
Mg++
Na+
K+
HCO3-
H+
END

Minerals
Gypsum      -label default  -rate -6.00
Calcite     -label default
END
```

CONCLUSION AND PERSPECTIVES

1 *Conclusion*

Several countries have proposed to confine their radioactive wastes in deep geological facilities that are based upon the multi-barrier concept. In France, Switzerland and Belgium, argillaceous formations are considered as a potential host-rock, with their ability to sustainably confine the radionuclides. Indeed, this type of material displays very good containment properties, *i.e.* high retention capacity and very low permeability. However, some of the radioactive waste would release large amount of soluble salts that would generate a saline plume towards the natural medium. The presence of saline plume may further enhance some physicochemical reactions such as mineral precipitation/dissolution. In this situation, these reactions may locally alter the natural host-rock containment properties and therefore induce changes in transport properties of radionuclides. Thus, for safety assessment of such facility, the evolution of rock containment properties in response to these physicochemical phenomena over large time and space scale needs to be investigated. This can be done by determining impacts of each of these phenomena on intact rock properties (*i.e.* porosity, diffusivity of reference tracers) at the laboratory scale. Then, using chemistry transport codes, a process-based approach, these impacts can be calculated to larger times and space scales. But these codes rely on empirical relationships (e.g. Archie's law) to describe the feedback of chemistry on the pore structure and therefore on the transport properties (e.g. diffusion). Thus, prior to long-term prediction of mineral perturbation impacts on rock intact properties, it is essential to test the robustness of this relationship by means of lab-scale experiments.

In this view, this thesis work dealt with developing laboratory experiments to estimate mineral precipitation impacts on intact properties of proxy porous materials under diffusive transport regime and the capability of REV chemistry transport codes to reproduce such an experimental dataset. The proxy materials were chosen because claystone of the argillaceous formations possess very low intrinsic permeability (diffusion of ionic species is the governing transport phenomena) and heterogeneous pore network with presence of clayey minerals of negative surface charge. In such scenario, there is sorption of cationic species and exclusion of anionic species from the pore network. Thus, in absence of lab-scale experiments on simple proxy materials, it is complex to engineer lab-scale setup that can derive interpretable data for precipitation impacts on intact claystone properties.

In this study, each proxy material addresses a physical or surface property that is found in claystones. The first proxy material is micritic chalk: it presents spatial variability in properties, such as heterogeneous pore structure and reactive surface area for mineral precipitation. The second material is compacted illite: it presents pore size distribution and negative surface charge closer to claystones. The third material is compacted kaolinite: it represents an intermediate between chalk and illite in terms of surface charge and pore size distribution. The final goal of these experiments was to demonstrate "whether Archie's relationship can be generalized for clogging phenomena on any porous media." For such demonstration, the following three questions needed to be answered.

1. Can clogging phenomena be generalized for materials with same porosity but different pore size distributions?
2. Will a same precipitating mineral lead to same effectiveness of clogging on two materials with different pore size distributions and different surface charge properties?
3. Will precipitated minerals of very different intrinsic properties, such as solubility or kinetic rate of precipitation, leads to same impact on diffusivity of a single porous material?

To find possible answer of the first two questions barite precipitation experiments were carried in chalk, illite and kaolinite materials and, for the final question, barite and gypsum precipitation in chalk were carried out. These sulfate alkali mineral (i.e., barite and gypsum) were selected as they present two extremities in reference to their kinetic rate of precipitation and solubility.

From the end-results of all the experiments following answers can thus be concluded:

1. Barite precipitation in chalk and kaolinite showed that different pore size distributions led to very different impact on evolution of barite mineral in each case and consequently a different impact on diffusivity of water tracer. Thus, barite precipitation results for one porous material cannot be used to predict the possible impact of precipitation on another porous material, even when they have similar porosity.
2. The illite results showed that since inhibition of barite precipitates in majority of the pores is suspected, barite precipitation had no impact on diffusivity of water tracer. This inhibition of barite precipitates was not observed in chalk and kaolinite. Thus, the experimental results derived on materials with large pores and/or neutral surface cannot be used to predict possible impacts of precipitation on material with very small pores containing negative surface charge.

3. The barite and gypsum precipitation experiments in chalk showed that the intrinsic property of each mineral along with spatial variability in properties led to very distinct evolution of each mineral. This distinct evolution then led to very different impact on water tracer diffusivity.

The experimental results also showed that the newly formed barite mineral in pores of chalk and kaolinite samples possessed negative surface charge. Thus, barite precipitates added semi-permeable membrane behavior to chalk and kaolinite sample and consequently, a strong exclusion of ^{36}Cl was observed. Thus, these experiments show that barite mineral forming on neutral pore surface will have negative surface charge. However, in illite no impact on diffusivity of this tracer was observed. Therefore, the surface charge of barite forming on negative surface charged clayey mineral still remains unknown.

To check the predictability limit of Archie's relationship, barite and gypsum experiments were reproduced at 1D and 2D using two chemistry transport codes (HYTEC and CrunchTope). The end-results for 1D showed that the experimental results can only be reproduced after proper fitting of some parameters like cementation factor, supersaturation or kinetic rate of precipitation. However, these fitting or proper adjustments can only be performed from the end-results of experiments. Thus, for long term simulations on larger time and space scales where the precipitation phenomena will occur for large set of minerals on complex porous materials, such fitting would have to be calibrated beforehand. On the contrary, for 2D simulations, when the structural information such as heterogeneous diffusivity field was taken into account in the chalk simulation script, the codes managed to accurately describe the impact of spatial variability on evolution of gypsum and barite in chalk, with a consistent of parameters for both experiments and without adjustment.

Other approaches integrating a description of the pore structure are currently an active field of research. However, the computer intensity is such that their usability in safety assessment is still remote. Pending computing development avoiding such technical problems, the use of REV approaches and empirical laws associated with conservative safety margins are still necessary to forecast the global evolution of a system.

The first general conclusion regarding REV simulation is that a very careful assessment of all the processes is key to a correct simulation. In this case, the importance of spatial heterogeneity and the differences in chemical behavior (supersaturation, kinetics) were greater than the actual cementation factor, although they had been largely underestimated in *a priori* simulations. In this

case, a consistent model was prepared, that can effectively reproduce both experiments, even though the evolutions in each experiment are very different.

Second, although Archie's law cannot represent the structural evolution of the pore network, and particularly does not integrate the differentiate behavior of different minerals, it can still be useful to represent the evolution of a system, provided all other relevant processes are well considered. With this conclusion in mind, well-devised experiments are still required to ensure that models are correctly calibrated before attempting the upscaling in time and space.

2 Perspectives

Since last decade, several experimental and numerical approaches have been developed to understand the evolution of a precipitating mineral in porous media. One such experimental approach is to apply classical nucleation theory (which has been extensively used in crystal chemistry) to study mineral precipitation in porous media. The main goal behind this approach is to develop supersaturation-nucleation-time (S-N-T) diagrams for a given precipitating mineral(Prieto, 2014). *E.g.* It is known that barite mineral precipitation is governed either by homogeneous or heterogeneous nucleation phenomena. To initiate each nucleation process, a given solution needs to overcome the supersaturation with respect to barite mineral. As soon as this supersaturation is achieved within the solution, clusters of barite are formed. However, these clusters need to overcome the interfacial energy to form stable barite nuclei and initiate precipitation. Using S-N-T diagrams, one can determine the time and supersaturation that is required to initiate homogeneous and heterogeneous driven nucleation barite precipitation. Such S-N-T diagrams were developed in (Prieto, 2014) and (Poonoosamy et al., 2016) to determine pore size dependent nucleation phenomena. In a given set of conditions, using S-N-T diagrams both studies showed that at given supersaturation, the time required to initiate homogeneous nucleation was short in larger pores. Similarly, these diagrams showed that in smaller pores the time to initiate heterogeneous nucleation was short.

In a similar approach, (Emmanuel & Berkowitz, 2007) by means of numerical simulations compared the evolution of a given pore size distribution using classical kinetic rate equation and pore size solubility model. In pore scale solubility model the thermodynamic solubility is replaced by “a pore controlled solubility” in which the solubility is constrained by the interfacial energy and the pore diameter, *i.e.* $S_d = S_o exp\left(\frac{\gamma}{d}\right)$ where d is the radius of the pore (m), S_o is the bulk solubility ($m^3.mol^{-6}$) and γ is the interfacial energy ($J.m^{-2}$). Using classical kinetic rate equation (constant solubility model) and PCS model the evolution of a sandstone pore size distribution (containing pores ranging between 10^{-8} m to 10^{-4} m) in response to stylolite precipitation was simulated. The end simulations showed that for constant solubility model precipitation resulted in total clogging of small and intermediate pores (10^{-8} m to 10^{-6}). However, the simulations using PCS model showed that intermediate pores ($10^{-6.5}$ m) were filled rapidly and the nanopores were completely left unfilled. These simulations showed that classical kinetic rate equation resulted in evolution of poly-modal system into unimodal system, whereas for PCS, the system evolved from a polymodal to a bimodal system.

Both of these examples show that the initial characteristics of the pore structure of the studied porous material and the intrinsic properties of the precipitating mineral are required to go further in predicting the evolution of the material pore structure in response to precipitation.

Similarly, the chalk, kaolinite and illite results in the current work highlight the importance of the pore structure characteristics in governing the effectiveness of precipitation phenomena. However, there are still some tasks that need to be completed. These tasks are necessary to experimentally demonstrate the role played by the pore size in precipitation. *E.g.* in illite case, inhibition process due to pore size was observed. However, the pore sample also possesses negative surface charge. Thus, it is complex to decipher from these results as in which pore inhibition of precipitation due to exclusion of sulfate ions from the pore and in which inhibition due pore size took place. For this purpose, barite precipitation in kaolinite sample of pore size distribution closer to illite can be studied. A detailed characterization of precipitation in this experiment using post-mortem techniques such as X-ray tomography, FIB-SEM or neutron scattering can be used to determine the minimum pore size in which barite precipitation can occur. These results can then be used to properly explain the inhibition process in illite.

To study the impact of variation in pore structure characteristics, precipitation experiments can be performed into systems of varying surface charge and pore size distributions. For pore size distribution cases, illite compacted at lower dry density can be studied. For variation in surface charge impact (thickness of double layer, affinity extent of cationic reactant towards clay surface), experiments at higher background electrolyte and/or different illite conditioning (sodium conditioning or calcium conditioning) can also be studied. Finally, to determine the combined impact of pore structure characteristics and intrinsic properties of mineral on clogging effectiveness, different mineral can be used in the precipitation study. *E.g.* Celestite presents an intermediate between gypsum and barite in terms of solubility and rate of precipitation. This mineral can be studied in chalk, kaolinite and illite to determine its effectiveness in these systems. Note that in the current thesis preliminary experiments were carried out to study gypsum precipitation in compacted illite and kaolinite samples. The dry density of each sample was like barite experiments. However, first results showed precipitation on the sample surface and no gypsum precipitation into the sample. Thus, a simpler proxy material presenting a pore size distribution a little bit larger than to illite and kaolinite case can be used to determine the threshold of pore size below which gypsum precipitation is inhibited. Such pore size distributions can be found in samples like tight chalk and argillaceous-chalk (see (Descostes et al., 2012; Mallon & Swarbrick, 2008).

Moreover, barite experiments in chalk and kaolinite showed that at equilibrated conditions newly formed barite possessed negative surface charge. This additional surface charge led to significant exclusion of ^{36}Cl from the precipitated zone. Such associated semi-permeable membrane effect of newly-formed precipitates can have deciding role for deep geological waste concept but also for ions transport in site remediation, and Li-ion battery research in which pore clogging is limiting factor for the discharge capacity (Bardenhagen et al., 2015). Several studies have shown that by means of potential determining ions (PDI), the surface charge of barite or celestite minerals can be controlled (and even reversed) (González-Caballero, Cabrerizo, Bruque, & Delgado, 1988; Hang, Shi, Feng, & Xiao, 2009). Thus, barite experiments can be launched in different porous systems. At one point when all reactants are consumed to precipitation in sample, the reservoirs can be spiked with such potential determining ions. After this step, the impact of surface charge change on diffusion of cationic and anionic species can be studied.

In addition to precipitation, a second mineral perturbation that is extensively studied in literature is mineral dissolution phenomena. In present thesis, a brief overview of a robust experimental data set from works of (Berthe *et al.*, 2011) has been presented. This works showed that dissolution phenomena led to generation of two dissolved zones. At the inlet of reactive solution, a complete dissolution of carbonate mineral in claystones and in the deeper section, a generation of newly-formed preferential pathways. The latter contributed to increase in diffusivity of water and anionic tracers. However, to strengthen this work, especially regarding the role played by the pore size on the extent of dissolution, several dissolution experiments on proxy material need to be performed. These proxy materials should present distribution of calcite mineral similar to claystones. Some of the proxy materials that can be used for such study can be calcite-cemented sandstone or preparing compacted sample with a mixture between barite/gypsum illite and kaolinite powder, and chalk of micritic, tight and argillaceous family.

Finally, the complementary results of barite precipitation in kaolinite at reactant concentration of 4 mM and 20 mM showed generation of cracks after longer experimental times into the sample. This addresses this issue of mechanics in such system. Thus, along with precipitation experiments proposed previously, the diffusion cells can be attached to displacement probes to measure the pressure evolution as barite/gypsum or any other mineral starts to precipitate into the studied porous samples. Such pressure probe testing can be carried out on material of different tightness and precipitation of different amount of same mineral. For each case, the threshold pressure after which crack will occur can be determined. Thus, a range of pressure thresholds can be obtained. If the pressure is significant, then a set of experiments could be devised in triaxial cells in pressure/constraint conditions representative of the storage.

In addition to this broad and extensive range of experimental work, following are some numerical works that are also needed to be carried out:

1. to develop models that can integrate characteristics of the porous materials (pore size distribution, surface charge);
2. to develop kinetic rate relationship to take into account dependence of precipitation on pore size (Emmanuel & Berkowitz, 2007) and also on the type of growths (nucleation, supersaturation);
3. to develop models able to take into account surface charge of newly formed minerals (semi-permeable effect), if any.

To conclude, all the experiments and numerical work carried out in this thesis and the one that are proposed in perspectives will inevitably help increase the predictability of chemistry transport codes.

3 References

Bardenhagen, I., Yezerska, O., Augustin, M., Fenske, D., Wittstock, A., & Bäumer, M. (2015). In situ investigation of pore clogging during discharge of a Li/O2battery by electrochemical impedance spectroscopy. *Journal of Power Sources*, *278*, 255–264. https://doi.org/10.1016/j.jpowsour.2014.12.076

Berthe, G., Savoye, S., Wittebroodt, C., & Michelot, J. L. (2011). Changes in containment properties of claystone caprocks induced by dissolved CO2seepage. *Energy Procedia*, *4*, 5314–5319. https://doi.org/10.1016/j.egypro.2011.02.512

Descostes, M., Pili, E., Felix, O., Frasca, B., Radwan, J., & Juery, A. (2012). Diffusive parameters of tritiated water and uranium in chalk. *Journal of Hydrology*, *452–453*, 40–50. https://doi.org/10.1016/j.jhydrol.2012.05.018

Emmanuel, S., & Berkowitz, B. (2007). Effects of pore-size controlled solubility on reactive transport in heterogeneous rock. *Geophysical Research Letters*, *34*(6), 1–5. https://doi.org/10.1029/2006GL028962

González-Caballero, F., Cabrerizo, M. A., Bruque, J. M., & Delgado, A. (1988). The zeta potential of celestite in aqueous electrolyte and surfactant solutions. *Journal of Colloid And Interface Science*, *126*(1), 367–370. https://doi.org/10.1016/0021-9797(88)90131-2

Hang, J., Shi, L., Feng, X., & Xiao, L. (2009). Electrostatic and electrosteric stabilization of aqueous suspensions of barite nanoparticles. *Powder Technology*, *192*(2), 166–170. https://doi.org/10.1016/j.powtec.2008.12.010

Mallon, A. J., & Swarbrick, R. E. (2008). Diagenetic characteristics of low permeability, non-reservoir chalks from the Central North Sea. *Marine and Petroleum Geology*, *25*(10), 1097–1108. https://doi.org/10.1016/j.marpetgeo.2007.12.001

Poonoosamy, J., Curti, E., Kosakowski, G., Grolimund, D., Van Loon, L. R., & Mäder, U. (2016). Barite precipitation following celestite dissolution in a porous medium: A SEM/BSE and µ-XRD/XRF study. *Geochimica et Cosmochimica Acta*, *182*(April), 131–144. https://doi.org/10.1016/j.gca.2016.03.011

Prieto, M. (2014). Nucleation and supersaturation in porous media (revisited). *Mineralogical Magazine*, *78*(6), 1437–1447. https://doi.org/10.1180/minmag.2014.078.6.11

RÉSUMÉ

Plusieurs pays tels que la France, la Belgique et la Suisse prévoient de confiner leurs déchets radioactifs de moyenne et haute activité à vie longue dans des installations souterraines sises au sein de formations argileuses profondes. Ces formations constituent en effet de très bonnes barrières ultimes contre la dispersion des radionucléides, de par leur grande capacité de rétention et leur très faible perméabilité. Néanmoins, la dégradation de certains colis de déchets devrait libérer d'importantes quantités de sels nitratés et sulfatés solubles. Ainsi, ces panaches salins en déséquilibre chimique avec l'encaissant devraient conduire à des phénomènes de dissolution/colmatage, faisant évoluer localement la structure porale de la roche argileuse. Aussi, pour estimer la performance de telles installations souterraines, l'évolution des propriétés de confinement de ces roches en réponse à ces processus physicochimiques se doit d'être étudiée, et ce, sur des échelles de temps et d'espace représentatives du stockage. Cela est réalisé à l'aide de codes couplés chimie-transport basés sur une approche continue, avec la définition de volumes élémentaires représentatifs (VER). Cependant, ces codes s'appuient pour leurs simulations sur des relations empiriques, telle la relation d'Archie, utilisée pour décrire l'effet de rétroaction de la chimie sur les propriétés de transport diffusif. De ce fait, il est primordial, avant les simulations long-termes. Dans ce cadre, le présent travail de thèse s'est intéressé au développement de telles expériences de diffusion réactives pour estimer (i) l'impact de la précipitation de minéraux sur les propriétés de confinement de matériaux poreux "modèles" et (ii) la capacité des codes de chimie-transport à reproduire ce jeu de données expérimentales. La mise au point de ces expériences simplifiées a nécessité de se focaliser sur trois matériaux poreux « modèles », de la craie, de la kaolinite et de l'illite, choisis pour décrire une propriété spécifique des roches argileuses (charges de surface des argiles ou la structure du réseau poreux). Par ailleurs, deux minéraux sulfatés, gypse et barytine, ont été sélectionnés comme minéraux susceptibles de précipiter car ils représentent deux extrêmes vis-à-vis de leur cinétique de précipitation et de leur solubilité. Dans un premier temps, les propriétés initiales de chaque matériau « modèle » ont été déterminées (distribution de taille de pores, coefficient de diffusion effectif (De) des traceurs de l'eau (HTO ou HDO) ou d'un traceur des anions (36Cl-)). La précipitation de la barytine a été étudiée sur les trois matériaux « modèles », tandis que celle du gypse uniquement au travers des échantillons de craie. Durant ces expériences de diffusion réactives, l'évolution des concentrations des réactifs dans les deux réservoirs enserrant l'échantillon poreux a été suivie, et, après un temps t, le 36Cl- et/ou les traceurs de l'eau ont été injectés dans le réservoir amont pour diffuser au travers des échantillons déjà impactés par la précipitation. En complément des essais de diffusion, des caractérisations des échantillons par micro-tomographie X (µCT) et par observation au Microscope électronique à Balayage (MEB) ont permis de préciser le rôle joué par la structure porale initiale du matériau « modèle » et celui des propriétés intrinsèques du minéral précipitant. Enfin, l'estimation de la robustesse des codes de chimie transport a été réalisée à l'aide de deux codes, HYTEC et CrunchTope à l'aide de simulations 1D et 2D.

MOTS CLÉS

Argilites, matériaux poreux modèles, impact d'un panache salin, loi d'Archie, expériences de diffusion traversante, simulation numérique VER

ABSTRACT

Several countries such as France, Belgium and Switzerland have proposed to host a deep geological facility to confine high and mid-level long lived radioactive waste into argillaceous formations. Such formations are considered as a potential host-rock, because of their very high containment properties, i.e. high retention capacity and very low permeability. However, decay of some radioactive waste is expected to release large amount of soluble salts of nitrate and/or sulfate nature. These saline plumes should generate physicochemical imbalance and, by enhancing mineral dissolution/clogging, could make evolve the local rock porous network. Thus, for safety assessment of such facility the evolution of rock containment properties in response to these physicochemical phenomena over large time and space scale needs to be investigated. This can be done by using diffusion-reaction numerical simulators based on equivalent (macroscopic) continuum approach considering representative elementary volume (REV). But these codes rely on empirical relationships, such as the Archie's law used to describe the feedback of chemistry on the diffusive transport properties. Thus, prior to long-term prediction, it is essential create a data to test and improve the description of the feedback of chemistry on transport. In this view, this thesis work dealt with developing such reactive diffusion experiments to estimate mineral precipitation impacts on containment properties of porous materials under diffusive transport regime and the capability of REV chemistry transport codes to reproduce such an experimental dataset. In order to design these simplified experiments, three proxy porous materials (micritic chalk, compacted kaolinite and compacted illite) were chosen to address specific property describing claystones (clay surface charge, pore size distribution). Two sulfate-alkali minerals, namely barite and gypsum were selected as precipitating minerals, since they present two extremities in reference to their kinetic rate of precipitation and solubility. In a first step, intact properties of each proxy material were determined (pore size distribution, effective diffusion coefficient (De) of water tracers (HTO & HDO) and anionic tracer, $^{36}Cl^-$). Barite precipitation was studied in all the proxy materials and gypsum precipitation was studied in chalk only. During these through diffusion experiments, we monitored the reactant concentration evolution in the reservoirs at both ends of the sample and, after a known experimental time, 36Cl- and/or water tracers could diffuse through the porous samples impacted by precipitation. In addition to diffusive testing, the combined impact of pore structure and intrinsic property of mineral (solubility and kinetic rate of precipitation) on final evolution of mineral in each proxy material was also quantified using X-ray tomography (µCT) and Scanning Electron Microscopy (SEM). Finally, to test the robustness of chemistry transport codes, the results from the reactive diffusion experiments where barite or gypsum precipitated in chalk were numerically described in 1D and 2D using two codes namely HYTEC and CrunchTope.

KEYWORDS

Claystones, proxy porous materials, saline plume impact, archie's law, through-diffusion experiments, REV numerical simulation